Comportement en fatigue à grand et très grand nombre de cycles du DP600 acier dual phase : corrélation entre la température, la vitesse de déformation, et les mécanismes de déformation

Noushin Torabiandehkordi

2017-ENAM-0020

École doctorale n° 432 : Science des Métiers de l'ingénieur

Doctorat ParisTech

T H È S E

pour obtenir le grade de docteur délivré par

l'École Nationale Supérieure d'Arts et Métiers

Spécialité " Mécanique-Matériaux "

présentée et soutenue publiquement par

Noushin TORABIAN DEHKORDI

le 22 juin 2017

High and very high cycle fatigue behavior of DP600 dual-phase steel: correlation between temperature, strain rate, and deformation mechanisms

Comportement en fatigue à grand et très grand nombre de cycles du DP600 acier dual phase : corrélation entre la température, la vitesse de déformation et les mécanismes de déformation

Directeur de thèse : **Véronique Favier**
Co-encadrement de la thèse : **Justin Dirrenberger, Saeed Ziaei-Rad**

Jury

Mme Véronique DOQUET, Directeur de recherche CNRS, Ecole Polytechnique	Président
M. André CHRYSOCHOOS, Professeur, Université de Montpellier	Rapporteur
M. Heinz Werner HÖPPEL, Docteur ingénieur privat-docent, Universität Erlangen-Nürnberg	Rapporteur
M. Samuel FOREST, Directeur de recherche CNRS, Mines ParisTech	Examinateur
M. Bastien WEBER, Docteur ingénieur, ArcelorMittal Maizières	Examinateur
Mme Véronique FAVIER, Professeur, Arts et Métiers ParisTech	Examinateur
M. Justin DIRRENBERGER, Maître de conférences, Conservatoire National des Arts et Métiers	Examinateur
M. Frédéric ADAMSKI, Maître de conférences, Conservatoire National des Arts et Métiers	Examinateur
M. Saeed ZIAEI-RAD, Professeur, Isfahan University of Technology	Examinateur

T H È S E

Arts et Métiers ParisTech - Campus de Paris
PIMM

To My Mother

For all she has given me in life,

To the Memory of My Father

Who would not see me graduate but he would have been the most proud,

To My Husband: Pejman

For all his love and support.

Preface

Yesterday I was clever, so I wanted to change the world.
Today I am wise, so I am changing myself.

Jalaluddin Rumi, Persian poet (1207-1273)

Another summer is approaching and this doctoral thesis is coming to end. I have inexplicable feelings as my long educational carrier is almost at its end. Reading the keywords of my thesis, I find some words about which I did not have any clear idea three years ago. During this three year study I have learnt a lot, however, I find myself at the beginning of a long path, obsessed by a lot of questions and full of enthusiasm for learning more. During this three year journey, besides the scientific development aspects, I obtained valuable experiences which I carry with me for the rest of my life. Looking back, I have experienced both gratifications and disappointments. I may summarize my motivation state during the past three years by a multi-stage diagram inspiring from the so-called multi-stage S-N curve of the materials up to very high cycle fatigue regime! Nonetheless, my diagram has an inverted trend compared to the latter. Stage I of this curve corresponds to the first year of my doctoral studies that has passed with an increasing trend of enthusiasm and desire. Then it reached a steady state or even a slightly decreasing trend in the second year (stage II) accompanying by some difficulties, frustrations, and confusions. Afterwards at the beginning of the third year (stage III) the motivations started to increase sharply thanks to the hard efforts, support of my marvelous supervisor, as well as new interesting findings and finally reached a maximum at the end, where I am standing today. Whether this diagram reaches a plateau, continues to increase, or even degrades in the coming years (let us say in the very high cycle regime!) is not clear. So here, I would like to develop my own theory: “there exists an infinite motivation in life which always encourages us to go ahead”. This is a theory that I hope to prove to myself during the coming years.

Paris, 10 May 2017

Noushin Torabian Dehkordi

Acknowledgement

Undoubtedly, none of the tasks described in the coming pages would be accomplished without the cooperation with committed and generous people who supported me during this doctoral study.

Firstly, I would like to express my sincere gratitude and my special appreciation to my supervisor, Ms. Véronique Favier, for her warm and enormous support and encouragement all through my PhD studies. I have been highly influenced by her immense knowledge, hardworking, sense of responsibility and above all by her extremely amicable personality. Véronique, je vous adresse mes remerciements les plus sincères pour votre confiance, patience, et soutien. Je suis énormément reconnaissante d'avoir la chance de travailler avec vous.

My profound acknowledgement goes to my co-supervisor, Mr. Justin Dirrenberger for his aid, and his fruitful comments. I deeply appreciate his high sense of responsibility and his encouragements during the past three years. My especial thanks belong to Mr. Frédéric Adamski for his help and guidance, especially in the field of microscopic observations, which have played an important role in this work. Besides, I would like to thank Mr. Saeed Ziaei-Rad for his valuable advices especially in the field of Finite Element Simulations that gave me an insight into the future work of the present study.

I express my greatest thanks to the jury members: Mr. André Chrysochoos, Mr. Heinz Werner Höppel, Ms. Véronique Doquet, Mr. Samuel Forest, and Mr. Bastien Weber for accepting to evaluate my doctoral thesis. Moreover, my particular thanks goes to Mr. Bastien Weber for providing the material and for the fruitful discussions.

Special mention goes to Mr. Nicolas Ranc for his valuable help and guidance in the field of ultrasonic fatigue tests and thermographic studies under fatigue loading. I also express my warmest thanks to Mr. Cyril Gorny for his generous technical aids during my experimental studies. I would also like to thank all the members of PIMM laboratory for their conviviality that encouraged me

to work enthusiastically and cheerfully.

Finally, I extend my deepest gratefulness to my family for their endless love, help, and support;

Words are not enough to express my profound gratitude to my beloved mother. Undoubtedly, all I am I owe to her. Thank you Mom for your unconditional love and support. You have always been my source of inspiration and strength. Thank you for giving me everything and for always believing in me. This is your encouragement which has always motivated me to try, to resist, and not to lose the hope.

I also thank my loving sisters, Mahsan and Mahrokh for all their support and kindness.

At last but not least, I would like to thank the person who brighten up my life every day; my beloved husband Pejman, whose presence is my thesaurus. Coming to France and conducting this PhD thesis is just one part of the lovely journey that I have started beside him. I thank you Pejman from deepest of my heart, for your love, your patience, and your support, without which it would not be possible to conduct this doctoral study.

Abstract

This work is an attempt towards a better understanding of the high cycle and very high cycle fatigue behaviors of a ferritic-martensitic dual-phase steel, with a regard to temperature and strain rate effects, resulting from accelerated fatigue loading frequencies. The influence of frequency on fatigue response of DP600 steel was investigated by conducting ultrasonic and conventional low frequency fatigue tests. Fractography studies and microscopic observations on the surface of specimens were carried out to study the deformation and fracture mechanisms under low and ultrasonic frequencies. Moreover, in situ infrared thermography was carried out to investigate the thermal response and dissipative mechanisms of the material under fatigue tests. The S-N curves were determined from ultrasonic 20-kHz fatigue loadings and conventional tests at 30 Hz. Fatigue life for a given stress amplitude was found to be higher in the case of ultrasonic fatigue whereas the fatigue limit was the same for both cases. Moreover, crack initiation was always inclusion-induced under ultrasonic loading while under conventional tests it occurred at slip bands or defects on the surface. The inevitable temperature increase under ultrasonic fatigue at high stress amplitudes along with the rate dependent deformation behavior of ferrite, as a body centered cubic (BCC) structure, were found as the key parameters explaining the observed fatigue behavior and thermal response under low and ultrasonic frequencies. The discrepancies observed between conventional and ultrasonic fatigue tests were assessed through the mechanisms of screw dislocation mobility in the ferrite phase as a BCC structure. The higher fatigue life and inclusion-induced crack initiations in the case of ultrasonic loading were attributed to the dynamic strain aging, which resulted from the high temperature increases at high stress amplitudes. The existence of a transition in deformation regime from thermally-activated to athermal regime under ultrasonic fatigue loading by increasing the stress amplitude was confirmed. Below the fatigue limit, deformation occurred in thermally-activated regime while it was in athermal regime above the fatigue limit. Under conventional loading deformation occurred in athermal regime for all stress amplitudes. From the analysis of the experimental data gathered in this work, guidelines were given regarding the comparison and interpretation of S-N curves obtained from conventional and ultrasonic fatigue testing. A transition map was produced using the experimental results for DP600 steel as well as data available in the literature for other ferrite-based steels, showing the correlation between thermally-activated screw dislocation movement and the absence of failure in very high cycle fatigue.

Keywords: Very high cycle fatigue, Ultrasonic fatigue, Dual-phase steel, Frequency effect, Infrared thermography, BCC structure, Dislocations, Strain ageing.

Résumé

Ce travail vise à améliorer notre compréhension du comportement en fatigue à grand et très grand nombre de cycles d'un acier ferrito-martensitique dual phase, notamment les effets de la température et de la vitesse de déformation résultant de chargements cycliques à haute fréquence. L'effet de la fréquence sur la réponse en fatigue de l'acier DP600 a été étudié en effectuant des essais de fatigue sur une machine ultrasonique travaillant à 20 kHz et sur une machine conventionnelle travaillant à des fréquences inférieures à 100 Hz. Des études de fractographie et des observations microscopiques à la surface des échantillons ont été effectuées pour étudier les mécanismes de déformation et de rupture. De plus, la thermographie infrarouge in situ a été utilisée pour étudier la réponse thermique et les mécanismes dissipatifs du matériau lors des essais de fatigue. Les courbes S-N ont été déterminées à partir de chargements de fatigue ultrasoniques à 20 kHz et d'essais conventionnels à 30 Hz. La durée de vie pour une amplitude de contrainte donnée est plus élevée dans le cas de la fatigue ultrasonique bien que la limite de fatigue soit identique dans les deux cas. L'augmentation inévitable de la température en fatigue ultrasonique à fortes amplitudes de contraintes, ainsi que le comportement dépendant de la vitesse de déformation de la ferrite, en tant que structure CC, ont été trouvés comme les paramètres clés expliquant le comportement observé en fatigue, et la réponse thermique sous les fréquences faibles et ultrasoniques. Les écarts observés entre l'essai de fatigue conventionnel et celui ultrasonique ont été évalués à travers les mécanismes de mobilité des dislocations vis dans la phase ferritique de structure cubique centrée (CC). La durée de vie plus élevée et l'amorçage de la fissure principale sur une inclusion observés en fatigue ultrasonique ont été attribués au vieillissement dynamique résultant du fort auto-échauffement du matériau aux fortes amplitudes de contraintes. L'existence d'une transition du régime thermiquement activé au régime athermique avec l'augmentation de l'amplitude de contrainte a été mise en évidence. Au-dessous de la limite de fatigue, la déformation a lieu dans un régime thermiquement activé alors qu'elle est dans un régime athermique au-dessus de la limite de fatigue. En fatigue conventionnelle, la déformation est athermique pour toutes les amplitudes de contrainte. Une carte de transition a été produite en utilisant les résultats expérimentaux pour l'acier DP600 ainsi que les données disponibles dans la littérature pour d'autres aciers à base de ferrite, montrant ainsi la corrélation entre le mouvement des dislocations vis thermiquement activé et l'absence de rupture en fatigue à très grand nombre de cycle.

Mots-clés : Fatigue à très grand nombre de cycles, Fatigue ultrasonique, Acier dual phase, Effet de fréquence, Thermographie infrarouge, Structure cubique centré, Dislocations, Vieillissement dynamique.

Contents

Notations

E	Young's modulus
ν	Poisson's ratio
ρ	Mass density
C	Specific heat
k	Heat conduction coefficient
μ	Elastic modulus
η	Viscous modulus
σ_y	Yield strength
σ_{ut}	Ultimate tensile strength
σ_D	Fatigue limit
ω	Angular frequency
f	frequency
U	Cyclic displacement amplitude
κ	Wavenumber
λ	Wavelength
c	Wave propagation velocity
σ_a	Cyclic stress amplitude
σ_c	Critical stress amplitude
σ_{mc}	Mean critical stress amplitude
σ_b	Critical buckling stress
K	Column effective length factor
u	Axial displacement
σ	Axial stress
S	Cross section area
u_s	Displacement amplitude at the ultrasonic horn output
R	Fatigue stress ratio
β	Constant parameter
ϑ	Constant parameter
L	Ultrasonic specimen length
F	Cyclic force
N	Number of cycles
N_f	Number of cycles to failure
ΔK	Stress intensity factor
ΔK_{th}	Threshold stress intensity factor
T_c	Critical temperature
T_{mc}	Mean critical temperature
t	Time
θ	Mean steady-state temperature increase
S_{th}	Thermoelastic heat source
d_1	Intrinsic heat dissipation
$\tilde{d}_1$	Mean dissipated energy
r	External volume heat source
τ	Time constant
$\dot{\varepsilon}$	Strain rate
σ_G	Athermal component of the flow stress

σ^*	Thermal component of the flow stress
T_0	Transition temperature
$\dot{\varepsilon}_0$	Transition strain rate
Δ	Laplace operator
div	Divergence operator
$grad$	Gradient operator

Introduction

Motivations

During the long history of fatigue characterization of metallic materials, numerous investigations have been carried out by many research groups, leading to introduction of several fundamental aspects. One of the most important concepts regarding the fatigue behavior of ferrous metals is the distinct fatigue limit which these materials show at the number of cycles below 10^7, namely the high cycle fatigue (HCF) regime. This conventional fatigue limit has been the basis of engineering design for decades. However, after reports were published in the 1980s on the fatigue failure of metallic materials at loading amplitudes below the conventional fatigue limit at very high number of cycles, a new insight was gained into the fatigue characterization of materials: *Fatigue design based on the conventional fatigue limit does not necessarily guarantee an infinite fatigue life*. Accordingly, a new field of fatigue studies was introduced to academic and industrial research communities concerning the fatigue characterization at the number of cycles above 10^7, which was named as very high cycle fatigue (VHCF).

In recent years, due to economic and environmental considerations, many steel-made components of railways, vehicles, bridges, and offshore structures have to endure for long term loadings up to 10^8-10^{10} cycles. Therefore, there has been a strong demand of various areas of industries for VHCF characterization of materials in order to ensure the long-term safety of various structural components. Regarding the time-consuming and costly nature of conventional fatigue testing methods, the development of ultrasonic fatigue machines was a milestone in the field of VHCF characterization of materials. Working at a resonant frequency of 20-30 kHz, ultrasonic systems enable fatigue loadings up to very high number of cycles in a reasonable testing time. However, this accelerated testing method has been always accompanied by a main question: are the fatigue properties obtained from ultrasonic loading similar to those measured by conventional low frequency testing? The answer has remained unclear for most metallic materials and thus the so-called "frequency effect" has been controversial among researchers. Moreover, this high frequency can result in strong heating of metals undergoing ultrasonic fatigue tests. This issue can be considered as a problematic aspect of ultrasonic fatigue tests which needs to be investigated.

Considering the strain rate- and temperature-dependent nature of materials with body centered cubic (BCC) structure, application of ultrasonic frequency, which renders both high strain rate and temperature increase effects, could bring up challenges for fatigue characterization of these materials. Several published reports have confirmed the existence of frequency effect and strong self-heating in the case of ferrite-based steels. In addition abnormal thermal responses have been

reported for some of these steels under ultrasonic fatigue loading without any explanation for the cause of these phenomena. Nonetheless, there is a lack of coupled thermal and mechanical investigations to explain the mechanisms behind the frequency influence on fatigue behavior of these materials by correlating the strain rate and temperature effects. The present work is an attempt towards filling this gap. For this purpose, DP600 dual-phase steel was selected to be studied. This choice of material is motivated from two practical aspects: Firstly, this dual-phase steel can be a good representative of ferrite-based steels, the study of which can give rise to a better understanding of strain rate and temperature effects on fatigue response of materials containing BCC-structured phases. Secondly, enough attention has not been paid in the literature to VHCF behavior of ferritic-martensitic dual-phase steels and specifically there is not any published data on fatigue characterization of this material under ultrasonic loading. The main objectives of the present research as well as the employed approach will be described in the following sections.

Objectives

Based on the research motivations introduced in the preceding section, the main objectives of the present work can be summarized as follows;

- Correlating the thermal response to the fatigue and deformation behavior of the material;
- Determination of S-N curves up to HCF and VHCF regimes via conventional and ultrasonic fatigue tests, respectively;
- Identifying the fracture mechanisms and deformation modes in HCF and VHCF ranges;
- Studying the effect of frequency on fatigue life and fatigue limit of the material;
- Investigation of the effect of frequency on crack initiation, fracture mechanisms, and deformation regimes;
- Studying the effect of frequency on surface temperature evolution under fatigue loading and on dissipated energy per cycle;
- Justifying the discrepancies between conventional and ultrasonic fatigue testing results by introducing the mechanisms behind the thermal and fatigue response under low and ultrasonic frequencies;
- Developing guidelines regarding the occurrence or absence of failure in VHCF regime based on the experimental data obtained for DP600 steel.

Approach

The methodology employed in this study to accomplish the aforementioned objectives is detailed in the following:

- Conduction of conventional low frequency fatigue tests as well as ultrasonic 20-kHz fatigue loadings;
- In situ infrared thermography under both conventional and ultrasonic fatigue tests;
- Interrupted fatigue tests along with scanning electron microscopy (SEM) and optical microscopy observations on the specimens surface;
- SEM observations on specimens surface after rupture and also fractography studies by SEM observations on fracture surfaces;
- Comparison and interpretation of S-N curves obtained from ultrasonic and conventional fatigue tests;
- Developing a temperature-strain rate transition map to correlate the fatigue response of the material to deformation mechanisms.

Manuscript Structure

This thesis consists of six chapters which are briefly outlined in the following:

Chapter 1 is dedicated to the literature review. In this chapter, the main concepts related to VHCF of metallic materials and ultrasonic fatigue loading principals are introduced. The so-called "frequency effect" under ultrasonic loading and its related mechanisms for low carbon steels and high strength steels are described. Afterwards, thermographic studies as rapid fatigue characterization approaches are introduced and related application examples are provided for conventional and ultrasonic fatigue loadings. Finally, the main characteristics of dual-phase (DP) steels are specified. The main results of researches conducted on microstructural investigations of DP steels under fatigue loading, including microstructural effects on fatigue behavior of DP steels, thermographic studies under fatigue loading, and VHCF investigations of DP steels are presented.

Chapter 2 deals with the introduction of the studied material and the experimental procedure employed in this work. All testing setups and procedures, including the ultrasonic fatigue machine, the servo-hydraulic conventional fatigue testing system, infrared thermography technique, and the detail of specimens design and preparation are introduced in this chapter.

Chapter 3 presents the experimental results obtained from thermographic studies and self-heating measurements. The presented results include the temperature variations under cyclic loading, self-heating curves, heat source estimation and dissipated energy per cycle measurements under ultrasonic 20-kHz loadings as well as conventional 50- and 80-Hz frequency fatigue tests.

In Chapter 4, the fatigue characterization results obtained from ultrasonic and conventional fatigue tests are presented. These results include the S-N curves, fractography studies, and microscopic observations on the specimens surfaces to reveal the deformation mechanisms, fatigue crack initiation and growth, and fracture mechanisms under 20-kHz and 30-Hz frequencies. The effects of frequency on fatigue life, fatigue limit, deformation and fracture mechanisms are shown in this chapter.

Chapter 5 is dedicated to the discussions and justifications related to the experimental observations presented in Chapters 3 and 4. By correlating the temperature and strain rate effects, the influence of frequency on fatigue life and thermal response of the material is explained and mechanisms are proposed for the observed thermal and fatigue responses.

Finally, the main conclusions of this research and the perspectives for the future work are described at the end of the manuscript.

Chapter 1

Literature Review

1.1 Very High Cycle Fatigue Concepts

1.1.1 Background

"There is no infinite fatigue life in metallic materials". This well-known sentence is the topic of the lecture presented by Claude Bathias [1] in "EUROMECH 382" conference held in Paris in 1988, which was the first conference on fatigue life in gigacycle regime. Traditionally, the concept of fatigue limit at $N=10^7$ cycles has been the basis of fatigue design since the late 19th century and is still in use today; it has been believed that metallic components under fatigue loading do not fail provided that the loading amplitude remains below a critical value i.e. the endurance limit. Therefore, the fatigue limit typically defined at $N=10^7$ cycles, corresponding to the high cycle fatigue (HCF) regime, has been widely used for the design of components subjected to cyclic loading. However, it was in the 1980s when for the first time the Japanese researchers challenged the concept of conventional fatigue limit by reporting material failure beyond 10^7 cycles at amplitudes below the conventional fatigue limit [2]–[5]. The Paris conference can be considered as the starting point of focused academic research in the field of very high cycle fatigue (VHCF), called also gigacycle fatigue, which corresponds to fatigue loadings at very high number of cycles up to 10^8 and more [6]. VHCF failure has been confirmed to exist in various types of metallic materials and steels, see e.g. the pioneer works of Bathias [1], Mughrabi [7], Murakami et al. [8], [9], Nishijima et al. [10], Stanzl-Tschegg et al. [11], and Wang et al. [12]. Many steel-made components of railways, vehicles, bridges, as well as vibrating or rotating machine components such as roller bearings and axels of high-speed trains, require not only high strength but also excellent fatigue properties to endure 10^8 cycles or even longer life time when exposed to cyclic loading. Therefore, in recent years has there been an increasing interest in the so-called VHCF behavior of metallic materials.

1.1.2 The S-N data and the fatigue limit

The VHCF behavior varies from material to material and, up to now it is not possible to make an accurate prediction for the VHCF behavior based on theoretical models. Therefore, the experimental data for different materials is of great importance in this field. The experimental observations reported in the literature during the last decade have revealed that some materials display a fatigue limit at typically 10^6-10^7 cycles while most others exhibit gradual decrease in fatigue strength for gigacycle ranges of loading [13]. Accordingly, several studies evidenced

that Wöhler-type S-N curves or Coffin-Manson fatigue diagrams display a second fatigue limit in the VHCF range [1], [8], [10]. In this case the fatigue diagram is called step-wise or duplex, or more generally, multistage. Moreover, it has been reported that by transition from LCF to VHCF regime, the origin of fracture changes from surface to the interior at non-metallic inclusions. This concept will be addressed in Section 1.1.3.

The materials that can exhibit multi-stage fatigue life diagrams would be categorized into two main classes [7]: Type I materials which exhibit surface failure initiation in VHCF regime. They typically consist of single phase face-centered cubic (FCC) metals such as copper which do not contain inclusions. In contrast, type II materials such as high strength steels which contain heterogeneities in the form of inclusions, pores and coarse second phase particles, display internal crack initiation in VHCF regime. Figure 1-1(a) illustrates the schematic Coffin-Manson plot (plastic strain amplitude $\Delta\varepsilon_{pl}/2$ versus number of cycles to failure N_f) for type I materials, which describes the fatigue life of materials from LCF to VHCF regime. In this case, above the persistent slip band (PSB) threshold, fatigue cracks initiate at the sites of emerging PSBs at the surface, where the rapid formation of extrusions and gradually increasing surface roughness lead to fatigue crack initiation [14]. At VHCF regime, at stress levels below the conventional fatigue limit, fatigue failure can occur because although the stress amplitude is too low for PSBs to develop, the accumulation of slightly irreversible random slip can result in a sufficient surface roughening to initiate surface fatigue cracks [7]. Mughrabi [15] explained that at even lower stress amplitudes irreversibility of slip becomes negligible, leading to a final fatigue limit. Surface crack initiation mechanisms will be explained in more detail in Section 1.1.3.

The schematic Wöhler diagram proposed by Mughrabi [16] for type II materials such as high strength steels is presented in Figure 1-1(b). In reality, the transition between the different ranges is gradual along with some scatter and overlap [7]. In this case, in LCF regime (Region I) fatigue failure is initiated mostly at PSBs at the surface. In VHCF regime (Region III) fatigue failure can occur at stress amplitudes below the conventional limit, originating mostly from internal defects. In this case, finally a true ultimate fatigue limit (Region IV) at sufficiently low stress amplitudes has been considered to exist [10], [17]. However the existence of a final fatigue limit in Region III has been disputed by other researchers, see e.g. [1], [8], [13]. Based on the controversy about the existence of the ultimate fatigue limit in VHCF regime, Pyttel et al. [18] proposed a more general schematic S-N diagram for type II materials as shown in Figure 1-2.

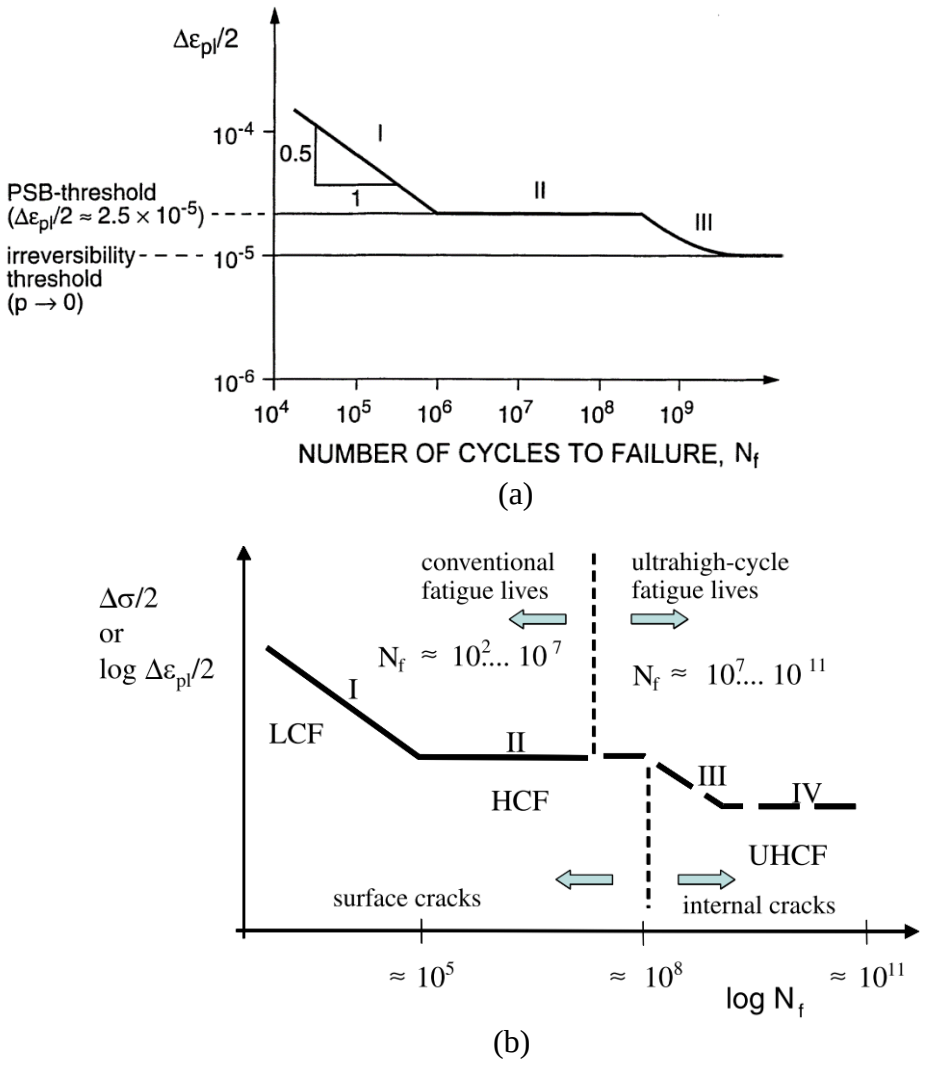

Figure 1-1 **(a)** Schematic Coffin-Manson type fatigue life diagram for ductile type I materials [7] **(b)** Schematic Wöhler diagram for type II materials [16].

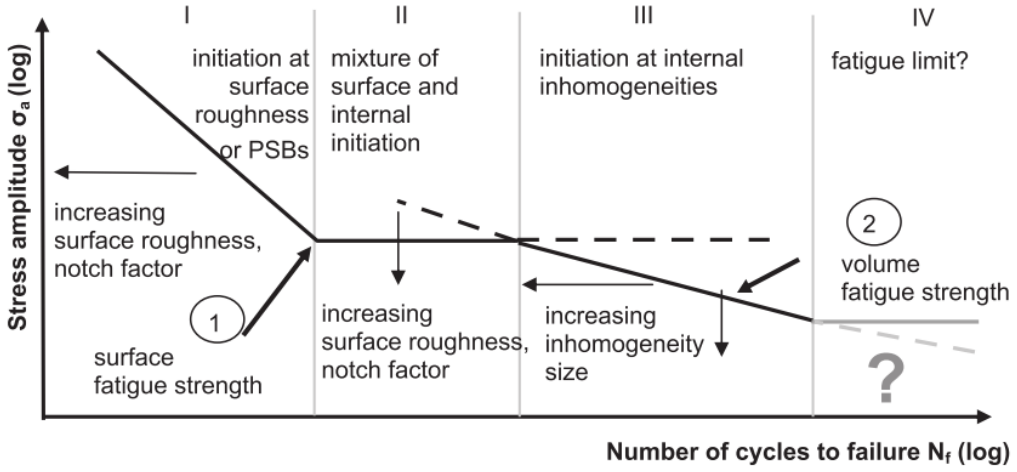

Figure 1-2 Schematic illustration of duplex S-N curve for type II materials [18].

The S-N curves obtained by Sakai et al. [19] for high-carbon bearing steel via axial and rotating-bending loadings are presented in Figure 1-3. A similar trend resulting in duplex S-N curves was found in both diagrams but separation of the S-N curves for the respective fracture modes was more distinct in the case of rotating bending. The transition from surface to internal fatigue failure initiation can be observed in these diagrams.

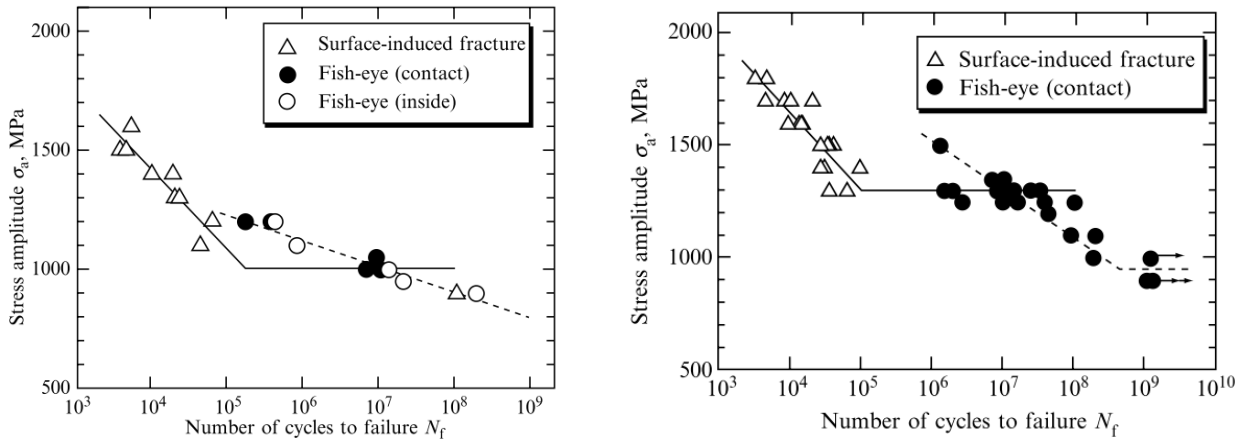

Figure 1-3 S-N diagrams for high-carbon bearing steel obtained under **(a)** Axial loading **(b)** Rotating bending [19].

1.1.3 Fatigue fracture mechanisms

As mentioned earlier, broad experimental evidences suggest that with increasing number of cycles there is a gradual shift from surface to internal inclusion-induced fatigue failure initiation [1], [8], [9], [20]–[22]:

- At high loading amplitudes (LCF) usually many crack initiation sites can be detected at the surface, originating from persistent slip bands (PSBs).
- At lower loading amplitudes (HCF), similar crack initiation sites can be detected at the surface but they are fewer in number than LCF conditions.
- At very low loading amplitudes (VHCF), cyclic slip at the surface is very small and does not give rise to surface roughening thus there is almost no crack growth from the surface and cracks usually form at internal inclusions, which act as stress raisers and promote more slip.

At large fatigue lives the fatigue crack initiation accounts for the vast majority of the total fatigue life [7], [13], [17], [18], [23]. For instance, Wagner et al. [24] showed that for a BCC polycrystal Armco iron loaded up to the VHCF ranges crack initiation consumes ~90% of the fatigue life. Therefore, in the VHCF regime crack initiation is life-determining and it is hence problematic to consider only the propagation of fatigue cracks in terms of fracture mechanics approach. Thus it is important to pay more attention to the fatigue crack initiation in studies concerning VHCF regimes. It should be mentioned that inclusion induced internal cracks can also form in the LCF and HCF ranges but they are not life-determining as long as there are cracks which grow faster from the surface into the interior.

The mechanisms behind the switch from surface to interior crack initiation have been much debated in the literature. It is commonly admitted that cracks dominantly initiate from the surface of the specimen because the cyclic plasticity is larger within the grains located at the surface than within the bulk grains [25]. It has been also reported that the competition between surface and internal crack initiation is highly affected by the surface residual stresses, as compressive residual stresses are favorable for internal crack [26], [27]. In addition, the mean stress value has also been reported to affect the surface to internal crack initiation transition [28], [29]. In a recent work, Gaur et al. [29], studied the effect of mean stress on fatigue crack initiation and growth. They showed that non-defect-induced surface crack initiation occurred most often for R=-1,-0.5, and 0, while for R=0.25 either surface or internal crack initiations from pores or chemically inhomogeneous areas, leading to the fish-eye pattern in the latter case, were dominant.

In the duplex S-N curve of type II materials, generally the first S-N curve in short-life region corresponds to the surface-initiated fracture while the second one in the long-life regime is related to interior-initiated fracture [30]. In other words, it is believed that the transition from surface to internal crack initiation often leads to a duplex S-N curve [17], [31]. It should be noted that although fatigue fracture is mainly caused by the internal inclusions in VHCF regime, surface initiated fracture can also occur in this regime if the defects such as the inclusions are located at the surface [30]. However, from the statistical point of view occurrence of such surface fracture initiations in VHCF regime is rare [30].

In the following sections, the crack initiation mechanisms in different fatigue regimes for type I and II materials will be briefly explained.

- Surface crack initiation in LCF and HCF regimes

Except for some exceptions (internal metallurgical defaults, machining induced surface defects, and compressive residual stresses at the surface), quite generally, in conventional fatigue regimes ($N<10^7$cycles), fatigue damage in ductile materials originates from cyclic strain localization in PSBs at the surface [7], [32]–[34]. This is the case for both aforementioned type I and II materials. It is well accepted that through the back-and-forth slipping of dislocations under cyclic loading, notch-like swellings and deepenings are formed at the surface which are usually called extrusions and intrusions [5], [14], [35]–[37]. The formation of the so-called extrusions/intrusions morphology gradually increases the roughness of the surface up to a critical roughness leading to transgranular crack initiation. In addition the intrusions can be considered as notches with a notch root of atomic dimension which act as stress raisers and thus are potential sites of crack nucleation [38], [39].

Several models have been proposed for the relief evolution along the PSBs. These models are generally based on voids production and diffusion in the PSBs or slip irreversibility. EGM model proposed by Essmann et al. [14] was based on the annihilation of edge dislocations, which preferentially occurs in the walls, where there is a high edge dislocation density. According to this model, vacancies or interstitials are created after two edge dislocations on separate glide planes annihilate [40]. Polak [35] developed a model based on EGM model in which diffusional effects occurring between PSB and matrix are taken into account. Polak and Man [39] proposed that the continuous formation, annihilation and migration of point defects cause the mass redistribution within PSB and between the PSB and the PSB/matrix boundary. This redistribution results in local tensile and compressive stresses that are the sources of slip irreversibility within PSB. Dislocations movements result in the relaxation of the local tensile and compressive stresses leading to the formation of extrusions and intrusions. Figure 1-4 illustrates the well-known irreversible extrusion/intrusion model for the crack initiation at PSBs in the conventional fatigue life regime.

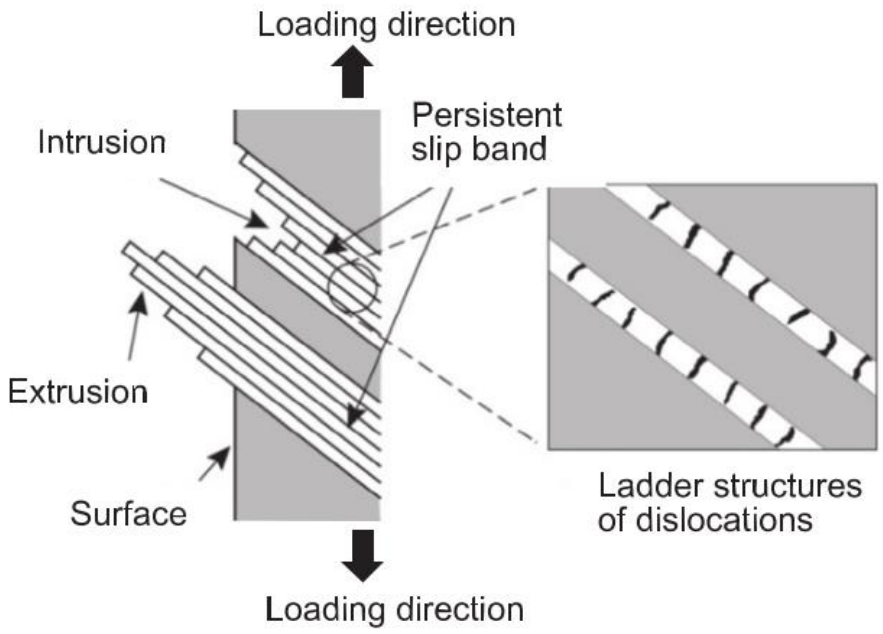

Figure 1-4 Surface fatigue crack initiation mechanism [30].

- Surface crack initiation in VHCF regime (type I materials)

As previously mentioned in Section 1.1.2, for type I materials with no inclusion, VHCF failure can occur at stress amplitudes below the HCF conventional fatigue limit (Region III in Figure 1-1(a)). In this case, fatigue failure initiates at the surface. Mughrabi [7], [16] explained the crack initiation mechanism as shown schematically in Figure 1-5. In this case, although the stress is too low for PSBs to form, cyclic deformation will be accommodated by homogeneous random slip in the matrix dislocation structure, leading to a gradual surface roughening effect. When a critical surface roughness is reached, some valleys in the surface roughness profile act as strong stress raisers so that the local stress at these sites can exceed the PSB threshold resulting in “embryonic” PSB formation. Such PSBs only extent to a modest depth into the material. By increasing the number of cycles cyclic strain is localized in the PSBs and they can extend deeper into the material leading to stage I crack initiation.

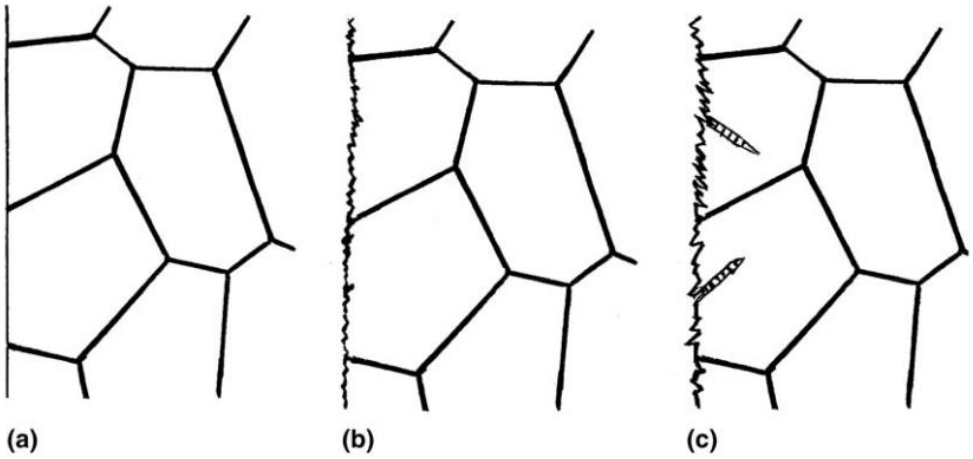

Figure 1-5 Schematic illustration of the mechanism of fatigue failure initiation in the VHCF regime for type I materials: **(a)** Initial state **(b)** Early stage of roughening **(c)** Crack initiation and PSB formation [16].

- Internal inclusion-induced fatigue failure initiation in VHCF regime (type II materials)

In gigacycle regime, corresponding to the second S-N curve (Region III in Figure 1-1(b) and Figure 1-2), fatigue failure generally originates from internal inclusions. In the case of high strength materials, internal inclusion-induced rupture in VHCF regime leads to the so-called "fish-eye" fracture [10], [17]–[19], [22], [31], [41]. The fish-eye which is a characteristic feature of the VHCF failure could be defined as the circular area that surrounds failure origin site, and is formed as a result of internal circular crack propagation.

Figure 1-6 shows the typical fish-eye fracture surface and a higher magnification of the inclusion at the center of the fish-eye for a bearing steel specimen ruptured in gigacycle regime [42]. Generally, there are three mechanisms of fatigue crack initiation at inclusions: (i) debonding of inclusion (ii) cracking of the inclusions (iii) slip band crack emanating from an uncracked inclusion [43]. The first mechanism has been reported in high strength steels while the last two mechanisms were reported to be operative in high strength aluminum [43]. However, there is a lack of experimental studies to discern which crack initiation mechanisms actually operates [16].

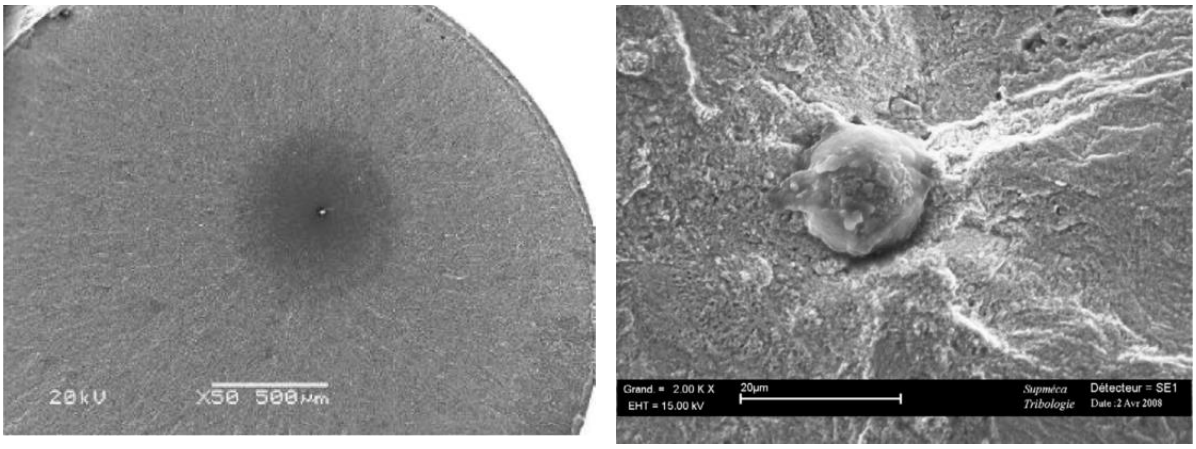

(a) (b)

Figure 1-6 Fish-eye fracture initiation in bearing steel **(a)** Entire fracture surface **(b)** Higher magnification of the inclusion [42].

Usually for high strength steels, a characteristic rough region indicating fine granular morphology occurs around the inclusion at the center of the fish-eye. This area which has a different fractography appearance compared to its surrounding has been named in different ways depending on the related observation approach; This region is named as fine granular are (FGA) by Sakai et al. [19], optically dark area (ODA) by Murakami et al. [8], and also granular-bright facet (GBF) by Shiozawa et al. [4], [31]. The term FGA is more frequently employed in the literature and will be also used in the present study. In Figure 1-7(a), the main regions on the fish-eye fracture surface, including the FGA, are distinguished for a Cr-Ni-W gear steel. In addition, Figure 1-7(b) shows the morphology of the FGA around the inclusion for a bearing steel ruptured in VHCF regime. The morphologies of different areas on the internal inclusion-induced fracture surface are shown schematically in Figure 1-7(c).

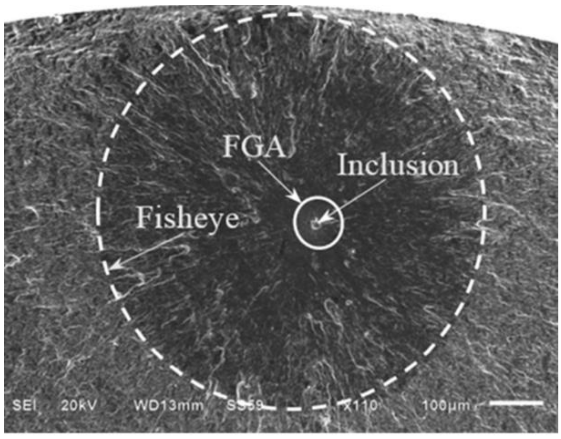

(a)

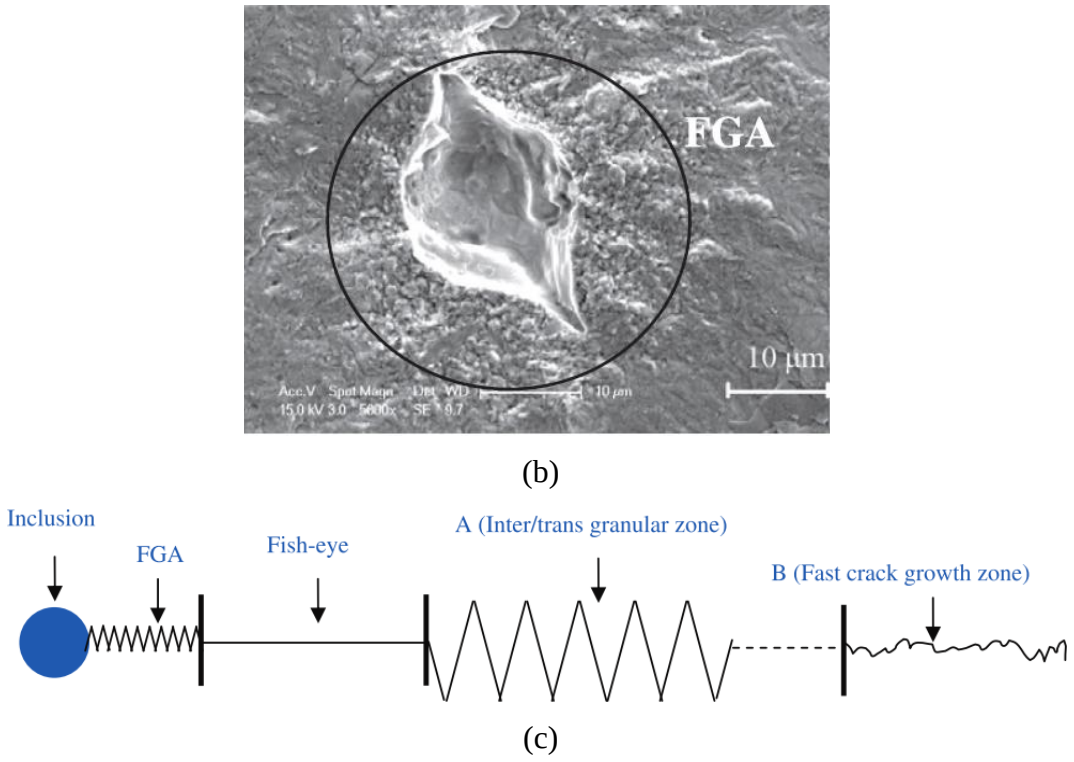

Figure 1-7 **(a)** A typical example of internal inclusion-induced fracture surface with FGA [44] **(b)** Rough morphology of the FGA [45] **(c)** Schematic representation of the morphologies of different areas at the fish-eye fracture surface [45].

It is believed that the formation of FGA corresponds to the period of VHCF crack initiation and consumes most of the fatigue life [16], [44]. Several models have been proposed to explain its formation, such as "hydrogen-embrittlement-assisted cracking" by Murakami et al. [3], and "dispersive decohesion of spherical carbide" by Shiozawa et al. [31]. Moreover, Sakai [22] proposed that micro-scale polygonization is caused in the lath-martensite around the inclusion during a long sequence of cyclic loadings and the FGA is formed as a result of debondings of such very fine subgrain boundaries. Then he proposed a three step mechanism for fatigue crack initiation in VHCF regime, as illustrated in Figure 1-8 [46]: (i) FGA formation by intensive polygonization (ii) Nucleation and coalescence of micro-debondings (iii) spread of micro-debondings over the FGA and formation of a penny-shape crack around the inclusion.

Grad et al. [47] suggested that the refinement of the crystalline structure around the inclusion during the cyclic loading leads to the FGA formation. Nakamura et al. [48] reported that the FGA is formed du to cyclic compression between the fine concavo-convex surfaces.

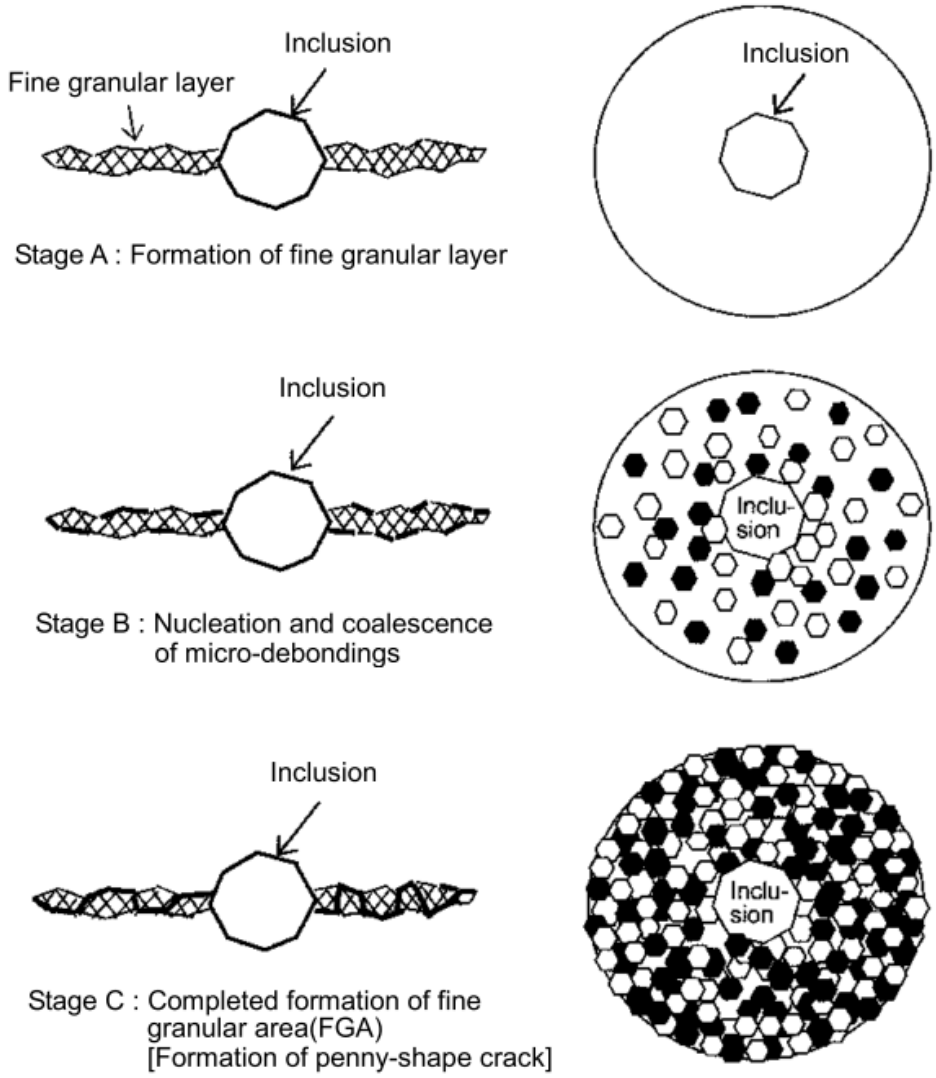

Figure 1-8 Internal inclusion-induced fatigue crack initiation mechanism, proposed by Sakai [46].

Figure 1-9 illustrates the schematic of crack growth diagram representing three different regions; Region III corresponds to unstable crack propagation leading to final fracture [19]. Region II represents the stable crack propagation which can be described by the Paris law and corresponds to the flat area of fish eye surface. Finally, Region I in which the crack growth rate is very small is correlated to the crack nucleation in FGA and is seldom discussed in the literature [49].

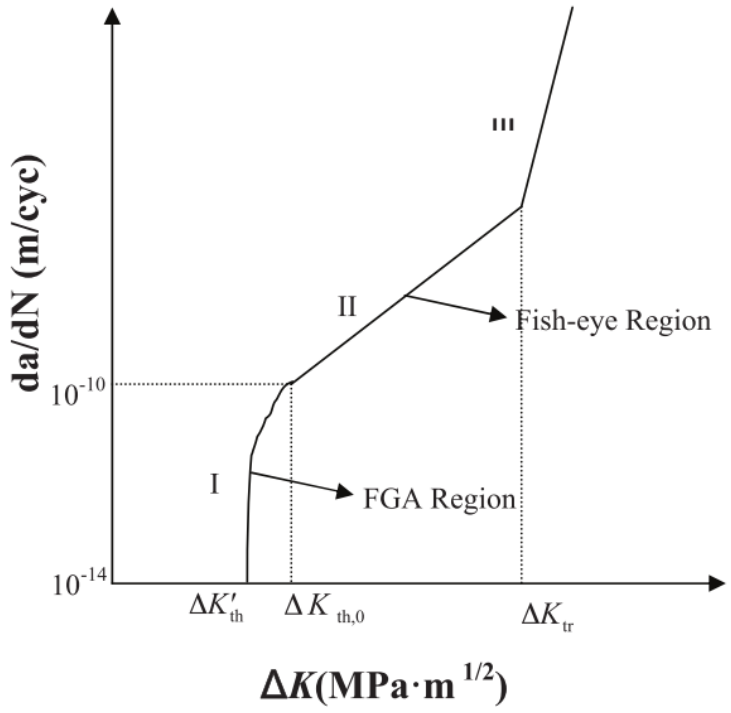

Figure 1-9 Classic crack growth diagram [49].

Fish-eye fracture is not always accompanied by the FGA formation [30], [50]. Figure 1-10 shows an example of fish-eye fracture surface without FGA in the case of high strength steel ruptured in VCF regime. It is believed that FGA appears around the inclusion only if the stress intensity factor, Δk, at the edge of the inclusion is less than the threshold value of crack propagation, ΔK_{th} [22], [46]. If the stress intensity factor value at inclusion edge exceeds the threshold value of ΔK_{th} the FGA does not appear and the crack is supposed to grow from the edge of the inclusion following the Paris law [50]. In addition, it has been reported that the FGA formation requires at least 10^7 cycles under fully reversed fatigue loading (R=-1). Moreover, the formation of FGA is more obvious in high strength steels but there is no clear evidence of FGA for the other materials. The only non-ferrous alloy for which fracture pattern of fish-eye has been reported is Ti-6Al-4V [51]–[53]. In this case, a much rougher area was detected around the initiation site but no FGA formation was found.

In spite of the proposed mechanisms and explanations available in the literature, the influential factors and the related mechanisms of FGA formation have not been fully understood yet and are remained as open questions.

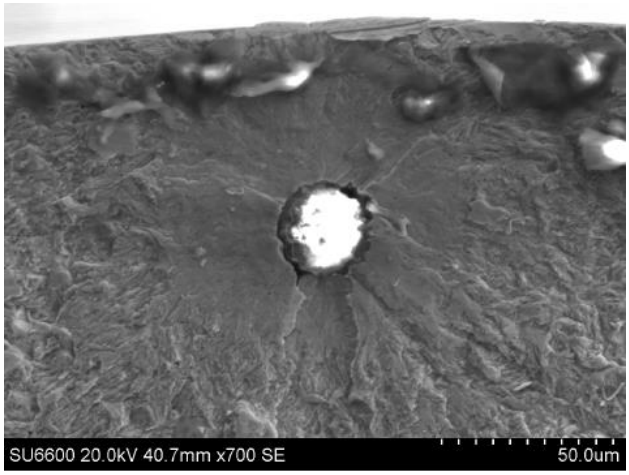

Figure 1-10 Inclusion-induced internal fracture without FGA formation [50].

- Internal non-inclusion induced crack initiation

In spite of the well-established concept of internal inclusion-induced crack initiation in VHCF regime, a few reports exist revealing another type of internal crack initiation in the VHCF regime, which is non-inclusion, induced. For instance, Yu et al. [54]–[56] showed that for bainite/martensite high strength steels both non-inclusion-induced and inclusion-induced crack initiations occur under VHCF tests. In the case of non-inclusion crack initiation, crack was initiated directly from the microstructure of substrate. In this case, the FGA was formed in the center of the fish-eye, as shown in Figure 1-11 (the term ODA was used by the authors). They explained that this phenomenon is related to the competition between the microstructure type and inclusion level to dominate the VHCF behavior.

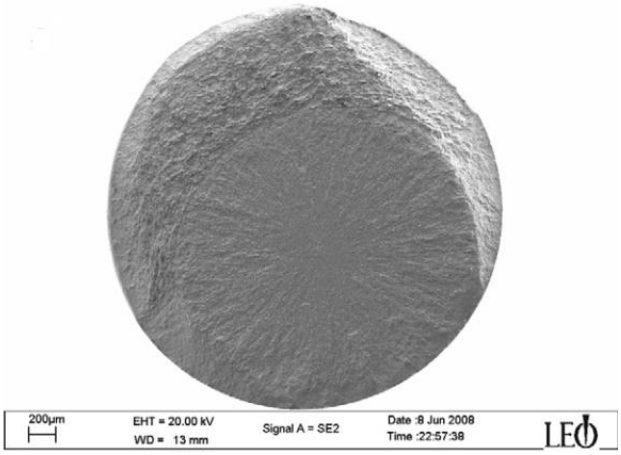

(a)

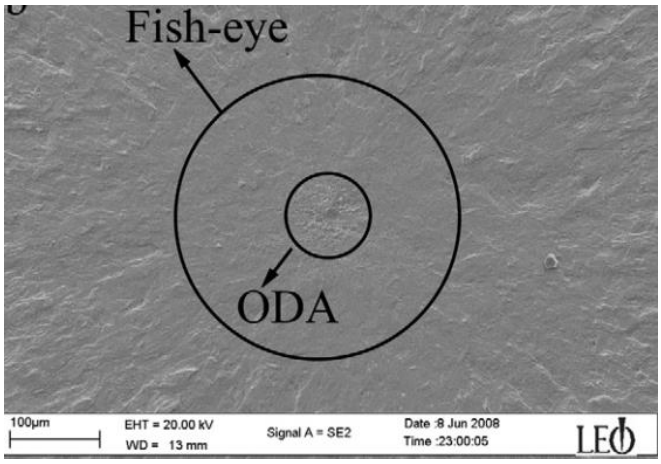

(b)

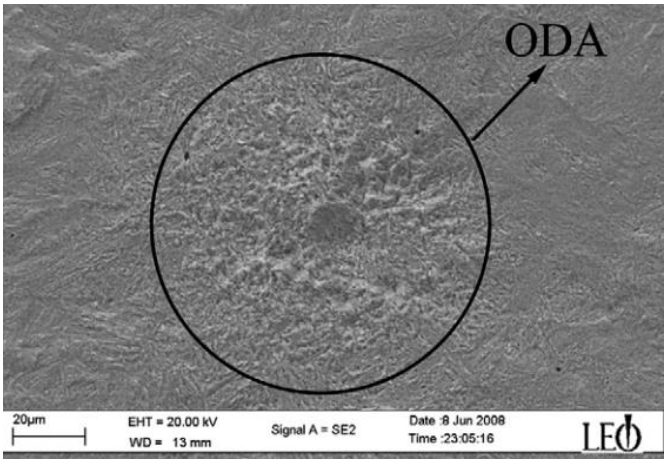

(c)

Figure 1-11 Internal non-inclusion induced fracture of bainite-martensite steel ruptured at $\boldsymbol{\sigma_a}$= 500 MPa, N_f=2.218×10^8 cycles: **(a)** Entire fracture surface **(b)** Fish-eye region **(c)** Higher magnification of FGA (ODA) [54].

1.2 Ultrasonic Fatigue Testing

1.2.1 Introduction of fatigue loading techniques

In the field of mechanical engineering, a variety of components such as automobile parts, train wheels, axles, tracks, and aircraft components are subjected to cyclic loading. Therefore, fatigue testing to assess the resistance of a specific material against cyclic loading has been of great importance in engineering design. Generally speaking, fatigue characterization of materials can be carried out by employing four main types of testing machines:

I. Servo-hydraulic testing systems

These machines which are usually used for fatigue testing in conventional regimes ($N<10^7$ cycles) typically work at frequencies in the range of 10 Hz to 100 Hz. A hydraulic cylinder, which is driven by a servovalve-feedback control, is used to load the specimen. In this procedure, since the oil pressure should be generated anew for each cycle, the overall energy consumption is high.

II. Resonant and forced-vibration machines

Traditional resonant testing machines are mechanical vibration systems consisting of a spring-mass, which functions as an electromagnetically driven oscillator vibrating at its eigenfrequency. In this system, the specimen is part of the vibration system. Resonant fatigue testing systems allow higher testing frequencies and lower power consumption compared to servo-hydraulic machines. The typical frequencies of these systems lie in the range of 50-250 Hz. Nowadays a variety of forced vibration-based systems working at frequencies of 500 Hz or 1.8 kHz are also available [57], [58]. Electromagnetic resonant fatigue test machines working at the frequencies of 40-300 Hz have been also developed [59].

III. Rotating bending systems

Rotating bending systems were the first fatigue testing machines and Wöhler was the first who used them for measurements of fatigue data and defining the endurance limit [60]. The first reports of VHCF rupture of high strength steels ($N_f>10^8$ cycles) at amplitudes below the conventional fatigue limit were developed by using this type of fatigue loading system [2]–[5]. Rotating bending fatigue machine applies a predefined bending stress to a cylindrical specimen via a certain bending moment. Figure 1-12 shows a rotating bending

machine developed by Sakai at al. [61]. These systems, which can achieve frequencies ranging from 0.1 Hz to 200 Hz, are robust and reliable with a cheaper construction and operation than the servo-hydraulic machines. One disadvantage of this machine is that since the specimen usually rotates around the bending stress axis, the stress distribution along the cross section is not uniform. Employing multiple-axis cantilever type rotating bending fatigue machines considerably reduces the testing time [62]. Generally, application of rotating bending fatigue machines has made an important contribution to material fatigue characterization in VHCF regimes, especially by Japanese and Chinese scientists, see e.g. [9], [19], [22], [43], [63]–[66].

Figure 1-12 Dual-spindle rotating bending fatigue testing machine [61].

IV. Ultrasonic machines

Present developments of new industrial machines provide possibility of higher loadings, higher speeds and high reliability in order to increasing efficiency as well as cost saving. Therefore, many industrial and vehicle components have to withstand a large number of cycles, more than 10^8, during service. The conventional fatigue testing does not have practical capability to provide fatigue results in the VHCF regime. This could be successfully accomplished using ultrasonic fatigue test machines, which work at frequencies in the range of 15-30 kHz with the typical frequency of 20 kHz. This high

frequency offers drastic decrease in time and subsequently in cost of fatigue testing. In fact ultrasonic fatigue testing is a resonance technique operating at the frequency of ~20 kHz which can reduce the testing time by a factor of 20-100 as compared to the aforementioned techniques [60]. The main components of an ultrasonic fatigue system are a power generator, a piezoelectric transducer, an ultrasonic horn (mechanical amplifier), and measuring and controlling units. The ultrasonic fatigue specimen is usually axially symmetrical with a round or rectangular cross-section. The detail of the ultrasonic machine components and specimen design will be presented in Chapter 2. Concerning the high applied frequency, special attention should be given to the heat damping and controlling the temperature increase. Generally, liquids or compressed air can be used for cooling the specimen. In addition, loading with periodic interruptions (pulsed loading) is a possible procedure to avoid the specimen heating [67].

1.2.2 History of ultrasonic loading

The first application of resonance fatigue testing refers to the beginning of 20th century, when Hopkinson developed the first electromagnetic resonance system in 1911, working at the frequency of 116 Hz [68]. Up until then, the maximum achievable testing frequency with a mechanically driven system was 33 Hz [68]. In 1925 Jenkin used the similar technique to achieve the frequency of 2.5 kHz to test copper, iron and steel wires [68]. After 4 years, in 1959 the test machine of Jenkin and Lehmann reached a 10-kHz frequency with a pulsating air resonance [68]. However, it was in 1950 when the most important step in development of ultrasonic fatigue testing was taken by Mason [69], who introduced for the first time the piezoelectric and magnetostrictive types of transducers. These transducers were capable of translating 20-kHz electrical signals into displacement-controlled 20-kHz mechanical vibrations. He employed the 20-kHz ultrasonic waves to induce material fracture in fatigue. Today, the design of Mason's machine is the basis of most modern ultrasonic fatigue testing machines. The first endurance measurements and S-N curve determinations under fully reversed ultrasonic loadings were conducted in 1959 after the proposition of Neppiras [70]. Afterwards, ultrasonic fatigue testing had been increasingly employed since the 1970s, see e.g. the pioneer works of Awatani et al. [71] in Japan, the research group of Weiss [72], [73], and in particular Stanzl-Tschegg [74] in Austria. For the first time, ultrasonic fatigue crack growth and threshold measurements were started in about 1973 [75]. At that time, the existence of a

fatigue limit in VHCF regime was not the key issue and the obtained S-N data did not go beyond 10^8 cycles. The main objectives of ultrasonic fatigue tests at this period was to conduct time-saving fatigue tests, to study the effect of high frequencies on fatigue process and to control the consistency of the data obtained from ultrasonic test with those measured from conventional fatigue loadings [6]. After introduction of the concept of material failure possibility in VHCF regimes at amplitudes below the conventional fatigue limit, Bathias started his work in ultrasonic fatigue loading with the primary goal of investigating whether a fatigue limit exist in VHCF range of 10^{10} cycles [1]. Moreover, Bathias with Wu [76] and Ni [77] developed computer controlled systems for ultrasonic fatigue testing enabling to follow exactly the desired loading sequences and consequently conducting variable amplitude fatigue loadings by ultrasonic machines.

Today, different ultrasonic fatigue systems are available developed by commercial manufacturers or research institutions. In spite of differences in process control, obtainable accuracy, and possible testing applications, all these ultrasonic systems share the same basic mechanical principles. Constant amplitude and random amplitude ultrasonic testing methods have been employed in industrial applications such as aircraft, automobile, railway, and offshore structures. Particularly, some in-service loading conditions of aircraft fall into the ultrasonic region, for which the application of ultrasonic loading is of great importance [68].

1.2.3 Advantages and drawbacks

Primarily, due to the extremely high loading frequency of 20 kHz, ultrasonic fatigue loading considerably reduces the testing time and makes it possible to investigate the VHCF properties of materials in a reasonable time. For instance, it takes 14 hours to reach 10^9 cycles with ultrasonic loading, while using the conventional fatigue machines with a working frequency of 100 Hz, a time period of 4 months is required to go up to 10^9 cycles. Thus, the rapidity and effectiveness are the most remarkable advantages of ultrasonic testing method. Possibility of variable-amplitude loadings, low energy consumption and maintenance costs, and low noise are some other positive points of this loading technique [60]. In addition, possibility to measure the fatigue crack threshold at very slow crack growth rate is a strong advantage of ultrasonic loading [78], [79].

On the other hand, this accelerated loading technique brings out several shortcomings. All vibrating parts including the specimen should be precisely shaped and sized, and no industrial component testing is possible [60]. The ultrasonic experiments are displacement-controlled and stresses cannot be measured directly. A major problem of ultrasonic loading is the heating of the specimen due to the ultrahigh frequency. Therefore, it is necessary to cool down the specimen by compressed air or nitrogen gas, or by applying intermittent loading method. The last but not least shortcoming of ultrasonic loading is the possible frequency effect on fatigue response of the material [78]. This is the subject of the following section, in which the effect of ultrasonic frequency on fatigue characterizations of materials will be discussed in more detail.

1.2.4 Frequency and temperature effects

As mentioned in the previous section, owing to a high frequency of usually 20 kHz, ultrasonic loading technique allows to reach very high number of cycles in a reasonable time and at lower costs compared to conventional low frequency loadings. However, the potential influence of this ultrasonic frequency on fatigue response of the materials, i.e. the so-called “frequency effect”, has been controversial among researchers [79].

Generally, the influence of frequency stems from two main sources: strain rate effects and time-dependent influence of environment. The former is the case for high ductility and strain rate sensitive materials such as low-carbon steels, while the latter has been reported for some FCC materials such as aluminum alloys [60], [79]–[81]. Low- and medium-carbon ferritic steels exhibit clear discrepancy between fatigue life and fatigue strength, obtained from ultrasonic loading and those measured from conventional fatigue tests [79]. In this case, as a general trend, ultrasonic loadings produce higher fatigue lives than low frequency tests. The elevated fatigue life and fatigue limit under ultrasonic loading have been mostly attributed to the increase of the yield strength due to increasing the strain rate [79], [81]–[86]. The S-N data of several carbon steels obtained from ultrasonic testing and conventional low frequency tests (with the frequencies in the range of 10 to 400 Hz) are presented in Figure 1-13. All these data confirm a frequency effect on fatigue response of the material so that ultrasonic frequency results in higher fatigue limit and fatigue strength.

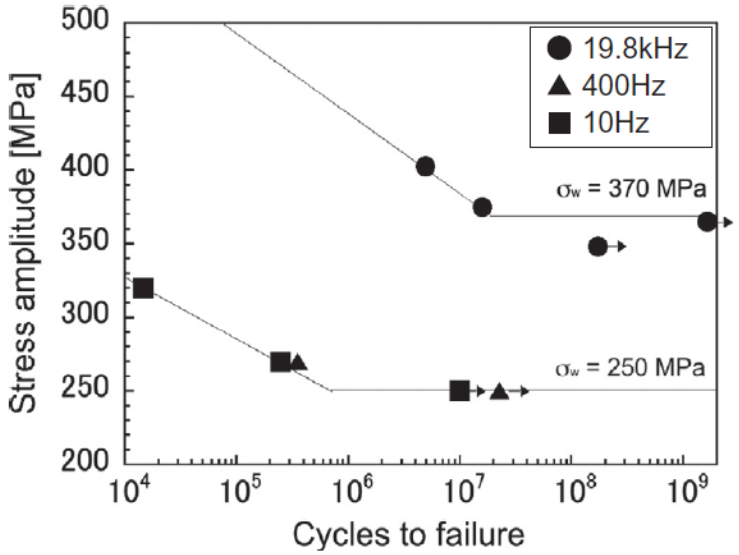
Stress amplitude [MPa]
Cycles to failure
19.8kHz
400Hz
10Hz
σw = 370 MPa
σw = 250 MPa

(a)

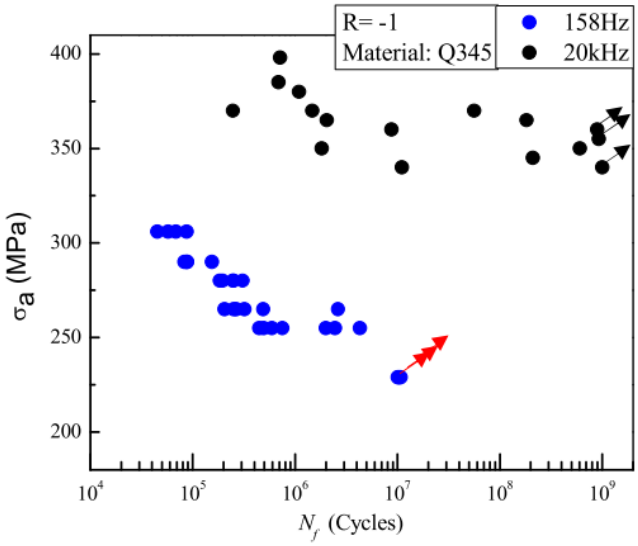
R= -1
Material: Q345
158Hz
20kHz
σa (MPa)
Nf (Cycles)

(b)

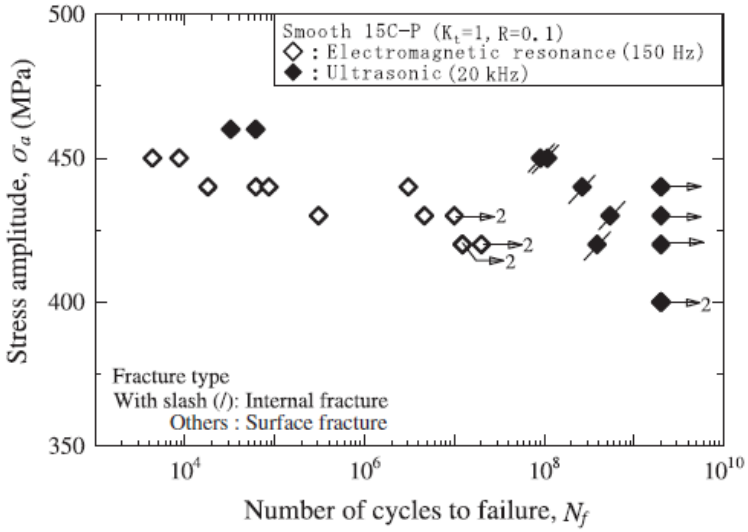
Smooth 15C-P (Kt=1, R=0.1)
◇ : Electromagnetic resonance (150 Hz)
◆ : Ultrasonic (20 kHz)
Fracture type
With slash (/): Internal fracture
Others : Surface fracture
Stress amplitude, σa (MPa)
Number of cycles to failure, Nf

(c)

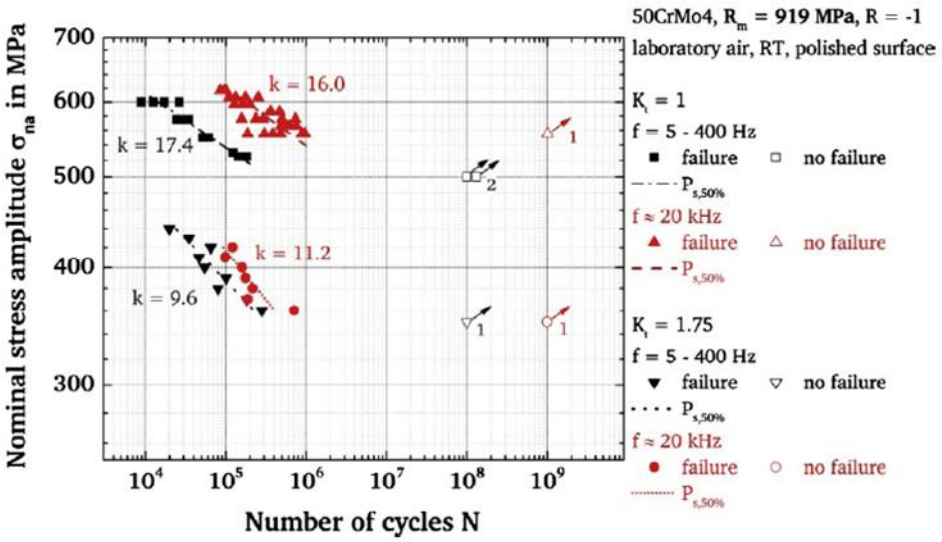

(d)

Figure 1-13 S-N data obtained from ultrasonic and conventional fatigue tests for **(a)** middle carbon steel JIS S38C [83] **(b)** Low-carbon steel Q345 [84] **(c)** Fine-grain 15C-P steel [87] **(d)** 50CrMo4 steel [81].

Tsutsumi et al. [82] reported for a low carbon steel that in the case of conventional fatigue tests the slip bands were abundant in a large area around the crack but scarce under ultrasonic loadings (Figure 1-14). They stated that the longer fatigue life and the higher fatigue limit of low-carbon steels under ultrasonic fatigue are due to a reduction in crack tip cyclic plasticity and subsequent lower crack growth rate during ultrasonic loading, as shown schematically in Figure 1-15.

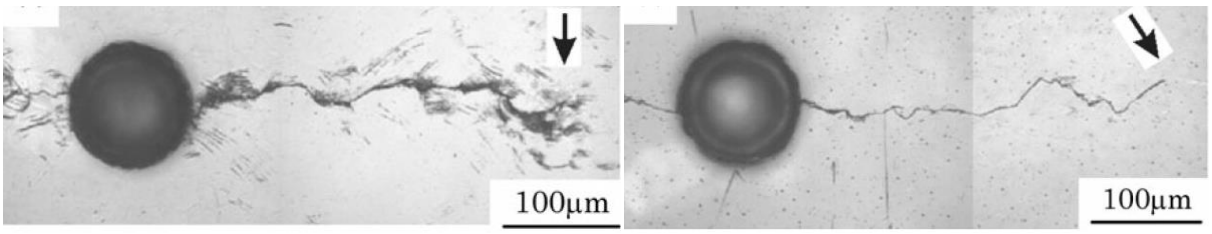

(a) (b)

Figure 1-14 (a) Crack under conventional loading (R = -1, f=10 Hz, σ_a=190 MPa, N = 3.6×10^5 cycles, N_f = 5.1×10^5 cycles) (b) Crack under ultrasonic loading (R = -1, f=20 kHz, σ_a =233 MPa, N = 3.6×10^5 cycles, N_f = 5.1×10^5 cycles) [82].

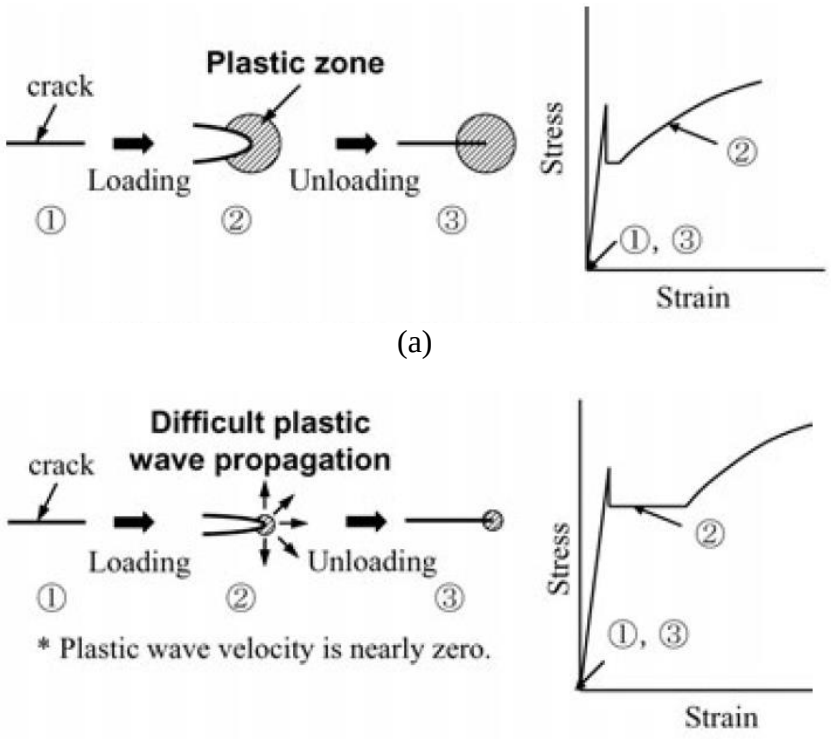

Figure 1-15 Schematic illustration of crack growth mechanisms under conventional and ultrasonic fatigue tests **(a)** Conventional fatigue test **(b)** Ultrasonic loading [82].

Guennec et al. [85], [86] conducted conventional fatigue tests with the frequencies in the range of 0.2 Hz to 140 Hz, as well as ultrasonic 20-kHz fatigue loadings for S15C low-carbon steel and reported a clear frequency effect on the S-N properties, as shown in Figure 1-16(a). They normalized the S-N data by the yield stress at the individual frequencies, as shown in Figure 1-16(b). They concluded that the increase in the yield stress due to increasing the strain rate might explain the elevated fatigue properties by increasing the frequency under usual frequency ranges (0.2-140 Hz) but not for an increase from conventional frequencies to the ultrasonic one. They maintained that under ultrasonic loading conditions some other factors in addition to the strain rate effect on the yield stress should be taken into account. They attributed the higher fatigue life and fatigue strength of the low-carbon steel, under ultrasonic loading to transition of crack initiation mode from the usual transgranular, often reported at lower loading frequencies, to intergranular crack initiation at ultrasonic frequencies. They also showed that under usual frequencies of 0.2-140 Hz, dislocation dipoles as ladder or cell structures are induced whereas in the case of 20-kHz ultrasonic loading, long segments of screw dislocations are produced [86]. These results revealed the fact that the screw dislocations were nearly immobile during the conducted ultrasonic tests. Magnin and Driver [88] also reported that the

transition from transgranular to intergranular damage results in longer fatigue lifetimes by increasing the loading frequency. A surface-to-internal-crack initiation transition has been reported by Furuya et al. [87] as the cause of longer fatigue life of ultrafine-grain steel under ultrasonic fatigue testing.

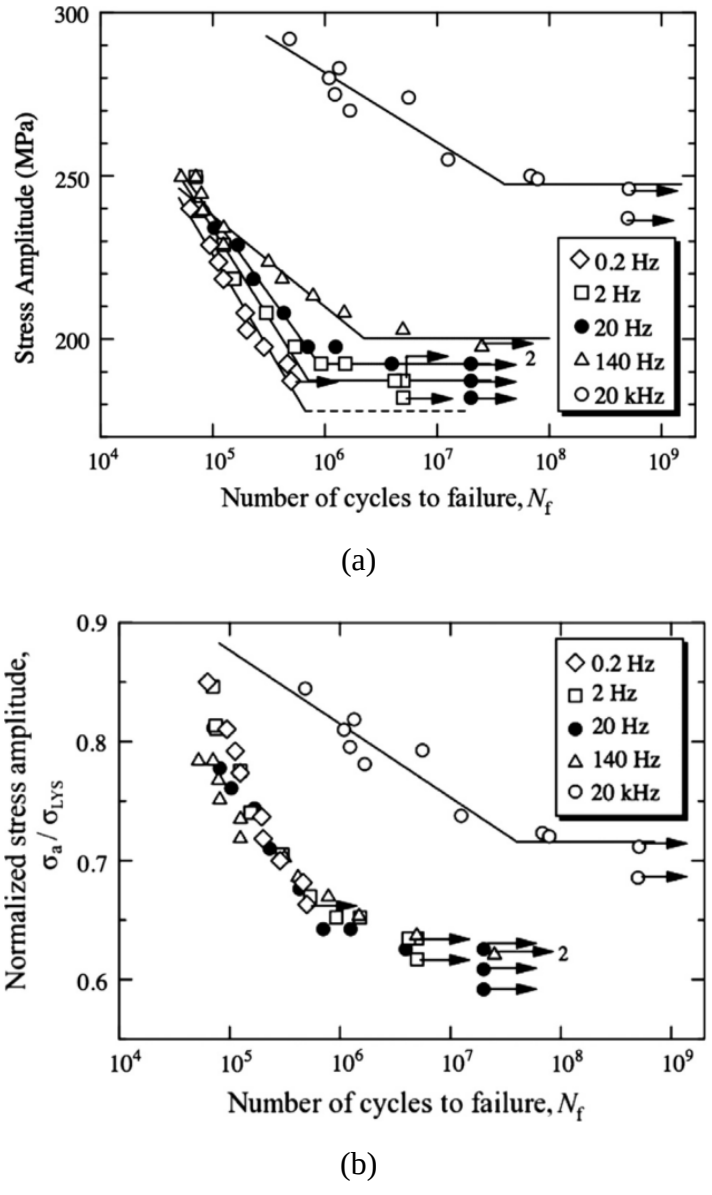

Figure 1-16 (a) S-N data of S15C steel under different frequencies **(b)** Normalized S-N data [85].

On the contrary to low and medium strength steels, high alloy and high strength steels (e.g. martensitic stainless steels) are less susceptible to frequency effects and often there is a good agreement between their fatigue life obtained from ultrasonic loadings and that measured from

low frequency fatigue tests [12], [42], [89]–[91]. For instance the S-N data reported for some high strength steels at conventional and ultrasonic frequencies are presented in Figure 1-17. According to Mayer [79], why the fatigue properties of high strength steels are not sensitive to the loading frequency is due to the very small plastic strain rate involved in HCF and VHCF loadings of these materials.

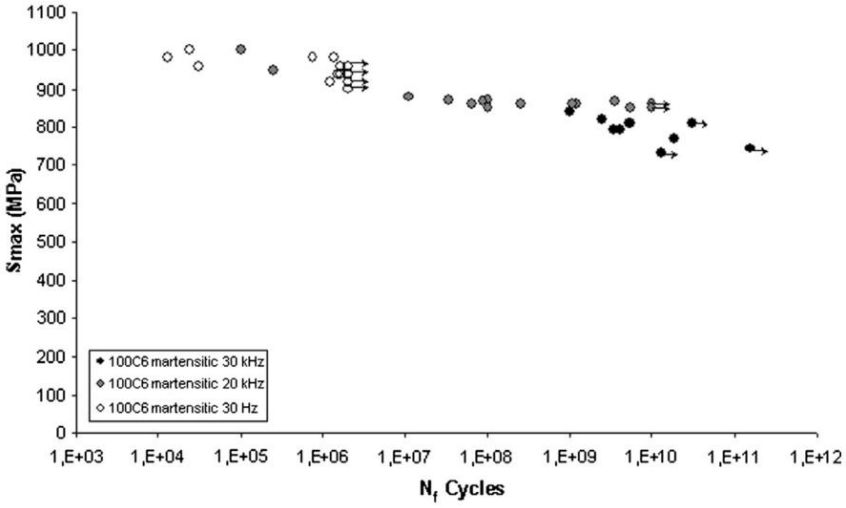

(a)

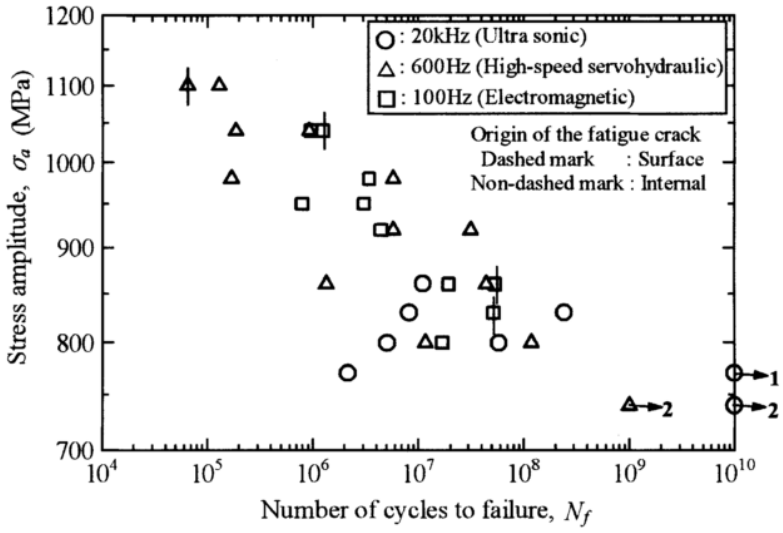

(b)

Figure 1-17 S-N diagrams of high strength steels under conventional and ultrasonic frequencies **(a)** NF 100C6 martensitic steel [42] **(b)** JIS SNCM439 steel [90].

As mentioned previously, strain rate and environmental effects are considered as the main causes of frequency effects in ultrasonic fatigue loading. Because of the high frequency,

significant temperature rises can occur under ultrasonic fatigue loading of metals especially at high stress amplitudes [92]. Thus, temperature can be considered as a third cause of frequency effect in ultrasonic testing [81], [82]. Since heating can usually be avoided by cooling the specimen during the test or by employing intermittent loadings, temperature has not been commonly considered as an effective factor on material fatigue response but is recognized as a rather fictitious effect, which should be excluded by effective cooling or measuring by pulse-pause testing. However, the effect of heat generation cannot be impeded for all materials under ultrasonic fatigue loading even by cooling the specimen and using a pulse-pause mode [55], [93], [94]. For instance, Peng et al. [93] stated that for structural steels with low tensile strength the specimen is prone to heating and burning at high stress amplitudes even by employing intermittent loading along with cooling systems. Ranc et al. [95] reported strong temperature increase up to few hundreds of degrees for C45 steel under ultrasonic loading, in spite of using cooling systems. Yu et al. [55] affirmed that for bainite-martensite steels under intermittent ultrasonic loading, when the stress level is high, the generated heat cannot be dissipated effectively in spite of maximizing the interruption time and minimizing the oscillation time. They found that although the extension of interruption time can improve the VHCF properties, the fatigue life and fatigue limit are lower in ultrasonic loading compared to the conventional 165-Hz frequency tests, as shown in Figure 1-18. They assigned this reduction to the high temperature, which worsens the fatigue properties of the material.

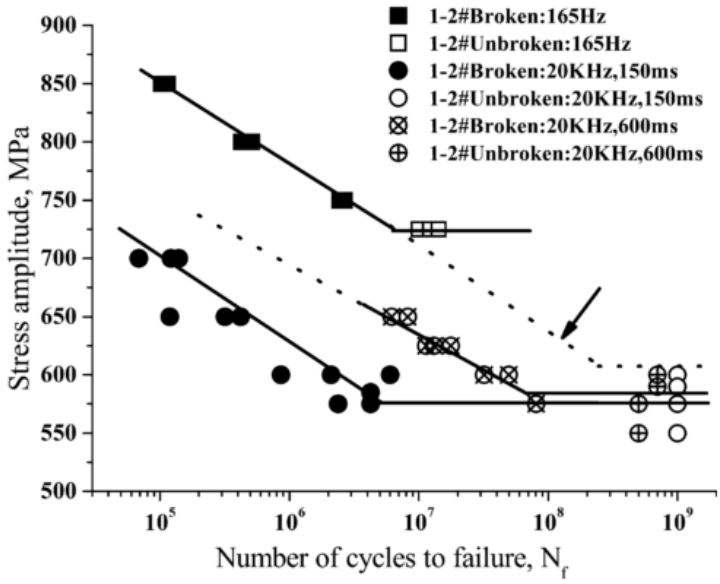

Figure 1-18 S-N diagram of a bainite/martensite steel under 165-Hz and 20-kHz fatigue tests [55].

1.3 Thermographic Studies under Fatigue Loading

1.3.1 Background

Because of the costly and time-consuming nature of traditional fatigue-characterization experiments, several alternative approaches have been developed to carry out a rapid evaluation of fatigue properties. Since fatigue loading is an energy-dissipating process, it is accompanied by temperature variations of the material that undergoes a fatigue test. Therefore, most alternative fatigue characterization methods are based on a thermographic analysis of the material under fatigue loading. The thermographic method is based on the analysis of the surface temperature of a specimen subjected to cyclic fatigue loading. In situ thermographic monitoring allows the detection of fatigue damage in the early stages of fatigue life [96]. Thus, some researchers have employed this approach as a nondestructive evaluation of materials under cyclic loadings (see, e.g. the pioneer works of Stromeyer [97] and Luong [98]). In addition to its rapidity, thermal analysis of fatigue damage provides additional information about the cracks position and dimension [99].

The thermographic fatigue characterization and damage analysis have been performed in the literature via two main approaches:

- Measurements and monitoring of the superficial temperature during fatigue loading (see e.g. [100], [101]). The corresponding procedure of determination of fatigue limit is to subject the specimen to gradually increasing stress amplitudes until failure along with temperature recording. The fatigue limit can be evaluated considering either the steady-state temperature T, or the heating rate ($\Delta T/\Delta N$), where N is the number of cycles. Both procedures involve linear regression straight lines to approximate the thermal data and subsequently find the fatigue limit [99].
- Evaluation of dissipative sources which employs the heat diffusion equation to separately estimate the coupling sources and the dissipative sources to analyze the fatigue process (e.g. [102], [103]). The dissipated energy can also be useful in determination of the fatigue limit and also to detect local plastic deformation [98].

The succeeding paragraphs (Sections 1.3.2 and 1.3.3) provide a brief review to the fatigue thermographic studies reported in the literature.

1.3.2 Thermographic studies under conventional fatigue loadings

The aforementioned thermographic measurements have been widely used to model or predict HCF material properties such as fatigue life or fatigue limit under conventional low frequency fatigue tests. For instance, Munier et al. [104] employed self-heating measurements to develop the S-N-P curves (i.e. stress amplitude-number of cycles to probability of failure) for a variety of steel grades. Figure 1-19(a) shows their obtained S-N-P curves for DP600 steel. They used a two scale probabilistic model with two dissipative mechanisms to estimate the mean endurance limit of the material based on self-heating measurements, as shown in Figure 1-19(b).

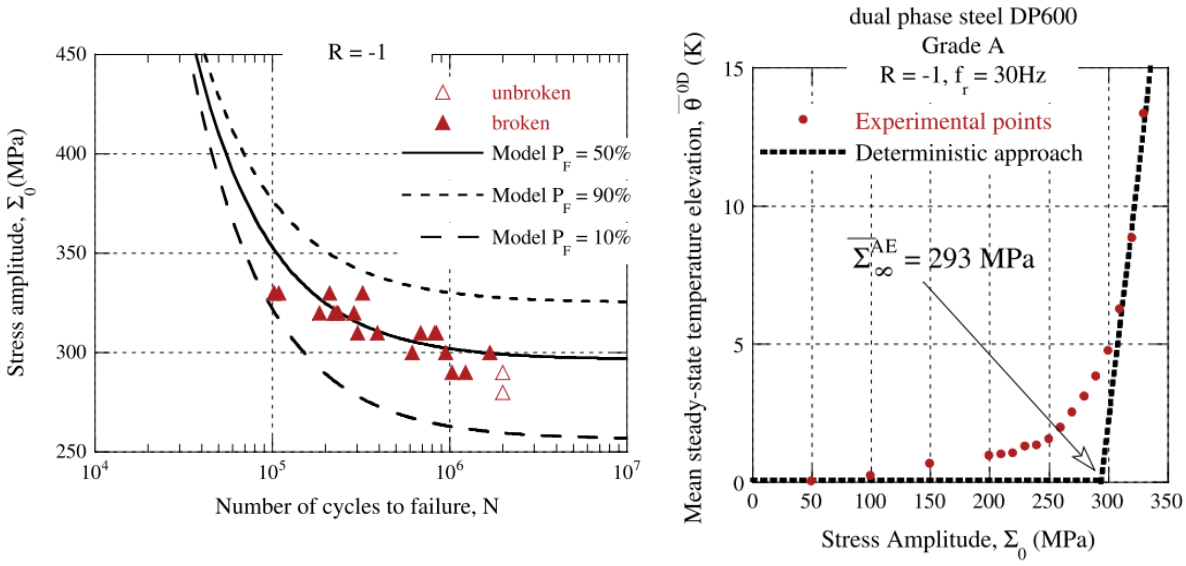

(a) (b)

Figure 1-19 Identification of **(a)** the mean endurance limit **(b)** the S-N data, for DP600 steel based on self-heating measurements [104].

Guo et al. [105] developed a calculation model based on intrinsic dissipation for rapid evaluation of high cycle fatigue parameters (fatigue limit and S-N curve). They verified this model based on the experimental observations for a kind of martensitic stainless steel. By analysis of their experimental results, they showed that there is a critical stress amplitude, σ_0, at which the intrinsic dissipation mechanism transits from internal friction to the combined effect of internal friction and microplasticity, as shown schematically in Figure 1-20. They indicated that this critical stress amplitude corresponds the fatigue limit of the material.

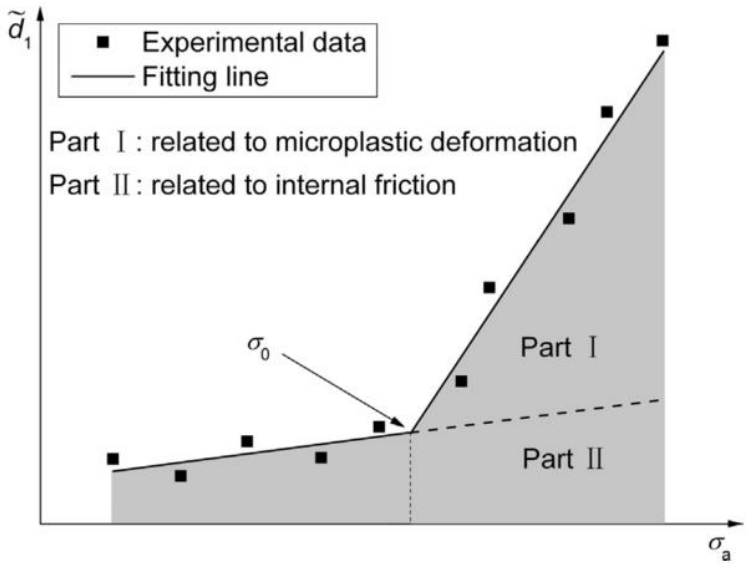

Figure 1-20 Determination of the fatigue limit based on the energy method [105].

1.3.3 Thermographic studies under ultrasonic fatigue loadings

Ultrasonic fatigue loading may induce a much higher temperature increase than conventional fatigue tests that use frequencies below 100 Hz. Therefore, several research studies have been conducted on thermal measurements and calorimetric studies for metallic materials under ultrasonic fatigue loading in high and very high cycle fatigue ranges. These research works can be categorized into two groups: (i) fatigue damage and crack initiation investigations (ii) rapid estimation of fatigue properties. Each category will be introduced in the following sections.

- Fatigue damage and crack initiation investigations

The first category consists of studies that have used dissipation estimations to investigate the fatigue damage process and crack initiation mechanisms in HCF and VHCF regimes [42], [92], [96], [106]–[111]. For instance, Bach et al. [111] developed a new method to monitor irreversible plastic deformation during ultrasonic fatigue loading based on dissipated energy. According to the results obtained for three ferritic-pearlitic steels, they suggested that a particular energy density has to be achieved to promote crack initiation during cyclic loading (see Figure 1-21). Finally, they concluded that infinite fatigue life is possible when cyclic irreversible deformation is too small to provide the stress required for crack initiation or when the nucleated cracks cannot overcome the first microstructural barriers.

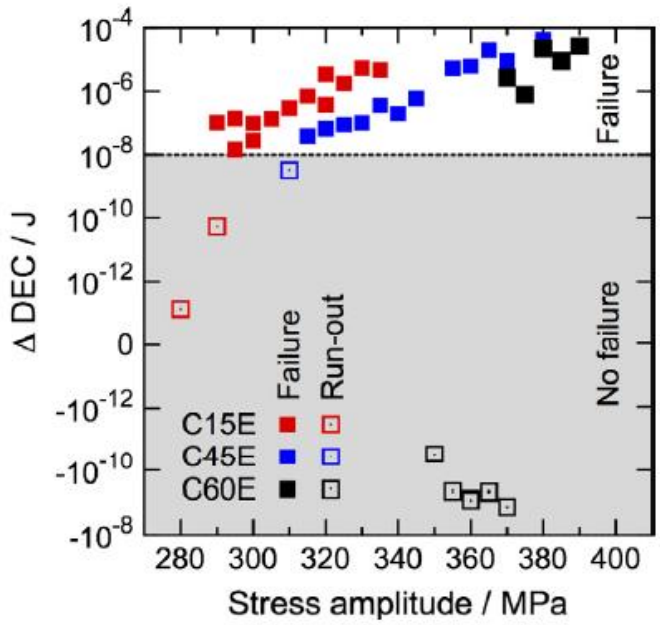

Figure 1-21 Dissipated energy per cycle (Δ DEC) versus stress amplitude for C15E, C45E, and C60E steels [111].

Xue et al. [107] and Wagner et al. [96] employed in situ thermography and fracture surface analysis for different steels and aluminum alloys under ultrasonic fatigue loading and showed that a correlation exists between the temperature fields in the specimen and the fatigue damage process. Krewerth et al. [112] adapted in situ thermography method for ultrasonic loading of G42CrMo4 steel. They correlated the fractography and thermography for precise determination of the crack initiation site, and the time of the final crack growth. Moreover, they used this technique to study crack initiation at non-metallic inclusions. Wang et al. [113] studied the first signs of fatigue crack initiation in HCF regime for Armco iron under ultrasonic fatigue. From temperature recording, they measured the intrinsic dissipation fields and showed that above a given stress amplitude slip marks can be clearly observed on the specimen surface, which was correlated to the main energy dissipation sources. Moreover, as the crack starts to grow, due to the plastic zone at the crack tip a rapid increase can be observed in the temperature. Based on this concept, the number of cycles at crack initiation can be determined from the temperature recording during cycling. This method has been employed by several authors to determine the number of cycles at crack initiation [24], [42], [92], [96]. For instance Bathias [42] employed this method in the case of VHCF of 4240 steel, as shown in Figure 1-22.

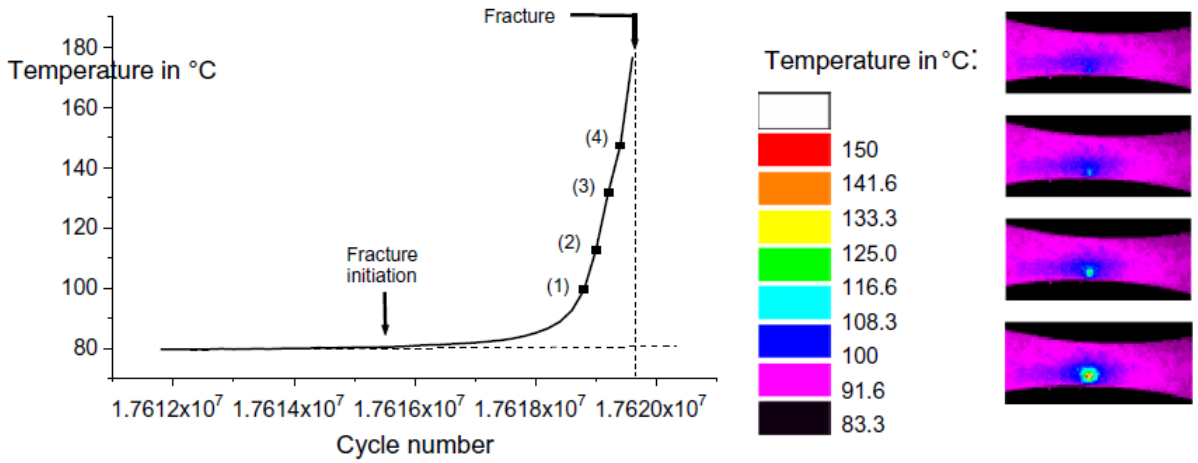

Figure 1-22 Crack initiation detection in VHCF regime by employing thermal measurements [42].

In general, for both low- and high-frequency fatigue tests, the classical temperature evolution of a material that undergoes fatigue straining and damage up to failure consists of three main stages. The first stage is an initial increase at the beginning of the test, the second stage is associated with a steady-state or a slight increase and the last stage is a final sharp increase that is related to fracture initiation (see e.g. [42], [114]). Figure 1-23 illustrates schematically these three stages of temperature evolution. However, some thermal studies of ferrite-based steels under ultrasonic fatigue loadings revealed abnormal thermal responses.

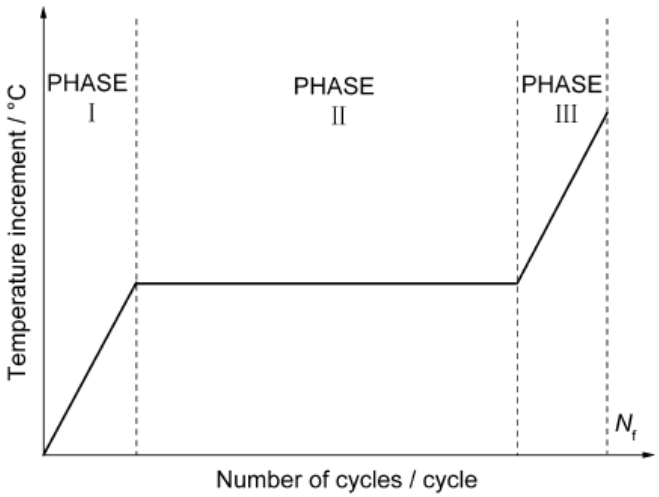

Fig. 1. Typical temperature evolution during fatigue test.

Figure 1-23 Schematic representation of temperature evolution under fatigue loading [105].

Ranc et al. [20] observed that ferritic-pearlitic C45 steel that was loaded cyclically at 20 kHz did not follow this classical thermal response and exhibited a steep increase in temperature up to a few hundreds of degrees, which did not lead to a final rupture. Huang et al. [115] observed a similar abnormal thermal response for another ferritic-pearlitic steel (A48 steel according to the French standard), which showed an unusual change in temperature increase rate without any fracture initiation. This kind of abnormal thermal response has been also reported for Ti-6Al-4V alloy [116]. However, no explanation was provided for the mechanisms behind such abnormal thermal responses under fatigue loading.

- Rapid estimation of fatigue properties

The second group of research works on thermal measurements under ultrasonic fatigue loading has employed thermal response of materials for the rapid estimation of their fatigue properties. For instance, Huang et al. [117], [118] investigated the fatigue dispersion of a titanium alloy and a low carbon steel in VHCF regime using a 20-kHz ultrasonic testing machine. They observed that a plot of the variations of mean stationary temperature increment versus stress amplitude comprised two linear curves with an intersection point, as shown in Figure 1-24. They attributed the change in the slope of this plot to a change in dissipation mechanism from anelastic to inelastic (similar to what has been widely reported for metals under conventional low-frequency fatigue tests, e.g. in [105], [119]).

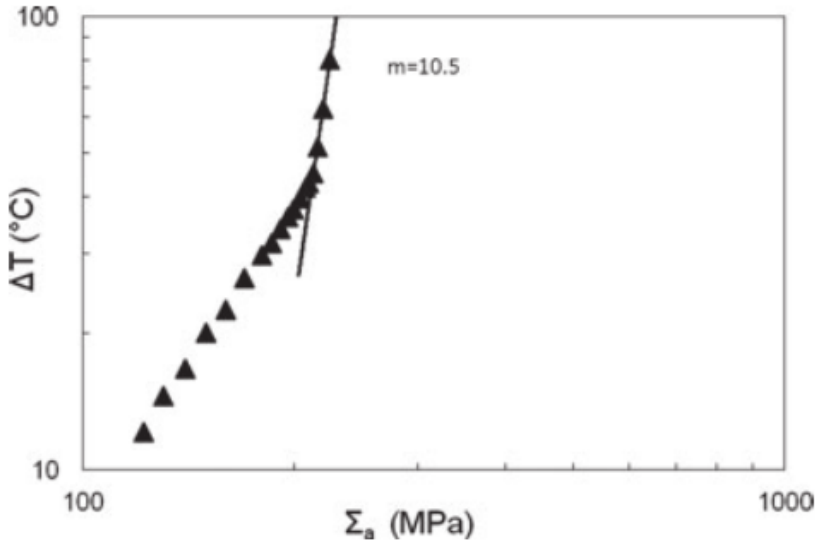

Figure 1-24 Bilinear relationship between the mean temperature and stress amplitude for low carbon steel under ultrasonic fatigue loading [118].

Giertler and Krupp [120] conducted successive ultrasonic fatigue tests along with in situ infrared thermography for 50CrMo4 tempered carbon steel, as shown in Figure 1-25(a), to correlate the local plastic deformation and the macroscopic fatigue behavior. They measured the fatigue limit of the material by plotting the change in the temperature versus the corresponding stress amplitude, as presented in Figure 1-25(b). They observed two different regimes in temperature-stress amplitude diagram. In the first regime temperature changed with the stress amplitude almost linearly and then the temperature increased exponentially in the second regime. They correlated the first regime to local plastic deformation and the second regime to fatigue crack propagation. Using a linear fit through each region, the intersection of the two lines was found to occur at the stress amplitude of 483 MPa. Therefore, the fatigue limit obtained from thermal measurements under ultrasonic loading was in a good agreement with the fatigue strength obtained from conventional 95-Hz fatigue tests (490 MPa), while the fatigue limit obtained directly by ultrasonic tests was significantly higher (680 MPa) due to the frequency effect.

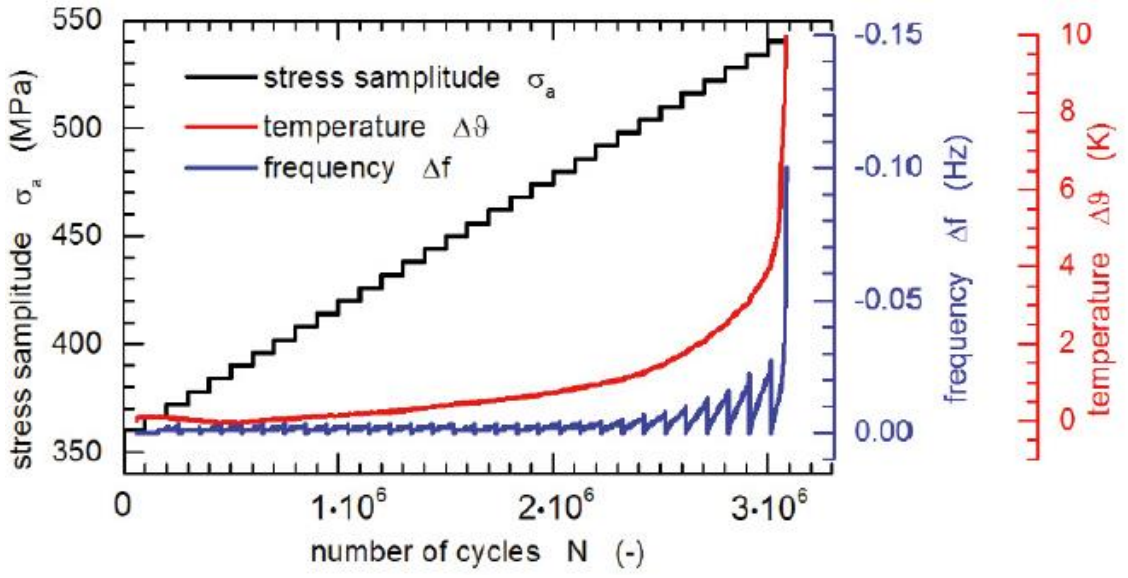

(a)

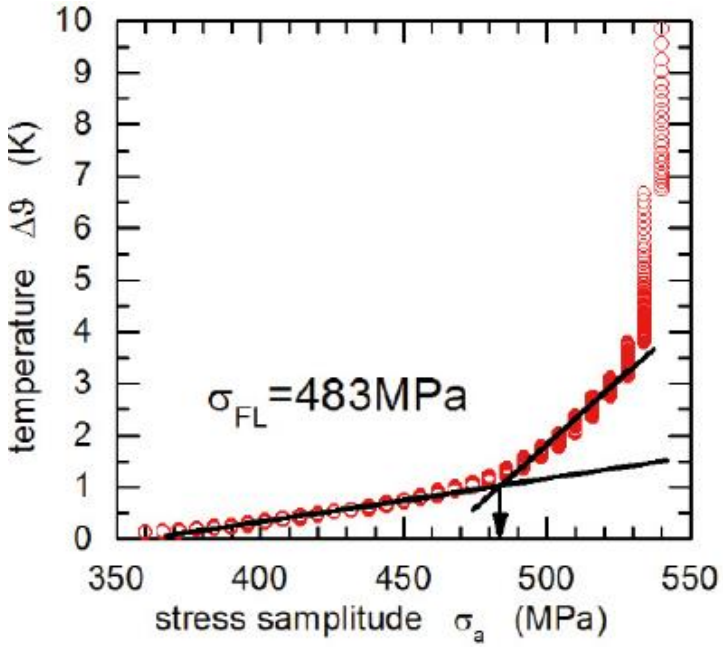

(b)

Figure 1-25 Stepwise ultrasonic fatigue loading of 50CrMo4 steel **(a)** Temperature and frequency changes during loading **(b)** Fatigue limit determination [120].

1.4 Dual-Phase Steel

1.4.1 Introduction

Development of advanced high strength steels (AHSS) was a profound progress in the field of steel production, fueled by the strong demands of automotive industry. Dual-phase (DP) steels which are the most developed and widely used AHSS in automotive manufacturing [121], were developed in the mid-seventies, however their industrial production began in the 1990s [121]. DP steel contains hard martensite islands dispersed in a soft ferrite matrix, as shown in Figure 1-26. This composite microstructure with a soft matrix and a hard reinforcement phase provides an interesting combination of high strength and good formability. Therefore, the passenger safety and weight saving issues, which require a good strength/total elongation balance, are the driving forces for the development and use of DP steels in automotive-related sheet forming operations. Due to their high energy absorption capacity and fatigue strength, cold-rolled DP steels are well suited for structural and safety parts of cars (for crash resistance) such as longitudinal beams, cross members, and reinforcements. In addition, the hot-rolled dual-phase steels with the tensile strength of 590-600 MPa (DP590/DP600) are extensively used for the

automobile wheels fabrication [122], [123]. A schematic representation of DP steel application in automotive manufacturing is presented in Figure 1-27.

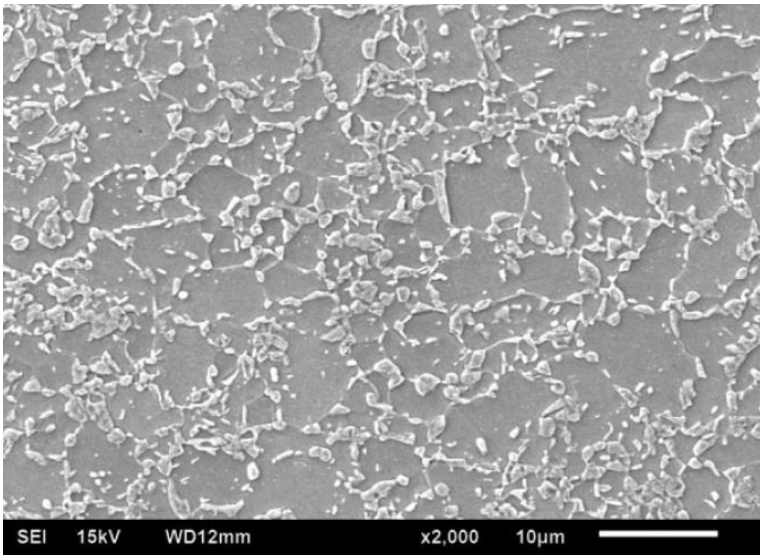

Figure 1-26 microstructure of DP780 steel microstructure [124]. The bright grains ere martensite and the dark grains are ferrite.

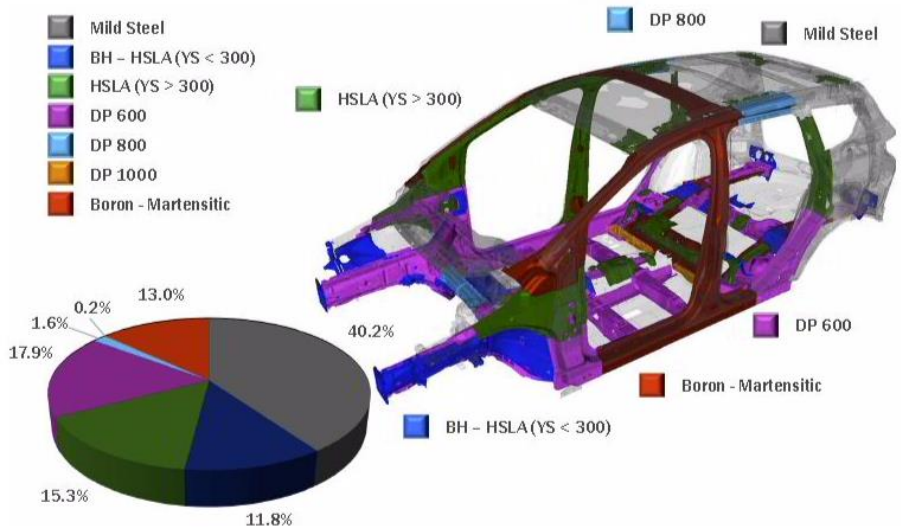

Figure 1-27 DP steel usage in car body [125].

DP steel sheets can be produced by hot or cold rolling. The most common way to produce the dual-phase microstructure is by an intercritical annealing, where austenite and ferrite are stable, followed by a fast quench, resulting in transformation of austenite to martensite. The result is a soft phase of ferrite with imbedded hard particles of martensite. Due to the characteristic of high ultimate tensile strength, low yield strength, good strain hardening, good formability, DP steels have a unique position among advanced high strength steels, as shown in Figure 1-28.

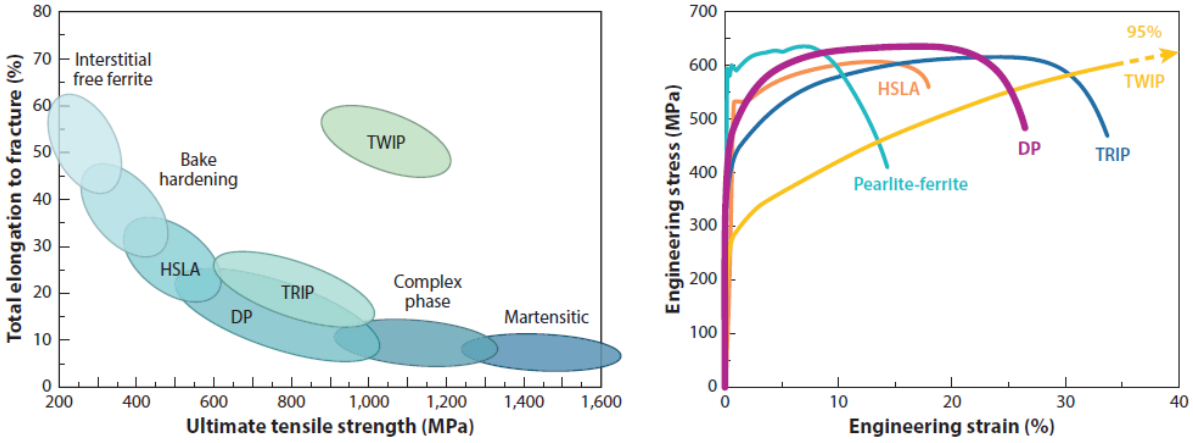

Figure 1-28 Comparison of the mechanical properties of dual-phase steels with other advanced high strength steels [126].

1.4.2 Microstructural investigations of DP steels under fatigue loading

Many researchers have been working on the relationship between the microstructure and mechanical properties of DP steels. Of many papers that have appeared in this area, few have been concerned with the microstructural investigations of fatigue behavior of ferritic-martensitic dual-phase steels, especially in the high and very high cycle regimes. The published works in the field of microstructural studies of DP steels under fatigue loading can be categorized into three main groups: (i) investigations of microstructural effects on fatigue behavior, (ii) thermal studies and self-heating measurements under fatigue loading, and (iii) very high cycle fatigue studies. These categories of research works will be introduced in the following sections.

- Microstructural effects on fatigue behavior of DP steels

The majority of published works in the field of microstructural studies of DP steels under fatigue loading, is allocated to investigations of the effects of morphology, martensite or carbon content and microstructural features on fatigue crack initiation or failure mechanisms of the material (see e.g. [127]–[132]). These works mostly deal with the low cycle fatigue (LCF) regime. For instance, Hadianfard [128] has studied the low cycle fatigue behavior and failure mechanisms of DP600 steel by conducting interrupted LCF tests, scanning electron microscopy (SEM), transmission electron microscopy (TEM), and X-ray diffraction (XRD). It was shown that at high strain amplitudes damage initiated by fractured martensite particles while at low strain amplitudes damage started from ferrite/martensite interfaces and passed through the areas with low martensite densities. Motoyashiki et al. [129] studied the effects of microstructural features such as grain orientation, as well as phase and grain boundaries on crack initiation and crack propagation behaviors in the early stages of fatigue life in a ferritic-martensitic dual-phase steel. They found that surface crack nucleation occurred quite frequently at ferrite/martensite and ferrite/ferrite boundaries, followed by crack propagation in the ferrite grains. This initiation mode was attributed to the mismatch stresses at ferrite/martensite phase boundaries and at high-angle grain boundaries.

- Thermographic studies of DP steels under fatigue loading

The second category includes the research works which examine the fatigue behavior of DP steels in terms of calorimetric effects or self-heating measurements [103], [104], [133]–[138]. For instance, Munier et al. [104] developed the S-N-P diagram for DP600 steel based on thermographic studies, as previously presented in Figure 1-19. In another work, Munier et al. [138] employed self-heating measurements under cyclic loading to predict the high cycle fatigue properties of DP600 steel for different values of pre-strain. Boulanger et al. [103] studied the fatigue behavior of a dual-phase steel in term of thermal effects in order to match the energy manifestations of fatigue and constitutive equations drawn up in a thermodynamic framework. Doudard et al. [133], [134] extended a two-scale probabilistic model for HCF accounting for failure and thermal effects during cycling. They applied this model to DP60 steel [134] DP600 steel [133] under 10-Hz cyclic loadings and showed that the model is able to identify not only the mean fatigue limit but also the scatter of classical fatigue results. Figure 1-29 shows their measurements of temperature evolution and S-N data for DP600 steel.

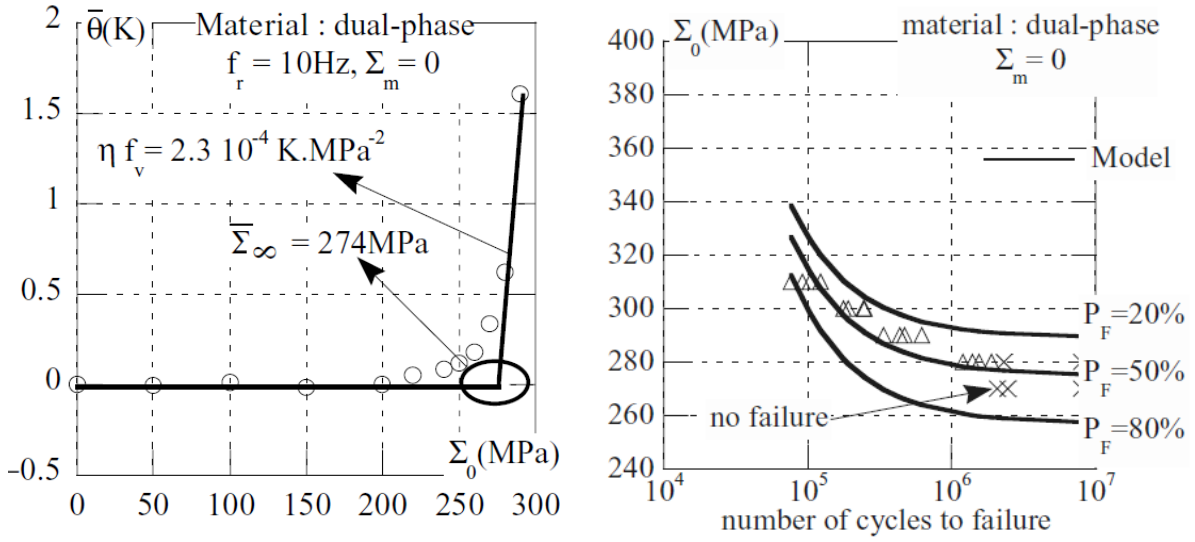

(a) (b)

Figure 1-29 Thermal measurements and fatigue data for DP600 steel **(a)** Temperature evolution versus stress amplitude **(b)** S-N curves obtained from the probabilistic model based on thermal measurements compared to those measured from experiments [133].

Connesson et al. [136] measured the dissipated energy for DP600 steel under traction-traction uniaxial fatigue tests and reported that the dissipated energy depends on material plastic strain. They concluded that the dissipated energy measurements under cyclic loading can be employed as a non-destructive criterion to monitor the microstructural evolution of the material. Moreover, they reported an excellent reproducibility between different specimens of DP600 for dissipated energy measurements under cyclic loading.

Mareau et al. [137] developed thermal measurements for a dual-phase steel under fatigue loadings with different loading ratios (R=-1 and R=-1/3). They measured the dissipated energy per cycle and developed the heating curves as shown in Figure 1-30.

By studying the effect of mean stress on dissipated energy, they reported the existence of two different dissipative mechanisms. At low stress amplitudes there was no mean stress effect suggesting that the dissipative mechanism is anelastic and the strain is recoverable. On the other hand, at high stress amplitudes the results were in agreement with the observation of PSBs, implying that the deformation is unrecoverable and dissipation mechanisms are inelastic.

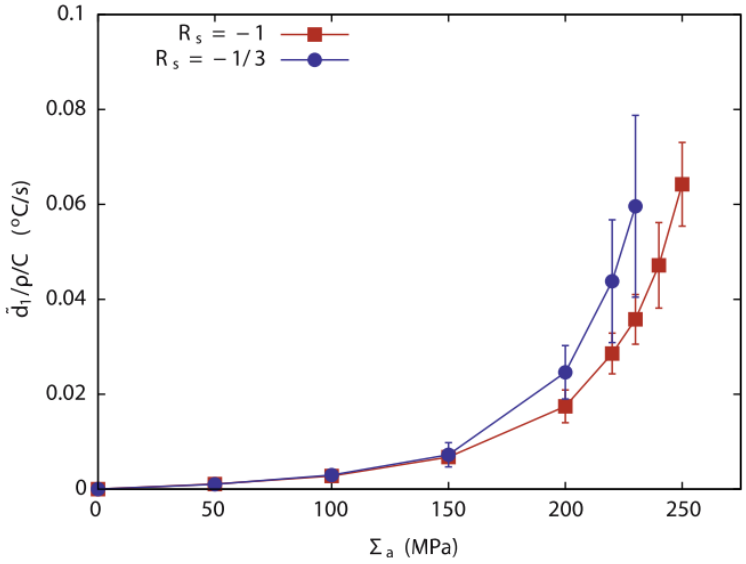

Figure 1-30 Dissipated energy per cycle under fatigue loadings with different loading ratios for a dual-phase steel [137].

Blanche [139] conducted energy measurements during HCF testing at 30-Hz frequency and determined the change in dissipated energy and stored energy over cycles. He found that both energies gradually rose over cycles, indicating a continuous fatigue process.

- VHCF investigations of DP steels

The third group of research works concerned with fatigue behavior of dual-phase steels is related to the very high cycle fatigue studies. Despite several works concerning VHCF of bainite-martensite dual-phase steels [54]–[56], [140], duplex austenitic-ferritic steels ([141]–[143]), or two-phase ferritic-pearlitic steels (see e.g.[111], [144]), published literature data are scarce in the field of VHCF investigations of ferritic-martensitic dual-phase steels; it is limited to the work of Chai in 2006 [145] in which VHCF tests have been performed to investigate the subsurface non-defect fatigue crack origins (SNDFCO). In this work, rotating bending fatigue tests were conducted with a frequency of 600 rpm or 10 Hz up to VHCF regimes to determine the S-N curves and fracture mechanisms. Multi-stage S-N data were obtained as presented in Figure 1-31(a). In addition, a transition of fatigue crack initiation from surface defects and subsurface inclusions to SNDFCO was reported by increasing the fatigue life. Figure 1-31(b) shows the fracture surface with SNDFCO. The author explained that SNDFCO is a damage process caused by cyclic plastic deformation in the soft phase because of deformation mismatch between two phases.

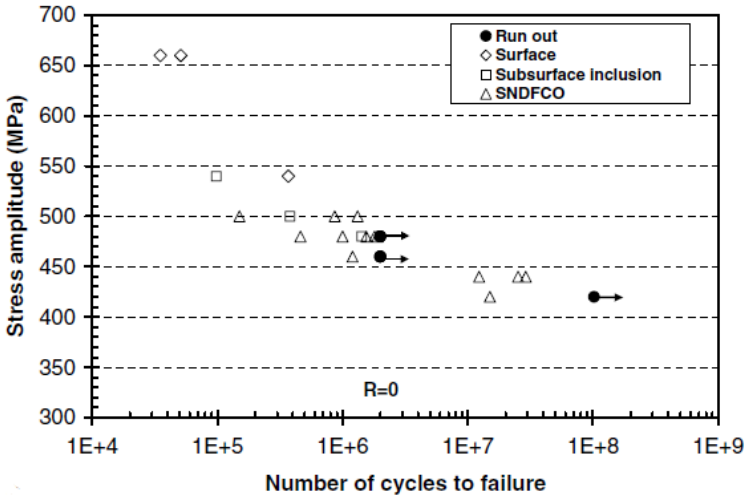

(a)

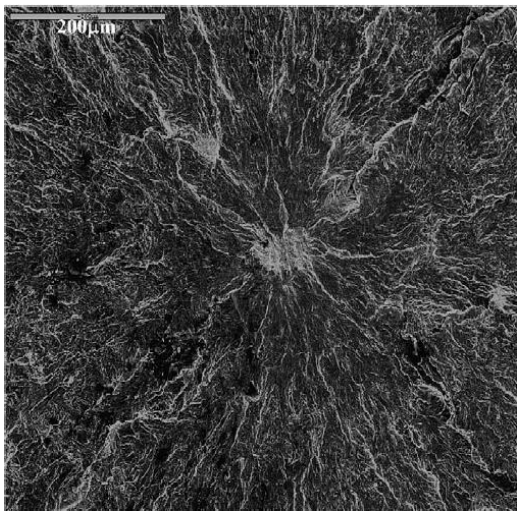

(b)

Figure 1-31 VHCF behavior of a dual-phase steel under rotating-bending loading **(a)** Multi-stage S-N diagram **(b)** Fracture surface with SNDCFO (σ_a = 620 MPa, N_f= 3.60×10^{6}cycles) [145].

1.5 Conclusions and Positioning of the Present Research Work

According to the literature review presented in the preceding sections, there is an evident lack of microstructural investigations of HCF and especially VHCF behavior of DP steels in the published literature. As mentioned earlier, the main application of DP steels is for safety parts in car bodies and for wheel applications. The service conditions predominantly represents HCF and even VHCF conditions for these automotive parts [146]. In addition, knowledge of initiation and propagation of fatigue cracks and deformation mechanisms in high and very high cycle regimes are of great importance, as they can provide an insight into the alloy design and applications.

In this regard, ultrasonic loading technique is an effective tool for VHCF characterization of materials (see Section 1.2), but raises the controversy about the frequency effect, especially for metals with BCC structure, for which the deformation behavior is strain rate dependent. Despite the numerous reports on the so-called frequency effect on fatigue behavior of materials with BCC structure, no systematic investigation has been made on the potential ultrasonic frequency effects on fatigue response of DP steels, the main deformation-carrying constituent of which is ferrite with a BCC structure. More generally, evidence is needed to ensure the applicability of ultrasonic loading to BCC materials with complex microstructures, a good representative of which is dual-phase ferritic-martensitic steel.

In a variety of research works on fatigue loading of BCC materials, the temperature increase has been reported to be less than 100°C, therefore the effect of temperature increase on the fatigue and deformation of the material has not been studied (see e.g. [24], [81], [86], [95], [111]). However, is the temperature effect really negligible? In addition, in some research works concerning thermal measurements of ferrite-based steels, an abnormal thermal response was observed under ultrasonic fatigue loading, in the sense that a steep increase occurred in temperature up to a few hundreds of degrees which did not lead to a final fracture (see e.g. [95], [115]). However, no explanation has been provided for these kinds of abnormal thermal responses.

The present work aims at explaining the high and very high cycle fatigue behavior of ferrite-based steels accounting for strain rate and temperature effects. For this purpose, DP600 dual-phase steel, which consists of a ferrite matrix containing martensite islands, is investigated under 20-kHz ultrasonic loading as well as conventional low frequency fatigue tests. In both cases, the S-N curves are obtained and the effect of frequency on fatigue life and fatigue limit is studied. Fractography studies are conducted to reveal the crack initiation and fracture mechanisms in high and very high cycle regimes. In addition, the effect of frequency on crack initiation and material failure is investigated. Moreover, thermographic measurements are performed and mechanisms are proposed to explain the observed abnormal thermal response of some ferrite-based steels under ultrasonic loading and correlate it to the fatigue and deformation behavior. A strain rate-temperature transition map is developed to correlate the fatigue response of the material to deformation mechanisms by gathering the results of the present research and data from literature for ferrite-based steels.

Chapter 2

Material and Methods

Résumé

Matériau et Méthodes

Ce chapitre traite de l'introduction du matériau et de la procédure expérimentale utilisée dans ce travail. Le matériau étudié est l'acier dual phase DP600 qui a été fourni par ArcelorMittal sous forme de feuilles laminées à chaud de 3,6 mm d'épaisseur. Grâce à ses propriétés mécaniques élevées, cet acier permet d'alléger les structures par une réduction des épaisseurs. Il peut être notamment utilisé dans l'automobile pour les voiles de roues, les profils allégés, et les coupelles d'amortisseurs. La microstructure du matériau, contenant 15 vol.% de martensite, a été étudiée par microscopie optique (MO), microscopie électronique à balayage (MEB) et diffraction d'électrons rétrodiffusés (EBSD). Aucune différence considérable n'a été détectée dans la morphologie des grains dans la direction de laminage, la direction traverse, et la direction normale. À partir de l'analyse EBSD, la taille moyenne des grains a été obtenue à 7µm. Deux types d'analyse ont été réalisés dans ce travail : (i) études par thermographie pour étudier la réponse thermique du matériau sous chargement de fatigue, (ii) essais de fatigue afin d'établir la courbe S-N, étudier les mécanismes de déformation et les faciès de rupture. Pour chaque analyse, deux types d'essais de fatigue ont été effectués : chargement de fatigue ultrasonique à 20 kHz et essais de fatigue conventionnelle à des basses fréquences de 30, 50 et 80 Hz. Tous les essais de fatigue ont été réalisés en traction-compression avec un rapport de charge R = -1. Des éprouvettes plates à section rectangulaire ont été utilisées. Les dimensions des éprouvettes de fatigue ultrasonique ont été obtenues en résolvant les équations de vibration afin d'atteindre une fréquence de vibration résonnante de 20 kHz pour l'éprouvette. Les éprouvettes de fatigue conventionnelle ont été conçues de telle sorte que, pour une même amplitude de déplacement, la répartition de la contrainte au voisinage du centre de l'échantillon soit équivalente à celle des échantillons pour la fatigue ultrasonique. Dans les deux cas, l'amplitude de chargement était faible de sorte que l'échantillon se déforme élastiquement du point de vue macroscopique. Toutes les éprouvettes ont été électropolies après le polissage mécanique, afin d'éliminer les contraintes résiduelles en surface induites par le polissage. En outre, la thermographie infrarouge in situ a été utilisée pour enregistrer la température moyenne sur la surface de l'échantillon sous chargement de fatigue. Dans tous les cas, la température a été mesurée au centre de l'éprouvette dans une zone circulaire de diamètre 1 mm. Enfin, afin de caractériser le comportement mécanique du matériau à haute température, des essais de traction uniaxiale ont été effectués à 350 ° C.

2.1 Material

2.1.1 Introduction and properties

As explained earlier in Chapter 1, dual-phase steels consist of hard martensite islands dispersed in a soft ferritic matrix, which has a body-centered cubic (bcc) structure. Usually they are low-carbon materials with 10-40 vol.% martensite. Thanks to their composite microstructure (soft-matrix/hard-reinforcement), DP steels exhibit early and continuous yielding, high initial strain hardening rate as well as high overall strength and ductility.

The material studied in this research was a commercial DP600 dual-phase steel. This ferritic-martensitic steel which contains 15 vol. % martensite was supplied as hot-rolled sheets of 3.6 mm thickness by ArcelorMittal. Due to its high strength, hot-rolled DP600 steel is a good candidate to reduce the weight of automotive components by decreasing their thickness. Some of the automotive applications of this steel are wheel webs, shock towers and fasteners. An application example of hot-rolled DP600 is presented in Figure 2-1.

Figure 2-1 Wheel web made up of hot-rolled DP600 [147].

The chemical composition and the mechanical properties of the material are presented in Table 2-1 and table 2-2, respectively. There is no significant mechanical anisotropy as far as the yield and ultimate tensile strengths are concerned.

Table 2-1 DP600 chemical composition [104].

Alloying element	C	Mn	Si	Cr	Ni	Al	Nb
% weight	0.0748	0.933	0.213	0.727	0.020	0.039	0.0425

Table 2-2 Mechanical properties of DP600 steel in the rolling direction [104].

Young's Modulus (GPa)	Yield strength (MPa)	Ultimate tensile strength (MPa)	Elongation (%)	Mass density (kg/m^3)
210	440	650	20	7800

2.1.2 Microstructural characterization

The material microstructure was investigated by Optical Microscopy (OM), Scanning Electron Microscopy (SEM), and Electron Backscatter Diffraction (EBSD). Transverse and longitudinal sections of the sheets were prepared followed by conventional metallographic sample preparation including grinding, polishing and etching. In this work the rolling, transverse, and normal directions will be represented by R, T, and N, respectively, as shown schematically in Figure 2-2.

The samples for OM and SEM observations were prepared by grinding down to 2000-grit silicon carbide (SiC) papers, polishing with the diamond paste of 9 and 3µm, and a final polishing step with colloidal silica suspension (OP-S suspension produced by Struers). Finally, for revealing the microstructure the polished samples were etched by 2% Nital solution. For EBSD analysis, the mechanically polished specimens were electrolytically polished by a Struers Lectropol-5 electropolishing device. The electrolyte A2 produced by Struers was used. The operating voltage, the duration and the flow rate were 28 V, 30 seconds and 10, respectively.

The optical microscopy observations were made in different planes and the results are presented in Figure 2-3. No considerable difference was detected in the grains morphology in three planes of observation. Figure 2-4 shows the SEM micrograph of the material microstructure.

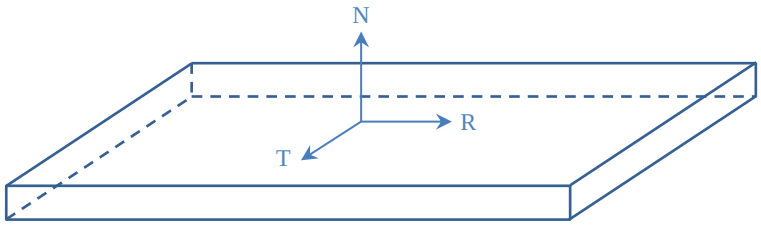

Figure 2-2 Directions of the rolled-sheet of material

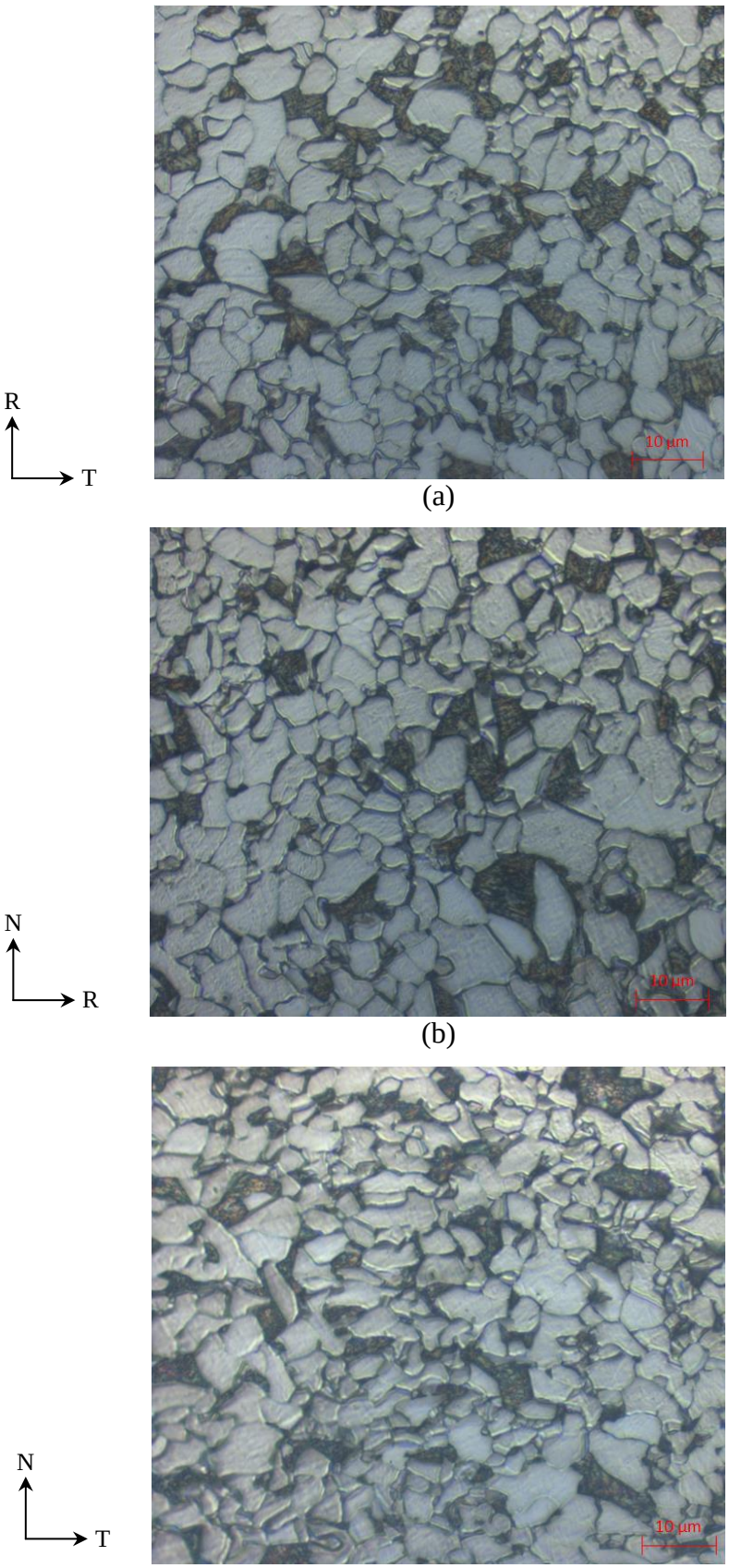

Figure 2-3 Dual-phase microstructure obtained from optical microscopy in three observation planes (dark grains are martensite and bright grains are ferrite): **(a)** T-R plane **(b)** R-N plane **(c)** T-N plane.

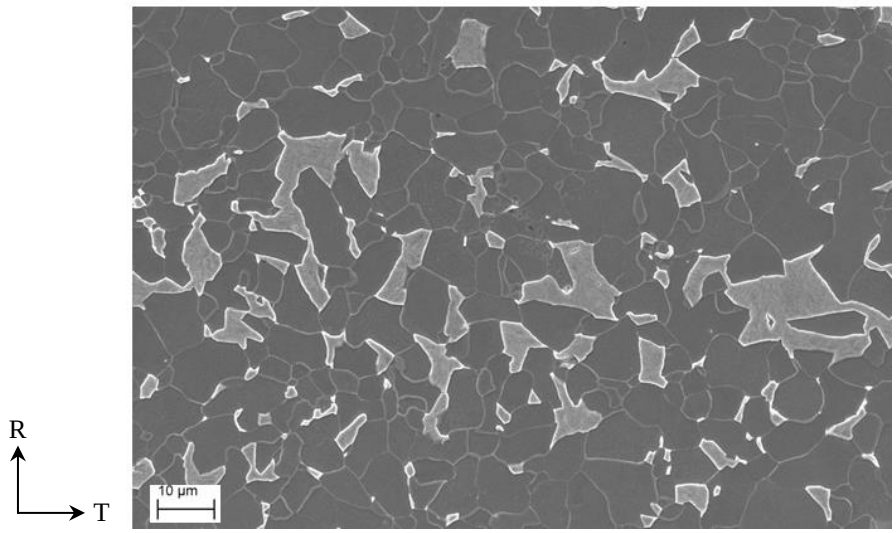

Figure 2-4 SEM micrograph of DP600 steel microstructure (dark grains are ferrite and bright grains are martensite).

From EBSD analysis, the mean grain size (diameter) was obtained as 7 µm for the ferrite phase with a standard deviation of 2.5 µm. Figure 2-5 shows the grain size distribution diagram. The orientation map obtained from EBSD analysis is depicted in Figure 2-6. These results reveal an isotropic distribution of grain sizes.

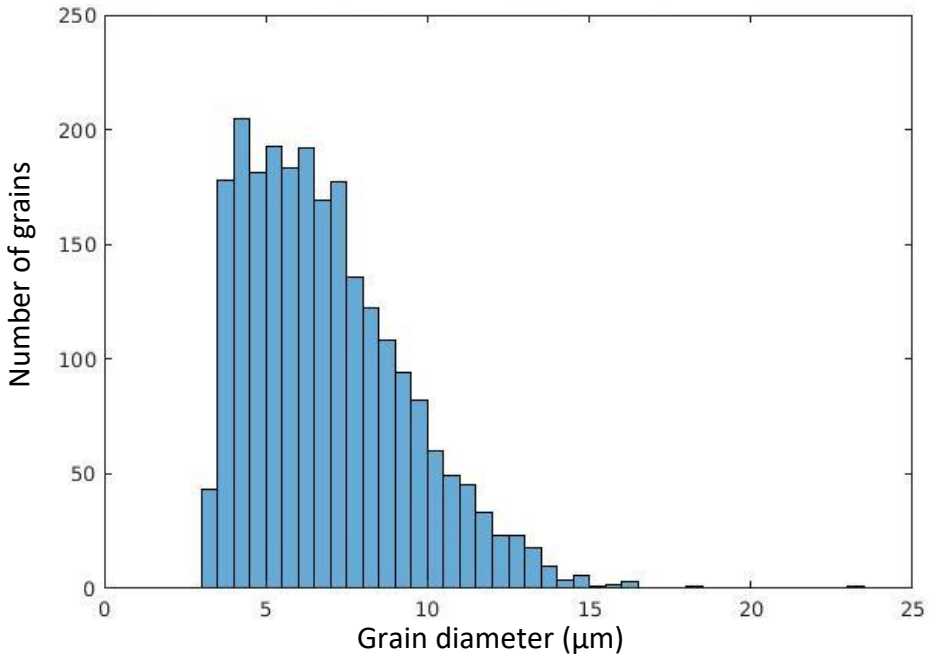

Figure 2-5 Grain size distributions.

Figure 2-6 Inverse pole figure about the normal direction (martensite grains are represented in black).

2.2 Experimental Method

In the present research work, two main categories of experiments were conducted for the fatigue characterization of the material: ultrasonic fatigue loadings at 20 kHz and conventional fatigue tests at low frequencies of 30, 50, and 80 Hz. In the following sections, the principles of each fatigue loading technique including the testing set-up, specimen design, and specimen preparation will be introduced. Afterwards, the infrared thermography method which was employed to study the thermal response of the material under fatigue loading will be briefly explained. Finally the experimental procedure adapted to meet the main objectives of this work will be demonstrated.

2.2.1 Ultrasonic fatigue loading

- Testing set-up

Owing to a high frequency of usually 20 kHz, ultrasonic fatigue testing technology provides a time saving and economical method to obtain fatigue data in very high cycle regime ($N>10^9$) Table 2-3 compares the time necessary to reach very high number of cycles using 100-Hz conventional testing and ultrasonic 20-kHz fatigue loading.

Table 2-3 Ultrasonic versus conventional fatigue testing.

Number of cycles	Conventional (100Hz)	Ultrasonic (20 kHz)
10^7	1 day	9 minutes
10^9	4 months	14 hours
10^{10}	3 years	6 days

The first ultrasonic fatigue testing machine was constructed by Mason in 1950 [148]. He introduced a piezoelectric transducer that transformed 20 kHz electrical signals into mechanical vibrations of the same frequency. His 20-kHz machine is used today as a basis for most modern ultrasonic fatigue testing equipment. Due to the lack of standardization, the ultrasonic test machines differ from laboratory to laboratory but there are four main concepts that are common to all of them:

1. A power generator that transforms 50- or 60-Hz voltage signal into 20 kHz ultrasonic electrical sinusoidal signal.

2. A piezoelectric converter that transforms the electrical signal into longitudinal ultrasonic waves and mechanical vibration of the same frequency.

3. An ultrasonic horn that amplifies the vibration coming from the converter in order to obtain the required strain amplitude in the middle section of the specimen.

4. The specimen, which is subjected to the loading created by the mechanical wave.

An ultrasonic fatigue system is schematically shown in Figure 2-7. The main function of the ultrasonic system is to make the specimen vibrate in ultrasonic resonance at its first longitudinal mode. The horn and test specimen are excited at 20 kHz and are therefore, sized to vibrate at this frequency. In other words, the natural frequency in the first longitudinal mode of the horn and the specimen is equal to 20 kHz. In fact, in the steady state a stationary wave of frequency of 20 kHz is established throughout the system. At the beginning of the loading, the duration of the transient regime corresponds to the time required for the stationary wave to be established and the vibration amplitude applied to the specimen to reach the set-point u_s. A stationary wave is a wave in a medium in which each point on the axis of the wave has an associated constant amplitude. The locations at which the amplitude is minimum are called nodes, and the locations where the amplitude is maximum are called antinodes. The converter, horn, and specimen form a mechanical vibration system with four stress nodes (null stress) and three displacement nodes (null displacement) for an intrinsic frequency of 20 kHz. In Figure 2-7, points B and C

(connection points), as well as point A and the converter top are stress nodes. The specimen center is a displacement node. The displacement amplitude reaches its maximum at the end of the specimen while the strain attains the maximum in the middle section of the specimen that produces the required fatigue stress. Figure 2-7 shows the pattern of displacement and stress amplitudes in the steady state. In the case of ultrasonic fatigue tests, it is the amplitude of displacement at the output of horn, u_s, which is imposed to the specimen and can be controlled to obtain the desired stress amplitude at the center of the specimen.

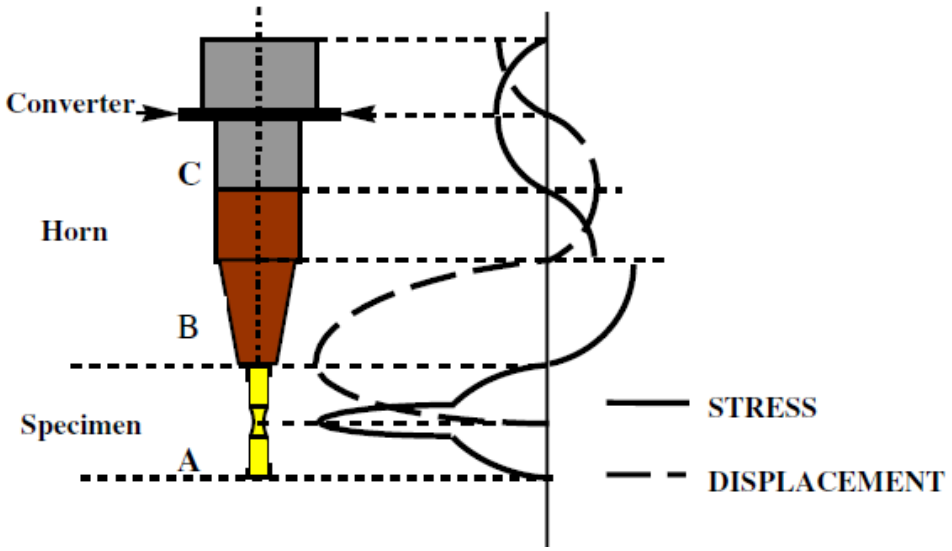

Figure 2-7 Ultrasonic fatigue test system and the stress-displacement field [148].

Classical ultrasonic fatigue testing is displacement-controlled fully reversed push-pull cycling (R=-1). The applied loading amplitudes are very low and material deformation can be considered elastic from macroscopic point of view. During the tests, the maximum strain values can be measured directly using miniature strain gauges suitably positioned on the sample surface. Depending on the specimen loading, the horn is designed so that the displacement is amplified between B and C (see Figure 2-7), usually three to nine times. The high applied frequency leads to high temperature increases during loading. In order to prevent significant temperature rises the specimen should be cooled or intermittent pulse-pause loading technique should be applied. In the present work a continuous loading technique was employed (intermittent loading method was not used) and an air-cooling system was used to cool down the specimen. The cooling system consists of three air guns disposed around the specimen, which blow the compressed air with a temperature of ~ -10°C. The employed ultrasonic testing equipment is shown in Figure 2-8.

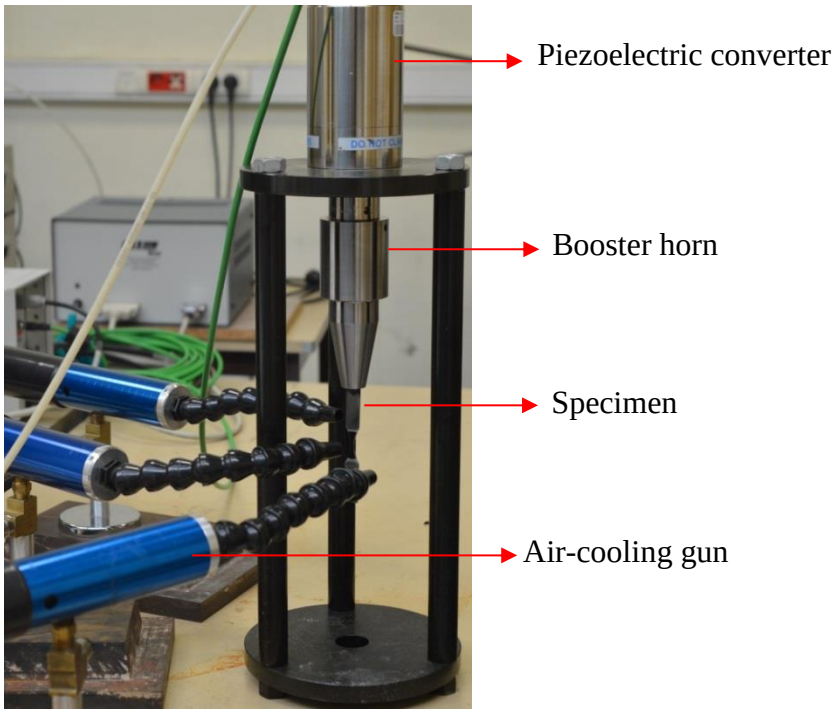

Figure 2-8 Ultrasonic fatigue testing equipment.

- Wave propagation and vibration

When the piezoelectric converter begins to vibrate, it creates a wave that propagates in the horn. This wave interacts with all the interfaces it encounters, i.e. with the horn / specimen and specimen / air interfaces. As explained in Ref. [149], using the results of elastic calculations it appears that:

- At the horn / specimen interface, the wave is totally transmitted from the horn to the test specimen.
- At the specimen / air interface, the wave is totally reflected into the specimen.
- Back to the horn / specimen interface, the wave is totally transmitted from the specimen to the horn.

It is assumed that the wave remains longitudinal, the amplitude of the wave is constant, and its velocity depends on the medium in which it propagates. In steady state, the displacement field within the specimen is therefore the sum of the field created by the incident wave, $\vec{U_i}$, and that

created by the reflected wave, $\vec{U}_r$. For example, in the case of a specimen with constant cross section, these fields can be written as [149]:

$$\vec{U}_i(x,t) = \frac{u_s}{2}\sin(\omega_s t - \kappa x)\vec{x}$$
$$\vec{U}_r(x,t) = \frac{u_s}{2}\sin(\omega_s t + \kappa x)\vec{x} \quad (2.1)$$

Where ω_s is the angular velocity of the vibrations ($\omega_s = 2\pi f_s$ and f_s is the vibration frequency). $\kappa = {2\pi}/{\lambda}$ is the wavenumber in which λ denotes the wavelength. Thus, the total displacement field is written as [149]:

$$\vec{U}(x,t) = u_s\cos(\kappa x)\sin(\omega_s t)\vec{x} \quad (2\text{-}2)$$

This displacement field is the characteristic of a stationary wave. As the variable of time, t, and of space, x, are separated there are some points which have a zero vibration amplitude. In our case, the vibration node must be located at the center of the specimen and the antinodes must be at the ends. Therefore, the length L of a specimen with constant cross section should be equal to $L = {\lambda}/{2}$. The wavelength is defined as $\lambda = {c}/{f_s}$ where c is the velocity of wave propagation. For a longitudinal wave in a solid medium, c depends on material properties and is defined as:

$$c = \sqrt{\frac{E(1-\nu)}{(1+\nu)(1-2\nu)\rho}} \quad (2\text{-}3)$$

where E denotes the Young modulus, ν is the Poisson ratio, and ρ is the mass density. By assuming a specimen with constant cross section and one-dimensional conditions, the wave velocity can be determined from Eq. (2-3) by neglecting the Poisson effect (ν=0) as:

$$c = \sqrt{\frac{E}{\rho}} \quad (2\text{-}4)$$

Thus the length of an ultrasonic specimen with constant cross section is obtained as:

$$L = \frac{1}{2f_s}\sqrt{\frac{E}{\rho}} \quad (2\text{-}5)$$

- Specimen design

Eq. (2-5) describes the specimen design principle in which the specimen length is determined so that $f_s = 20$ kHz. However, this equation is only valid for a cylindrical specimen with a constant cross section and by considering one-dimensional conditions. In practice, to increase more the stress concentration at the center of the specimen in order to accelerate the fatigue test, an hourglass-shaped specimen with circular or rectangular cross-section is preferred over the simple cylindrical specimen. With an hourglass-shaped specimen, the magnitude of the strain wave amplitude is amplified for a given input. However, the variable cross-section complicates determination of the resonance length. In the present work, hourglass-shaped specimens with rectangular cross section were employed, as shown in Figure 2-9.

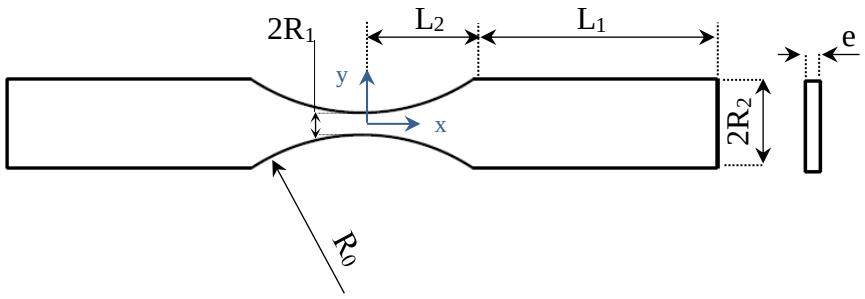

Figure 2-9 Geometry of the ultrasonic fatigue specimen (total specimen length is $L = 2L_1 + 2L_2$).

The present problem is assumed one-dimensional and displacements are considered to occur along the axis of the specimen. The coordinate along the specimen axis is denoted by x. It is also assumed that plastic deformations are negligible in the presence of elastic deformations. Thus, the behavior of the material will be considered as linear elastic with a Young's modulus denoted by E.

Writing the dynamic equilibrium equation for a section of the material comprised between two sections of the respective abscissas x and x + dx results in [68]:

$$\sigma(x+dx,t)S(x+dx) - \sigma(x,t)S(x) = \rho S(x)dx\frac{\partial^2 u(x,t)}{\partial t^2} \tag{2-6}$$

where $u(x,t)$ is the axial vibration displacement at position x, $S(x)$ is the area of the cross section at position x which is subjected to the axial stress $\sigma(x,t)$. $S(x+dx)$ and $\sigma(x+dx,t)$

denote the cross section area and the stress at position $x + dx$, respectively. Eq. (2-6) can be rewritten as:

$$\frac{\partial \sigma(x,t)S(x)}{\partial x} = \rho \frac{\partial^2 u(x,t)}{\partial t^2} \tag{2-7}$$

By assuming linear elastic material behavior:

$$\sigma(x,t) = E\frac{\partial u(x,t)}{\partial x} \tag{2-8}$$

Consequently, the wave equation for the ultrasonic specimen with variable cross section can be written as:

$$\frac{\partial^2 u(x,t)}{\partial t^2} - c^2\left(\frac{\partial^2 u(x,t)}{\partial x^2} + \frac{\partial u(x,t)}{\partial x}\frac{S'(x)}{S(x)}\right) = 0 \tag{2-9}$$

where c is the wave velocity defined by Eq. (2-4).

In the steady state we look for solutions of stationary wave type as (see Refs. [68] and [149]):

$$u(x,t) = U(x)\sin(\omega_s t) \tag{2-10}$$

Replacing $u(x,t)$ in Eq. (2-9) with Eq. (2-10) leads to the following differential equation for displacement amplitude:

$$U''(x) + \frac{S'(x)}{S(x)}U'(\mathrm{x}) + \frac{\omega_s^2}{c^2}\mathrm{U(x)} = 0 \tag{2-11}$$

Concerning the boundary conditions, a displacement with the amplitude of u_s is imposed to the specimen end which is in contact with the ultrasonic horn ($U\left(\frac{-L}{2}\right) = u_s$) and the specimen is free at its other end ($U'\left(\frac{\mathrm{L}}{2}\right) = 0$), according to Figure 2-9. Equation (2.11) can be solved using a numerical method. In the present work, finite difference method was used. A MATLAB code was developed to solve the vibration equation and consequently calculate strain and stress fields along the specimen. The inputs to the code are as follows:

- The frequency of the vibration of the horn.
- The material properties including E and ρ.
- The dimensions R_1, R_2, L_2, and e.

- The applied displacement amplitude, u_s. It should be noted that the displacements, strains and stresses in the nodes are directly proportional to u_s, the choice of which has no effect on determination of L_1. Therefore, usually we take u_s = 1 µm.

The outputs of the code are:

- The length L_1.
- The profile of displacement, strain and stress along the specimen.
- The ratio of the maximum stress (at the center of the specimen) to the applied displacement amplitude (u_s), which is defined as $\beta = \frac{\sigma_{max}}{u_s}$ .This constant will be used in order to calibrate the ultrasonic machine.

R_1, R_2, and L_2 were determined according to experimental conditions and results reported in the literature [149], and L_1 was determined by iteration so that the stress vanishes at the end of the specimen. The details of the numerical solution and iterative procedure can be found in Ref. [149]. Moreover, R_0 is determined from the following geometrical relationship, based on Figure 2-9:

$$R_0 = \frac{L_2^2}{2(R_2 - R_1)} + \frac{(R_2 - R_1)}{2} \tag{2-12}$$

The dimensions of the ultrasonic specimen are presented in Table 2.4. Figure 2-10 shows the displacement and stress profiles along the specimen for the displacement amplitude of u_s = 1 µm. From this figure the ratio of maximum stress to displacement amplitude was obtained as β = -16.24 MPa/µm. In addition, the uniaxiality of the stress field in the ultrasonic specimen is confirmed in Ref. [150] through finite element simulations.

Table 2.4 Dimensions of the ultrasonic fatigue specimen.

R_0 (mm)	27.2
R_1 (mm)	1.5
R_2 (mm)	6.0
L_1 (mm)	33.0
L_2 (mm)	15.0
e (mm)	2.0

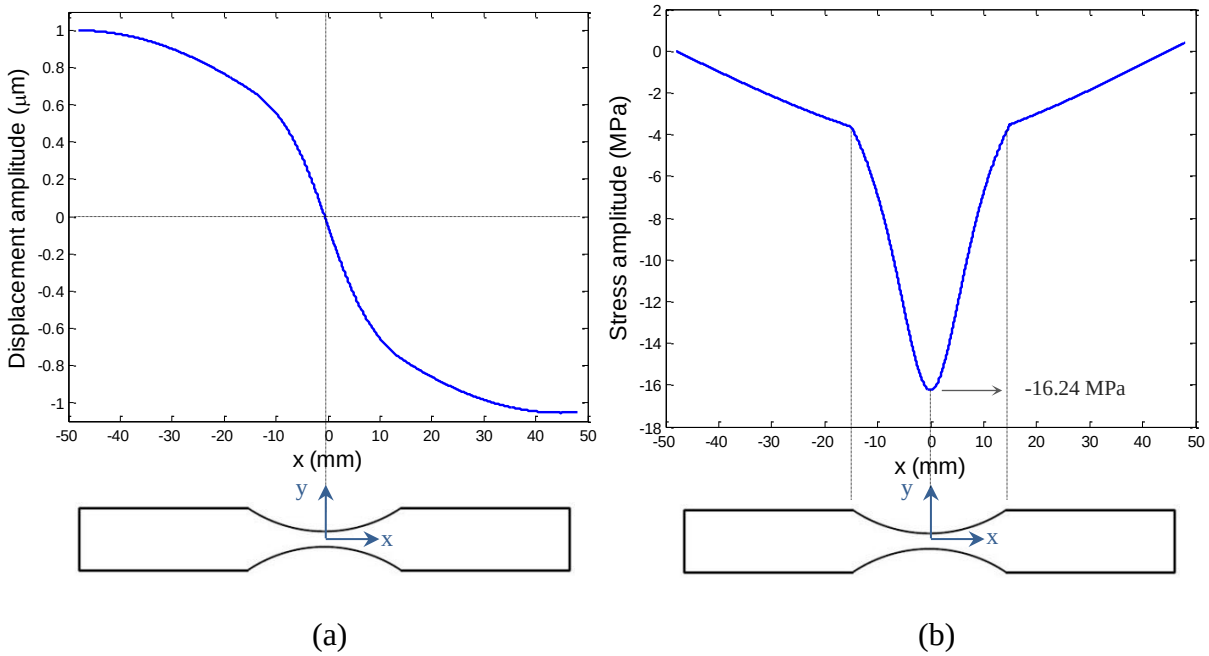

(a) (b)

Figure 2-10 (a) Displacement amplitude and **(b)** Stress amplitude distribution along the ultrasonic fatigue specimen axis for the applied displacement amplitude of u_s = 1 µm.

For a thin specimen loaded at stress ratio of R= -1, buckling can occur at the compressive half cycle. Thus, after determination of specimen dimensions, the critical buckling stress should be verified to be above the applied stress amplitudes during fatigue tests. The critical buckling stress can be determined from Euler critical buckling relationship, as follows:

$$\sigma_b = \frac{\pi^2 EI}{(KL_c)^2 S} \tag{2-13}$$

where E is the Young modulus, I is the area moment of inertia of the cross section of the column, S is the cross sectional area, and L_c is the unsupported length of the column. K denotes the column effective length factor, whose value depends on the conditions of end support of the column and equals to 0.5 in our case.

The buckling sensitive area of the fatigue specimen corresponds to the gauge part of the specimen whose section is variable. As the most unfavorable case, we assume a constant section equal to the smallest section of the specimen ($e \times 2R_1$) with the length of $2L_2$. From Eq. (2-13) the critical buckling stress amplitude is obtained as σ_b = 3070 MPa, which is much higher than

the yield strength of the material (σ_y = 440 MPa). Therefore, during the ultrasonic fatigue loadings of the material, the stress amplitude remains below the yield strength and considering the measured critical buckling stress, the specimen is safe from buckling phenomenon.

The fatigue specimens were manufactured in the rolling direction of the sheets by CNC milling machine. In order to attach the specimen to the horn, a screw was welded to the specimen by laser welding (the mass of the screw was not considered in the aforementioned specimen design procedure assuming that it does not have any affect on the specimen vibrations). The gauge part of all specimens were grinded with a sequence of SiC papers (220-1200) and finally were electropolished to remove residual stresses induced by the machining and mechanical polishing. The employed electropolishing parameters are presented in Table 2-5. After electropolishing the specimens were cleaned in ethanol solution using ultrasonic cleaner for 5 minutes. Surface profilometry analysis showed that electropolishing removes a material layer of ~1.6 µm. Figure 2-11 shows the ultrasonic fatigue samples after welding the screw and polishing the gauge part.

Table 2-5 Setting parameters for the electropolishing procedure of fatigue specimens.

Electrolyte solution	A2
Mask size	2 cm^2
Temperature	25°C
voltage	30 V
Flow rate	10
time	25 s

Figure 2-11 Ultrasonic fatigue specimens.

- Calibration of the ultrasonic machine

Before conducting fatigue tests, the ultrasonic machine should be calibrated in order to control the stress amplitude in the specimen. The variation of stress amplitude at the center of the specimen should be defined versus the applied vibration amplitude. In order to establish the calibration curve, the displacement amplitude at the end of the horn corresponding to each voltage level applied to the piezoelectric transducer was measured using a laser vibrometer, as shown in Figure 2-12.

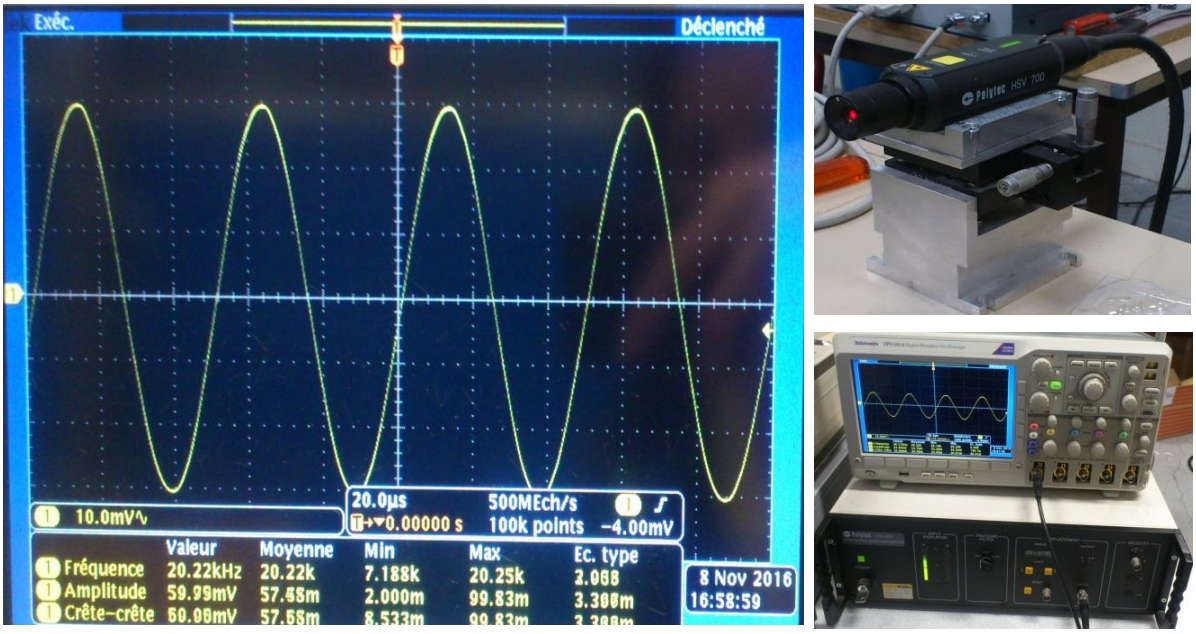

(a) (b)

Figure 2-12 Laser vibrometery to measure the real displacement amplitude at the free end of the horn **(a)** An example of the input signal measured by the oscilloscope **(b)** The laser vibrometer and the oscilloscope.

Generally, in order to carry out an ultrasonic fatigue test, a desired displacement amplitude value is input to the controlling software and the computer applies the corresponding voltage to the piezoelectric transducer. As a result, a sinusoidal displacement is imposed at the free end of the horn, the amplitude of which is different from the displacement value input to the software. The ratio of maximum stress to displacement amplitude, β, which was measured in the previous section, can be used to determine the stress amplitude at the center of specimen based on the measured real displacement amplitudes. The calibration curve was constructed for several measuring points for low displacement amplitudes ($u_s < 10$ µm). Since the applied

displacement amplitudes were small the heating of specimen was negligible and the cooling system which may disturb the measurements was not used. The calibration curve i.e. the variations of the maximum stress amplitude (at the center of specimen) versus the applied displacement amplitude (input to the controlling software) is shown in Figure 2-13. The calibration curve was established for the stress amplitudes more than two times lower than the yield stress of the material (440 MPa). In the following, it was assumed that this linear relationship is true even for higher stress amplitude up to 330 MPa.

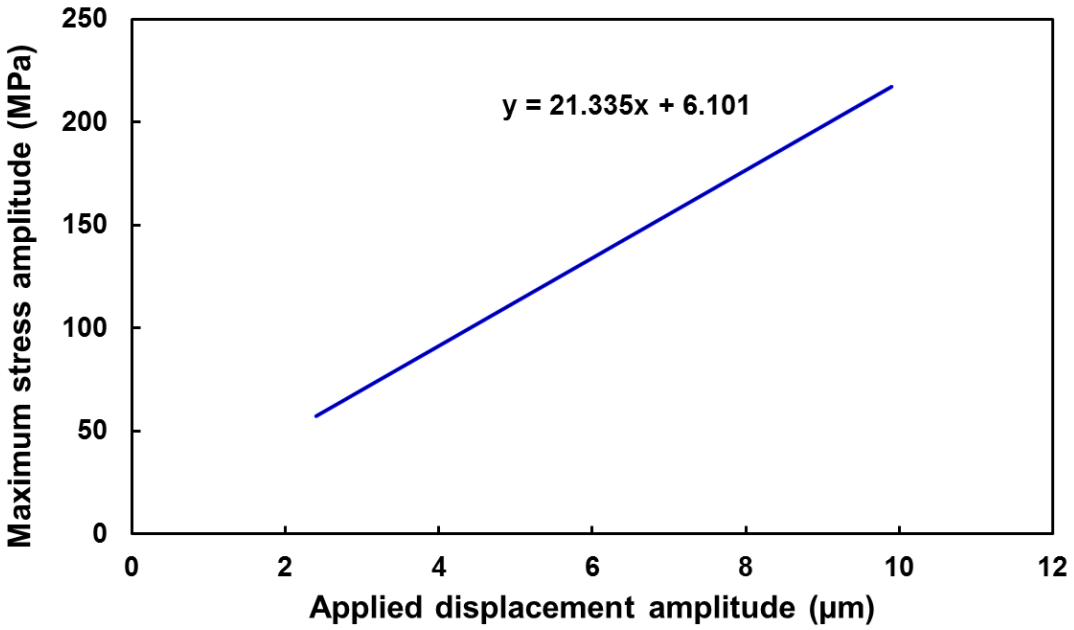

Figure 2-13 Variations of the maximum stress amplitude versus the applied displacement amplitude.

2.2.2 Conventional fatigue loading

- Testing set-up

Conventional low frequency fatigue tests were carried out at frequencies of 30, 50, and 80 Hz by using a 10-kN servo-hydraulic MTS machine, as shown in Figure 2-14. The specimen was fixed at one end and fully reversed sinusoidal shape load cycles were imposed at the other end (R=-1).

- Specimen preparation

Similar to ultrasonic samples, the conventional specimens were hourglass-shaped with the geometry shown in Figure 2-15. The dimensioning of the conventional fatigue specimens was carried out so that for the same displacement amplitude, the stress distribution in the neighborhood of the specimen center is equivalent to that of ultrasonic specimen. At the gauge part of the specimen, the dimensions of low-frequency samples were adjusted to be close to those of ultrasonic specimens in order to have similar volumes under loading. All parameters including l_1, l_2, r_1 , and r_2 were fixed and the value of r_0 was determined to have the similar stress gradients for low-frequency and ultrasonic samples in the vicinity of specimens centers.

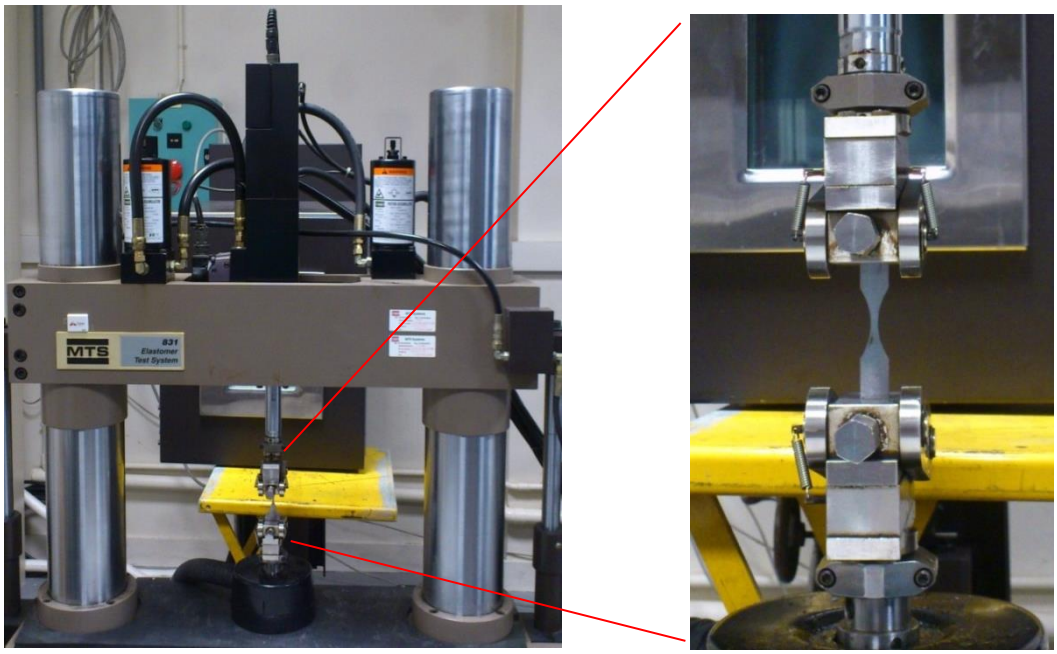

Figure 2-14 Conventional fatigue experimental set-up.

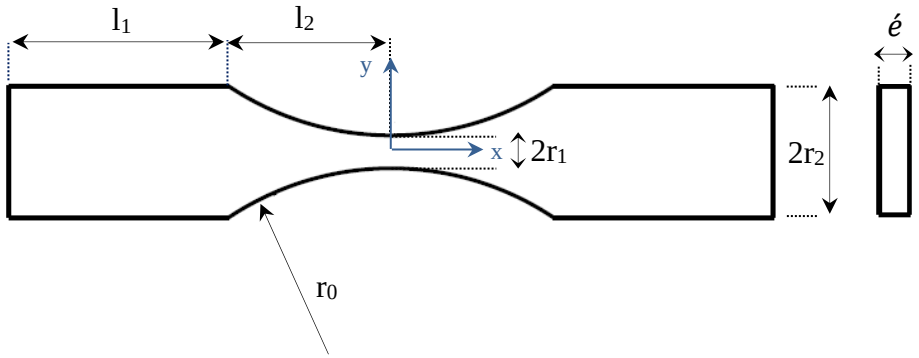

Figure 2-15 Geometry of conventional fatigue specimen.

The stress amplitude along the ultrasonic fatigue sample in the area close to the sample center can be approximated as [149]:

$$\sigma(x) = \sigma_0 + \sigma_0' x + \frac{1}{2}\sigma_0'' x^2 + O(x^2) \tag{2-14}$$

The stress amplitude should be maximum at the specimen center which results in $\sigma_0' = 0$. Moreover, the stress amplitude is directly proportional to the displacement amplitude imposed at the end of the specimen, u_s. Thus we can write $\sigma_0 = \beta u_s$ and $\sigma_0'' = \vartheta u_s$, where β and ϑ are constant parameters which are determined from the numerical calculation of stress profile along the ultrasonic specimen explained in the previous section. β is the ratio of maximum stress to displacement amplitude which was obtained as β = -16.24 MPa/µm (see Figure 2-10(b)). ϑ can be determined from the numerical calculation of the second derivative of stress at the specimen center for u_s = 1 µm. From the previously mentioned numerical calculation it was obtained as $\vartheta = 4.07 \times 10^5$ MPa/m^2/µm.

Consequently, Eq. (2-14) is simplified as:

$$\sigma(x) = (\beta + \frac{\vartheta}{2}x^2)u_s \tag{2-15}$$

For conventional fatigue specimen, the stress amplitude at the central part of the specimen can be calculated simply by dividing the applied force, F, to the cross sectional area which gives $\sigma(x) = {}^{F}/_{2e'r(x)}$, where e' is the specimen thickness and $r(x)$ can be determined as (see Figure 2-15):

$$r(x) = r_1 + r_0 - \sqrt{r_0^2 - x^2} \tag{2-16}$$

A second-order limited expansion results in:

$$r(x) = r_0 + \frac{x^2}{2r_1} \tag{2-17}$$

Finally, the stress amplitude at the central part of the conventional fatigue specimen can be obtained as:

$$\sigma(x) = \frac{F}{2e'r_1}(1 - \frac{x^2}{2r_0r_1}) \tag{2-18}$$

In order to have equivalent stress fields at the center of ultrasonic and conventional fatigue samples, the following relation should be satisfied:

$$\sigma(x) = \left(\beta + \frac{\vartheta}{2}x^2\right) = \frac{F}{2e'r_1}\left(1 - \frac{x^2}{2r_0r_1}\right) \quad (2\text{-}19)$$

Therefore, the radius r_0, of the conventional fatigue specimen can be determined as:

$$r_0 = \frac{-\beta}{\vartheta r_1} \quad (2\text{-}20)$$

Based on the calculated values of β and ϑ, r_0 was obtained as r_0 = 26.6 mm. The dimensions of the conventional fatigue specimen are presented in Table 2-6. The stress profiles along the ultrasonic and conventional specimens, obtained from MATLAB calculations, are compared in Figure 2-16.

The same calculations of critical buckling stress as in the case of ultrasonic specimen were done and the calculations revealed σ_b = 6908 MPa which is much higer then the yield stress of the material.

Table 2-6 Dimensions of the conventional fatigue specimen.

r_0 (mm)	26.6
r_1 (mm)	1.5
r_2 (mm)	6.0
l_1 (mm)	20.0
l_2 (mm)	15.0
e' (mm)	3.0

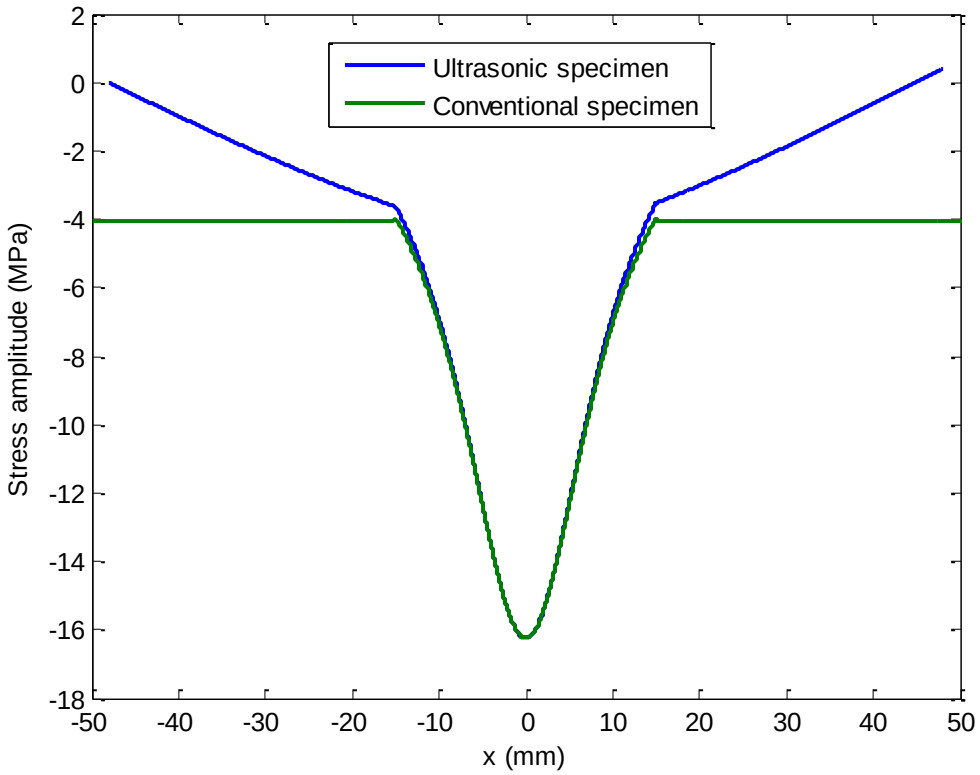

Figure 2-16 Stress distribution along the ultrasonic and conventional specimens (u_s = 1 µm) in the case of ultrasonic specimen and F = -146 N for the conventional sample)

The conventional fatigue specimens were manufactured in the rolling direction of the sheets by CNC milling machine. The same grinding and electropolishing procedure as in the case of ultrasonic specimens was applied to the gauge part of the specimen.

2.2.3 Infrared thermography

A thermographic camera which is also called an infrared (IR) or thermal imaging camera is a device which detects infrared energy and converts it into electronic signal which is then processed to produce a thermal image and perform temperature calculations. In this research work, a FLIR system IR camera was employed to measure the temperature evolution on the specimen surface during the fatigue tests, as shown in Figure 2-17. A spatial resolution of 0.024 mm per pixel was used. The acquisition frequency was 10 Hz. The temperature accuracy given by the manufacturer is 20 mK but it actually depends on the adjustment of the camera.

Considering the fluctuations in temperature, we considered that the accuracy is ±0.1°C. Specimens were coated with a high-temperature resistant and strongly emissive black paint to limit the errors associated with surface emissivity. In all cases, the mean temperature was measured at the center of the gauge part of the specimen in a circular area with a diameter of ~1 mm.

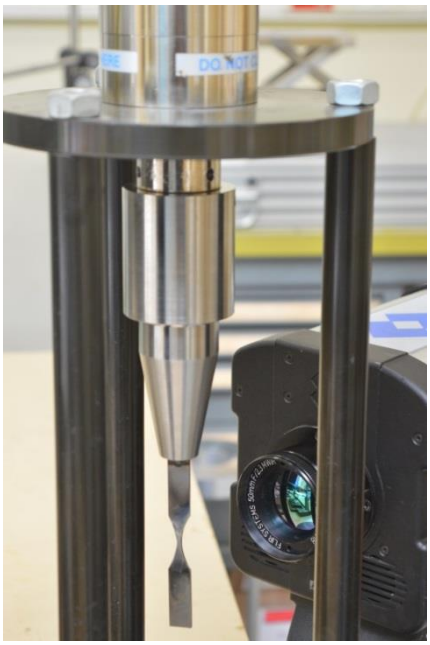

Figure 2-17 The infrared camera and the ultrasonic fatigue set-up.

2.2.4 Uniaxial tensile tests

In order to characterize the mechanical behavior of the material at high temperatures, uniaxial tensile tests were conducted at 350°C. The Instron 5881 tensile machine with the maximum capacity of 50 kN was employed (Figure 2-18). This tensile machine is equipped with a furnace allowing tests to be conducted at high temperatures up to 350°C. The tensile specimens were machined according to ASTM E8 [151] standard in the rolling direction. Figure 2-19 shows the geometry of tensile specimens. The tensile tests were conducted under displacement control at a constant crosshead speed of 5 mm/min.

Figure 2-18 Uniaxial tensile test set-up.

(a)

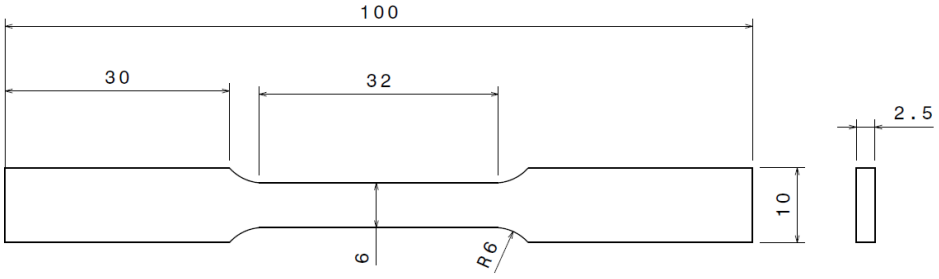

(b)

Figure 2-19 **(a)** Tensile test specimens **(b)** Specimen dimensions in mm.

2.2.5 Testing procedure

Two main categories of fatigue experiments were carried out in this work:

1. Thermography studies to investigate the thermal response of the material under fatigue loading.

2. Fatigue characterization tests to obtain the S-N curve, deformation mechanisms and fractography.

- Thermography studies

For both ultrasonic and conventional fatigue tests the thermography measurements consisted of a series of successive cyclic loadings for the same specimen with increasing stress amplitude, as illustrated in Figure 2-20. At each stress amplitude, a fatigue test was carried out up to 10^7 cycles in the case of ultrasonic fatigue and up to 2×10^4 cycles under conventional fatigue tests and the temperature field on the specimen surface was recorded. All testing steps were conducted at a constant stress amplitude, σ_a. At the end of each step, the testing machine was stopped and temperature measurements were continued for 2 min to record the temperature decrease of the specimen after stopping the test. A time gap of ~10 min between two successive steps ensured that the specimen temperature was homogeneous and equal to the ambient temperature before starting the next loading step. Fatigue tests were repeated for three samples to ensure result reproducibility. In the case of ultrasonic loading, the air cooling system was not used in order to measure the self-heating of the specimen under loading. In the case of conventional fatigue tests, thermography measurements were carried out for the frequencies of 50 Hz and 80 Hz. Lower frequencies were avoided since no considerable temperature increase occurs for low frequencies and temperature measurements would be more difficult in this case.

- Fatigue characterization studies

The S-N curves were obtained by 20-kHz ultrasonic loadings and conventional fatigue tests at the frequency of 30 Hz. This low frequency was applied for conventional tests to ensure that specimen temperature did not increase highly and remained around the room temperature under fatigue loading. In order to define the S-N curves, three samples were tested for each stress amplitude. In the case of ultrasonic loading, the specimens were cooled during the tests to decrease the effect of self-heating on the results.

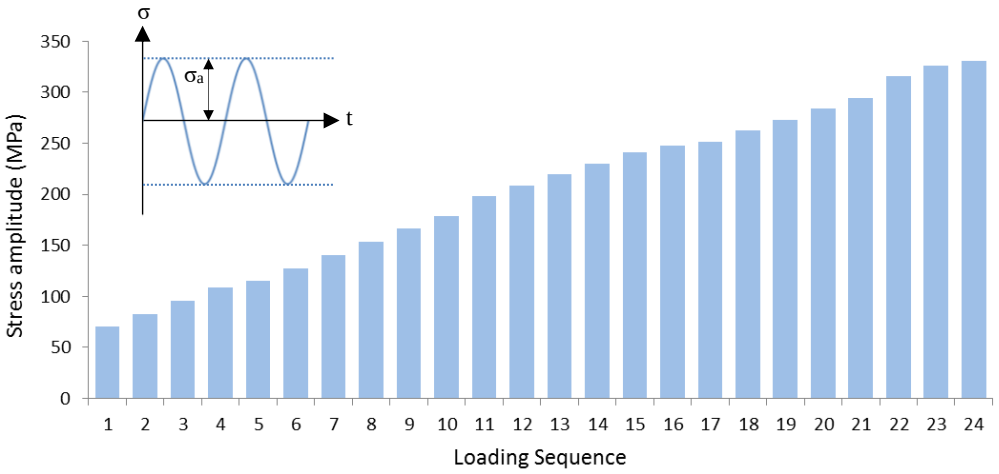

(a)

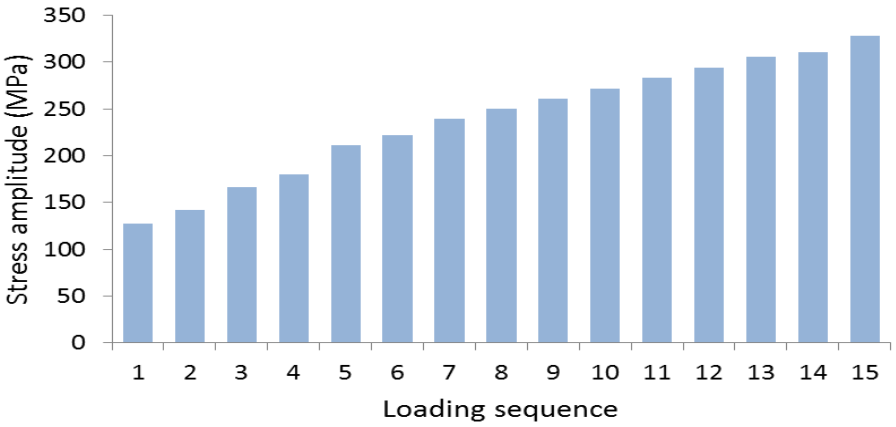

(b)

Figure 2-20 Successive fatigue loadings for thermography studies **(a)** Ultrasonic loading, each block consists of ~10^7 cycles **(b)** Conventional loading (each block consists of ~2×10^4 cycles).

Ultrasonic fatigue tests are displacement-controlled while conventional fatigue tests are performed under load-controlled conditions. In both cases loading amplitude was low so that the specimen deformed elastically from macroscopic point of view. Therefore the difference in the loading techniques does not have any strong impact on the results [79], [81]. Deformation and fracture mechanisms were investigated for both ultrasonic and conventional loadings through SEM observations. In the case of ultrasonic loading, before SEM observations the specimens were put in a rust remover solution (Evapo-Rust brand) to remove the oxide layer formed at the surface during loading, and facilitate the microscopic observations. This solution

is a non-toxic and non-corrosive water-based product which is generally employed for domestic uses and does not have any chemical attack effect [152]. The specimens were put in this solution for ~1 hour and then were rinsed, dried, and then were observed by SEM.

Each category is briefly introduced in the following sections. The general experimental method and objectives are briefly presented in Figure 2-21.

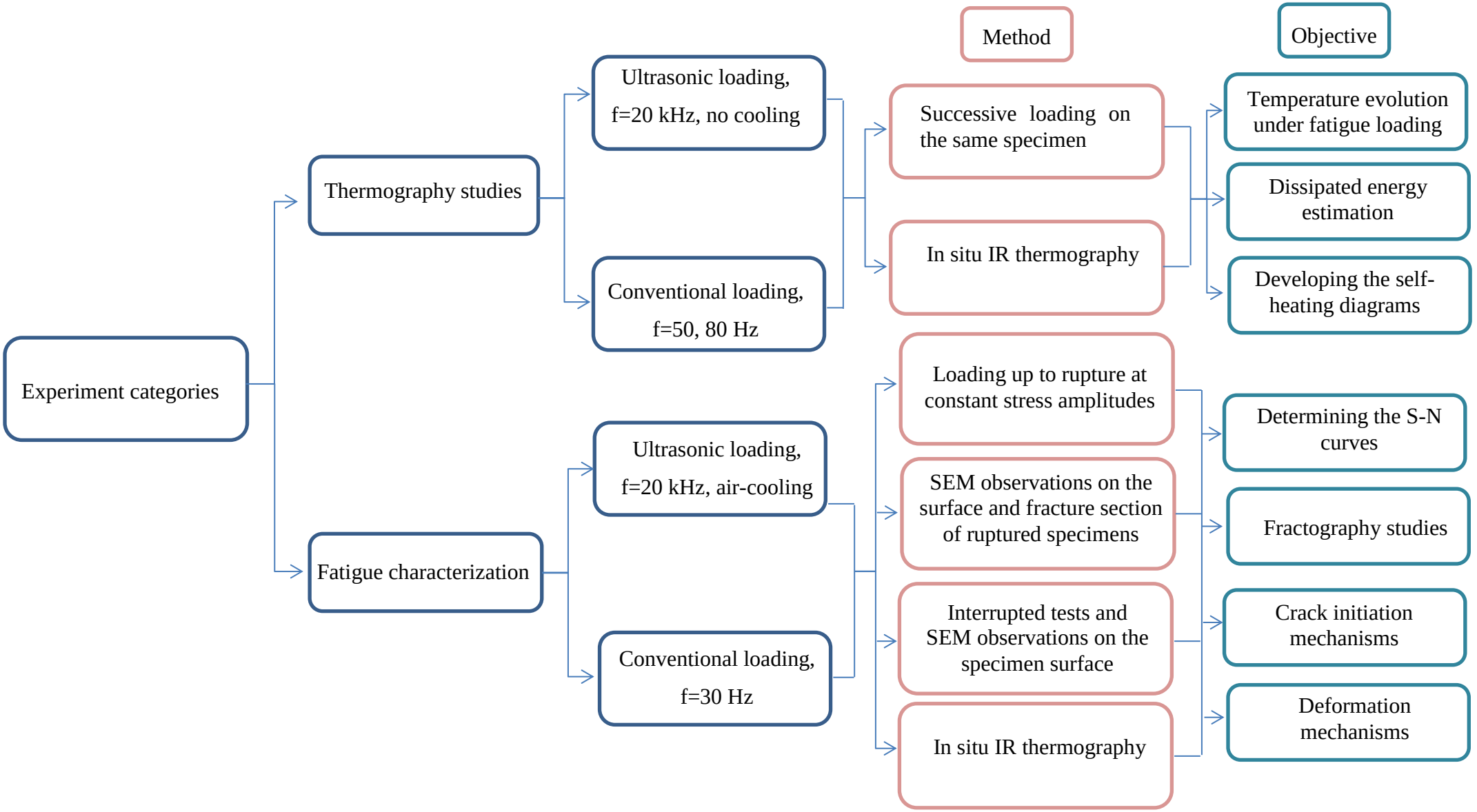

Figure 2-21 Experimental procedure.

Chapter 3

Thermographic Studies and Self-Heating Measurements

Résumé

Études thermographiques et mesures par auto-échauffement sous chargement de fatigue

Dans ce chapitre, les résultats obtenus à partir d'études calorimétriques lors des essais de fatigue ultrasonique et conventionnelle ont été présentés. On a constaté que sous chargement ultrasonique, il y a une amplitude de contrainte critique, au-dessus de laquelle un fort échauffement se produit avec une température qui augmente de plusieurs centaines de degrés. Dans ce cas, les images thermographiques ont révélé la formation d'une zone de température inhomogène qui se propage puis disparaît en augmentant le nombre de cycles. Sous les chargements conventionnels de 50 Hz et 80 Hz, le matériau a montré une réponse thermique classique et un champ de température homogène pour toutes les amplitudes de contraintes avant rupture. L'énergie dissipée par cycle a été mesurée en utilisant l'équation de diffusion de la chaleur. Pour les essais classiques, aucun effet de fréquence n'a été observé en fonction des résultats obtenus pour les fréquences de 50 Hz et de 80 Hz. Sous des chargements de fatigue ultrasonique aux faibles amplitudes de contrainte, l'énergie dissipée par cycle est une fonction quadratique de l'amplitude de contrainte. La comparaison des résultats a révélé que sous chargement ultrasonique, l'énergie dissipée est significativement inférieure à celle des essais de fatigue conventionnelle. En outre, la microscopie optique a révélé la formation de bandes de glissement persistantes à la surface des éprouvettes dans le cas de chargement cyclique à base fréquence, ainsi que des essais ultrasoniques à hauts amplitudes de contraintes. Cependant, pour les essais ultrasoniques à faible amplitude de contrainte, pour lesquelles aucun échauffement important n'a eu lieu, aucune bande de glissement n'a été détectée.

3.1 Introduction

Since fatigue loading is an energy-dissipating process, it is accompanied by temperature variations of the material that undergoes a fatigue test. In the present work, thermographic investigations were carried out on DP600 steel under ultrasonic and conventional fatigue loadings in order to correlate the thermal response of the material to the fatigue behavior and deformation mechanisms. As will be shown, the thermal response of the material plays an important role in understanding the deformation mechanisms under cycling at different frequency levels. This is why it is preferred to present the thermal investigation results prior to the fatigue characterizations which will be presented in Chapter 4.

In order to study the thermal response of material under ultrasonic and conventional low-frequency fatigue loadings, successive fatigue tests were carried out with increasing stress amplitude. Employing in situ infrared thermography, the mean temperature on the surface of the specimen was recorded. Self-heating diagrams were developed for this material based on mean temperature elevation. The mean dissipated energy per cycle was measured and the variations of this dissipation versus stress amplitude were studied. Infrared thermographic images were employed to develop a better understanding about the possible heating mechanisms. The obtained experimental results are presented in this chapter. It should be mentioned that part of the results presented in this chapter have been published in Journal of Materials Science and Engineering A [153].

3.2 Ultrasonic Fatigue Loading

3.2.1 Temperature variations during cycling

As mentioned in Chapter 2, successive steps of the ultrasonic fatigue tests were conducted with increasing stress amplitude and the mean temperature was registered at each step (see Figure 2-20(a)). For instance, Figure 3-1 shows the mean temperature evolution during one of the loading steps and the temperature field on the specimen surface. From this figure it is clear that the mean temperature increased rapidly at the beginning of the test (Stage I) and then stabilized at a steady-state value (Stage II). The stabilization of the temperature corresponds to a balance between the mechanical energy dissipated into heat and the energy lost by convection and radiation at the specimen surface and by conduction inside the specimen. Thus, the level of the

stabilized temperature is linked directly to the dissipation. Stage III shows the specimen natural cooling after stopping the test at 10^7 cycles. This cooling stage occurred because of the stop in dissipation (heat source) after stopping the test, and characterizes the heat losses due to conduction and convection. This is the classical temperature evolution of a material that undergoes fatigue straining (before rupture).

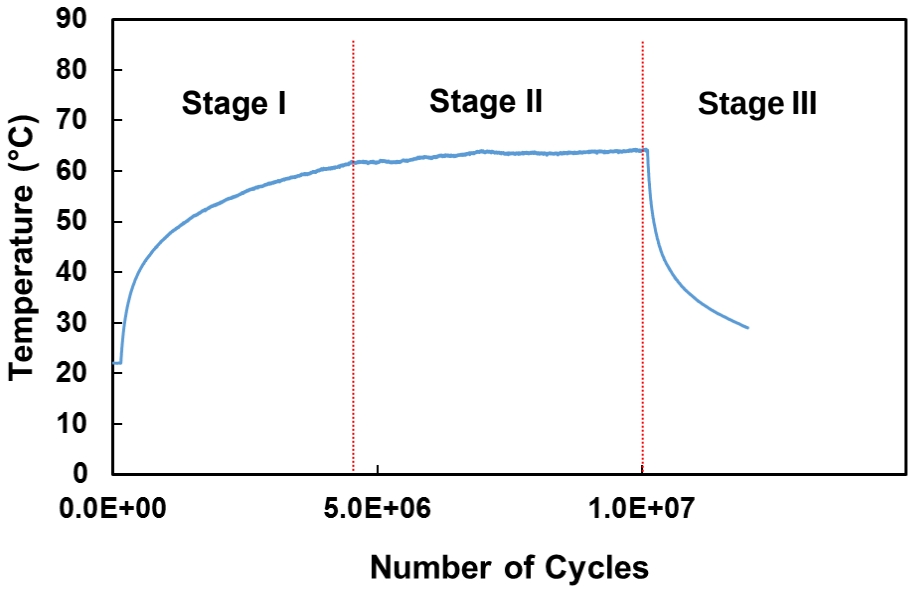

(a)

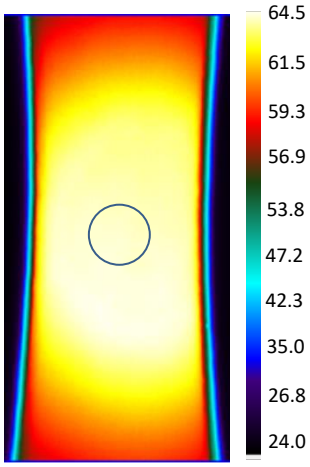

(b)

Figure 3-1 Loading step with σ_a = 209 MPa: **(a)** Temperature evolution versus time; **(b)** Temperature field on specimen surface at N = 9.9 × 10^6 cycles (mean temperature was measured in the circular area in the center of the specimen, where the temperature is uniform).

The evolutions of the mean temperature for some of the loading steps with different stress amplitudes are shown in Figure 3-2. This figure shows that by increasing the stress amplitude, the mean steady-state temperature grew gradually with the same trend as shown in Figure 3-1 until it reached ~100°C for the stress amplitude of 247 MPa (Curve (a) in3-2). However, by increasing the stress amplitude from 247 MPa to 251 MPa, the temperature evolution trend changed. The temperature was below 135°C during the early 8×10^6 cycles. At ~8×10^6 cycles, the mean temperature increased significantly, peaked at ~350°C and then decreased slightly before it stabilized at ~280°C (Curve (b)). The surface of specimen was oxidized due to the high temperature. In this case the loading frequency decreased very slightly (~0.06 Hz) after the strong heating and then stabilized again. For the next two loading steps with stress amplitudes of σ_a = 266 MPa and 273 MPa (Curves (c) and (d)), the temperature elevation was far less than the previous step at σ_a = 251 MPa. Increasing the stress to σ_a = 283 MPa (curve (e)) resulted in a significant increase in temperature with the same pattern as seen previously for σ_a = 251 MPa. These phenomena were repeated up to the specimen rupture at σ_a = 330 MPa. Indeed after the loading step with σ_a = 283 MPa (curve (e)), an increase in stress amplitude to 300 MPa in the following step resulted in a decrease in the temperature elevation, in the same way as that observed for σ_a = 266 MPa and 273 MPa. However, for the sake of brevity, the results of these subsequent loading steps are not presented in Figure 3-2. It should be mentioned that in Figure 3-2, for the loading steps with high stress amplitudes ($\sigma_a \geq 247$ MPa), the initial parts of the temperature evolution curves are missing because the temperature was less than the minimum recordable value according the infrared camera calibration.

Figure 3-3(a) shows the temperature distribution along the length of the specimen gauge part for some stress amplitudes. The temperature values have been measured along the central axes of the specimen as shown in Figure 3-3(b). The temperature reaches its maximum around the central part of the specimen. In order to study the temperature distribution in more details, the results for stress amplitude of 247 MPa are separately presented in Figure 3-4. According to this figure, there is little asymmetry in the temperature profile which results from the different boundary conditions at the specimen ends.

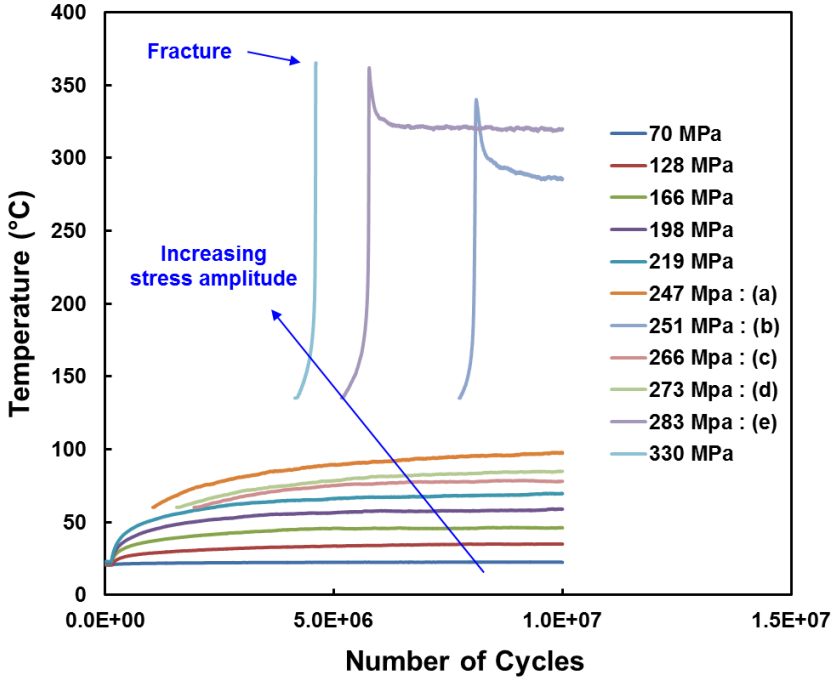

Figure 3-2 Temperature evolution versus number of cycles for different stress amplitudes before stopping the tests.

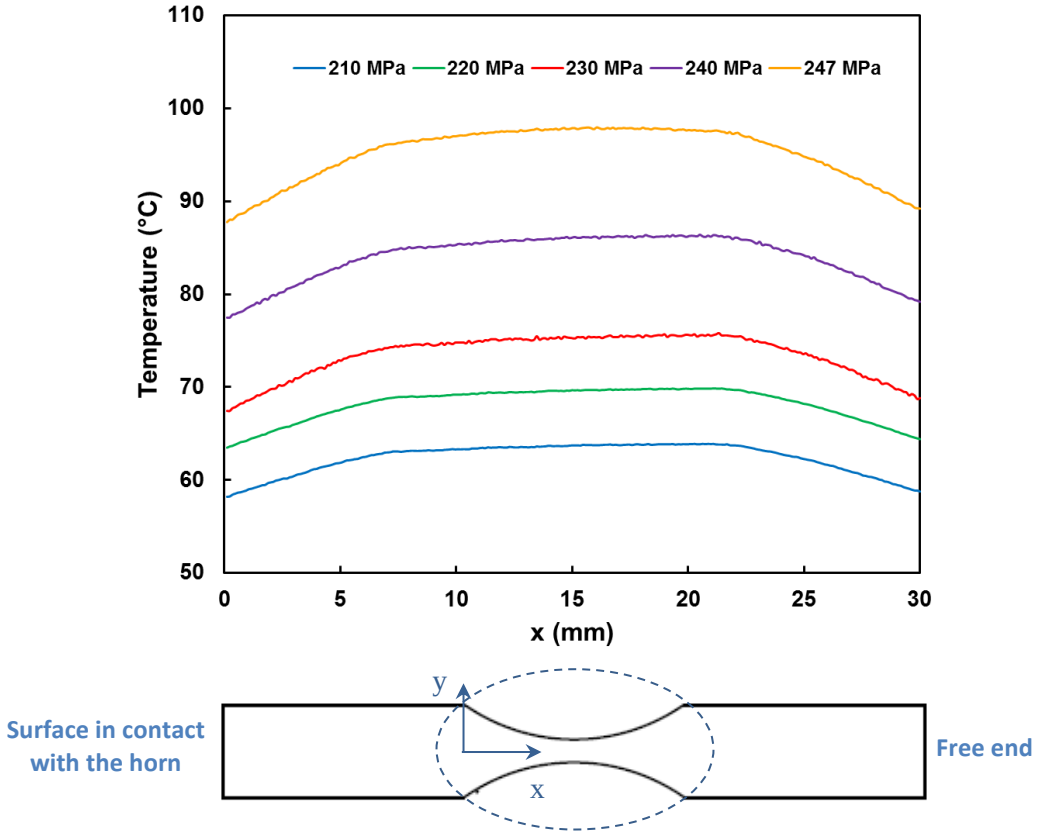

(a)

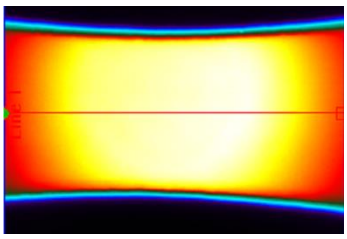

(b)

Figure 3-3 (a) Temperature profile along the specimen gauge part for different stress amplitudes under ultrasonic loading **(b)** A sample thermograph showing the central axes, along which the temperature values were plotted.

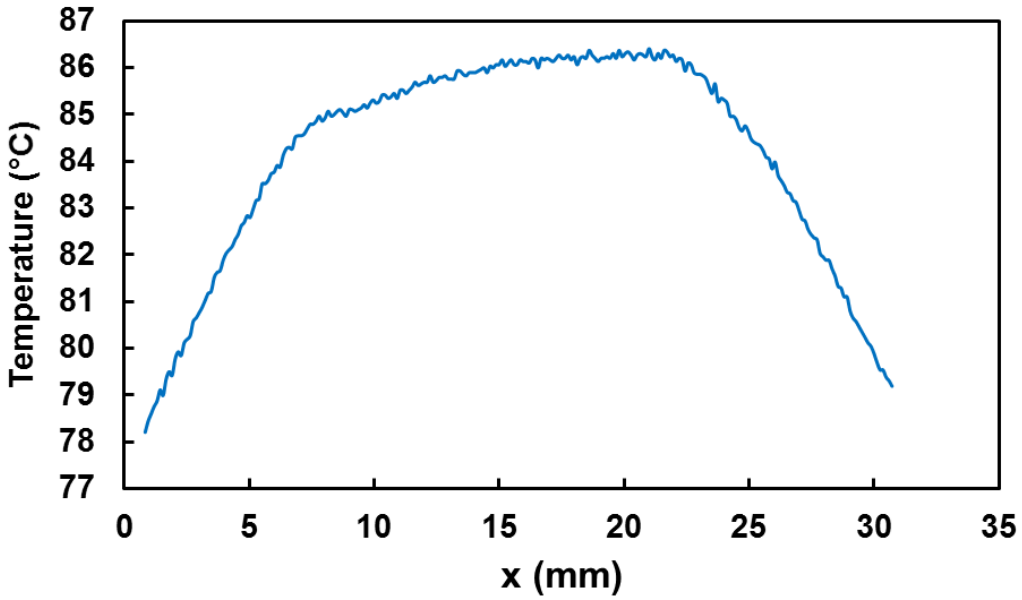

Figure 3-4 Temperature distribution along the specimen length for σ_a = 247 MPa.

3.2.2 Evolution of self-heating versus stress amplitude

For each loading step in Figure 3-2 and excluding the final step in which fracture occurred, the mean steady-state temperature elevation, which is defined as $\Delta T = T_{steady} - T_0$, is plotted versus the stress amplitude in Figure 3-5. T_0 is the initial temperature of the specimen that is recorded each time before starting the test.

Figure 3-5 shows that the temperature elevation increased gradually by increasing the stress amplitude up to a critical value, σ_c=247 MPa (Point A) which corresponds to a critical temperature, T_c≈100°C. Thereafter, an increase in the stress amplitude resulted in a significant increase in temperature elevation (Point B). For subsequent slight increases in stress amplitude, the temperature elevation decreased substantially (Points C and D) followed by another significant increase at σ_a = 283 MPa (Point E). This trend continued up to specimen rupture.

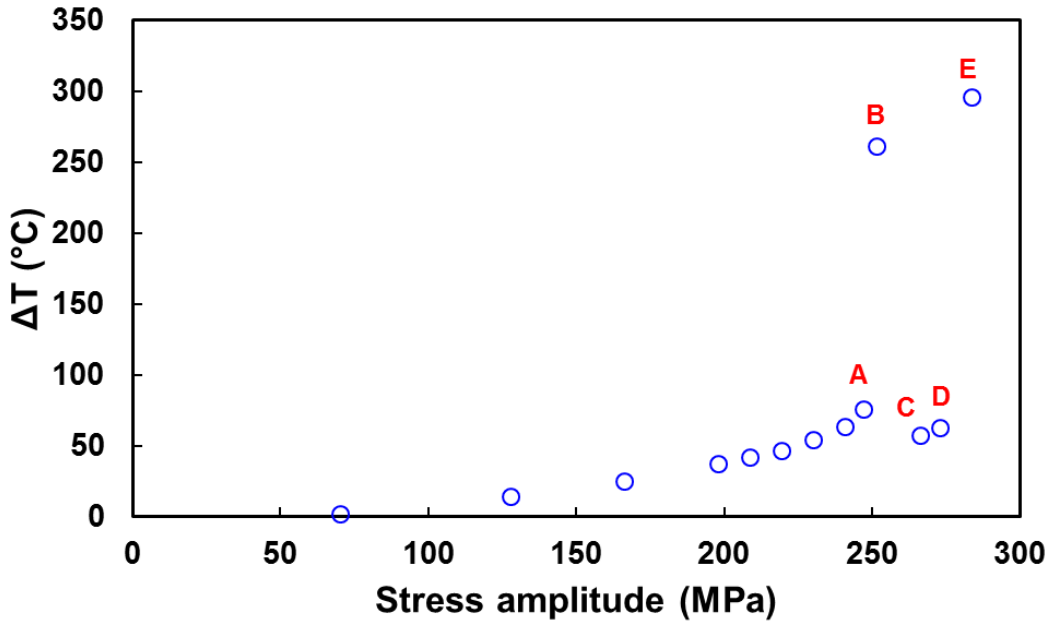

Figure 3-5 Stationary mean temperature increase versus stress amplitude for a specimen under successive ultrasonic fatigue tests.

Figure 3-6 shows the temperature fields on the specimen surface obtained from infrared thermography for $\sigma_a = \sigma_c$ = 247 MPa (Point A in Figure 3-5), in which the temperature field on the specimen surface is correlated with the temperature evolution during cyclic loading. This figure shows that the temperature was distributed homogenously through the specimen width with a maximum zone at the center of the gauge area. The temperature field pattern was the same for all stress amplitudes smaller than σ_c, with a difference only in steady-state temperature value, which increased with increasing stress amplitude. However, the temperature field was different for stress amplitudes greater than this critical stress amplitude, $\sigma_a > \sigma_c$, for which a sudden increase occurred in temperature elevation (stress amplitudes corresponding to Points B and E, in Figure 3-5).

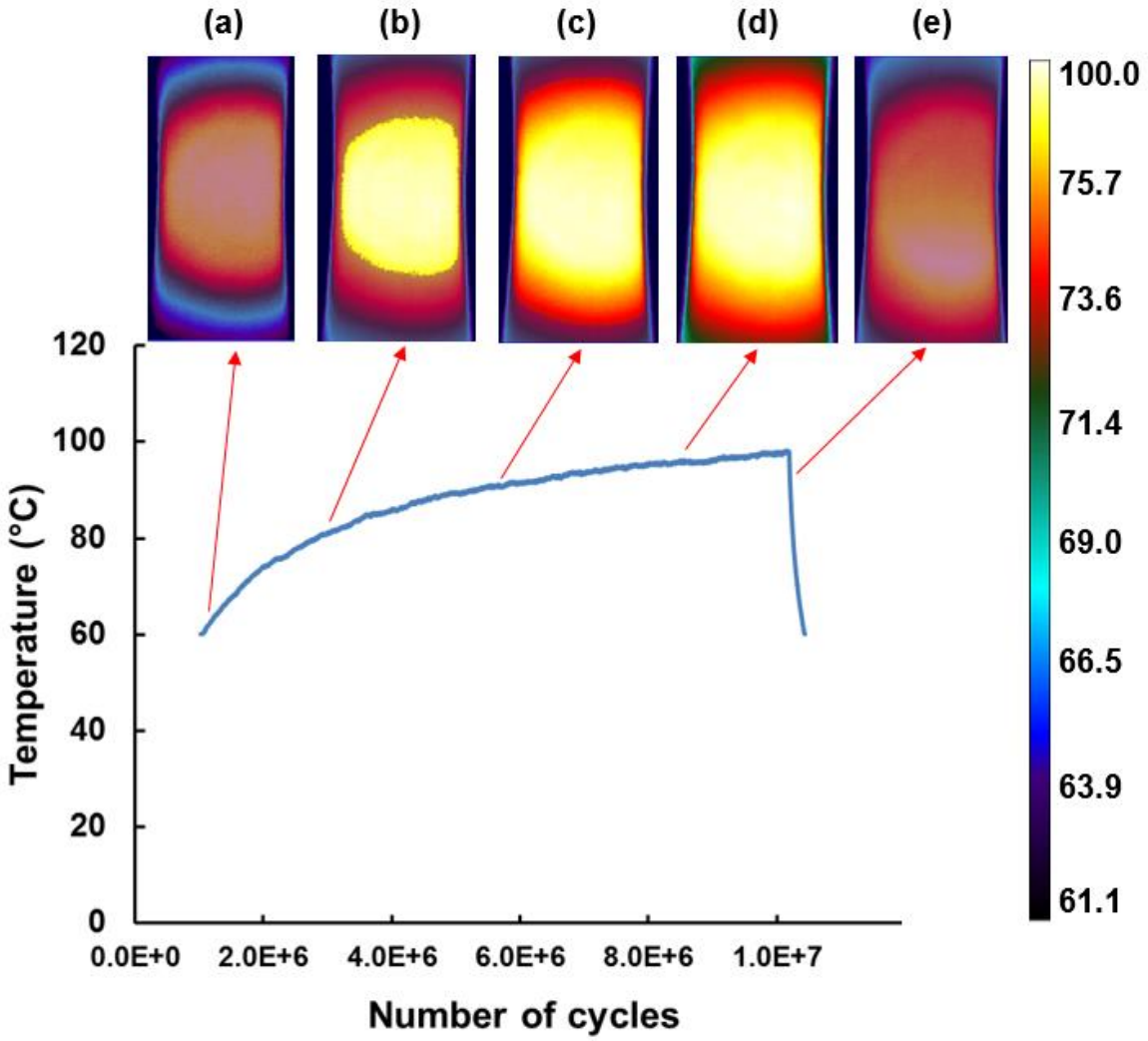

Figure 3-6 Temperature fields on specimen surface during fatigue loading and after stopping the test, for σ_a = 247 MPa.

The thermographic images obtained for σ_a = 251 MPa (corresponding to Point B in Figure 3-5) are presented in Figure 3-7. As shown in this figure, after 7.756×10^6 cycles, the temperature reached locally a minimum recordable value based on the camera calibration (T = 135°C) and then an inhomogeneous temperature zone was observed at the left side of the specimen gauge part. Afterwards, this zone propagated through the specimen with increasing the number of cycles. This observation indicates the initiation of a strong localized dissipative mechanism and a consequent creation of a high-temperature zone. Figure 3-7(d) and (e) show that after the temperature peaked at ~350°C, the localized dissipation stopped and the temperature field became homogeneous through the specimen width. In other words, homogeneous dissipation occurred and temperature stabilized at a high level.

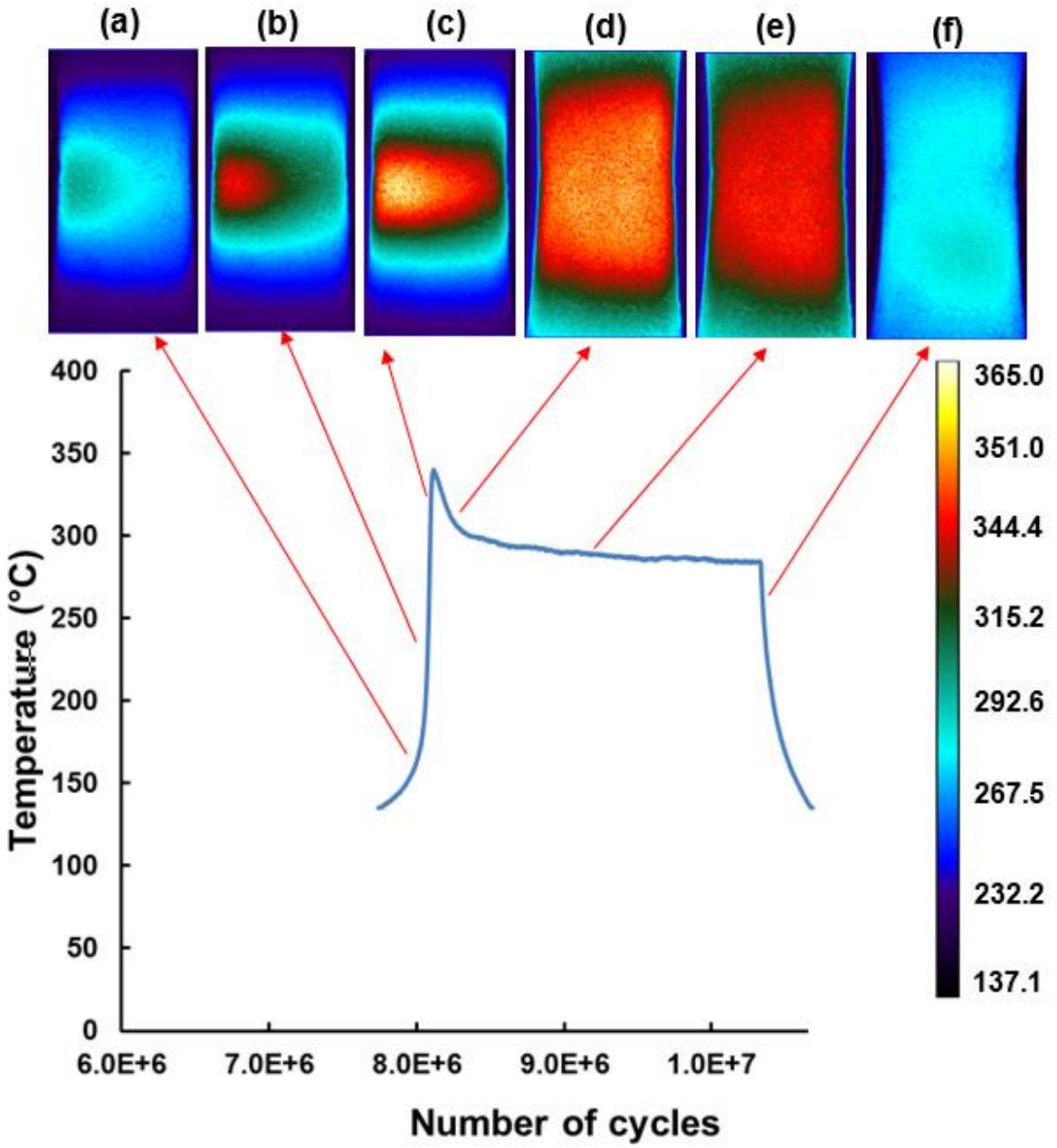

Figure 3-7 Temperature fields on the specimen surface during cyclic loading and after stopping the test, for σ_a= 251 MPa.

For the higher stress amplitudes (Point E in Figure 3-5) the same behavior was observed up to the stress value at which specimen rupture occurred. Figure 3-8 depicts the temperature field for σ_a = 330 MPa for different numbers of cycles up to rupture. Before N = 4.428 × 10^6 cycles, the temperature was less than the minimum recordable value based on the camera calibration. However, after this number of cycles, an inhomogeneous temperature zone was visible near the specimen edge. This inhomogeneous zone grew rapidly up to specimen fracture, which

corresponds to a maximum temperature. At this instant, the test stopped automatically and the temperature dropped suddenly. After the specimen cooled down, it was possible to observe the temperature distribution around the crack tip (Figure 3-8(f)).

In Figure 3-8(e), the white color means that the temperature exceeded the maximum recordable temperature of the camera (365°C) for ~0.4 s. For stress amplitudes corresponding to Points C and D in Figure 3-5, the temperature field pattern was the same as in Figure 3-6 (no localized dissipative zone was observed).

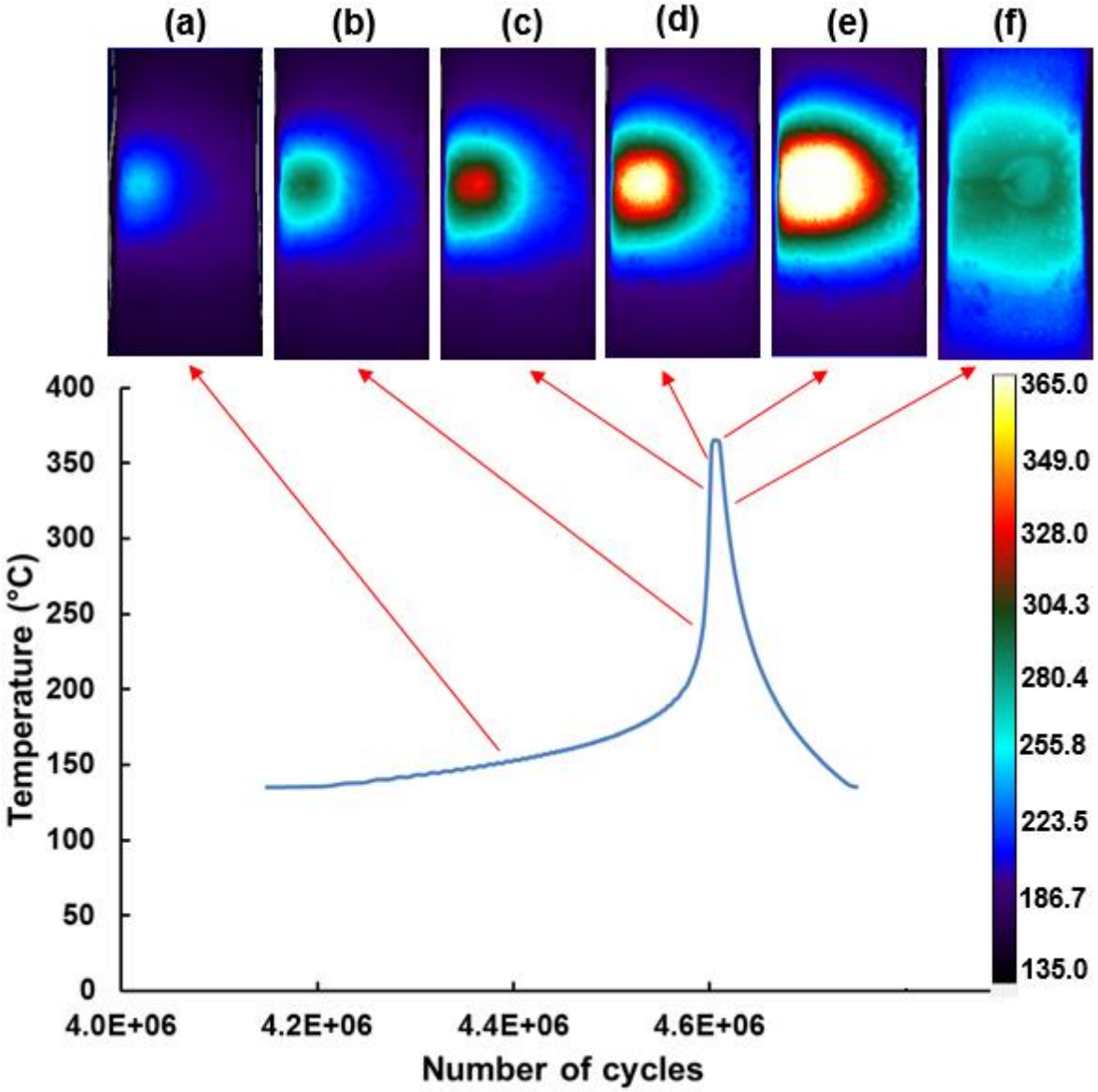

Figure 3-8 Temperature fields on the specimen surface for σ_a = 330 MPa.

Thermal measurements were repeated for several specimens to ensure reproducibility of the results. Figure 3-9 illustrated the temperature elevation versus stress amplitude for three specimens including the results previously shown in Figure 3-5. In Figure 3-9 the temperature increase results are presented just up to the first abrupt temperature increase. There is a good agreement between the measured data for the three specimens. It should be mentioned that a challenging point in experimental temperature measurements was adjusting the calibration of the camera according to the stress amplitude ranges. In some cases since the calibration was not adapted properly, the abrupt temperature increase was not recorded. Therefore, although measurements were carried out for numerous specimens, all temperature data were recorded for all tested specimens. However the data related to stress amplitudes below σ_c, for which no significant temperature elevation occurred was recorded for most of the specimens.

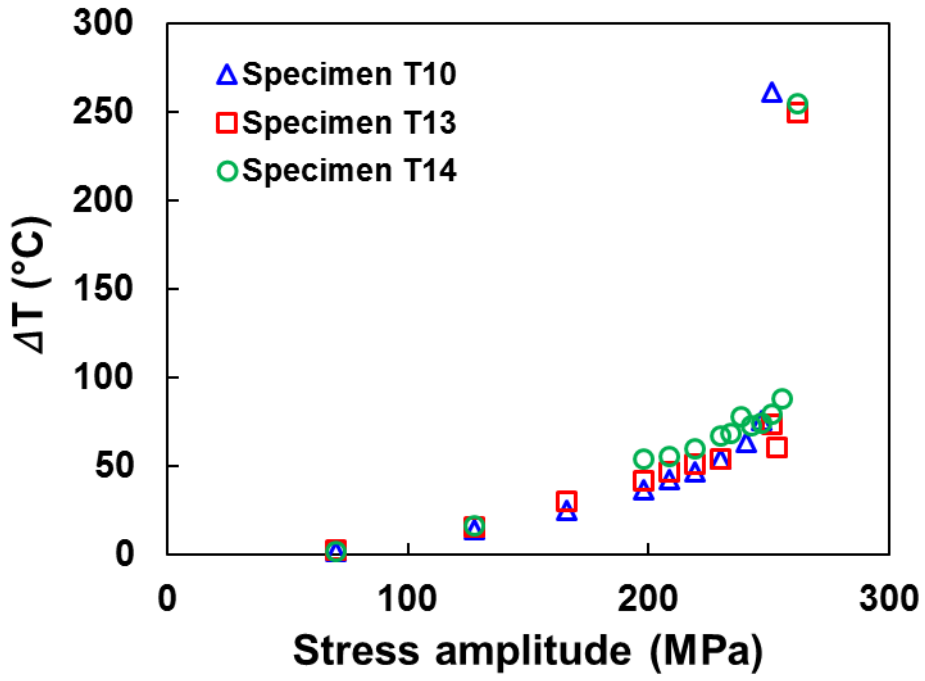

Figure 3-9 Mean temperature increase versus stress amplitude for three different ultrasonic specimens.

Figure 3-10 shows the measured critical temperature versus critical stress amplitude, for 5 specimens, including the ones presented in Figure 3-9. This figure shows that the critical stress amplitude and critical temperature values are very similar for all samples. σ_c was found to be in the range of 247 MPa to 256 MPa and the corresponding critical temperature ranges from 70 to 96°C. This result suggests that the abrupt temperature increase occurs above a specific stress

amplitude which coincides with a specific mean temperature. Therefore, σ_c and T_c can be related to material properties. The average values of the data plotted in Figure 3-10 will be considered as the critical stress and critical temperature of the material under ultrasonic loading as σ_{mc} = 252.7 $\pm$ 3.3 MPa and T_{mc} = 88.0 $\pm$ 11.8 °C, corresponding to plus or minus one standard-deviation.

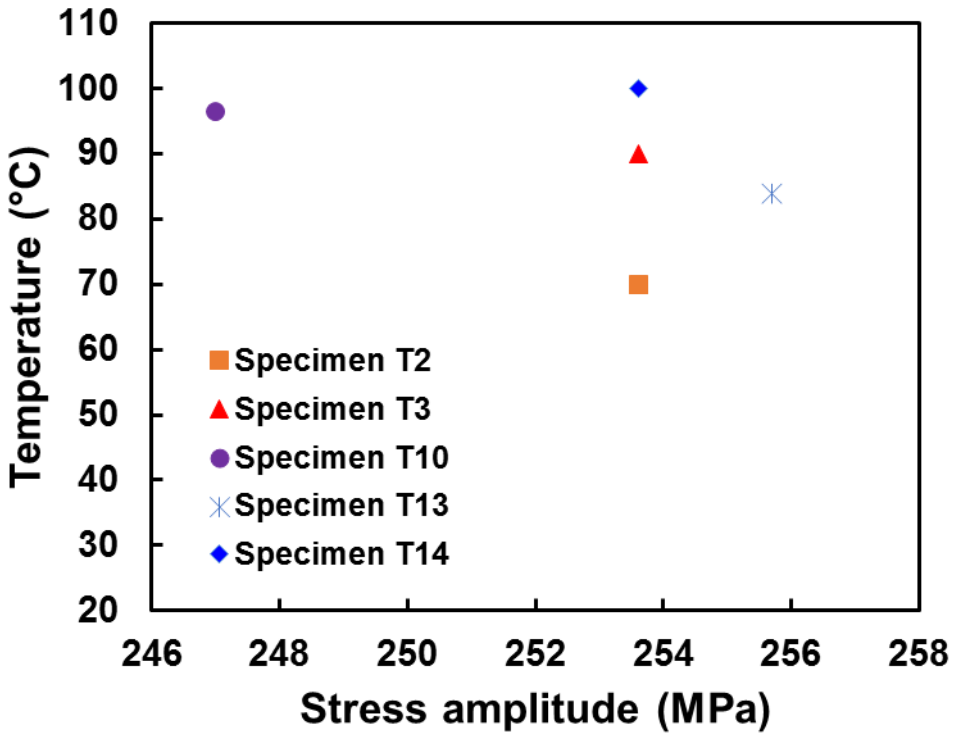

Figure 3-10 Critical stress amplitude and corresponding mean temperature for five different specimens under ultrasonic loading (each point is related to one specimen).

3.2.3 Heat source estimations

Temperature variation is not an intrinsic material response as it depends on the material diffusion properties and the thermal boundary conditions. Therefore, some methods have been developed to determine the heat source fields that accompany the temperature variations and these methods consider dissipated energy as a fatigue damage indicator. In other words, the dissipated energy in a unit volume of material is a more promising representation of the material behavior because of its clear physical meaning and its high sensitivity to microstructure evolution [105], [154].

In this study, the specific form of heat diffusion equation proposed by Boulanger et al. [103] is used to estimate the intrinsic dissipation from temperature measurements. Assuming there is no coupling between microstructure and temperature and neglecting the convective terms, the heat diffusion equation is written as:

$$\rho C\dot{T} - div\left(k\overrightarrow{grad\ (T)}\right) = s_{the} + d_1 + r \tag{3-1}$$

where ρ is the mass density, C is the specific heat, $\dot{T}$ denotes the time derivative of temperature, k is the heat conduction coefficient, s_{the} is the thermoelastic source, d_1 is the intrinsic heat dissipation and r is the external volume heat supply. Moreover, div represents divergence operator and $grad$ is the gradient. For the DP600 steel, $\rho = 7800$ kg/m^3 and $C = 460$ J/kg/°C [135].

It is assumed that the volume heat source is time independent so it is expressed as:

$$r = -kT_0 \tag{3-2}$$

in which T_0 is the initial equilibrium temperature. By assuming that the material parameters ρ, C and k are constant and by introducing the temperature increase $\theta = T - T_0$, the heat diffusion equation can be rewritten as:

$$\rho C\dot{\theta} - k\Delta\theta = s_{the} + d_1 \tag{3-3}$$

where $\dot{\theta}$ denotes the time derivative of temperature increase and Δ is the Laplace operator.

As suggested by Boulanger et al. [103], for symmetric boundary conditions, homogeneous heat source distribution, and initial conditions corresponding to a uniform temperature field, it can be assumed that heat losses are linear with respect to the temperature variation. Thus, $k\Delta\theta$ can be approximated by $-k\Delta\theta = \rho C\frac{\theta}{\tau}$, where τ is a time constant describing the thermal exchanges between the specimen and its environment. The heat diffusion equation is rewritten as:

$$\rho C\dot{\theta} + \rho C\frac{\theta}{\tau} = s_{the} + d_1 \tag{3-4}$$

The thermal boundary conditions are not symmetrical in this case because one end of the specimen is fixed to the horn and the other end is free as discussed by Blanche et al. [109]. However, the thermographic images that were presented in the previous section show that the specimen temperature field is symmetrical at low stress amplitudes (see Figure 3-3). That is

why Equation (3-4) is considered here. For high stress amplitudes the temperature field was not symmetric. Nevertheless, the aforementioned formulation was employed to make a rough estimation of dissipated energy at high stress amplitudes (Points B and E in Figure 3-5).

The time constant τ can be determined at the end of the test, just after the unloading when there is no applied stress; at this moment, the thermoelastic and intrinsic dissipation heat sources are zero whereas the temperature increase is not null ($\theta = T - T_0 \neq 0$). Therefore, the heat equation is reduced to:

$$\rho C\dot{\theta} + \rho C\frac{\theta}{\tau} = 0 \tag{3-5}$$

By solving the above equation, the theoretical relationship for temperature increase is obtained as:

$$\theta(t) = \theta_f \exp(\frac{-t}{\tau}) \tag{3-6}$$

where θ_f is the temperature increase that is measured when the loading stops. Thus τ is estimated by fitting the experimental data with the theoretical evolution of θ.

Because the loading frequency is much higher than the frame rate of the infrared camera (~100 Hz), it is not possible to measure the instantaneous value of θ, but only its average value can be determined over numerous loading cycles. Therefore, for any variable, by denoting:

$$\tilde{u} = \frac{1}{nT_1}\int_t^{t+nT_1} u dt = \frac{f}{n}\int_t^{t+T_1} u dt \tag{3-7}$$

where T_1 is the period of the loading, *f* is the loading frequency and *n* is the number of cycles, the heat diffusion equation can be rewritten as:

$$\rho C\dot{\tilde{\theta}} + \rho C\frac{\tilde{\theta}}{\tau} = \tilde{s}_{the} + \tilde{d}_1 \tag{3-8}$$

As stated by Boulanger et al. [103], the sum of the thermoelastic power over one loading cycle is null ($\tilde{s}_{the} = 0$), and thus the final form of the heat diffusion equation is obtained:

$$\rho C\dot{\tilde{\theta}} + \rho C\frac{\tilde{\theta}}{\tau} = \tilde{d}_1 \tag{3-9}$$

Therefore, in the stabilized regime, when $\dot{\tilde{\theta}} = 0$, the intrinsic dissipation averaged over numerous cycles is determined from Equation (3-9) as:

$$\rho C \frac{\tilde{\theta}}{\tau} = \tilde{d}_1 \tag{3-10}$$

The mean dissipated energy per cycle can be obtained as $\tilde{d}_1/f$, where f is the loading frequency.

This formulation was used to measure the dissipated energy per cycle versus stress amplitude and the results are presented in Figure 3-11. By increasing the stress amplitude up to 247 MPa the dissipated energy increases gradually. However, for higher stress amplitudes for which strong heating occurred (Points B and E in Figure 3-5), the dissipated energy per cycle is significantly higher than that of lower stress amplitudes. For instance at σ_a =251 MPa the dissipated energy is ~7 times as much as that at σ_a =247 MPa. If the results are replotted just for low stress amplitudes ($\sigma_a \leq 247$ MPa), where no strong heating occurs, the dissipated energy per cycle will be a quadratic function of stress amplitude, as shown in Figure 3-12.

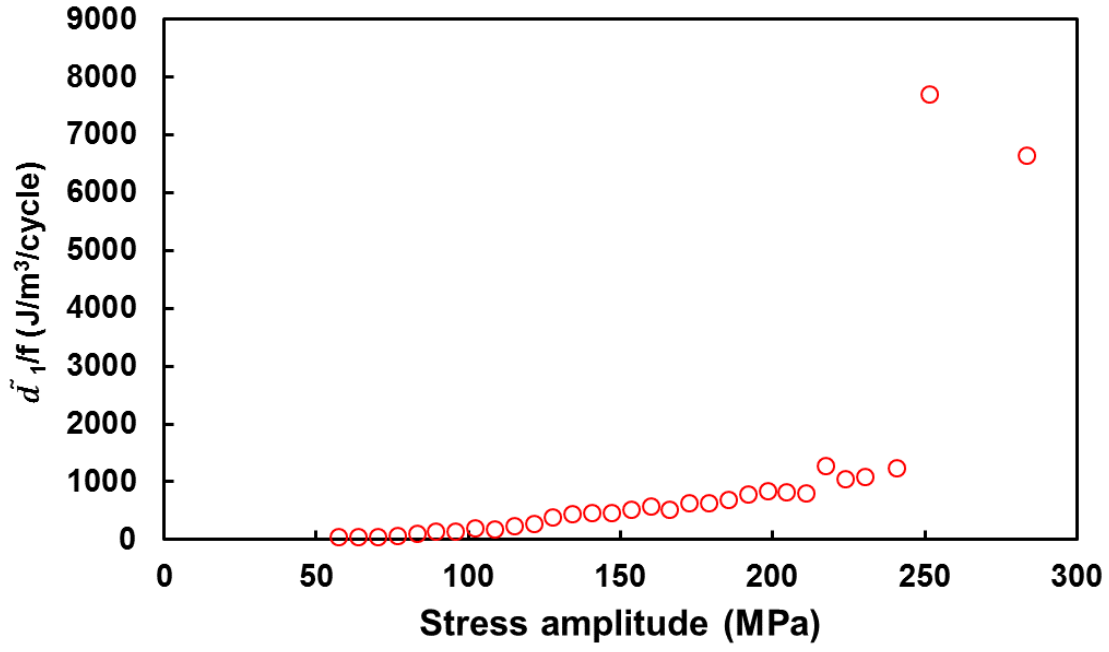

Figure 3-11 Mean dissipated energy per cycle versus stress amplitude, for DP600 steel under ultrasonic loading.

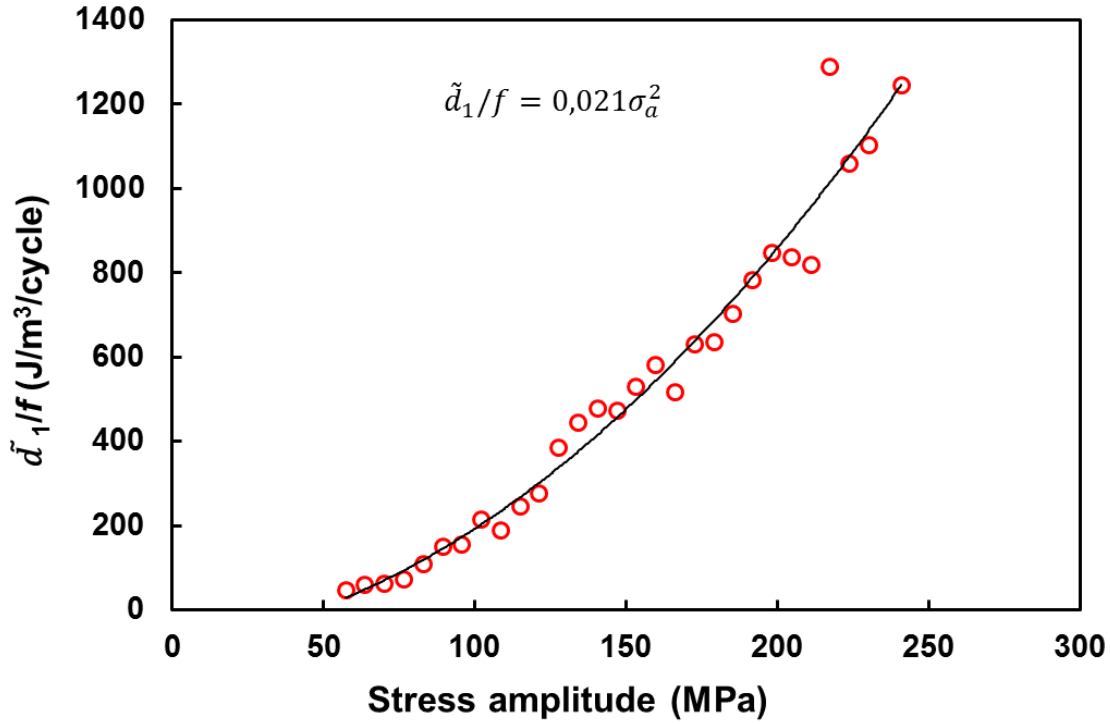

Figure 3-12 Mean dissipated energy per cycle versus stress amplitude, for low stress amplitudes (σ_a <250 MPa).

Favier et al. [110] measured the dissipated energy per cycle as a function of cycles up to 10^9 cycles for α-iron (ferrite) under 20-kHz fatigue loadings. Figure 3-13 shows their results for dissipated energy, indicated by $\overline{W}_d$, at the normalized stress amplitude of σ_a/σ_{ut}=30%. In our case, by normalizing the stress amplitude by the ultimate tensile strength presented in Table 2-2, it is found that at σ_a/σ_{ut}=30% (which corresponds to σ_a=200 MPa) the dissipated energy per cycle is ~800 J/m^3/cycle, which is in a good agreement with the results for α-iron presented in Figure 3-13. This is consistent with the fact that in DP steel the dissipated mechanisms occur in the soft ferrite phase.

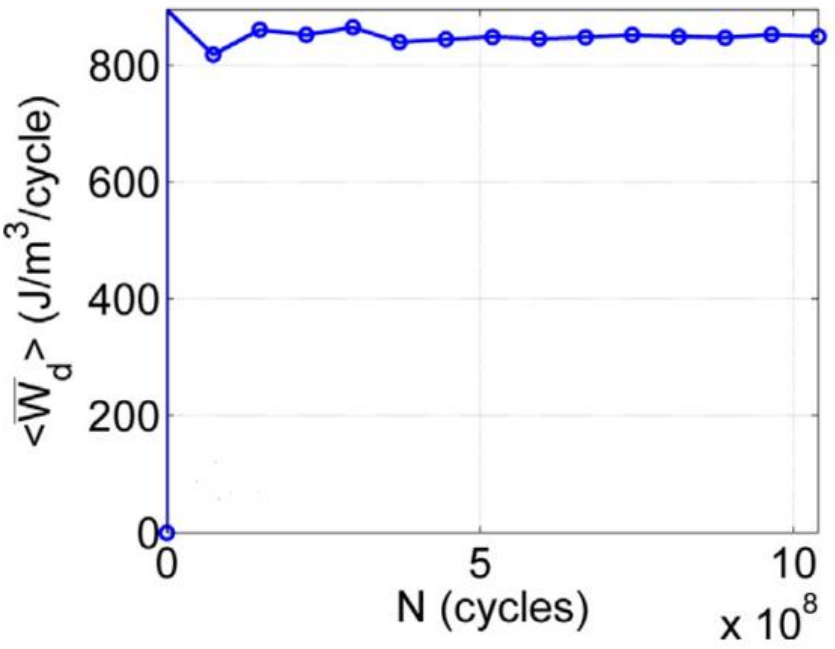

Figure 3-13 Dissipated energy for α-iron fatigued under 20-kHz loading up to 10^9 cycles at σ_a/σ_{ut} =30% [110].

3.3 Conventional Fatigue Loading

3.3.1 Temperature variations during cycling

Successive conventional fatigue loadings were carried out at the frequencies of 50 and 80 Hz, according to the procedure explained in Chapter 2 (see Figure 2-20(b)). The temperature evolution was measured using in situ infrared thermography, analogous to the case of ultrasonic loading. The evolutions of the mean temperature at the frequency of 80 Hz are presented in Figure 3-14 for some of the loading steps. In the case of conventional fatigue loading, the material showed a classical thermal response for all stress amplitudes before rupture. For stress amplitudes below 270 MPa the temperature increase was less than 2°C. By increasing the stress amplitude the steady state temperature increased gradually and reached ~45°C at σ_a =340 MPa. The specimen ruptured just after ~3000 cycles at σ_a =350 MPa. In Figure 3-15 temperature fields on the specimen surface are correlated to temperature evolution during cycling for the last step of loading which resulted in specimen rupture. The temperature distribution was homogenous though the specimen width up to the final fracture and no concentrated dissipative zone was observed, contrary to the case of ultrasonic fatigue loading.

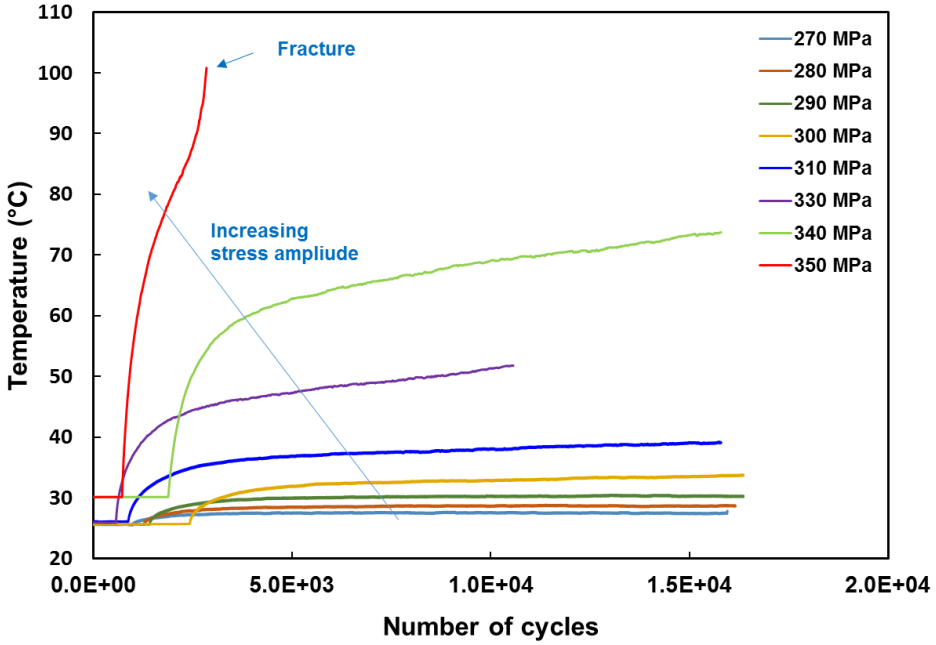

Figure 3-14 The mean temperature evolution versus number of cycles for several loading steps, before stopping the test (f = 80 Hz).

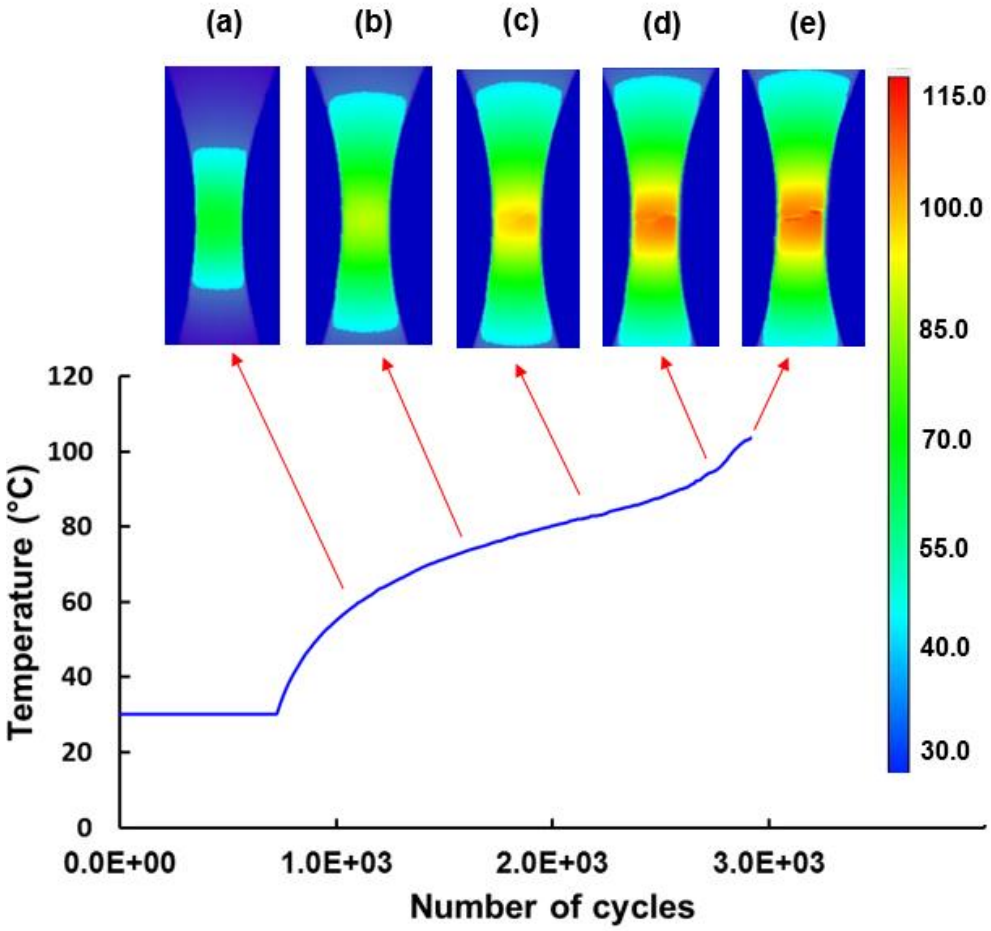

Figure 3-15 Temperature fields on the specimen surface under 80-Hz frequency loading up to final fracture, for σ_a = 350 MPa.

3.3.2 Evolution of self-heating versus stress amplitude

The mean steady-state temperature increase was measured for each loading step excluding the final step corresponding to the final rupture. The mean temperature increase is plotted versus stress amplitude in Figure 3-16, for the frequencies of 50 and 80 Hz. The temperature elevation increases gradually by increasing the stress amplitudes. The mean temperature increase was slightly higher for 80-Hz frequency loadings than that of 50-Hz fatigue tests for stress amplitudes above 280 MPa. The maximum difference is ~3°C which corresponds to σ_a=330 MPa.

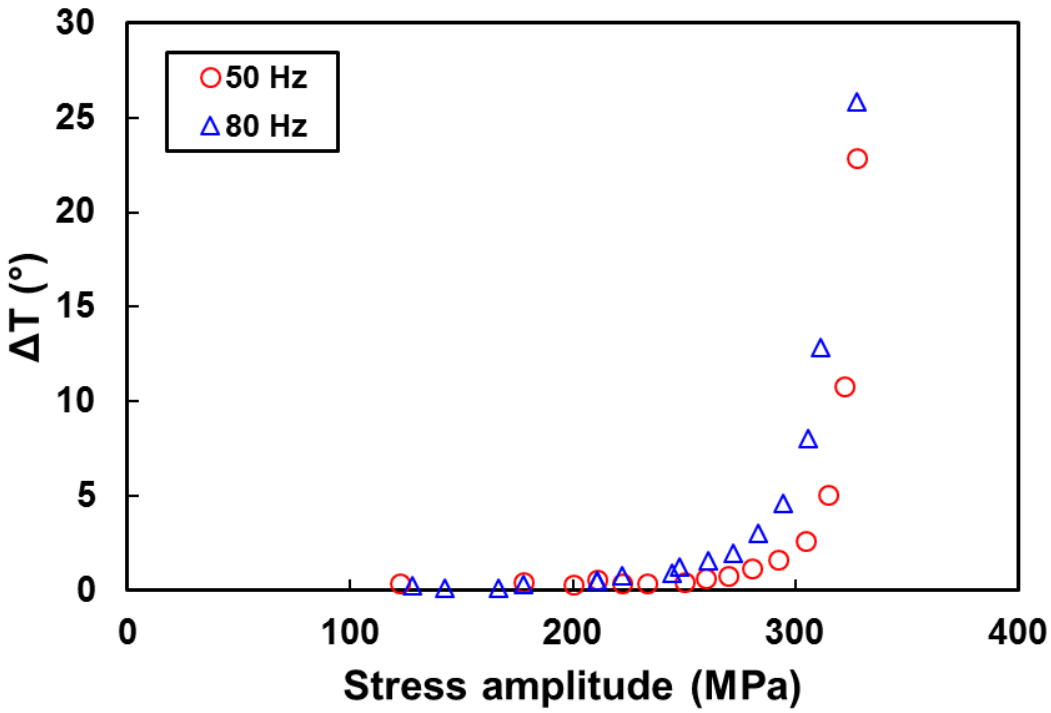

Figure 3-16 Mean temperature elevation versus stress amplitude for conventional fatigue tests.

3.3.3 Estimation of dissipated energy per cycle

The dissipated energy per cycle was measured for conventional 50- and 80-Hz fatigue tests with the same methodology as explained in Section 3.2.3 and the results are depicted in Figure 3-17. This figure shows that there is not any considerable frequency effect on dissipated energy per cycle in low-frequency ranges as the dissipated energy per cycle is quite similar for 50 Hz and 80 Hz.

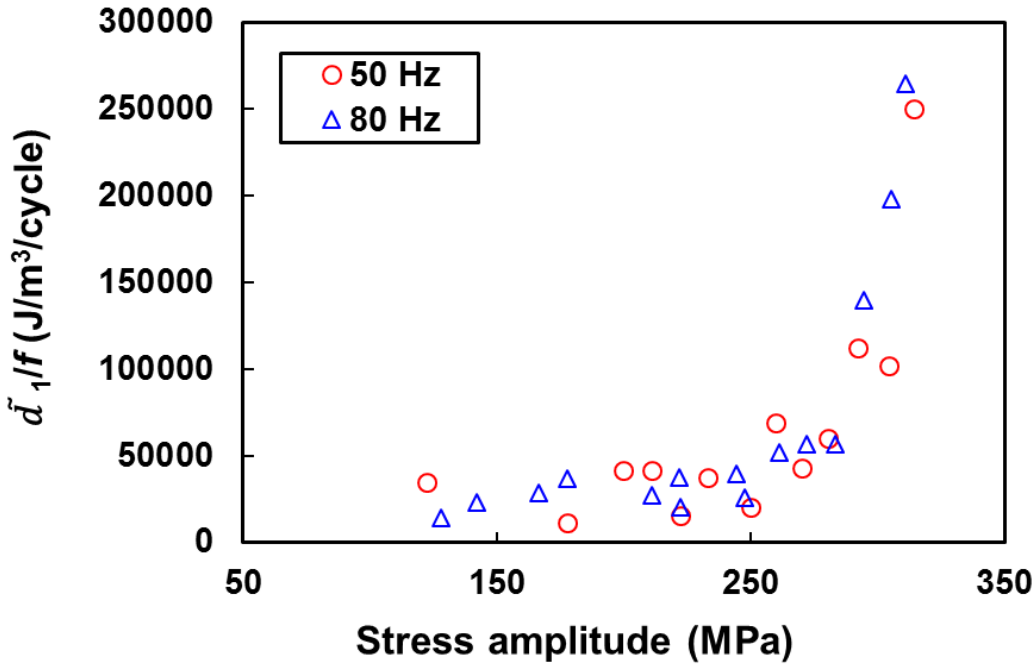

Figure 3-17 Dissipated energy per cycle for DP600 steel under conventional low-frequency fatigue tests.

3.4 Comparison of Ultrasonic and Conventional Fatigue Loadings

In order to study the possible effect of ultrasonic frequency on dissipation, the results obtained for 20-kHz (Figure 3-11) and 80-Hz frequencies are represented in logarithmic scale in Figure 3-18. From this figure it can be observed that for the same stress amplitude, the dissipated energy per cycle is much higher in the case of low-frequency 80-Hz cycling than ultrasonic loading at low stress amplitudes. For instance, at the stress amplitude of 200 MPa, the dissipated energy per cycle was ~30000 J/m^3/cycle for 80-Hz loading while it was ~900 J/m^3/cycle under ultrasonic testing tests (~30 times greater in the case of 80-Hz loading). However for high stress amplitudes (Points A and B) the ultrasonic results are closer to those of conventional 80-Hz. For instance, at the stress amplitude of 250 MPa, the dissipated energy per cycle was ~20000 J/m^3/cycle for 80-Hz loading while it was ~8000 J/m^3/cycle under ultrasonic testing (2.5 times greater in the cast of 80-Hz loading).

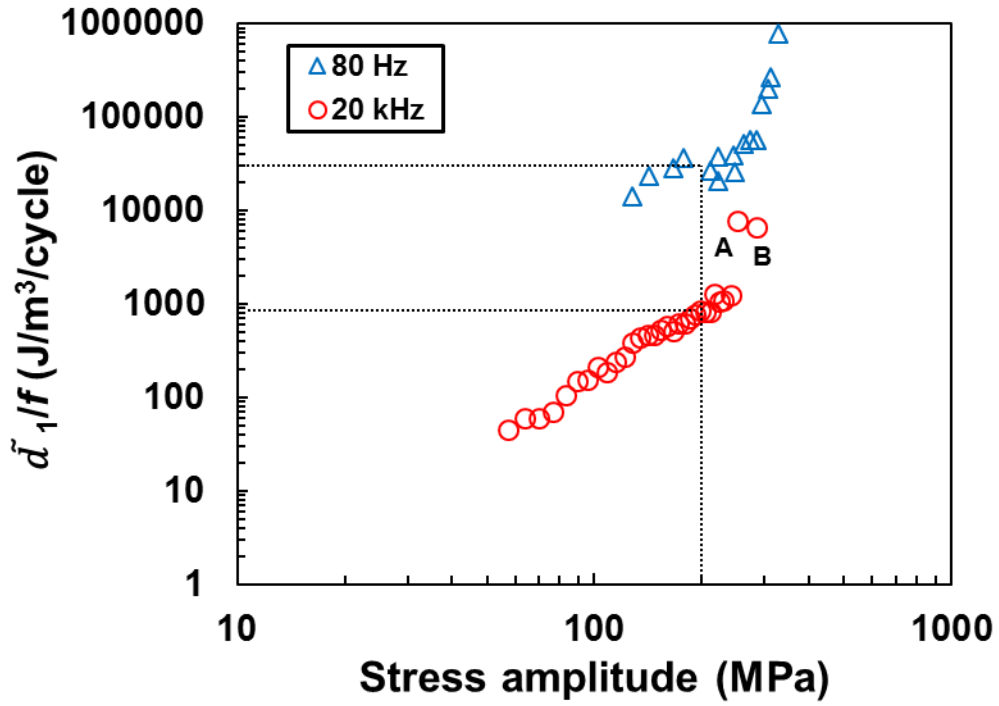

Figure 3-18 Effect of frequency on dissipated energy per cycle.

3.5 Microscopic Observations

Surface of ultrasonic and conventional specimens were observed by optical microscopy and SEM at different loading steps. Some representative OM images are correlated to the corresponding temperature evolution diagram in Figure 3-19 and Figure 3-20. For conventional fatigue samples slip bands (SBs) formed on the specimen surface from early stages of loading and were developed by increasing the number of cycles. However, in the case of ultrasonic loadings, no slip band was detected for $\sigma < \sigma_c$, while many slip bands and microcracks along the slip bands were observed on the surface of specimens loaded at $\sigma > \sigma_c$.

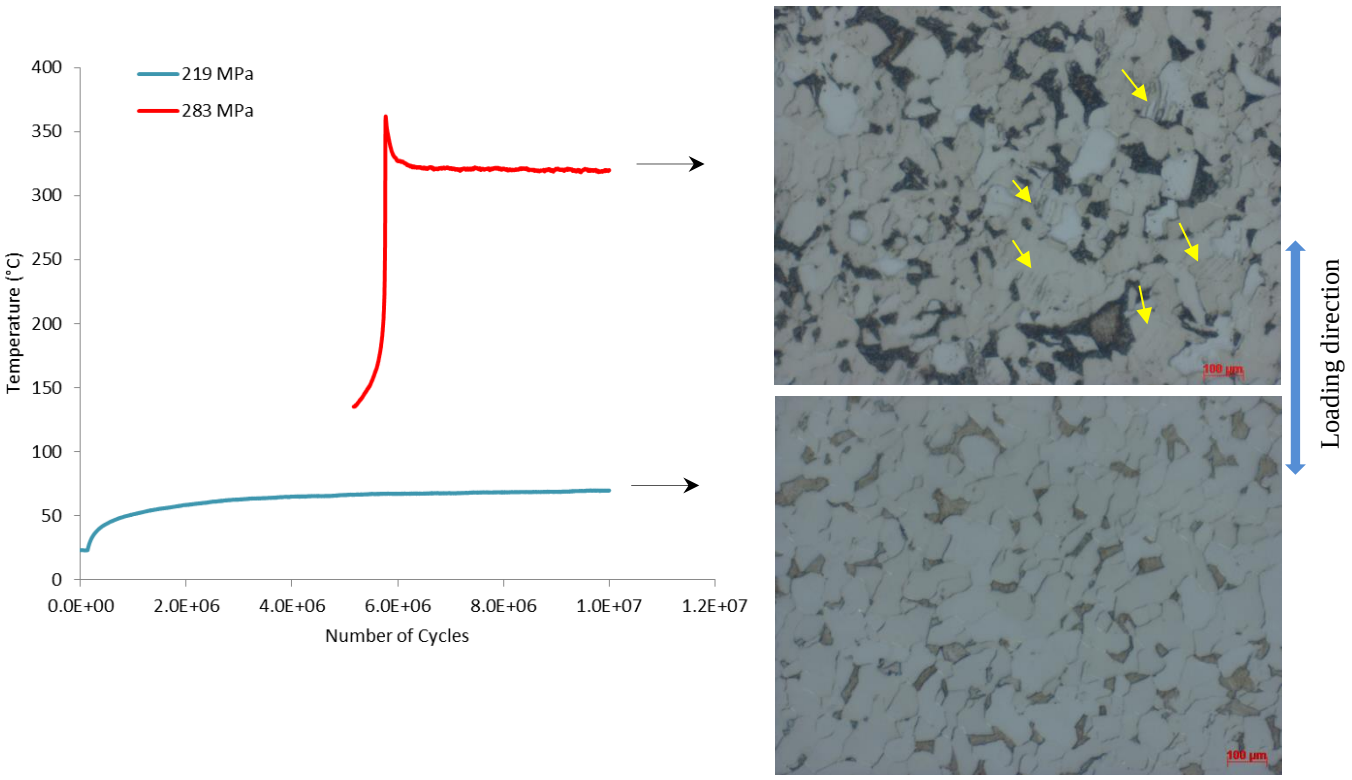

Figure 3-19 Optical microscopy observations on ultrasonic specimens under thermography studies (yellow arrows show the grains containing SBs).

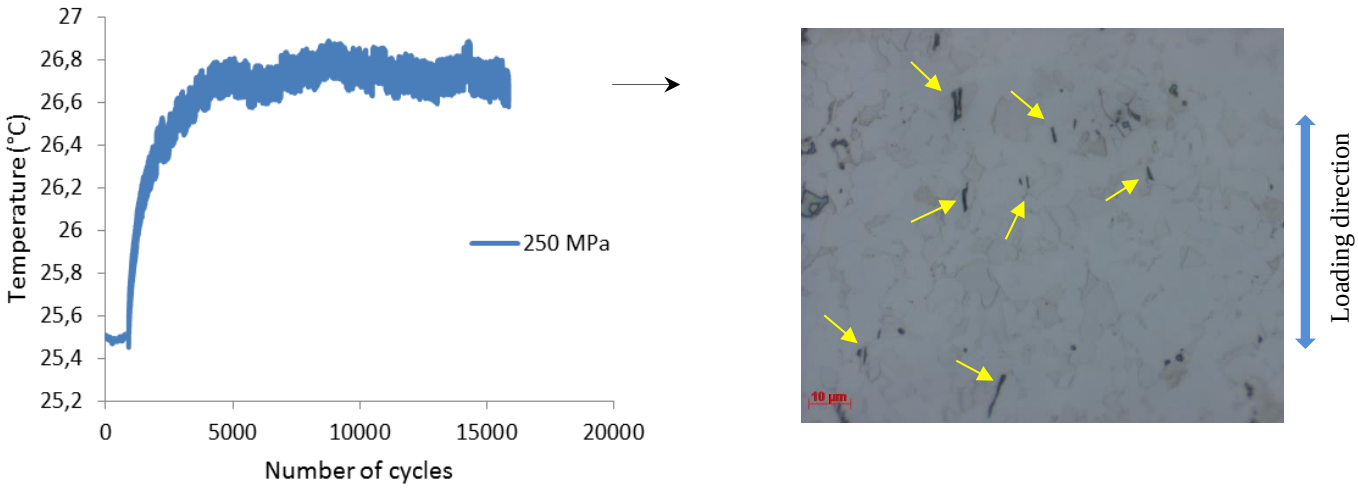

Figure 3-20 Optical microscopy observations on Conventional 80-Hz specimen (yellow arrows show SBs).

3.6 Concluding Remarks

In this chapter, the results obtained from calorimetric studies under ultrasonic and conventional fatigue tests were presented. It was observed that under ultrasonic loading there was a critical

stress amplitude, above which a strong heating occurred and temperature increased up to several hundreds of degrees. In this case, the thermographic images revealed the formation of an inhomogeneous temperature zone which propagated and then disappeared by increasing the number of cycles. Under 50-Hz and 80-Hz conventional loadings the material showed a classical thermal response and a homogeneous temperature filed for all stress amplitudes before rupture. The dissipated energy per cycle was measured using the heat diffusion equation. For conventional tests no frequency effect was observed according to the results obtained for 50-Hz and 80-Hz frequencies. Under ultrasonic fatigue loadings at low stress amplitudes the dissipated energy per cycle was a quadratic function of the stress amplitude. Comparison of the results revealed that under ultrasonic loading the dissipated energy was significantly lower than that of conventional fatigue tests. Moreover, optical microscopy revealed formation of slip bands on the surface of specimens in the case of conventional loadings as well as ultrasonic tests at high stress amplitudes. However for ultrasonic tests at low stress amplitudes for which no strong heating occurred, no slip band was detected.

Chapter 4

Fatigue Characterization of the Material

Résumé

Caractérisation de la fatigue sous chargement de fatigue ultrasonique et conventionnelle

Les observations expérimentales présentées dans ce chapitre révèlent une divergence entre les données S-N, la déformation et les mécanismes de rupture entre les chargements de fatigue ultrasonique et de fatigue conventionnelle à 30 Hz. La durée de la vie est plus élevée pour une amplitude de contrainte donnée dans des essais ultrasoniques alors que la contrainte limite de fatigue est presque identique pour les deux cas. À 20 kHz, la température de l'éprouvette augmente jusqu'à ~ 350 ° C dans les premiers stades du chargement cyclique à des amplitudes de contrainte au-dessus de la limite de fatigue, alors qu'à 30 Hz l'augmentation de la température reste inférieure à 15°C. Sous des chargements conventionnels, la rupture de fatigue est toujours déclenchée sur bandes de glissement à la surface de l'échantillon. L'amorçage de la rupture sous chargement ultrasonique se produit principalement à l'intérieur, mais quelques cas d'initiation de surface ont également été observés. Dans ce cas, les initiations de fissures de surface et internes ont été induites par la présence d'une inclusion. La surface de rupture en œil de poisson a été détectée pour l'initiation de la fissure induite par inclusion interne à 20 kHz. La zone granulaire fine (FGA) n'a pas été observée dans ce cas. Pour les chargements ultrasoniques et à basse fréquence, la croissance des fissures est transgranulaire et aucune fissure intergranulaire n'a été détectée. Les observations de SEM sur la surface des échantillons ont révélé que sous les essais ultrasoniques à des amplitudes de contraintes élevées (au-dessus de la limite de fatigue), de nombreuses bandes de glissement étaient formées sur la surface. Dans ce cas, de nombreuses cavités et microfissures ont été détectées le long des bandes de glissement. D'autre part, pour les essais ultrasoniques sous la limite de fatigue (les échantillons non-rompus), aucune bande de glissement n'a été observée sur la surface. Dans le cas des essais conventionnels, des bandes de glissement ont été formées sous la surface des premiers stades de chargement, même aux amplitudes de contrainte inférieures à la limite de fatigue. Cependant, dans ce cas, aucune cavitation n'a été détectée le long des bandes de glissement.

4.1 Introduction

The second part of experimental studies concerns fatigue characterization of the material under ultrasonic 20-kHz fatigue loadings as well as conventional low frequency tests. As previously mentioned in Chapter 2, in the case of ultrasonic tests, an air-cooling system was employed to reduce the temperature elevations during the tests. In addition, the conventional tests were conducted at 30-Hz frequency. The S-N curves were determined under both ultrasonic and conventional 30-Hz loadings. Scanning Electron Microscopy (SEM) observations were made on specimen surfaces before and after rupture. Moreover, fracture surface of all failed specimens were carefully observed by SEM paying attention to the crack initiation sites and material failure mechanisms. The experimental results are presented in the following sections. It should be mentioned that some of the results presented in this Chapter has been submitted to be published in the Acta Materialia Journal [155].

4.2 S-N Curves

The S-N data obtained from ultrasonic loadings and conventional fatigue tests is presented in Figure 4-1. Both S-N curves exhibit a rise in the number of cycles to failure with decreasing the stress amplitude, followed by a quasi-plateau suggesting the existence of a fatigue limit. The decreasing slope is about 40 MPa per decade for the 30 Hz fatigue and $10^4<N<10^6$ cycles. It is a little bit lower for 20 kHz fatigue testing, namely 20 MPa per decade, $10^6<N<10^8$ cycles. In the decreasing part of the curve, the data corresponding to the 30 Hz fatigue loading are much less scarce than the data associated with 20 kHz fatigue testing. Besides, it can be seen that for a given stress amplitude σ_a, the fatigue lifetime measured by ultrasonic loading was higher than that obtained from conventional tests. The number of cycles at the knee point obtained at 30 Hz was ~2×10^6 cycles, whereas the corresponding value at 20 kHz was ~3×10^8 cycles (see Figure 4-1). For a given number of cycles ranging from 10^6 to 10^7, where the data exist for both loading techniques, the fatigue strength is higher at 20 kHz than at 30 Hz. However, both frequencies have resulted in the same fatigue limit of $\sigma_D = 260 \pm 5$ MPa, determined based on the asymptotic line below which no failure occurred.

Based on infrared thermography measurements in the case of ultrasonic loadings at stress amplitudes above the fatigue limit (all points in the S-N diagram excluding the run-out points), strong heating occurred in the early stages of cycling, leading to significant temperature

increases up to ~350°C. However, at stress amplitudes below the fatigue limit, temperature remained below 40°C. In the case of 30-Hz frequency, temperature increase was negligible ($\Delta T<15°C$) in comparison with ultrasonic loadings and no cooling system was used.

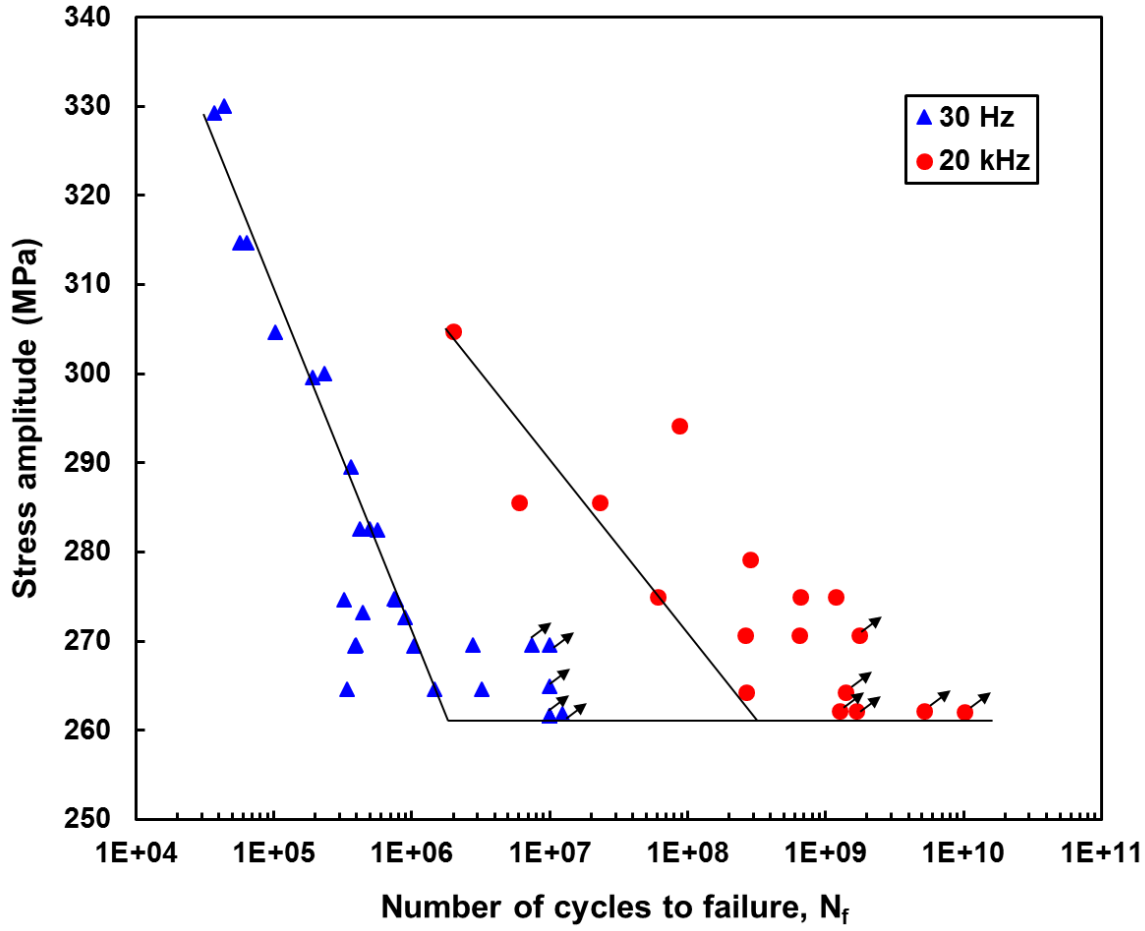

Figure 4-1 S-N data of DP600 steel, obtained from 20-kHz and 30-Hz fatigue loadings.

4.3 Fractography studies

Fracture surfaces of conventional and ultrasonic ruptured specimens were investigated by SEM and representative fractography results are presented in this section.

4.3.1 Conventional 30-Hz fatigue loading

For all specimens ruptured under 30-Hz frequency loading, fatigue crack initiated from slip bands or defects on the specimen surface. The characteristic flow lines emerging from the origin and progressing in the direction of crack propagation can be used to trace back the fracture origin. In this case, both single and multiple crack initiations were detected. For instance, two single crack initiation samples are shown in Figure 4-2 and Figure 4-3. Cracks mostly initiate from corners of the specimens which imply stress concentrations due to the sharp geometry. Figure 4-4 depicts two samples of multiple crack origins. In these figures the crack initiation sites are indicated by yellow arrows. The fracture surface can be separated into three typical areas, as indicated by a couple of dashed lines in Figure 4-2 (a); Region 1: crack initiation, Region 2: crack propagation, and Region 3: final rapid fracture. The higher magnifications of Regions 1, 2, and 3 are presented in Figure 4-2(b-d). As it is shown in Figure 4-2(c), the striations, which are a typical feature of fatigue crack propagation can be distinguished in some areas. The striation regions are very similar to the results reported by Irwan et al. [156] for HCF fracture of a DP600 steel under fully reversed loading. As shown in Figure 4-2(d), in the final failure zone bright areas containing arrays of dimples were detected.

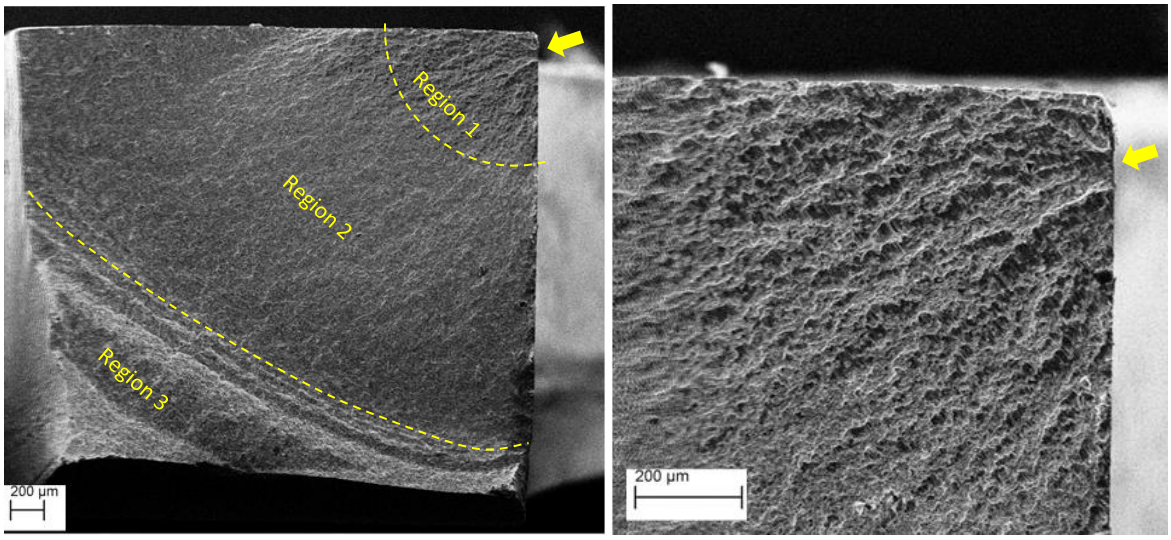

(a) (b)

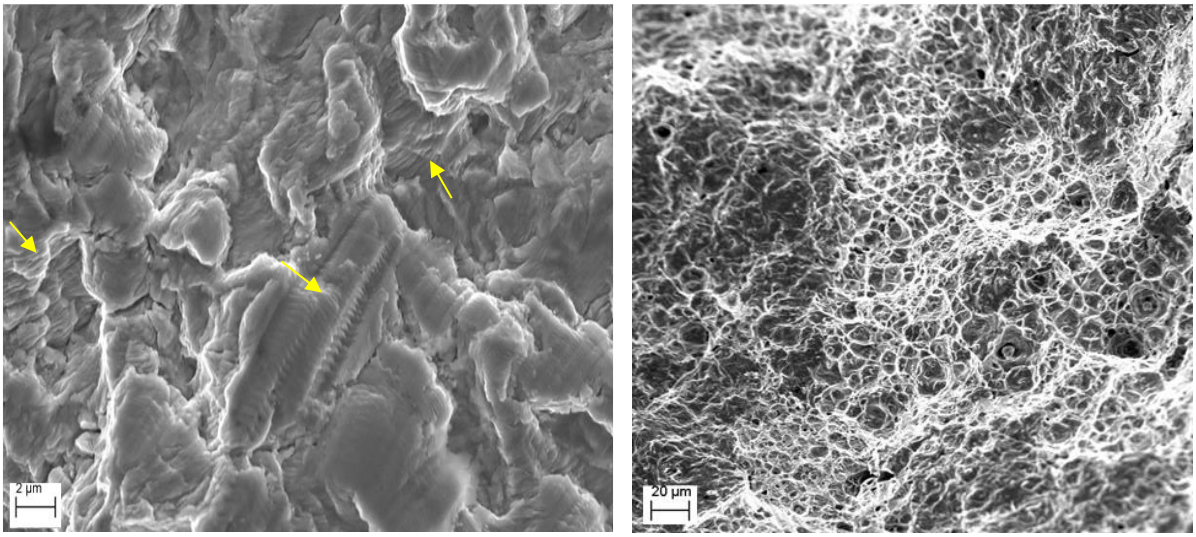

(c) (d)

Figure 4-2 (a) Fracture surface of a conventional fatigue specimen with single crack origin, $\sigma_a = 275$ MPa and $N_f = 7.7\times10^5$ cycles; **(b)** Higher magnification of Region 1 in (a) showing the fracture initiation zone; **(c)** Higher magnification of Region 2 in (a) indicating the regions with fatigue striations; **(d)** Dimples in the final failure zone.

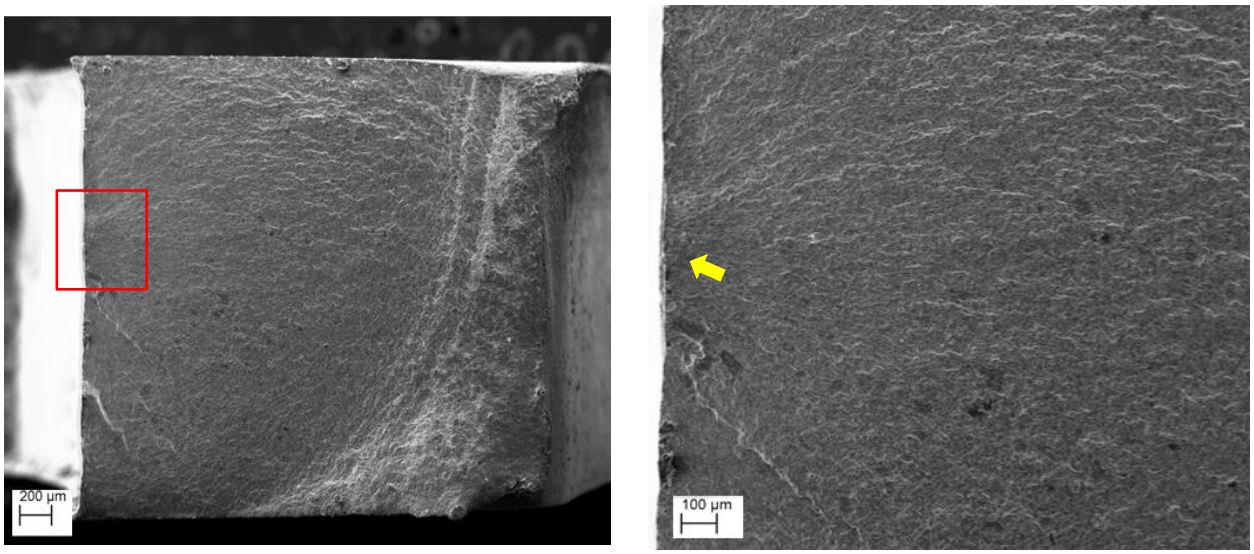

(a) (b)

Figure 4-3 Fracture surface with single crack origin located far from the specimen corner for a conventional fatigue sample ruptured at $\sigma_a = 265$ MPa and $N_f = 3.38\times10^5$ cycles.

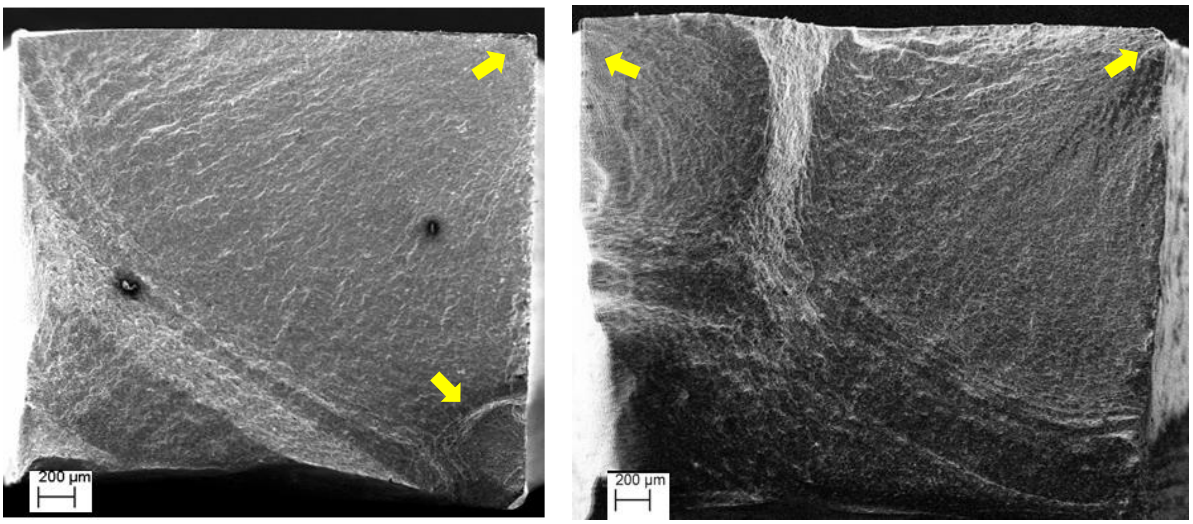

(a) (b)

Figure 4-4 Multiple fracture origins in conventional fatigue samples **(a)** $\sigma_a = 300$ MPa and $N_f=2.3\times10^5$ cycles; **(b)** $\sigma_a = 330$ MPa and $N_f=3.7\times10^4$ cycles.

Occurrences of single or multiple crack propagations under conventional fatigue tests are denoted by different marks in Figure 4-5. From this figure it can be also inferred that under low frequency tests, single cracks tend to occur at low stress amplitude levels whereas multiple cracks are more likely to happen at high stress amplitudes. Such a behavior has been also reported for a low-carbon steel by Guennec et al. [85].

4.3.2 Ultrasonic 20-kHz fatigue loading

In the case of ultrasonic fatigue tests, crack initiation was mainly internal, however some cases of surface crack initiation were also observed. In this case, crack initiation was always inclusion-induced for both internal and surface crack initiations. For instance, Figure 4-6(a) shows an inclusion-induced surface initiation sample for a specimen ruptured at $N_f = 6\times10^6$ cycles at stress amplitude of 286 MPa. Figure 4-6(b) shows the higher magnification of the crack initiation zone, in which inclusions can be seen on the specimen surface, as the cause of surface crack initiation.

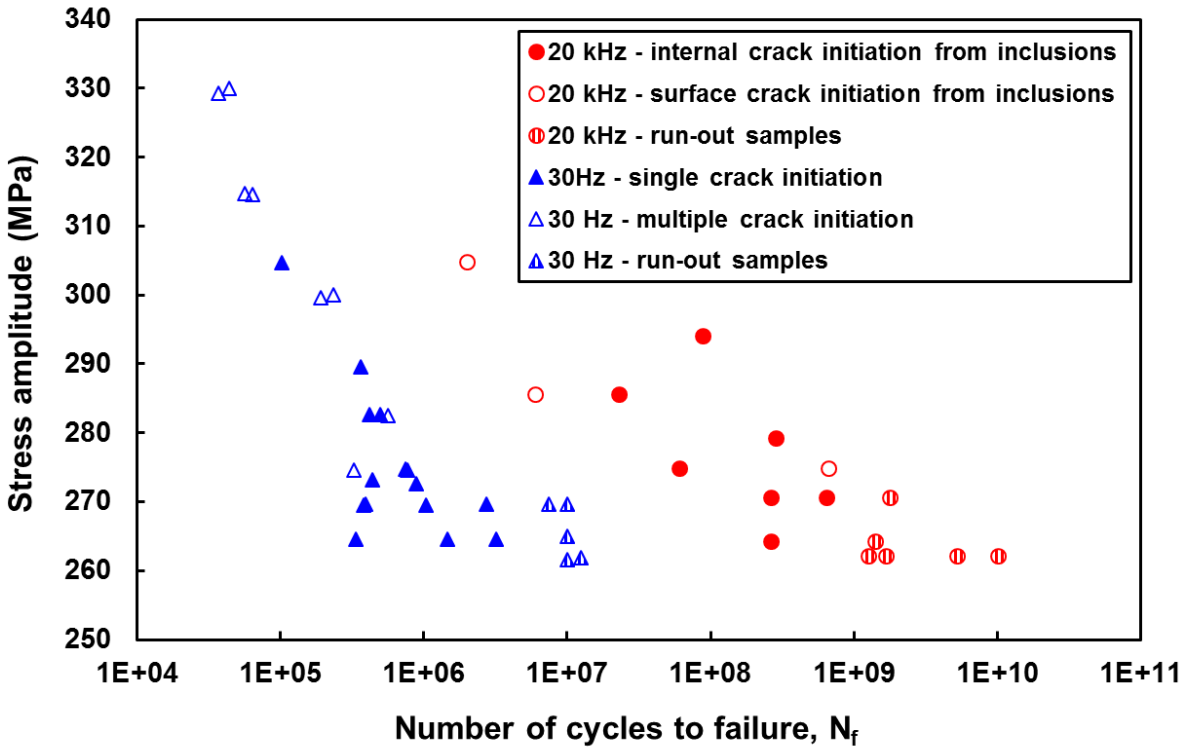

Figure 4-5 Summary of the fracture behavior of DP600 steel.

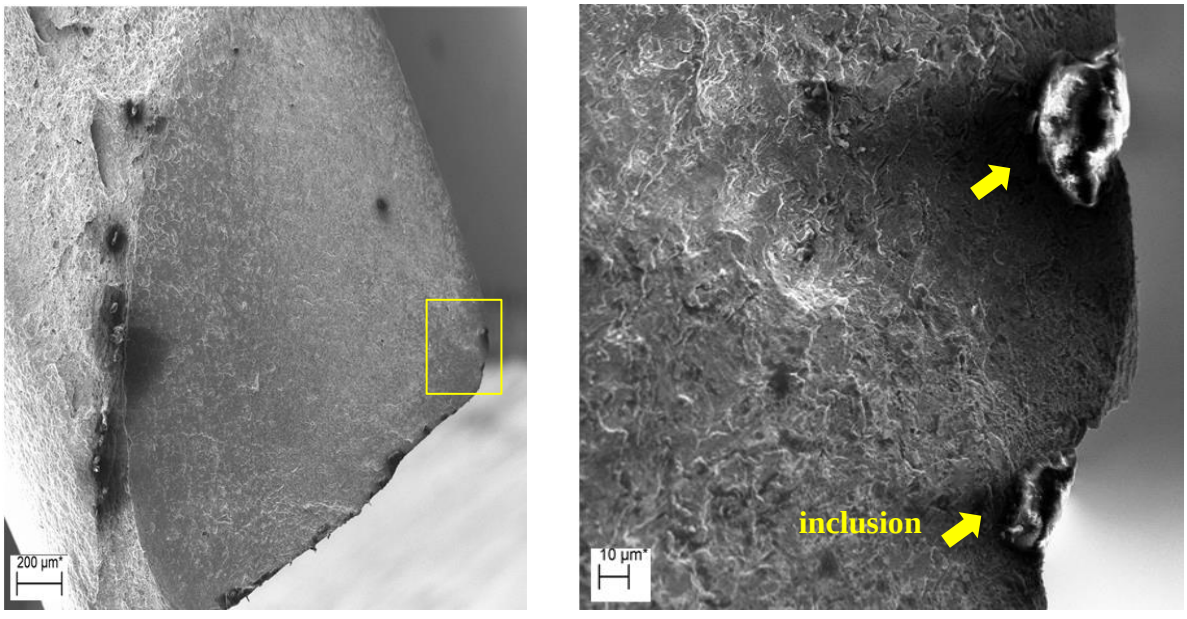

(a) (b)

Figure 4-6 Inclusion-induced surface fracture initiation for an ultrasonic specimen ruptured at σ_a =286 MPa, $N_f = 6\times10^6$ cycles **(a)** The entire fracture surface; **(b)** High magnification of the crack initiation zone in showing the inclusions at the surface.

Internal inclusion-induced crack initiation leading to fish-eye fracture, which is the typical characteristic of VHCF failure of high strength steels [157], was observed for the majority of specimens ruptured in VHCF regime under ultrasonic loading. Figure 4-6(a) shows the entire fracture surface of a specimen ruptured after $N_f = 6.1 \times 10^7$ cycles at $\sigma_a = 285$ MPa. The three typical regions of fish-eye facture surface are observed:

- Region 1 corresponds to the fish eye area, including the inclusion and initial flat area around the inclusion. The flat surface corresponds to stable crack propagation to form a fish-eye [22].

- Region 2, which has a radial ridge pattern, corresponds to the rapid crack propagation outside the fish eye [22]. This region contains many radial streaks in accordance with the propagation direction.

- Region 3 corresponds to the final rapid failure.

These three regions are indicated by a couple of dashed lines in Figure 4-7(a). A higher magnification of the boundary between Region 1 and Region 2 is shown in Figure 4-7(b). Appearance of these two regions is a typical characteristic of internal inclusion-induced fracture of steels [22]. A higher magnification of Region 2 is presented in Figure 4-7(c). This micrograph suggests a transgranular crack growth mode since the traces of the polycrystalline microstructure with grain boundaries are not visible. Fatigue striations were not detected in the crack propagation area. Dimpled areas were observed in Region 3 as shown in Figure 4-7 (d). A higher magnification of the inclusion and its counterpart surface are shown in Figures 4-8(a) and 4-8(b) respectively.

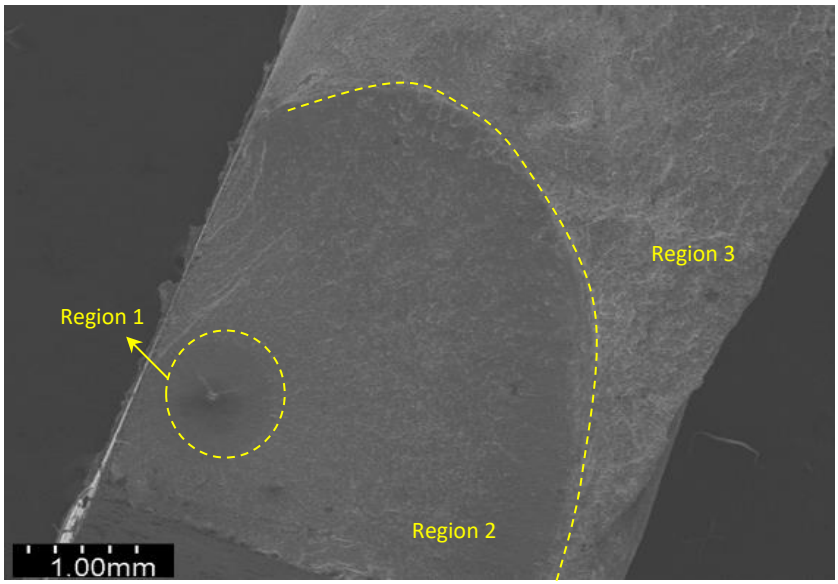
Region 1
Region 2
Region 3
1.00mm

(a)

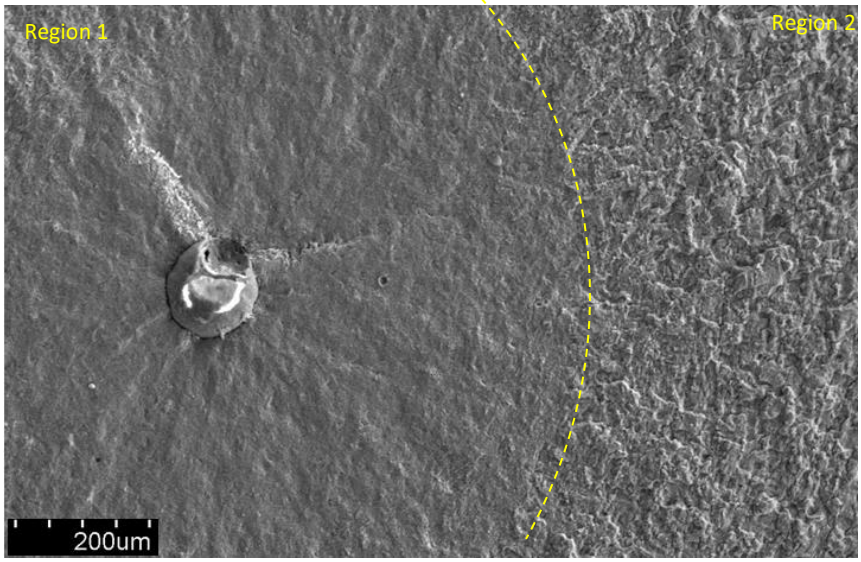
Region 1
Region 2
200um

(b)

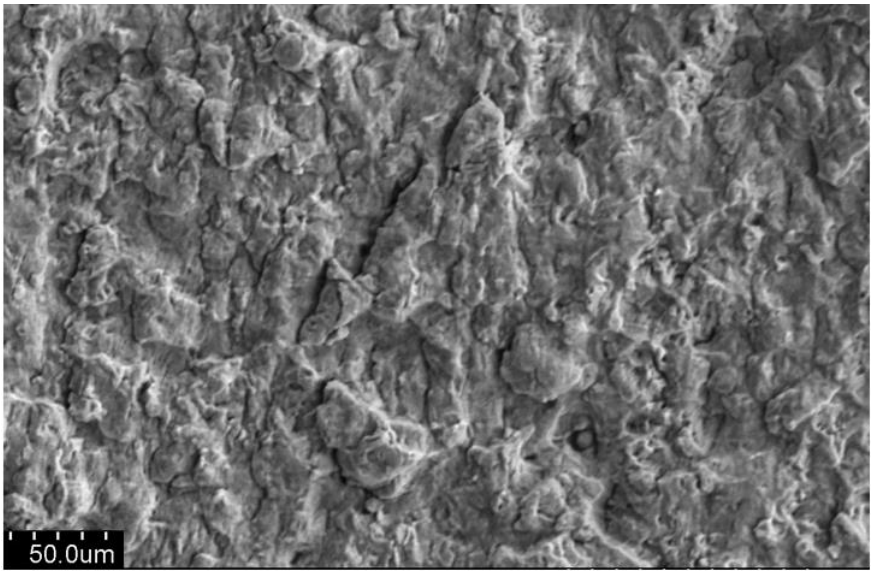
50.0um

(c)

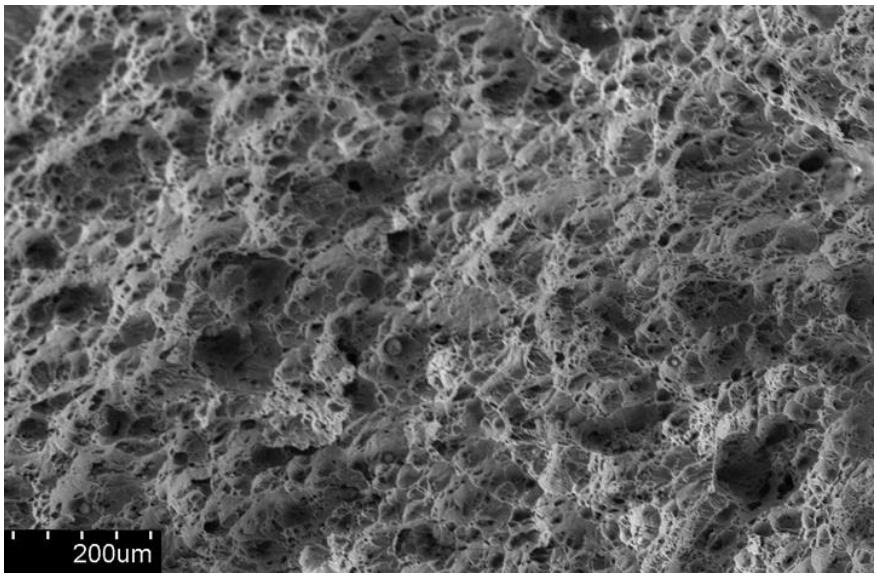

(d)

Figure 4-7 Fracture surface of an ultrasonic specimen ruptured after $N_f = 6.1\times10^7$ cycles at σ_a =275 MPa: **(a)** Entire fracture surface; **(b)** High magnification of (a) showing the inclusion at the center of the fish-eye; **(c)** Crack propagation area; **(d)** Final fast fracture area.

It is well supported in the literature that a characteristic area called Fine Granular Area (FGA) is often found around the inclusion at the crack origin [30], [49], [50], [66], [86], [158]–[160]. This is a relatively rough region with fine granular morphology. However such a characteristic area was not observed in the present case as shown in Figure 4-8, which depicts a higher magnification of the inclusion, previously presented in Figure 4-7(b). In the related literature, the absence of FGA around the inclusion has been attributed to the fact that the stress intensity factor range at the inclusion edge exceeds the threshold value for the crack propagation [30], [50]. Figure 4-8 also shows that particle-matrix debonding has occurred which can be a part of fatigue crack formation [161]. Moreover, this figure depicts that plastic localization bands have been formed near the inclusion. In most cases, non-metallic inclusions such as Al_2O_3, SiO_2, MgO, and CaO or sulfides are observed in the center of fish-eyes for structural metallic materials [30], [90], [161]. In our case, energy-dispersive spectroscopy (EDS) analysis revealed that the inclusions consist mainly of aluminum, magnesium and oxygen, as shown in Figure 4-9.

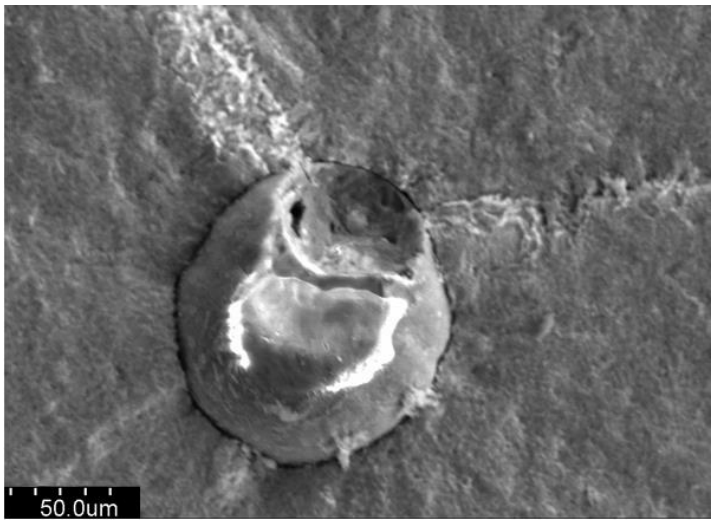

(a)

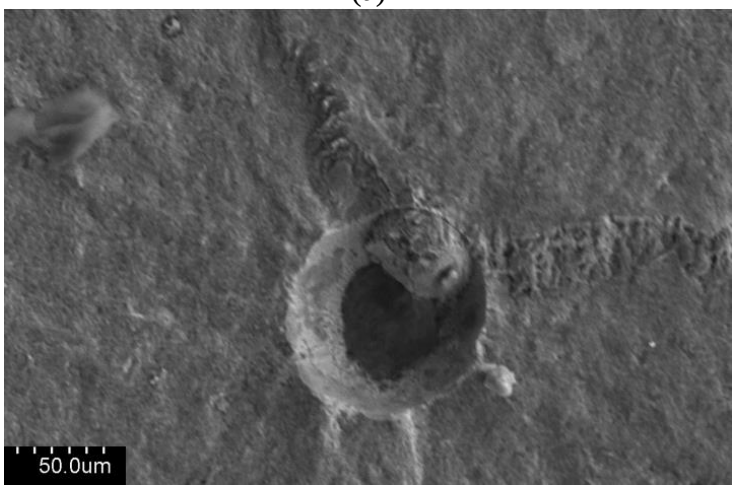

(b)

Figure 4-8 (a) High magnification of the inclusion at the center of the fish eye **(b)** The counterpart fracture surface corresponding to the inclusion.

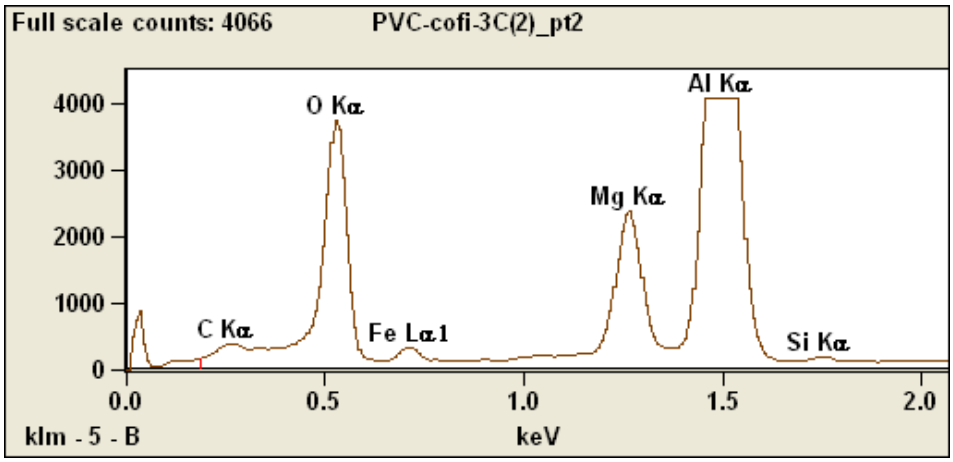

Figure 4-9 EDS spectrum of the inclusion.

Occurrences of surface- or internal inclusion-induced fracture modes under ultrasonic fatigue loadings are distinguished by different marks in Figure 4-5. In spite of existence of some surface-induced fracture cases in very high cycle regime, internal crack initiation is dominant in this regime and a transition can be recognized from surface fracture initiation to internal initiation by increasing the number of cycles from high cycle to very high cycle ranges. This transition from surface initiation to internal inclusion-induced crack initiation has been widely reported in the literature for different metallic materials including high strength steels [1], [30], [45], [160].

4.4 Surface Observations

Interrupted fatigue tests were conducted at 20-kHz and 30-Hz frequencies and surface of the specimens was observed by SEM at different loading stages. All observations were made along the central axis of the specimen around the center of the gauge part. Figure 4-10 shows the SEM micrograph of a specimen loaded at 20-kHz frequency at stress amplitude of σ_a =260 MPa, corresponding to the obtained fatigue limit, after N=1.6×10^9 cycles. The specimen was cooled during the test by an air-cooling system and the mean temperature was below 40°C in this case.

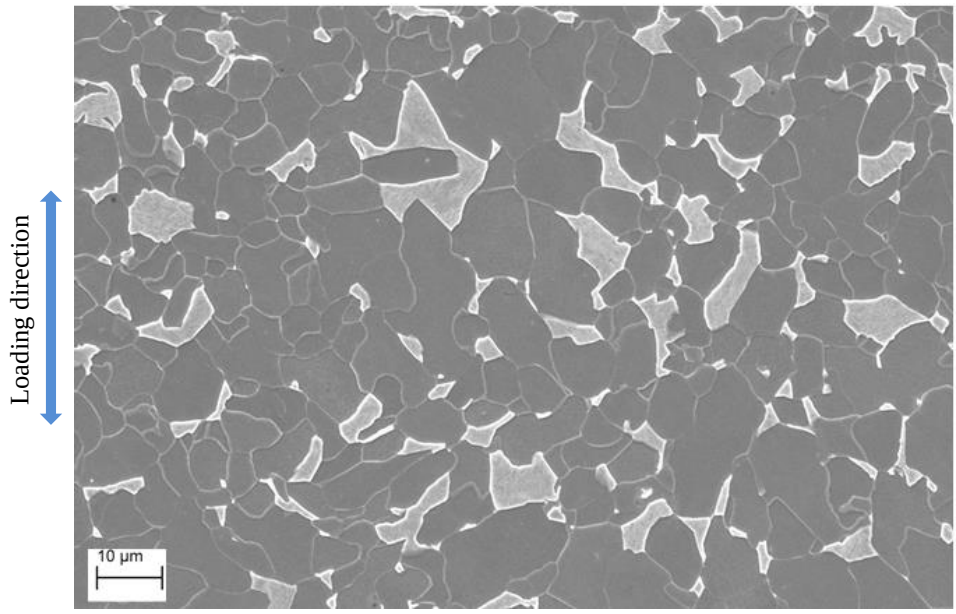

Figure 4-10 Surface of the specimen loaded under 20-kHz frequency at σ_a =260 MPa, N=1.6×10^9 cycles, T<40°C.

The same observations were carried out for a specimen loaded by 30-Hz frequency at σ_a =250 MPa, below the fatigue limit, after N=2×10^5 cycles and N=10^7 cycles and the results are presented in Figure 4-11. In Figure 4-10 the dark phase is ferrite and the bright phase is martensite. Since in the case of conventional 30-Hz frequency the experiment was long, the specimen surface was not so clean after loading. This is why the contrast in Figure 4-11 is different from Figure 4-10 and ferrite and martensite phases cannot be easily distinguished especially in Figure 4-11(b).

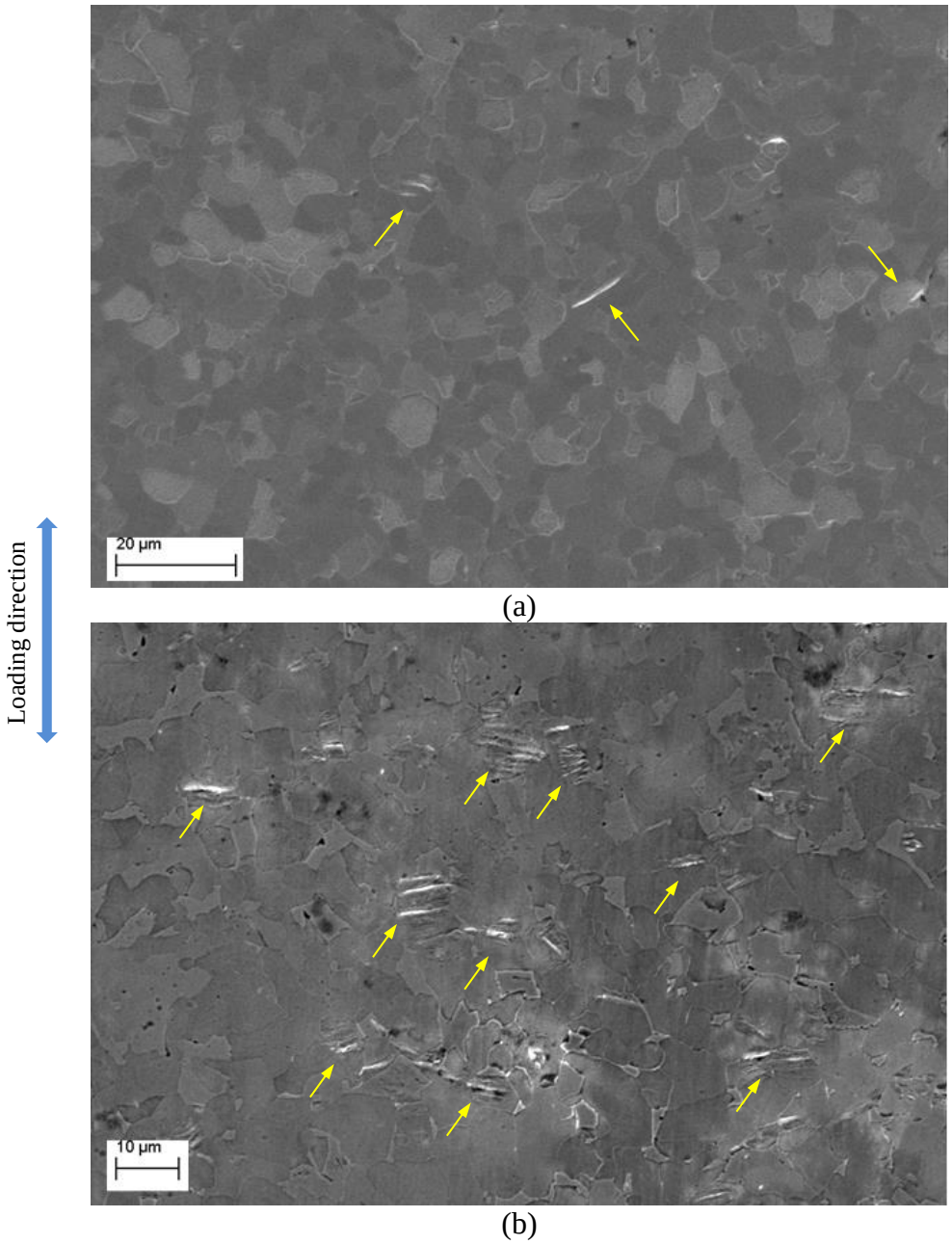

Figure 4-11 Appearance of slip bands in ferrite grains on the surface of the specimen under 30-Hz fatigue loading at σ_a =250 MPa after **(a)** N=2×10^5 cycles **(b)** N=10^7 cycles, ΔT<15°C.

Moreover, Figure 4-12 shows microcracks along the slip bands on the surface of a run-out conventional sample loaded at σ_a =250 MPa up to 10^7 cycles. As shown in Figure 4-10, in the case of ultrasonic loading no slip band was observed on the specimen surface even after 10^9 cycles. On the other hand, for 30-Hz conventional loading, SBs were formed in ferrite grains on the specimen surface in the early stages of loading (N<10^5 cycles) and were developed by increasing the number of cycles. The slip bands are indicated by arrows in the micrographs. SEM observations were also made on the specimen surface for ultrasonic loadings at stress amplitudes above the fatigue limit, which were accompanied by high temperature increases. In this case the surface of specimens was oxidized because of the high temperature increase under loading. Figure 4-13 shows the surface of an ultrasonic specimen loaded at σ_a =286 MPa. The test was stopped at N=10^6 cycles. This figure reveals formation of many slip bands as well as microvoids and microcracks along the slip bands in ferrite grains.

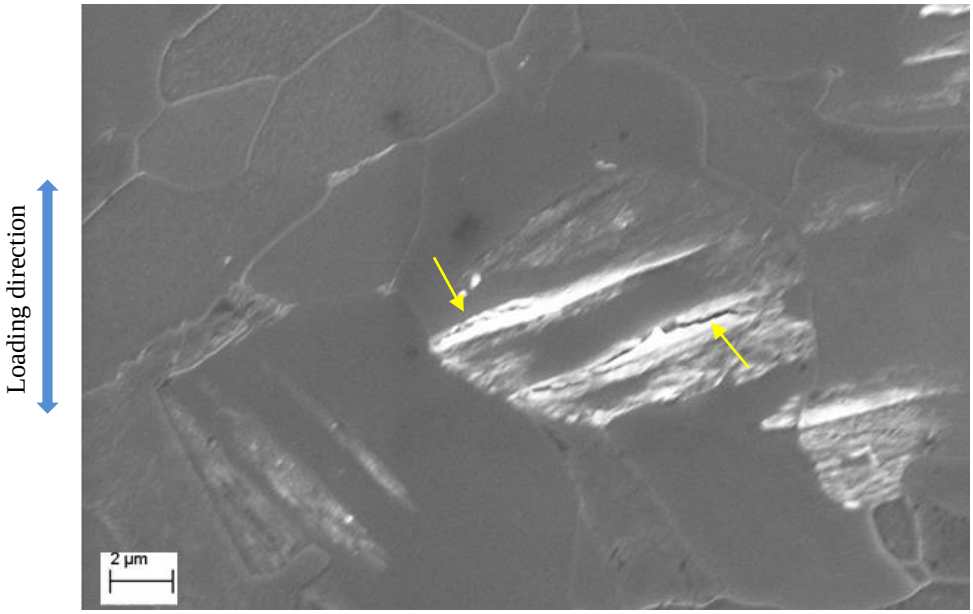

Figure 4-12 Microcracks detected on the surface of a run-out conventional specimen (σ_a =250 MPa, N=10^7 cycles, ΔT<15°C)

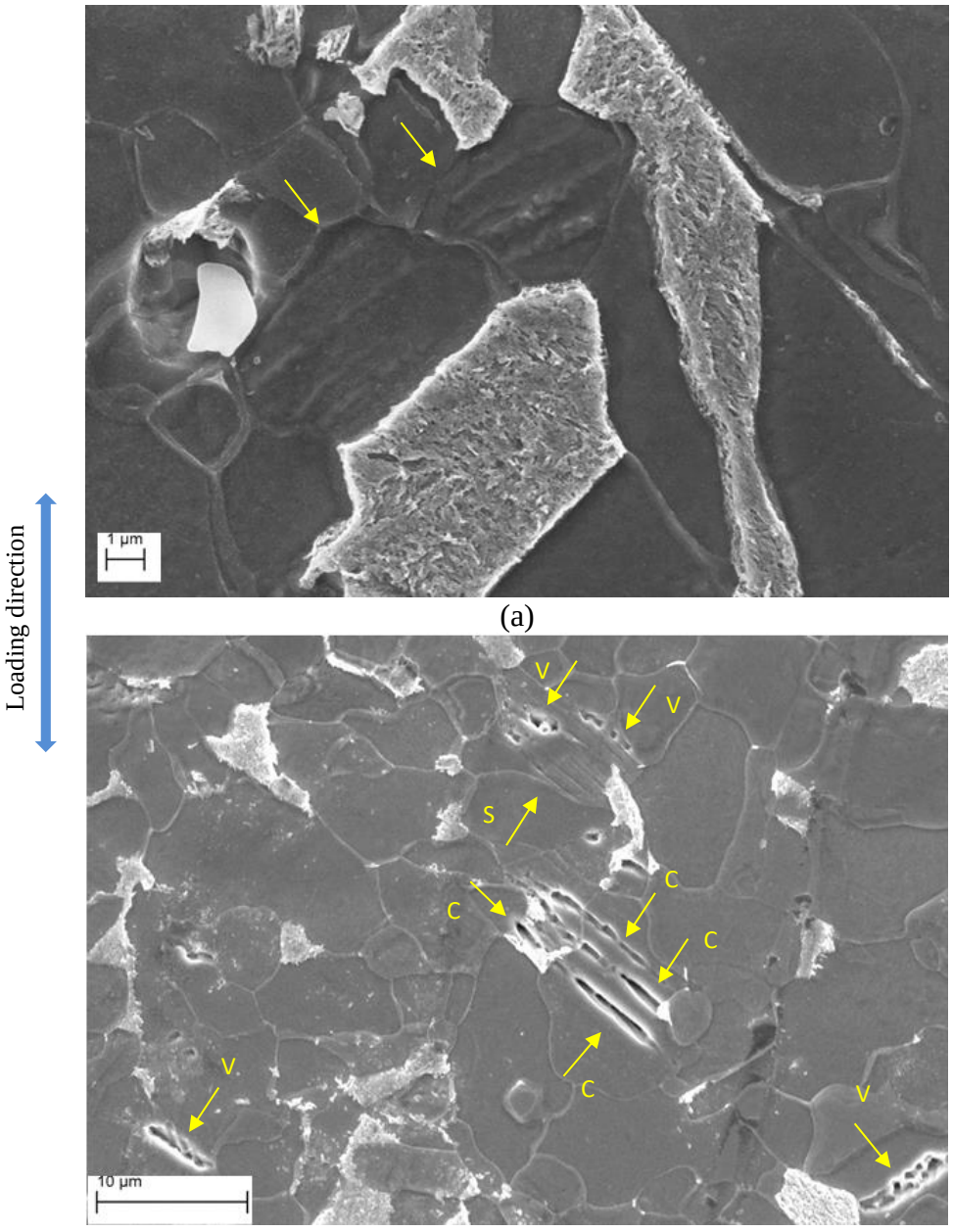

Figure 4-13 Surface of a specimen loaded under ultrasonic loading at σ_a =286 MPa, N=10^6 cycles, and T~350°C **(a)** Slip bands (arrows show the grains containing the slip bands); **(b)** Microvoids and microcracks (S: slip bands, V: microvoids, and C: microcracks).

Moreover, observations were made on the surface of ruptured specimens, in regions ~900µm away from the final crack. Figure 4-14 shows different regions on the surface of a specimen ruptured under ultrasonic loading at σ_a =292 MPa. Many micro-voids can be observed on the specimen surface. The microvoids form and coalesce along the slip bands inside ferrite grains. No void was detected in grain boundaries and the voids preferentially form in ferrite grains

surrounded by several martensite islands. Figure 4-15 shows microcracks resulted from void coalescence along the slip bands in ferrite grains for another ultrasonic specimen.

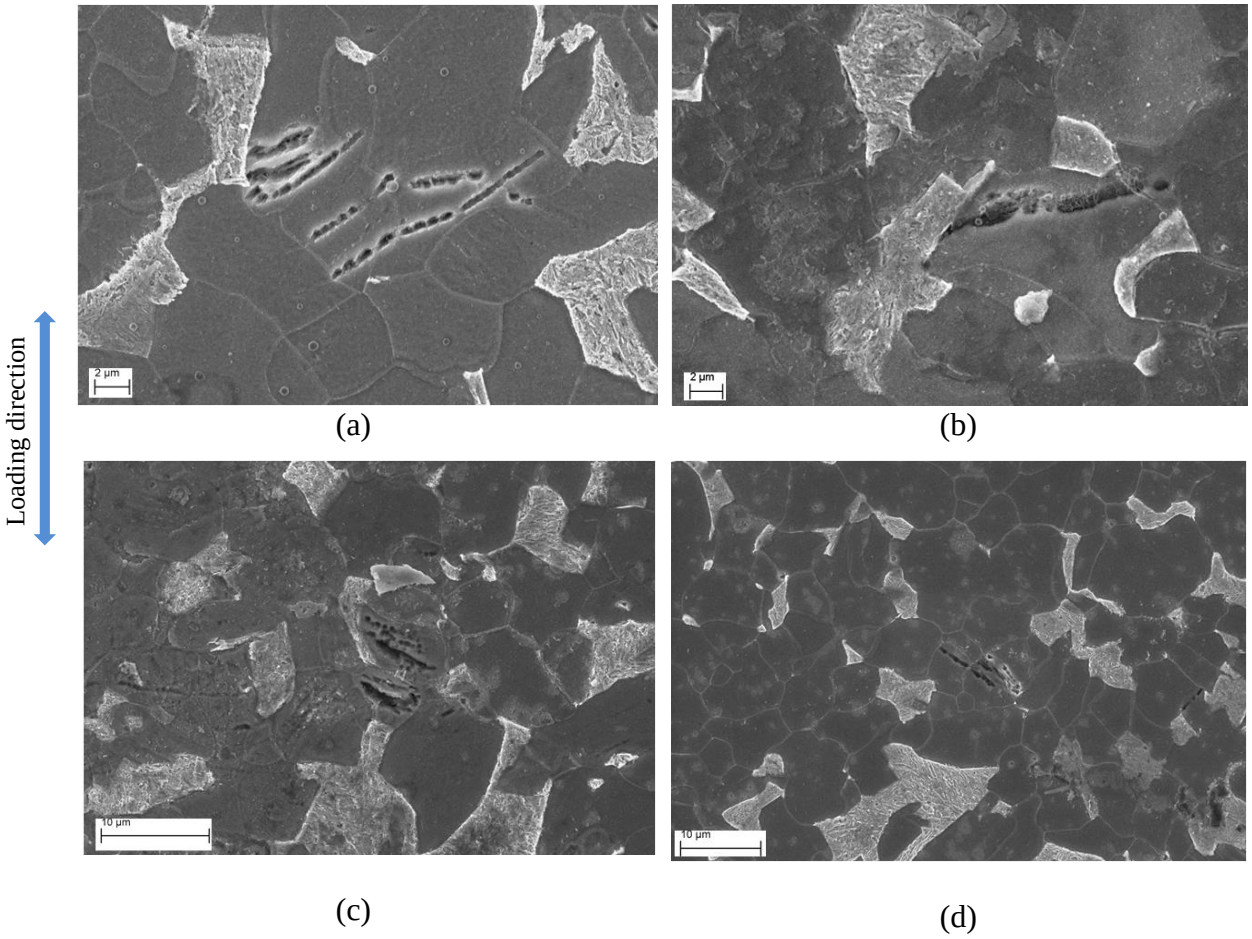

Figure 4-14 Microvoids initiation and coalescence inside ferrite grains at different regions on the surface of an ultrasonic specimen after rupture (σ_a =292 MPa, $N_f = 6.8\times10^7$, and T~350°C).

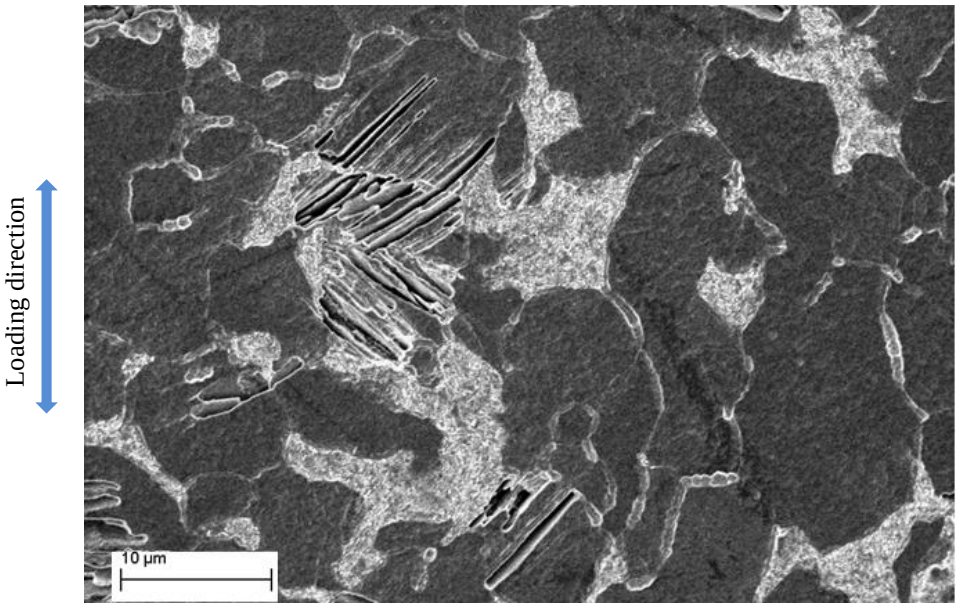

Figure 4-15 Microcracks along the slip bands in ferrite grains on the surface of an ultrasonic specimen after failure (σ_a =280 MPa, $N_f = 2.86\times10^8$ cycles, and T~350°C).

The observations results for specimens ruptured under conventional fatigue tests were different as shown in Figure 4-16. This figure depicts regions ~900µm away from the final crack on the surface of a conventional specimen ruptured after $N_f = 8.9\times10^5$ cycles at σ_a =272 MPa. Many slip bands can be observed as bright lines in ferrite grains, however, no void was detected, in contrary to the ultrasonic case. Microcracks are formed along the slip bands in some ferrite grains as indicated by arrows in Figure 4-16(b-c). This fracture mode is consistent with the well-accepted model for the crack initiation in the conventional fatigue regime ($N<10^7$ cycles), where the propagative fatigue cracks leading the specimen to the final fracture are caused by the persistent slip bands on specimen surface [30], [36]. In both, ultrasonic and low frequency loading results, all observed cracks were formed and propagated in a transgranular manner, no inter granular fracture was detected.

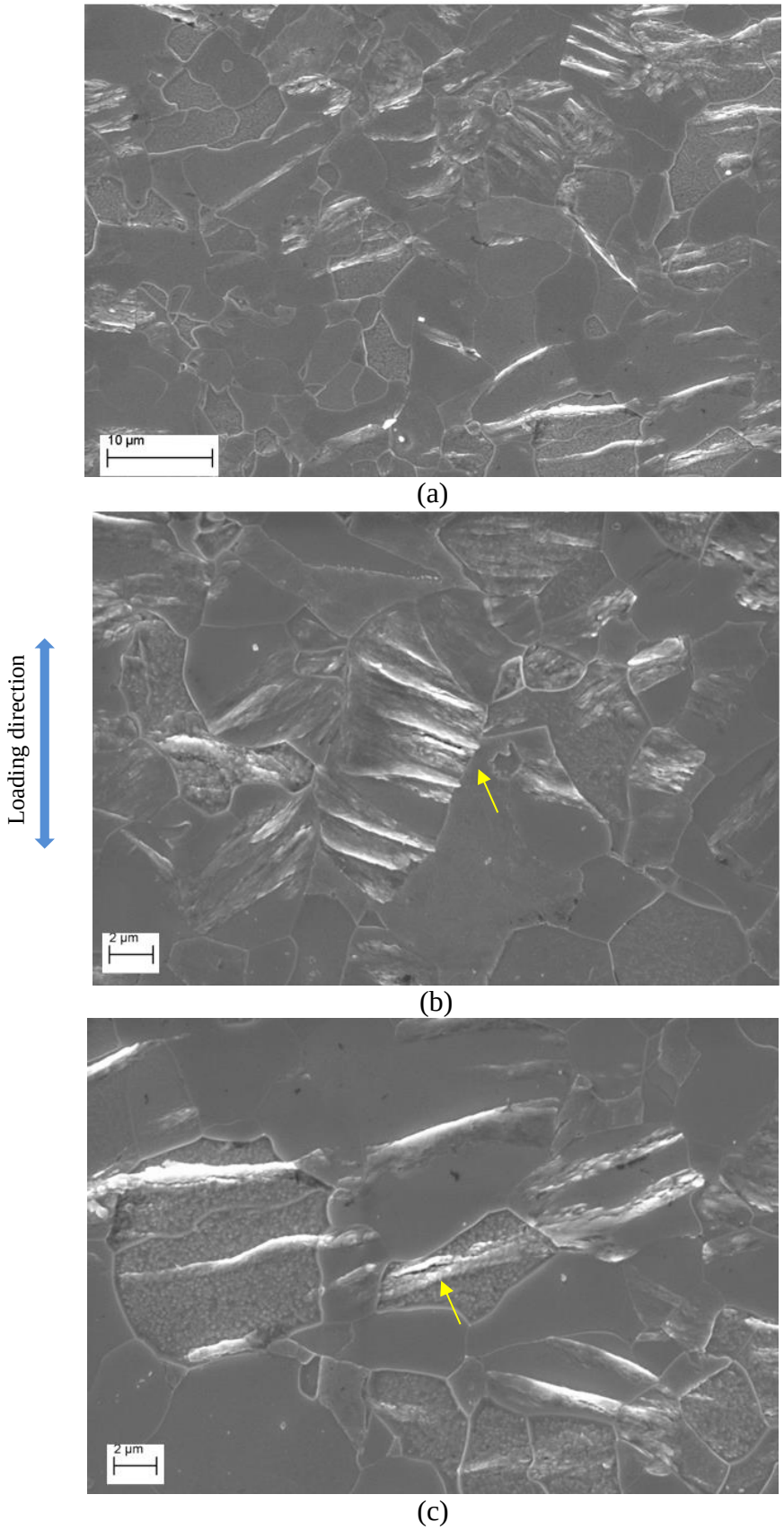

Figure 4-16 Specimen surface after failure under 30-Hz fatigue loading at $\sigma_a = 272$ MPa, N_f=8.9×10^5 cycles, and ΔT<15°C.: **(a)** Formation of many slip bands in ferrite grains; **(b-c)** Microcrack initiation along slip bands.

4.5 Slip Band Formation Inside of the Specimens

In order to study the possible formation of slip bands in the bulk of the material, several ultrasonic and conventional specimens were cut at the center, as schematically shown in Figure 4-17(a). The axial surface was mechanically polished but no electropolishing and no etching were carried out. SEM observations were conducted on the axial surface and the results obtained for an ultrasonic sample and a conventional specimen are shown in Figures 4-17(b) and 4-17(c), respectively. The obtained results revealed formation of slip bands and microvoids in the subsurface areas in the case of ultrasonic specimens, as presented in Figure 4-16(b). However, for conventional specimens slip bands and voids were not detected in the bulk of the material (Figure 4-17(c)).

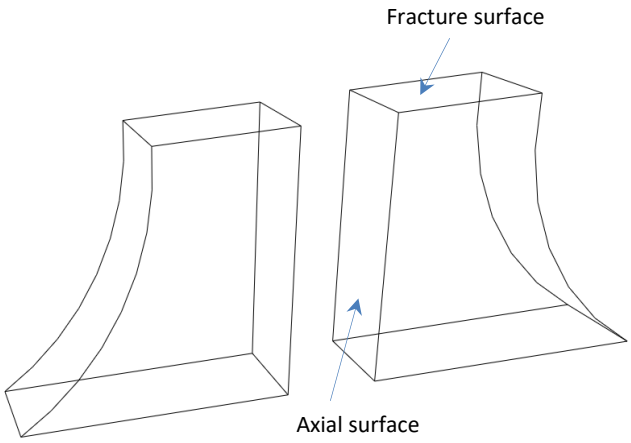

(a)

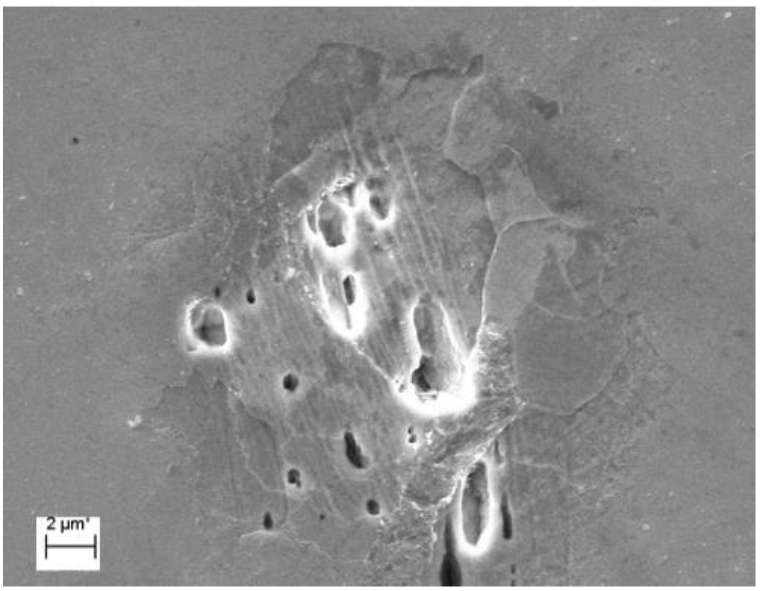

(b)

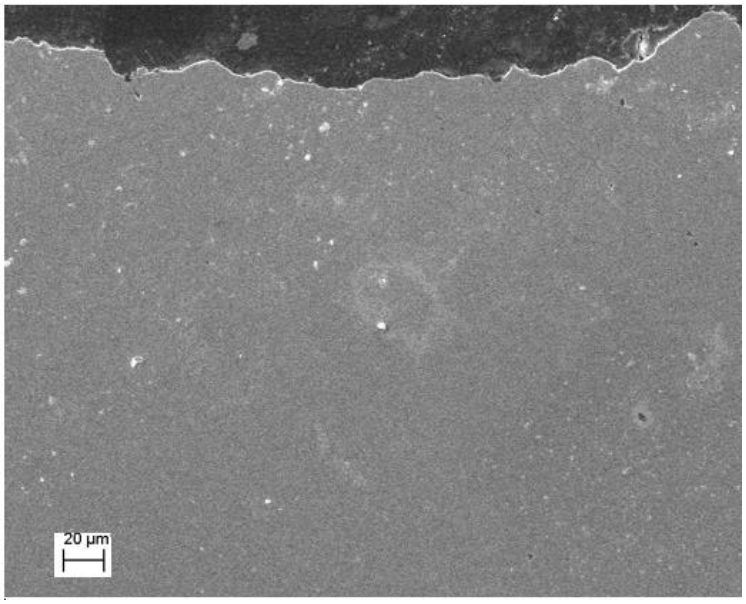

(c)

Figure 4-17 (a) Schematic of specimen cross sections after cutting **(b)** SEM observations in the bulk of an ultrasonic sample ruptured after $N_f = 6.1\times10^7$ cycles at σ_a =275 MPa **(c)** SEM observations inside of a conventional fatigue specimen ruptured under 30-Hz loading after $N_f = 4.2\times10^5$ cycles at σ_a =265 MPa.

4.6 Concluding Remarks

The experimental observations presented in this chapter revealed a discrepancy in S-N data, deformation, and fracture mechanisms between ultrasonic and conventional 30-Hz fatigue loadings. The fatigue life was higher for a given stress amplitude under ultrasonic tests while the fatigue limit was nearly the same for both cases. At 20-kHz frequency temperature increased up to ~350°C in the early stages of cycling at stress amplitudes above the fatigue limit while at 30-Hz frequency temperature increase was less than 15°C. Under conventional loadings fatigue failure was always initiated from the slip bands at the surface of the specimen. Fracture initiation under ultrasonic loadings mainly occurred in the interior, however few cases of surface initiation were also observed. In this case, both surface and internal crack initiations were inclusion induced. The so-called fish-eye fracture surface was detected for internal inclusion induced crack initiation at 20-kHz frequency. The fine granular area (FGA) was not observed in this case. For both ultrasonic and low frequency loadings crack growth was transgranular and no intergranular crack was detected. SEM observations on specimens surface revealed that under ultrasonic tests at high stress amplitudes (above the fatigue limit) many slip bands were formed on the surface. In this case many voids and micro-cracks were detected

along the slip bands. On the other hand, for ultrasonic tests under fatigue limit (the run-out samples) no slip band was found on the surface. In the case of conventional tests slip bands were formed under surface from early stages of loading even at stress amplitudes below the fatigue limit. However, in this case no void was detected along the slip bands.

Chapter 5

Discussions

Résumé

Discussions

Le chapitre 5 donne des éléments de discussions et d'explication des principaux résultats expérimentaux établis dans les chapitres 3 et 4. Ces résultats sont dans un premier temps rappelés. Les mécanismes de déformation de la phase ferritique de structure cubique centrée sont connus pour passer d'un régime thermiquement activé à un régime athermique selon les conditions de vitesses de déformation et de températures. Dans un premier temps, ces conditions ont été spécifiées pour tous les essais. Il est ainsi montré que les essais ultrasoniques à température inférieure à ~85°C sont associés à des conditions de vitesses de déformation et de températures correspondant au régime thermiquement activé. Au contraire, les essais ultrasoniques à température proche de 350°C et les essais sur machines conventionnels correspondent au régime athermique. Ce constat indique que dans les cas associés au régime thermiquement activé, les déformations locales sont principalement dues au mouvement de va-et-vient quasi recouvrable en traction-compression des dislocations coins. Au contraire, dans les cas associés au régime athermique, elles mettent en jeu le mouvement à des vitesses similaires des dislocations coins et vis conduisant à des réorganisations des structures de dislocations et à la localisation de la déformation. Cette différence de mécanismes permet d'expliquer la présence ou non de bandes de glissements en surface des éprouvettes sollicitées. Pour les essais ultrasoniques à ~350°C, des mécanismes de vieillissement dynamique et de diffusion/production de lacunes s'ajoutent. Ces mécanismes additionnels ont deux conséquences : le durcissement de la phase ferritique et la croissance et coalescence de cavités dans les bandes de déformation plastique. La courbe SN obtenue en fatigue ultrasonique a été retracée en normalisant l'amplitude de contrainte par la résistance maximale à la traction. On obtient alors une continuité des résultats obtenus à basse et haute fréquences, tous associés au régime de déformation athermique mais à des températures différentes. Ceci permet d'expliquer pourquoi la durée de vie pour les essais ultrasoniques est trouvée supérieure (atteignant le régime VHCF des très grands nombres de cycles) à celle caractérisée par les essais sur machines conventionnelles et la transition du site d'amorçage qui passe des bandes de glissement en surface pour les amplitudes de contrainte les plus grandes aux inclusions pour les plus faibles. Une carte donnant une corrélation entre les conditions de vitesses de déformation et de températures et le régime de rupture par fatigue avec les mécanismes d'amorçage associés est proposée en intégrant les résultats de cette étude mais aussi des résultats de la littérature. Enfin une discussion sur l'utilisation de l'énergie dissipée par cycle pour appréhender la réponse en fatigue et la limite de fatigue est proposée.

5.1 Summary of the Experimental Results

The main experimental outcomes presented in Chapters 3 and 4 which need to be discussed can be summarized as follows:

- Under successive ultrasonic fatigue loadings, an abnormal temperature evolution was observed at stress amplitudes above a critical stress value σ_c, in that temperature substantially increased up to ~350°C followed by a slight decrease and finally temperature stabilization.
- A quadratic evolution of the dissipated energy per cycle versus stress amplitude was found for low stress amplitudes ($\sigma_a < \sigma_c$) under ultrasonic fatigue loadings.
- Under conventional 50- and 80-Hz frequency fatigue tests a classical thermal response was observed for all stress amplitude ranges up to the final fracture.
- The mean dissipated energy per cycle estimated for low stress amplitudes ($\sigma_a < \sigma_c$) under ultrasonic loadings was lower than that of conventional loadings at the same stress amplitudes.
- Under conventional fatigue tests the dissipated energy per cycle versus stress amplitude was obtained to be nearly the same for 50- and 80-Hz frequencies, indicating no frequency effect on dissipated energy in the conventional frequency ranges.
- Despite using air-cooling systems during ultrasonic tests for determining the S-N curve, for all S-N data excluding the run-out points significant temperature increase occurred at the early stages of fatigue loading.
- There was a discrepancy between the S-N curve obtained from ultrasonic loading and that of conventional 30-Hz fatigue tests. For a given stress the fatigue lifetime measured by ultrasonic loading was higher than that obtained from 30-Hz loadings. However the fatigue limit was nearly the same for both frequencies.
- Fractography studies revealed that fracture under ultrasonic loading was always inclusion-induced and in most cases internal initiation leading to fish-eye fracture was observed.
- Under conventional loadings fracture was always initiated from the slip bands on the specimen surface and no inclusion-induced rupture was observed.
- SEM observations on the surface of specimens before and after rupture revealed that for ultrasonic loadings at stress amplitudes below the fatigue limit (including the run-out samples) no slip band was formed on the surface while at stress amplitudes above the

fatigue limit which resulted in significant temperature increases many slip bands were detected on the specimen surface. In the case of conventional 30-Hz loading, slip bands were formed on the surface of specimen in the early stages of loading even at stress amplitudes below the fatigue limit.

- In both ultrasonic and low frequency tests transgranular cracking along the slip bands was observed and no intergranular crack was detected. In the case of ultrasonic loading, many microvoids nucleated and coalesced along the slip bands resulting in microcrack initiations. This microvoids initiations and coalescences were not observed in the case of low frequency tests.

In this chapter, these experimental findings will be discussed and mechanisms will be proposed to explain the fatigue and thermal response of the material under ultrasonic and conventional frequency fatigue loadings.

5.2 Effect of Frequency on Deformation Regimes and Thermal Response of the Material

5.2.1 Background

In dual-phase steel, since the hardness of martensite is much higher than ferrite, it can be assumed that dislocation motions and plastic deformation occur in ferrite grains, as the ductile phase with a BCC structure. In BCC metals, the flow stress depends strongly on temperature and strain rate at low temperatures. It was first proposed by Seeger [162] that for BCC materials the flow stress σ, can be separated into an athermal component σ_G, and a thermal or effective component σ^*, as represented by Equation (5-1):

$$\sigma = \sigma_G + \sigma^*(\dot{\varepsilon}, T) \tag{5-1}$$

Where $\dot{\varepsilon}$ is the strain rate and T denotes the temperature. The athermal component represents the stress that a gliding dislocation requires to overcome the long-range elastic interaction with other dislocations. The thermal or effective component represents the stress required for screw dislocations to overcome short obstacles by thermally-activated mechanisms. It depends on temperature T, and strain rate $\dot{\varepsilon}$. This thermal component becomes negligible above a transition temperature, T_0 (or below a transition strain rate, $\dot{\varepsilon}_0$). For cyclic loading, Mughrabi et al. [163] defined two deformation regimes based on the transition temperature: (i) the thermally-

activated mode ($T < T_0$) where the screw dislocations are immobile and edge dislocations move to-and-fro in a non-hardening quasi-recoverable manner (ii) the athermal regime ($T > T_0$) where the mobilities of screw and edge dislocations are equivalent, multiplication of dislocations occurs, and screw dislocations can cross slip. In this regime, rearrangement of dislocations can take place and strain localization can occur in slip bands. The transition temperature, T_0, highly depends on strain rate and can be shifted to higher values by increasing the strain rate. For instance, according to the flow behavior diagram reported by Campbell and Ferguson [164] for a 0.12 wt.% carbon mild steel, T_0 would shift from 25°C to 100°C by increasing the strain rate from 0.01 s^{-1} to 1 s^{-1}. Therefore, the thermally-activated regime can be reached at high temperatures providing that the strain rate is sufficiently high. Figure 5-1 schematically shows the transition between these two deformation regimes.

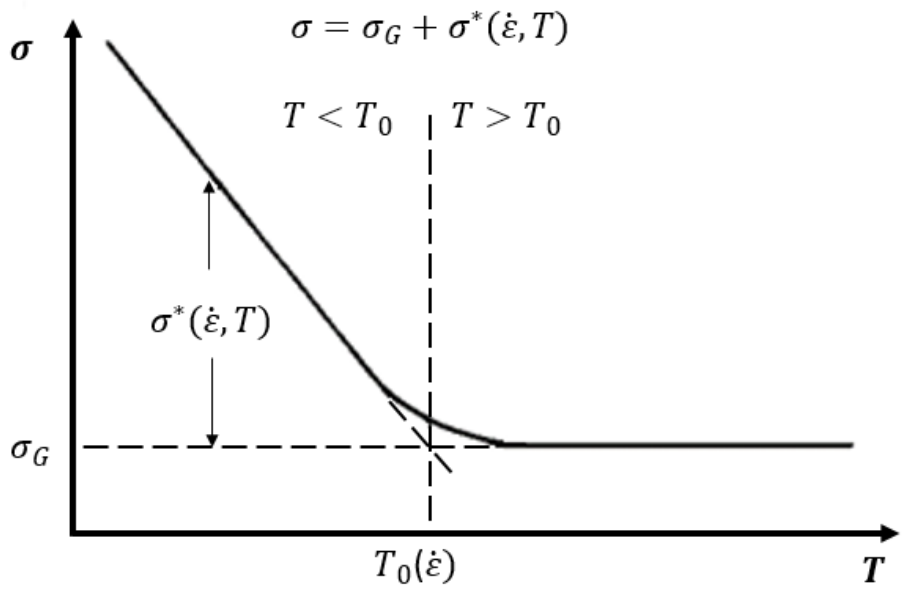

Figure 5-1 Schematic diagram of flow stress of BCC metals versus temperature, from [163].

In the following sections, this concept will be employed to explain the observed thermal response of the material under different frequencies.

5.2.2 Deformation regimes of DP600 steel at different fatigue loading conditions

Using experimental data for several low carbon steels, in 1966, Rosenfield and Hahn [165] suggested an empirical equation representing the transition between athermal regime and thermally-activated regime for low carbon steels as follows:

$$Log(\dot{\varepsilon}) = 1.39\sqrt{T} - 23.7 \quad (5\text{-}2)$$

Where $\dot{\varepsilon}$ is the strain rate and T is temperature in Kelvin. The strain rate amplitude can be calculated as $\dot{\varepsilon}_a = 2\pi f \frac{\sigma_a}{E}$, considering elastic macroscopic behavior. In the present work, for the first category of conventional fatigue tests concerning thermal measurements, the stress amplitudes ranged from 125 MPa to 330 MPa (as shown in Figure 3-16). Based on the aforementioned strain rate equation, the maximum strain rate was estimated to range from 0.17 s^{-1} to 0.46 s^{-1} for 50-Hz frequency tests and, 0.30 s^{-1} to 0.74 s^{-1} for 80-Hz loadings. In this case, according to Eq. (5-2) the transition temperature ranges from 0.1°C to 10°C for 50-Hz loadings and from 5°C to 15°C for 80-Hz fatigue tests. Therefore, based on the thermography results presented in Chapter 3 (see Figure 3-16), at all stress amplitudes the temperature was always above the corresponding transition temperature, as plotted in Figure 5-2(a-b). In this figure, the mean temperature-stress amplitude data determined from infrared thermography under successive fatigue loadings were replotted comparing to the transition temperature at each loading frequency. In the second category of fatigue tests for fatigue characterization of the material, 30-Hz conventional tests were conducted at the stress amplitudes in the range of 260 to 330 MPa (see Figure 4-1), which corresponds to maximum strain rates in the range of 0.23 s^{-1} to 0.3 s^{-1}. In this case the transition temperature is in the range of 0.3°C to 5°C according to Eq. (5-2) which is far below the room temperature (~22°C). As mentioned in Chapter 3, the specimen temperature under 30-Hz fatigue loadings was above the room temperature with a maximum increase of ~15°C, which was always higher than corresponding transition temperature. In summary, under all conventional low frequency fatigue tests, the specimen temperature was above the transition temperature and consequently material deformation is expected to occur in athermal regime.

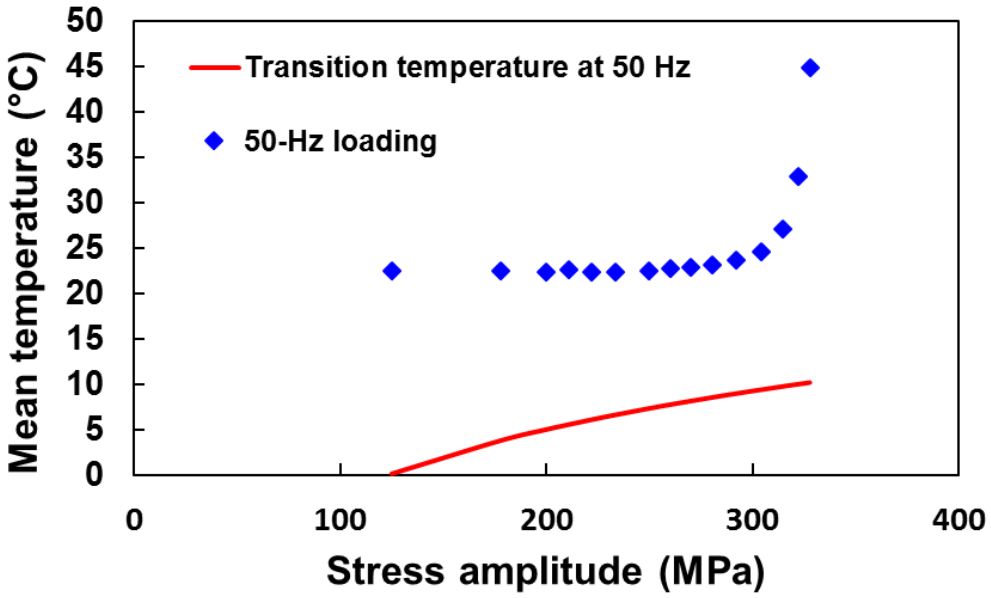

(a)

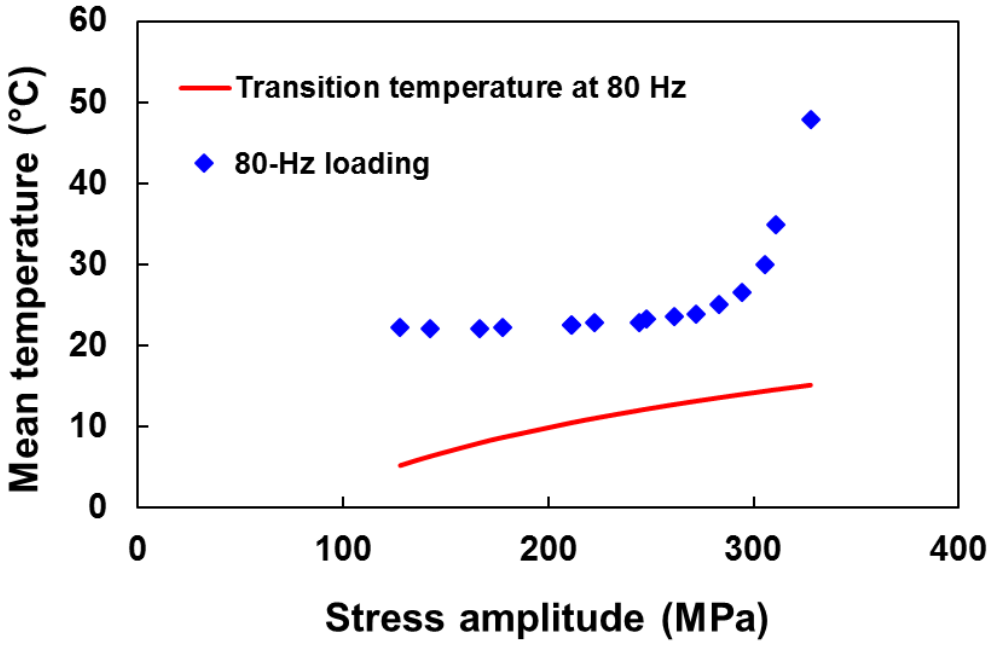

(b)

Figure 5-2 Mean temperature versus stress amplitude compared to the transition temperature at **(a)** 50-Hz frequency, **(b)** 80-Hz frequency.

The same investigations were carried out to reveal the deformation mechanisms under ultrasonic fatigue experiments. In the first category of ultrasonic fatigue tests, as explained in Chapter 3, by increasing the stress amplitude successively up to σ_c, the steady-state temperature of the material under cyclic loading increased gradually up to a critical value T_c (see Figure 3-

5). Then by increasing the stress amplitude a significant temperature increase occurred. For fatigue loadings at 20-kHz frequency, the deformation regime depends on stress amplitude because of the presence of strong self-heating. Based on the experimental observations it can be supposed that T_c is the transition temperature corresponding to σ_c, above which a transition occurs in the deformation regime. As a result, and as suggested by Favier et al. [110] for α-iron, the thermally activated mode, which is typical of a BCC structure, prevailed at room temperature for a 20-kHz cyclic loading at low stress amplitudes ($\sigma_a < \sigma_c$). Nonetheless, for ultrasonic loading at higher stress amplitudes ($\sigma_a > \sigma_C$) the specimen temperature increased to some hundreds of degrees, which is higher than the transition temperature so that the material deforms in the athermal regime. This transition results in a significant increase in dissipated energy per cycle and temperature because of the high mobility of the dislocations and their multiplication in the athermal regime. Because of microstructural and mechanical heterogeneities, the mechanisms associated with the athermal regime operated at one edge of the specimen and spread throughout the specimen width because of thermal diffusion. Figure 5-3 schematically correlates the thermal response of the material to the deformation regimes under successive ultrasonic loadings.

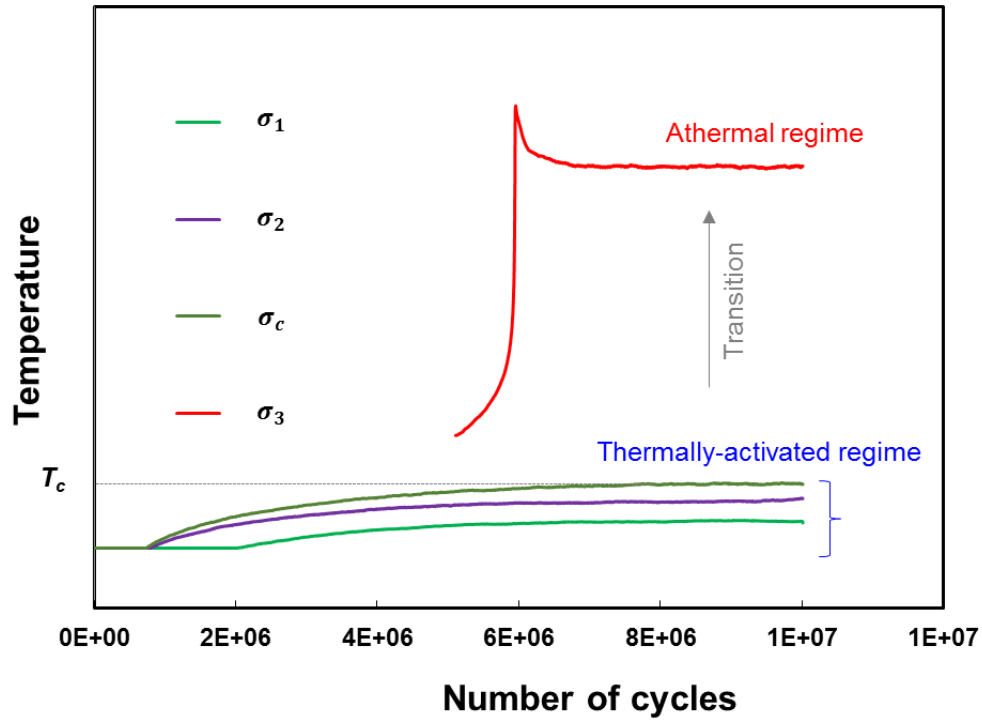

Figure 5-3 Schematic diagram of the correlation between thermal response of the material and deformation regimes under successive ultrasonic loading tests (σ_c represents the critical stress amplitude, and $\sigma_1 < \sigma_2 < \sigma_c < \sigma_3$).

The mean temperature-stress amplitude data determined from infrared thermography under successive fatigue tests were replotted comparing to the transition temperature in Figure 5-4. This figure shows that the specimen temperature increased by increasing the stress amplitude and finally exceeded the transition temperature at a critical stress amplitude. The experimental mean critical stress amplitude and mean critical temperature were found as $\sigma_{mc} \approx 253$ MPa and $T_{mc} \approx 88$°C. Based on Eq. (5-2), the transition temperature associated with $\sigma_{mc} \approx 253$ MPa is obtained as $T_0 \approx 74$°C, which is slightly below the mean critical temperature T_{mc}, obtained from thermographic measurements.

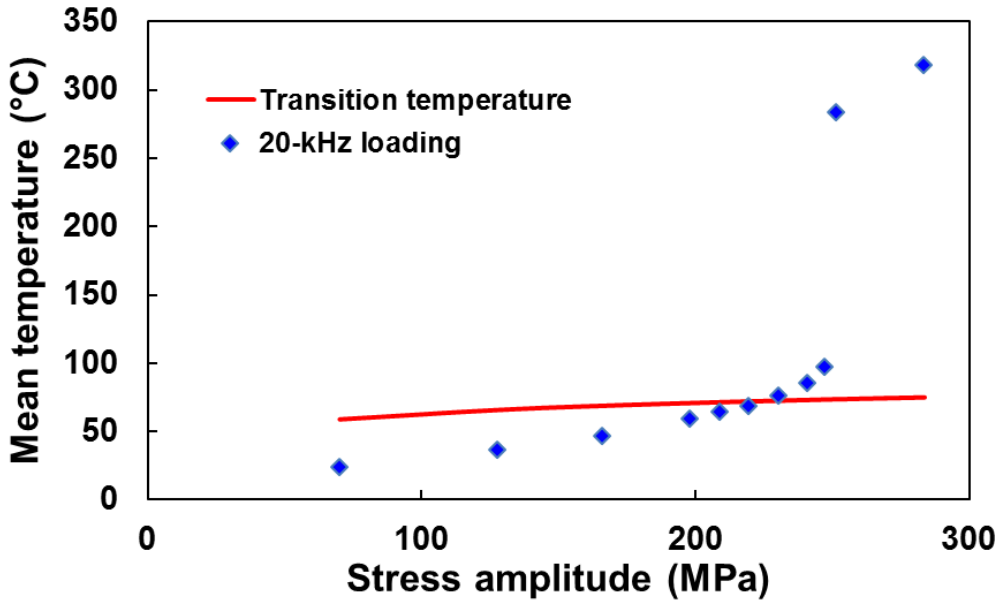

Figure 5-4 Mean temperature versus stress amplitude compared to the transition temperature at 20-kHz frequency.

All data presented in Figure 5-2 and Figure 5-4 are summarized in Figure 5-5, which shows the strain rate-temperature state of the material under conventional and ultrasonic fatigue loadings regarding the aforementioned deformation regimes. In this map the solid line represents the transition boundary between athermal and thermally-activated deformation regimes, indicated by Region I and Region II, respectively. Similar to the previous figures, this transition line was obtained from Eq. (5-2).

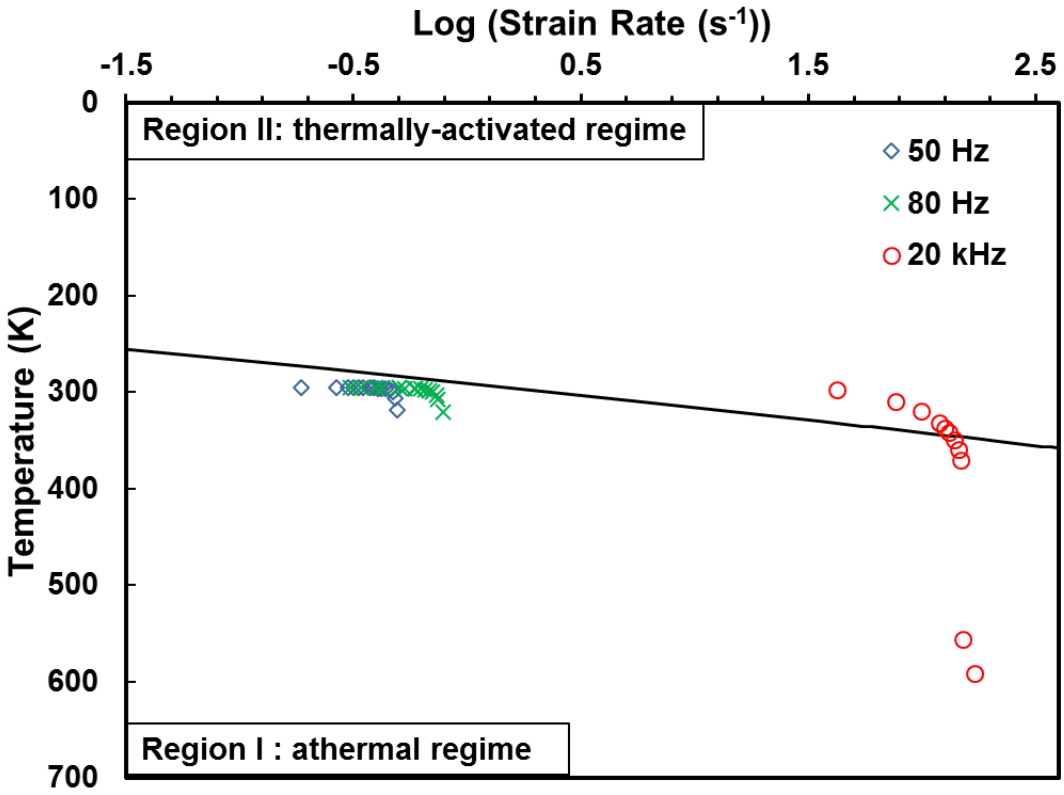

Figure 5-5 Strain rate-temperature state of the material under successive fatigue loadings.

The transition from the thermally-activated regime to the athermal regime can thus be considered as a possible mechanism that is responsible for the significant heating observed for high stress amplitudes ($\sigma_a > \sigma_c$). Another hypothesis that can be developed is that the strong heating mechanism is related to the initiation of short cracks and a resulting local plasticity at the crack tips; these short cracks are arrested by microstructural barriers after a small number of cycles.

In the second category of ultrasonic loading tests conducted to determine the S-N curves, for the stress amplitudes below the fatigue limit σ_D, (60 MPa< σ_a< 260 MPa), for which no strong heating occurred (T< 40°C), the maximum strain rate ranges from 36 $s^{-1}$to 156 s^{-1}. In these high strain rate conditions, the transition temperature ranges from 57°C to 74°C according to Eq. (5-2), therefore material is expected to deform in thermally-activated mode under ultrasonic loadings at low stress amplitudes. Nonetheless, for ultrasonic loadings at stress amplitudes above the fatigue limit (260 MPa $< \sigma_a <$ 305 MPa), which correspond to the maximum strain rates in the range of 156 s^{-1} to 182 s^{-1}, the specimen temperature increased to some hundreds of degrees. Therefore, in these cases the temperature is higher than the transition temperature

($74°C < T_0 < 78°C$) at the corresponding strain rates so that the material deforms in the athermal regime. All discussed deformation regimes under each loading condition are summarized in Table 5-1.

Table 5-1 Deformation regimes under different loading conditions

	$\sigma_a \leq \sigma_c$ or σ_D	$\sigma_a > \sigma_c$ or σ_D
Ultrasonic loading	Thermally-activated regime ($T < T_0$)	Athermal regime ($T > T_0$)
Conventional loading	Athermal regime ($T > T_0$)	Athermal regime ($T > T_0$)

The aforementioned deformation modes under different loading conditions are consistent with OM and SEM observations on the surface of specimens. As depicted in Figure 4-10, under ultrasonic loading at low stress amplitudes for which no strong heating occurred, no slip band was formed on specimen surface, even after a large number of cycles. On the contrary, ultrasonic loading at high stress amplitudes resulted in formation of many slip bands on specimen surface (see Figure 4-13). In addition, Figure 4-11 shows that under conventional low frequency fatigue tests slip bands were formed in the early stages of cycling even for low stress amplitudes below the fatigue limit and the density of slip bands increased by increasing the number of cycles. Formation of slip bands requires multiplication of dislocations and quite long-distance motions of edge and screw dislocations. In the thermally-activated regime, for stress amplitudes far below the yield stress, these conditions are not provided. In contrast, in the athermal regime, these conditions are provided and favor the formation of slip bands.

Comparison of Figure 4-14 and Figure 4-17 reveals that many voids were formed along the slip bands on the surface of ultrasonic specimens, whereas no void was observed on the surface of specimens in the case of conventional fatigue tests. It is known that slip bands produce vacancies which result in formation of tiny voids within the slip bands [166], [167]. In the present study, although in both cases (ultrasonic loading at high stress amplitudes and conventional fatigue tests) the DP600 steel deforms in athermal mode leading to formation of slip bands in ferrite grains, ultrasonic loading involves significant temperature increases. At high temperatures such as 350°C, compared to room temperature, the growth of voids is accelerated by the increase in vacancies amount and their diffusion [167]. In this case voids preferentially form in ferrite grains surrounded by several martensite islands. It could be due to

the localized deformation in these regions which stems from the inhomogeneity between the hard martensite and the soft ferrite phase, as already reported for the case of monotonic tensile loadings of dual-phase steels [168]–[171].

Nishijima and Kanazawa [10] results for carbon steels suggested that high temperatures induced the formation of an oxide film at the surface of the specimens which restrains the slip deformation at the surface. The dislocations cannot escape through the oxide film and so accumulate in a harder subsurface layer which is also called "debris" layer [172]. This "debris" layer which contains a higher concentration of dislocation promote the generation of vacancies and cavities within slip bands [172], [173]. This mechanism also seems to be in a good agreement with the voids observed within the SBs in Fig 4-12.

5.2.3 Complementary discussions on thermal response of the material under ultrasonic loading

Another point that should be studied regarding the thermal response of the material under successive loadings at 20-kHz frequency is the slight decrease in temperature before the final steady state for the loading steps that involve an abrupt temperature increase (Curves (b) and (e) in Figure 3-2). In general, a temperature decrease during a fatigue loading step can result from a change in heating sources [92] or a hardening mechanism in the material which reduces the heat dissipation that is deduced from plasticity. Ranc et al. [92] observed such a decrease in temperature for a martensitic steel containing some residual austenite in the microstructure. In their case, martensitic transformation occurred at the beginning of the fatigue tests and acted as a heat source. When the transformation ended, the dissipation decreased, which resulted in a slight decrease in temperature before saturation. However, in our case, the microstructure of the DP steel was stabilized and no phase transformation occurred. Therefore, the slight decrease in temperature before stabilization most likely arises from a hardening mechanism that is related to the high temperature that the material experiences under ultrasonic fatigue loading at high stress amplitudes. Guo et al. [174] also reported a decrease in temperature before final stabilization for a magnesium alloy under 100-Hz fatigue loading. They correlated this temperature decrease to work hardening effects leading to degradation in plastic deformability and consequently in heat dissipation.

According to the results reported by Ekrami [175], for dual-phase steels with different morphologies, the yield and ultimate tensile strengths increase with increasing testing temperature up to ~450°C and then decrease at higher temperatures. Up to 450°C, they observed clear serrations on the stress-strain curve. During cyclic loading, dynamic strain aging that results in a strong increase in stress amplitude was also observed [176], [177]. Dynamic strain aging is a strengthening mechanism in which interstitial solute atoms diffuse around the dislocations and act as obstacles for the dislocations movements. In our case, as shown in Figure 3-2, for $\sigma_a = 251$ MPa the maximum temperature was ~350°C immediately before the slight decrease in temperature. Therefore strain aging can result in material hardening. In the present work, in order to access the occurrence of dynamic strain aging at high temperatures, simple tensile tests were carried out on the material at room temperature as well as 350°C which corresponds to the high temperature values that the material experienced under ultrasonic fatigue loadings at high stress amplitudes. As mentioned in Section 2.2.4 the tensile tests were carried out under displacement control at a constant crosshead speed of 5 mm/min. The obtained engineering stress-plastic strain diagrams are presented in Figure 5-6. In this case, the ultimate tensile stress was obtained as $\sigma_{ut} = 740$ MPa which is higher than the corresponding value at room temperature, $\sigma_{ut} = 650$ MPa, as presented in Table 2-2. Moreover, serrations were observed on the stress-strain curve at 350°C. The serrated yielding indicates the occurrence of dynamic strain aging that affects material hardening. In iron-based alloys (BCC metals), this phenomenon is attributed to elastic interactions of glide dislocations with diffusing solute nitrogen and carbon atoms during deformation at high temperature [178].

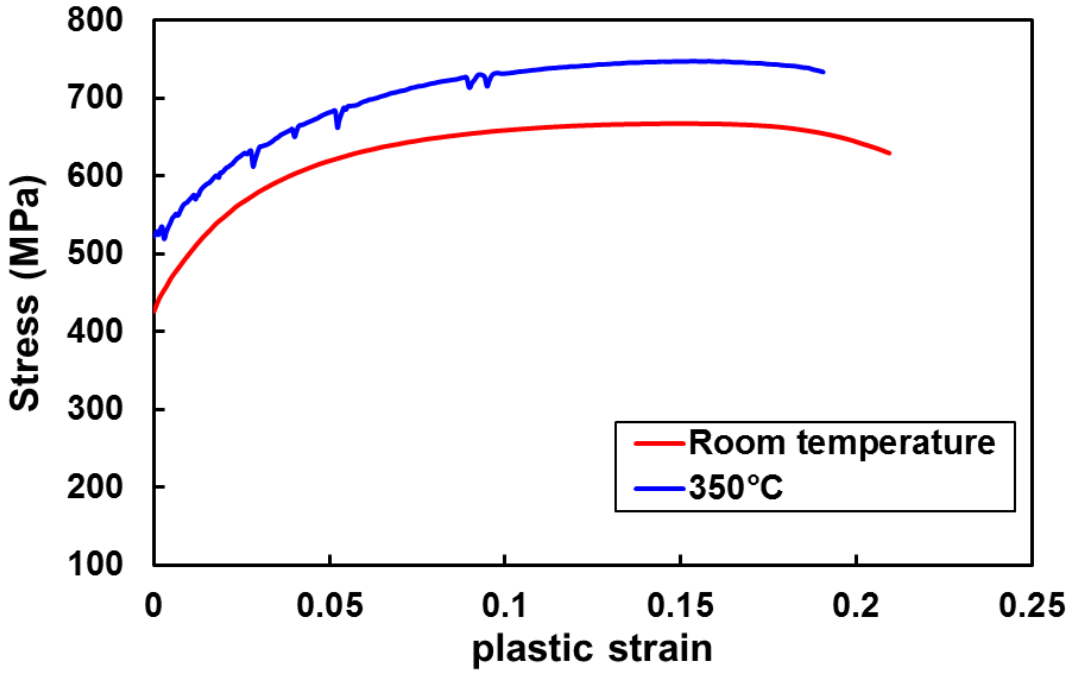

Figure 5-6 Experimental stress-plastic strain curve at room temperature and at 350°C.

Another hardening mechanism also can be supposed to occur as follows; in the athermal regime, the mobilities of screw and edge dislocations are similar and the mechanisms of multiplication of dislocations, such as Frank-Read sources operate much more easily than in the thermally-activated regime, leading to material hardening [176].

Therefore, based on the aforementioned concepts, at 350°C, because of dynamic strain aging and multiplication of dislocations the material was work-hardened, and consequently, the plastic dissipation decreased, which resulted in a decrease in temperature before saturation. In addition, with increasing temperature, the annihilation rate of dislocation increases while the multiplication rate remains approximately constant [26]. These competitive hardening-softening mechanisms led to a final saturation in temperature.

Afterwards, when the specimen cooled down and was loaded in the next loading step at higher stress amplitudes, the temperature elevation decreased (Points C and D in Figure 3-5) because the material was hardened in the previous step. Finally, at the next loading steps, thanks to an increase in stress amplitude, large dislocation motion occurred again in localized zones producing strong intrinsic dissipation and, once more, large temperature elevations.

5.3 Effect of Frequency on Fatigue Response of the Material

5.3.1 Effect of frequency on fatigue life

According to the experimental results presented in Section 4.2, the S-N curve was shifted to the right in the case of ultrasonic loading compared to conventional 30-Hz test results. As mentioned in Chapter 1, the longer fatigue life under ultrasonic loading is usually related to the smaller plastic deformation involved at high frequency due to the higher strain rate [79], [81]–[86]. However, in our case, as the loading conditions (temperature and strain rate) correspond to the athermal regime, no significant strain rate effect is expected. Under ultrasonic loadings at stress amplitudes above the fatigue limit strong heating mechanisms occurred and temperature increased up to several hundreds of degrees. As mentioned in the preceding section, in the case of dual-phase steel under high temperature cycling, dynamic strain aging is known to occur [153], which results in increasing the yield and tensile strengths of the material

The higher fatigue life under ultrasonic loadings can be attributed to dynamic strain aging. Therefore, in spite of the high mobility of screw dislocations in the athermal deformation regime, because of the high temperature, interstitial carbon atoms diffuse around the dislocations and restrict their movements temporarily. It is known that active slip bands are not effectively strengthened by strain aging [179], [180]. Nevertheless, strain aging strengthens the surrounding ferrite matrix. Consequently, slip bands develop as easily as at room temperature but the plastic zone at the crack tip is smaller and requires higher stresses to propagate than at room temperature. Subsequently, crack propagation in the matrix would be delayed, leading to an increase in the fatigue life for a given stress amplitude. The effect of strain aging on increasing the fatigue life of low-carbon steels at high temperatures have been already reported in the literature [10], [37], [177]. For instance, Nishijima et al. [10] conducted 10-Hz fatigue tests on a ferritic-pearlitic steel at high temperatures and showed that the fatigue life and fatigue strength are higher at 300°C and 400°C compared to the results obtained at room temperature. They attributed this increase in fatigue properties to dynamic strain aging, to which carbon and low–alloy steels are sensitive

In order to evaluate the effect of temperature and dynamic strain aging on the fatigue life, the results obtained from simple tensile tests carried out at 350°C, which were presented in Figure 5-6, were employed. The S-N curves presented in Figure 4-1 were replotted by normalizing the stress amplitude by the ultimate tensile strength at room temperature for conventional fatigue test results and by the ultimate tensile strength at 350°C for the ultrasonic loading results. The

S-N diagrams after normalizing the stress amplitude values are presented in Figure 5-7. It should be noted that in this figure run-out samples are not shown as in the case of ultrasonic loading the temperature of the run-out samples remained below 40°C and material deformation was in the thermally-activated regime. According to the normalized S-N curve, the stress ratio values for ultrasonic loading are below the corresponding values of conventional low frequency tests. This can explain the higher fatigue life for a given stress amplitude under ultrasonic loading.

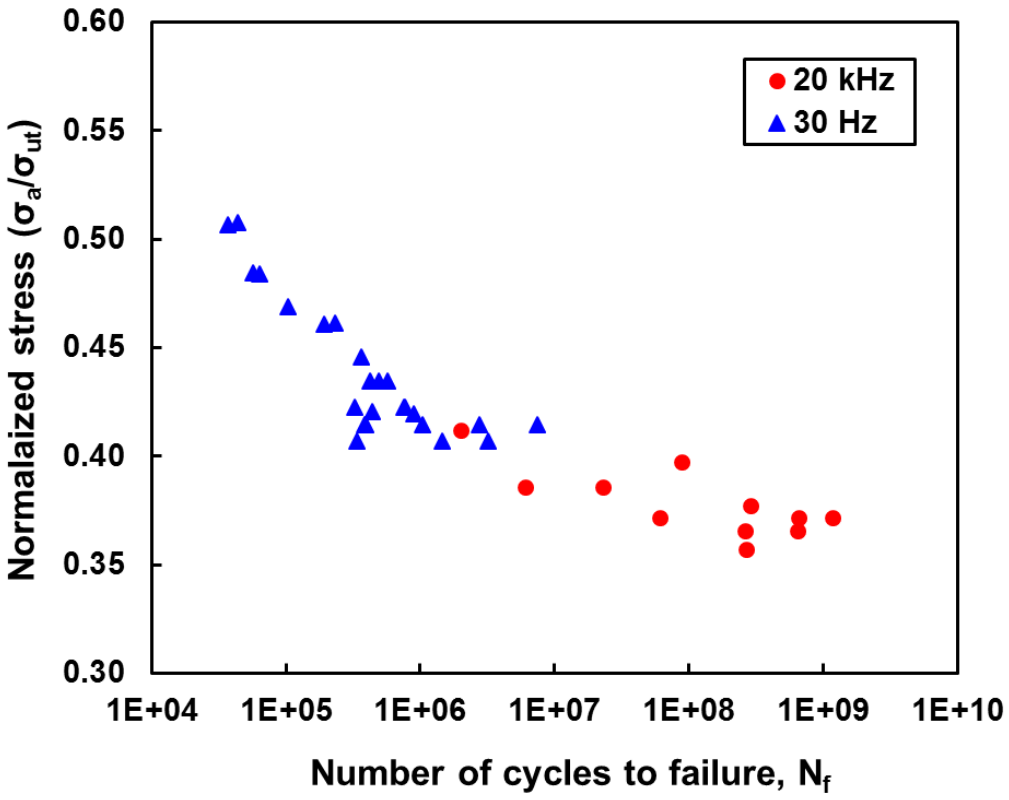

Figure 5-7 Assessment of the high temperature effects on the material S-N properties.

5.3.2 Effect of frequency on fatigue fracture

The microscopic observation results presented in Section 4.4 revealed a transgranular crack initiation mode for both ultrasonic and conventional fatigue loadings. In the athermal regime transgranular crack initiation has been reported to be related to local stress concentration at slip bands while in the thermally-activated regime intergranular crack initiation is predominant because of stress asymmetry and incompatible deformations at grain boundaries [88], [111], [176], [178]. It has been reported that for low-carbon steel, crack initiation mechanism changes from transgranular in conventional fatigue tests to intergranular in ultrasonic loading due to the

change in deformation regime [87], [181]. In these cases, material deformation mode was athermal under conventional loading, while the thermally-activated deformation regime was dominant under ultrasonic fatigue tests. However, for the present DP600 steel, due to strong heating during ultrasonic tests at high stress amplitudes, the deformation regime was athermal, similar to that of conventional low frequency tests. Therefore, in both ultrasonic loadings at high stress amplitudes and conventional low frequency tests, transgranular crack initiation occurs due to local stress concentration at slip bands.

Under conventional fatigue regime ($N<10^7$cycles) fatigue cracks are commonly initiated on the specimen surface due to the irreversible process of extrusions and intrusions within the slip bands [16]. In gigacycle regime, the internal defects play a more important role compared to surface damage especially if the surface is smooth [1]. According to the experimental observations presented in section 4.3, for all the specimens ruptured in the gigacycle regime ($N_f >10^7$) under ultrasonic loading, fracture was induced by inclusions, even for the few cases of surface fracture initiation. This observation correlates with the findings of Sakai et al. [30] for very high cycle fatigue and the explanation given by Mughrabi [16]: although the fatigue fracture in very high cycle regime mainly results from the internal inclusions, other types of fracture can occur, including surface fracture initiation when the defects or inclusions are located on the surface.

More specifically, according to Figure 4-5, for a given stress amplitude in the range of $264<\sigma_a<300$ MPa, where the data exist for both loading conditions, fracture was induced by inclusions under ultrasonic loading, while for the corresponding fracture cases under conventional loadings there was no inclusion-induced fracture. This can be explained according to the results presented in Figure 5-7. This figure shows that due to strain aging under ultrasonic loading, the stress amplitude normalized by the ultimate tensile stress were below the corresponding values under low frequency tests. The plastic deformation is thus reduced. Consequently, the cumulative slip irreversibility at the surface is probably reduced (even if it is enough to form extrusions) because of the material was strengthened by strain aging and/or because of the presence of an oxide layer[1]. Considering these mechanisms, inclusions, as zones of stress concentration due to metallurgical microstructure misfit, become the sites for initiation and propagation of cracks responsible for failure [5].

[1] In order to assess this hypothesis, more work is needed to measure the height of the extrusion by atomic force microcopy and to discern the presence of an oxide layer.

5.3.3 Correlation of deformation regimes with fatigue fracture

In order to correlate the fatigue behavior of the material to the strain rate and temperature conditions, a strain rate-temperature map associated with deformation mechanisms was developed based on the aforementioned transition formulation proposed by Rosenfield and Hahn [165] for BCC materials. The developed map is presented in Figure 5-8. This map focuses on the transition between athermal and thermally-activated regime, which are indicated as Region I and Region II, respectively. The solid line representing the transition boundary between these two deformation regimes was obtained from the empirical equation proposed by Rosenfield and Hahn for low carbon steels [165] (see Eq. (5-2)).

The data obtained in the present study for ultrasonic and 30-Hz frequency fatigue tests of DP600 steel was plotted in this transition map. Moreover, in order to enrich the analysis, the data reported in the literature for DP600 steel as well as several two-phase ferritic-pearlitic steels under 20-kHz and low frequency (f<150 Hz) fatigue tests was also plotted in this map. The data for DP600 steel were obtained from Munier et al. [138]. The mentioned ferritic-pearlitic steels whose data were extracted from literature are as follows: C15 steel (Bach et al. [111] and Guennec et al. [86]), C45 steel (Ranc et al. [95] and Bach et al. [111]), and finally Cr-Mo steels (Nishijima & Kanazawa [10] and Schneider et al. [81]). In addition to these two-phase steels, data reported for Armco iron by Vincent et al. [182] and Wagner et al. [24] was also plotted. Armco iron is single-phase ferrite containing 80 wt. ppm of carbon. Studying the pure iron is important since it is the main constituent of ferritic steels which mainly accommodates the deformation and also it can be considered as a model material representing the fatigue characteristics of BCC metals.

It should be noted that concerning the data obtained from the literature, only the information corresponding to the longest fatigue life (associated with the lowest stress amplitude) in the reported S-N curves was extracted and plotted in Figure 5-8. Table 5-2 summarizes the experimental information related to all data plotted in Figure 5-8, including the material, testing frequency, stress amplitude associated with the longest fatigue life, strain rate amplitude, and specimen temperature. Concerning the temperature, when self-heating developed during ultrasonic tests, the temperature was considered as the mean temperature was before rupture [95], [111]. In the case of low frequency tests, when no temperature information was provided, the tests were considered to be carried out at room temperature, RT (~22°C) without any self-

heating. This case includes the results related to Armco iron in [182], C15 and C45 steels in [111], and C15 steel in [86].

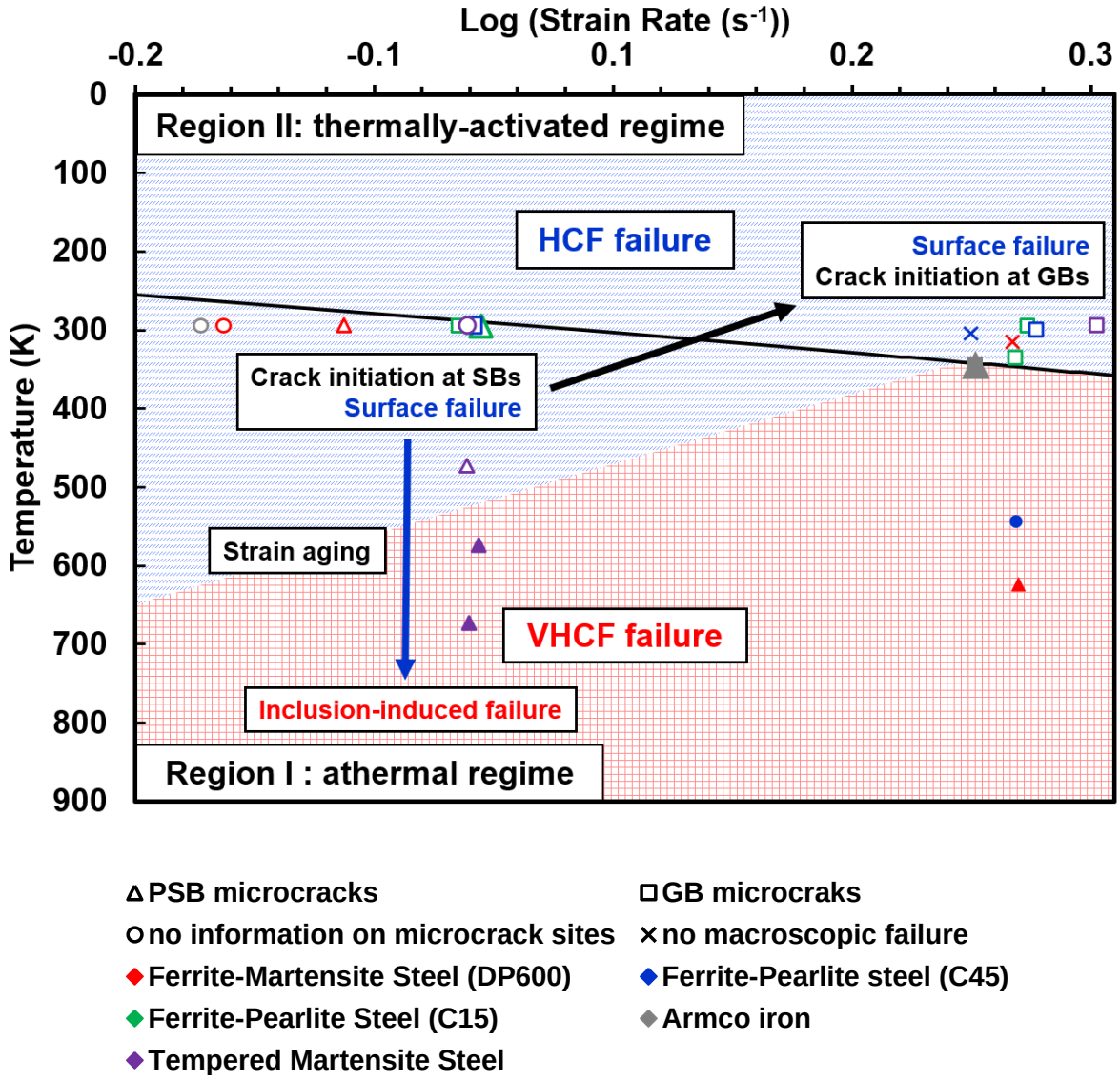

Figure 5-8 Regions of the temperature-strain rate spectrum of ferrite base steels that reflects different crack initiation mechanisms and fatigue failure behavior.

Table 5-2 Material and experimental properties of the data plotted in Figure 5-8.

Materials	Frequency (Hz)	Fatigue life (cycles)	Stress amplitude (MPa)	Strain rate (s^{-1})	Temperature (K)	Reference	Symbol in Figure 5-8
DP600	30	3.2×10^{6}	265	0.2	295 (22°C)	Present work	△
DP600	20000	2.6×10^{8}	265	159	~623 (350°C)	Present work	▲
DP600	20000	Infinite	240	144	<313 (<44°C)	Present work	×
DP600	10	1.2×10^{6}	250	0.07	295 (22°C)	Munier et al. [138]	○
50CrMo4	5-400	2×10^{5}	520	0.08-6.2	295 (22°C)	Schneider et al. [81]	○
50CrMo4	20000	1×10^{6}	560	335	<333 (60°C)	Schneider et al. [81]	□
1CrMo0.5	100	2.6×10^{6}	280	0.84	295 (22°C)	Nishijima & Kanazawa [10]	△
1CrMo0.5	100	2×10^{6}	260	0.78	473 (200°C)	Nishijima & Kanazawa [10]	△
1CrMo0.5	100	2.5×10^{8}	290	0.87	573 (300°C)	Nishijima & Kanazawa [10]	▲
1CrMo0.5	100	8×10^{8}	265	0.80	673 (400°C)	Nishijima & Kanazawa [10]	▲
C45 steel	20000	Infinite	250	150	305 (32°C)	Ranc et al. [95]	×
C45 steel	20000	4×10^{9}	260	255	~543 (270°C)	Ranc et al. [95]	●
C45 steel	20000	4×10^{7}	312	187	300	Bach et al. [111]	□
C45 steel	120	1.2×10^{7}	228	0.82	295	Bach et al. [111]	□
C15 steel	20000	1.2×10^{7}	290	174	295	Bach et al. [111]	□
C15 steel	120	1×10^{7}	200	0.72	295	Bach et al. [111]	□
C15 steel	20000	1.4×10^{7}	155	135	335	Guennec et al. [86]	□
C15 steel	140	1.5×10^{6}	210	0.88	295	Guennec et al. [86]	△
Armco iron	10	3×10^{6}	200	0.06	295 (22°C)	Vincent et al. [182]	○
Armco iron	20000	5×10^{9}	172	103	345 (77° ∈ [67-87°C))	Wagner et al. [24]	▲■

Concerning the largest fatigue life information available in the referenced literature, the data plotted in Figure 5-8 can be separated into two regimes:

1. The high cycle fatigue regime ranging from 2×10^5 to 4×10^7 cycles (open symbols and the region denoted by the blue hatch pattern).

2. The very high cycle regime for $N\geq2.5\times10^8$ cycles (full symbols and the region denoted by the red lattice pattern).

The data for HCF failure corresponds to temperatures around RT and are located close to the transition line; The HCF failures under low frequency tests are just below the transition line (Region I) while those under 20 kHz loading are located just above this line (Region II). The difference between these results comes from the sites of microcracks which are located at SBs for plots in Region I whereas they are located at grain or phase boundaries for those in Region II. These trends are consistent with the results reported by Sommer et al. [183] for α-iron with small carbon content.

In Region I, screw and edge dislocations have similar mobility allowing multiplication and rearrangement of dislocations to localize the deformation in SBs. Fatigue cracks initiate in a transgranular way at these SBs leading to a surface failure mode. On the opposite, in Region II, screw dislocations are much less mobile than edge dislocations preventing SBs from developing. As a result, cracks initiate at the grain and phase boundaries where the strain incompatibilities are the largest. In the thermally activated regime conditions, the plastic deformation is very low but sufficient to produce crack propagation in HCF regime. However, in the VHCF regime failure cannot occur since the stress amplitudes, which are even lower, cannot produce enough plastic deformation for crack propagation and fatigue failure. As shown in Figure 5-8, the data points for Armco iron loaded at 20 kHz are very close to the transition line. Interestingly, both transgranular at SBs as well as intergranular cracks were observed for this case [24]. These observations are consistent with the location of the data points in the strain rate–temperature map. Sommer et al. [183] showed that transgranular and intergranular crack initiations are competitive mechanisms depending mainly on the amount of involved plastic strain. Large plastic strain promotes transgranular cracks while small plastic deformation promotes intergranular cracks. In the case of Armco iron under 20 kHz loading, enough plastic deformation occurs to produce failure in the VHCF regime (up to 5×10^9 cycles).

The studied DP600 steel as well as the C45 steel in [95] loaded in the thermally-activated mode did not exhibit any failure, neither in the HCF nor in the VHCF regime. As expected, no slip band was detected on the surface of the specimens. For C45 steel applying 260-MPa stress amplitude led to a non-avoidable strong self-heating, resulting in a change in strain rate-temperature conditions from the thermally-activated regime to the athermal mode [95]. This change in deformation regime occurred at ~$N=8\times10^6$ cycles, before the failure of the specimen ($N_f=4\times10^7$ cycles). The results obtained in the present research for DP600 steel can be also explained by the same argument. Specimens loaded at stress amplitudes slightly above 260 MPa exhibited a strong self-heating before reaching failure. As a result, fatigue failure is only possible in the athermal regime.

From these findings, it can be concluded that as soon as the strain rate and temperature conditions under fatigue loading are such that thermally-activated mechanisms are involved, cracks initiate at grain or phase boundaries and result in failure in the HCF regime. No VHCF failure can take place in this case since failure in the VHCF regime involves even lower stresses. Locally at microstructural singularities, crack initiation could take place but in such ductile ferrite-based steels, in thermally-activated regime the mobility of screw dislocations is too low to create multiplication of dislocations and produce enough plastic deformation to cause crack propagation and macroscopic fatigue failure.

It is striking that the data corresponding to temperatures much higher than RT and typically above 200°C belong all to the Region I (athermal regime) and exhibits inclusion-induced VHCF failure. Athermal regime is consistent with the presence of SBs and transgranular microcracks at the surface of the specimens. As mentioned earlier, at these temperatures, carbon steels are sensitive to strain aging. As a result, ferrite is strengthened by solute atoms that segregate in the dislocations, leading to impeding their motion. Since the ferrite matrix is strengthened by strain aging the plastic zone at the crack tip is smaller and cracks require higher stresses to propagate than at temperatures below 200°C. These higher stress concentrations zone are preferentially found at inclusions because they lead to a higher accumulation of dislocations. This scenario explains why inclusion induced crack initiation were observed for high temperature loadings which is consistent with the discussions presented in Section 4.3. In addition, the increase in fatigue life results from the reduction in plastic deformation at the crack tip and the delay in crack growth in the strengthened ferrite matrix [179], as previously mentioned in Section 5.3.1.

5.3.4 Effect of frequency on fatigue limit

Based on the experimental observations, for stress amplitudes below the HCF limit determined by 30-Hz fatigue tests, slip bands and microcracks were also visible on the surface of the run-out specimens. These observations demonstrated that the 260 MPa HCF fatigue limit is not only related to slip activity and microcrack initiation. Moreover, in the case of 20-kHz loading no slip band was detected on the surface of run-out samples. It is well supported in the literature that the fatigue limit is not only related to slip activity and crack initiation. Rather, it corresponds to the stress threshold required to propagate the trapped microcracks [10], [30], [102], [184], [185]. Therefore, on the one hand, based on the previously mentioned strain aging effects in strengthening the ferrite matrix, it is expected that the fatigue limit is higher under ultrasonic loading. On the other hand, at high temperatures, such as 350°C compared to room temperature, the vacancy diffusion along the slip band is higher, leading to accelerating the voids growth. The presence of voids in the vicinity of inclusions could decrease the cohesion strength of the material to a point where crack propagation begins [186]. Consequently, microcracks propagate more easily at high than low temperatures leading to decreasing the fatigue limit normalized by the ultimate tensile strength. These competitive mechanisms finally led to the same absolute fatigue limit in ultrasonic loading and conventional tests. However further investigations are required to confirm this hypothesis which is the subject of the future work.

To summarize, in the present case of the DP600 steels loaded using continuous cycling at 30 Hz and 20 kHz, fatigue failure was observed only for strain rate-temperature conditions implying athermal deformation mechanisms. At 30 Hz, this condition is immediately satisfied, and the fatigue limit is associated with the stress threshold required to propagate cracks. This threshold was found to be ~260 MPa. At 20 kHz, the fatigue limit of 260 MPa corresponds to the critical stress amplitude σ_c, necessary to produce enough dissipated energy to get a self-heating above ~74°C. The origin of these two fatigue limits seems thus to be different. However, the fact that the fatigue limits are the same suggests that the self-heating above 74°C could be also related to crack propagation; short cracks could be formed but stopped because of the strain aging strengthening, as previously mentioned in Section 5.2.3 Thus σ_c could be also the threshold stress required to crack propagation which is consistent with the definition of fatigue limit.

5.4 Discussions on Dissipated Energy under Fatigue Loading

According to Figure 3-17, the mean dissipated energy per cycle is much lower under ultrasonic loading at low stress amplitudes (45 to 1200 J/m^3/cycle) in comparison with conventional 80-Hz fatigue tests (14000 to 52000 J/m^3/cycle). In athermal deformation mode, high mobilities of screw and edge dislocations lead to high energy dissipations while in the thermally activated mode low energy dissipation occurs because of to-and-fro motions of edge dislocations [153]. These mechanisms explain the gap between the two levels of dissipated energy. For ultrasonic loadings at high stress amplitudes for which material deforms in athermal regime (Points A and B in Figure 3-18) the dissipated energy is much larger than that at low stress amplitudes and approaches the dissipated energy values under conventional fatigue tests.

5.4.1 Correlation of dissipated energy with fatigue characteristics of the material

The dissipated energy per cycle is a measure of non-elastic deformation in the material under cycling. The slope of the dissipated energy versus number of cycles can be interpreted as a measure for the evolution of the microstructural changes. If this slope is negligible the change in dislocation structure is negligible and no fatigue failure occurs even up to very high number of cycles [111]. A particular change in dissipated energy per cycle can be a sign of enough internal changes to promote crack initiation during fatigue loading [111]. This concept is the basis of some alternative fatigue characterization methods based on thermal measurements, which are constituted in studying the evolution of the dissipated energy [32] and additionally the stored energy over cycles, to get insights into the possible fatigue failure [136], [139], [187].

Another approach for fatigue limit estimation based on dissipated energy measurements involves successive fatigue loadings up to a specific number of cycles with increasing the stress amplitude along with temperature and dissipation measurements and plotting the dissipated energy per cycle versus stress amplitude (see e.g. [105]). These methods consider that the fatigue limit corresponds to a critical stress amplitude at which the heat generation becomes much stronger. Therefore the slope of the self-heating diagram changes at the stress value corresponding to the fatigue limit. Guo et al. [105] associated this strong change in dissipated energy to transition in dissipative mechanism from anelasticity to a combination of anelasticity and microplasticity. Mareau et al. [119] and Connesson et al. [136] also reported a change in the slope of dissipated energy diagram versus stress amplitude because of the change in

dissipative mechanisms from anelasticity to inelasticity by increasing the stress amplitude. However, they did not report the relation between this slope change and the fatigue limit.

In the present work, the second approach was employed to study the potential relationship between dissipated energy variation and fatigue limit under ultrasonic and conventional fatigue tests and the results are discussed in the following paragraphs.

- Ultrasonic loading

Concerning the dissipated energy measurements for the stress amplitudes below the critical stress ($\sigma_a < \sigma_c$) shown in Figure 3-12, the change in dissipated energy per cycle with increasing stress amplitude is of quadratic form. Considering that the dissipated energy results from anelastic or inelastic material behaviors that are characterized by constant properties, the following expressions has been introduced in the literature for dissipated energy; by assuming a prescribed sinusoidal stress with amplitude σ_a and a Kelvin-Voigt model (spring and dashpot in parallel), the dissipated energy per cycle for anelastic behavior is [137]:

$$\frac{\tilde{d}_1}{f} = \frac{1}{f}\frac{2\eta(\pi\sigma_a)^2}{\frac{\mu^2}{f^2} + 4\pi^2\eta^2} \tag{5-3}$$

where μ and η are the elastic and viscous moduli, respectively. For inelastic behavior and a zero mean stress, the dissipated energy per cycle is [137]:

$$\frac{\tilde{d}_1}{f} = \frac{1}{f}\frac{{\sigma_a}^2}{2\eta} \tag{5-4}$$

In both cases, and considering constant material properties (μ and η), the dissipated energy per cycle is a quadratic function of the stress amplitude. According to the experimental results obtained in the present work, because the dissipated energy per cycle was a quadratic function of the stress amplitude for low stress amplitudes, it can be assumed that the material internal state remained nearly the same during cyclic loading. This is in a good agreement with the claim that in this case, the deformation and the dissipation result from the to-and-fro motion of edge dislocations.

However above a critical stress amplitude σ_c, strong heating occurred because of the transition to athermal deformation regime and then temperature reached a steady state. Interestingly, the measured mean critical stress amplitude σ_{mc}=253 MPa is in a good agreement with the fatigue limit of the material σ_D =260 MPa, below which no temperature increase occurred and material deformed in thermally-activated regime and no VHCF failure was observed. At stress amplitudes above the fatigue limit strong dissipation arose and VHCF rupture was possible because enough plastic deformation occurred. These observations suggest that the critical stress amplitude obtained from thermography measurements would correspond to the fatigue limit[1]. This hypothesis is supported by the aforementioned physical definition of fatigue limit of steels which states that the fatigue limit corresponds to a slightly higher stress level at which an initiated microcrack stops propagating at the first microstructural barrier [10], [30], [102]. Based on the thermographic images shown in Figure 3-7, at the moment of abrupt temperature increase at the stress amplitude slightly higher than σ_c, a concentrated high temperature zone was formed and spread through specimen width and then it disappeared after several cycles. It can suggest that microcracks have been initiated and then stopped by the microstructural barriers (grain or phase boundaries).

- Conventional fatigue loading

The experimental measurements for dissipated energy per cycle under 80-Hz frequency tests are replotted in Figure 5-9. As shown in this figure the slope of diagram changes at a critical stress amplitude of ~270 MPa. This critical stress amplitude is in a good agreement with the experimental fatigue limit at 10^7 cycles (σ_D =260 MPa) obtained in Chapter 4 by 30-Hz frequency tests. Based on this change in the slope of the diagram, two regions can be distinguished which are indicated as Region I and Region II in the figure. In both regions slip bands were found on the surface of the specimens. Therefore the change in the slope cannot be due to microplasticity initiation. In our case it can be suggested that the increase in the slope of the dissipated energy diagram versus stress amplitude is due to a change in the dissipative mechanisms from local plastic deformation to crack propagation over short distances which is

[1] The fatigue limit was slightly higher than $\sigma_{mc} \approx 253$ MPa measured by thermographic studies. This difference stems from the fact that the thermal measurements were carried out by successive loadings on the same specimen while the S-N data estimations were done by doing fatigue tests on virgin specimens for each stress amplitude.

consistent with the physical definition of the fatigue limit. This mechanism was also reported by Giertler and Krupp [120] for a tempered carbon steel.

The experimental dissipated energy measurements under 80-Hz and 50-Hz loadings are compared in Figure 5-10 with the results reported in the literature for DP600 steel [137]–[139]. Despite the differences in the values, which stem from different methods of dissipation estimations and temperature measurements uncertainty, the results are nearly of the same order at different stress amplitudes. According to Figure 5-10(b) the change in the slope of the diagram was observed for the data reported by Munier et al. [138].

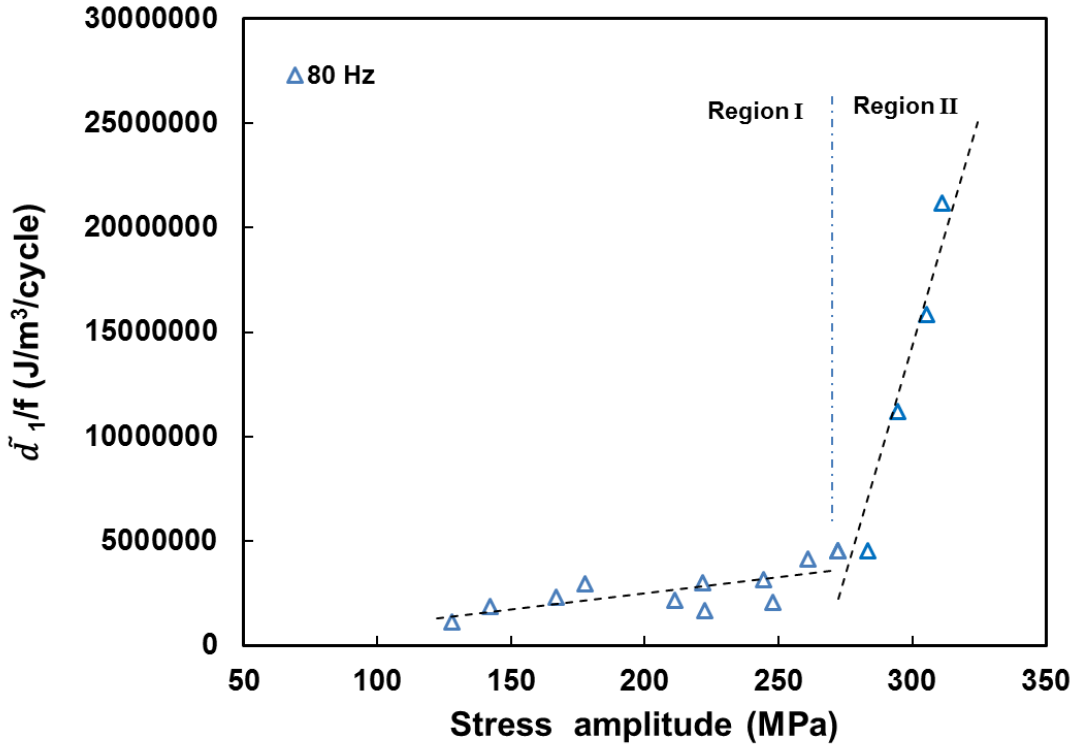

Figure 5-9 Dissipated energy per cycle versus stress amplitude under 80-Hz conventional fatigue tests.

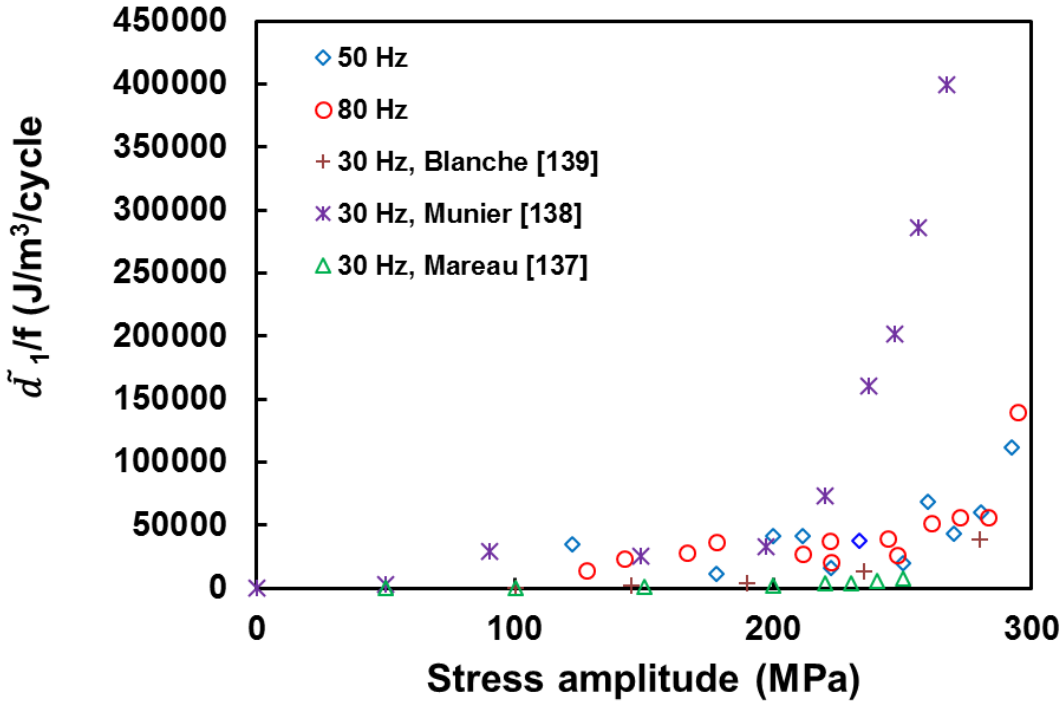

(a)

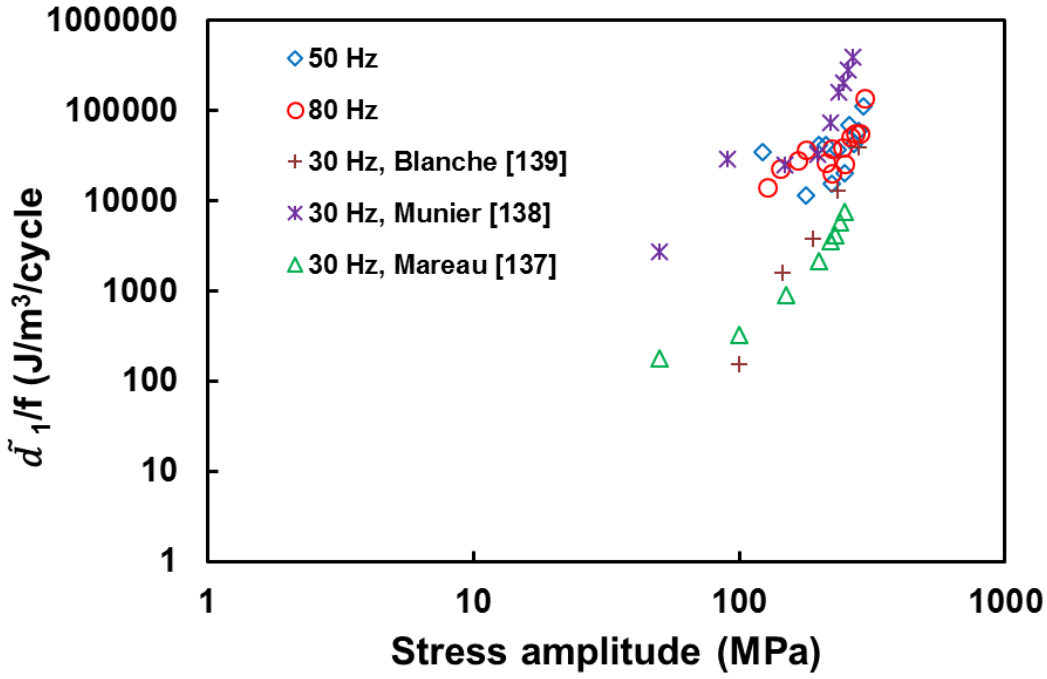

(b)

Figure 5-10 Comparison of dissipated energy per cycle for DP600 steel at different frequencies: **(a)** Classical diagram **(b)** Logarithmic scale.

Despite the quite acceptable fatigue limit prediction by the presented dissipated energy estimation method under successive fatigue loadings, some principal critics can be addressed

to this approach. In this method the cyclic loading steps are carried out up to a specific number of cycles where the mean temperature reaches a steady state or a slight increasing trend. This specific number of cycles was considered as 2×10^4 cycles under conventional fatigue loadings and 10^7 cycles for ultrasonic tests in the present work. Moreover, it was considered as 6000 cycles by Munier et al. [104], [138], and 10000 cycles by Guo et al. [105] and also by Giertler and Krupp [120]. However, Blanche [139] measured the dissipation energy after 15000, 65000, 115000, 165000, and 215000 cycles, and showed that the dissipated energy versus stress amplitude curve changes by increasing the number of cycles. Consequently, the critical stress amplitude from which a change in the slope of the curve is determined can change with the number of cycles. Besides, as reported by Favier et al. [110], in the case of ultrasonic fatigue tests, the steady state of the mean temperature does not necessarily lead to a steady state of the corresponding dissipated energy so that the dissipated energy can increase by increasing the number of cycles. Accordingly, measuring the dissipated energy evolution versus number of cycles would be a more promising approach to study the change in the dissipative mechanisms and correlating the thermal response of the material to fatigue properties such as the fatigue limit. In order to accomplish this aim, more precise two-dimensional (2D) dissipated energy estimations would be preferred to the 0D simplified approach used in the present study, especially in the case of ultrasonic loading at high stress amplitudes for which the temperature field is no more symmetric with regard to the specimen center and deformation occurs in athermal regime. In this case, a more rigorous and more reliable dissipated energy measurement enables to compare the dissipated energy under ultrasonic loading at high stress amplitudes with the corresponding results of conventional fatigue tests and verify if a minimum dissipated energy is required for the material to fail under fatigue loading. Considering the microstructural mechanisms behind the dissipative behavior, most researchers only study the phenomena on the surface of the specimen, while microstructural evolutions in the bulk of the material have been rather ignored. According to these considerations, the role of numerical simulations to understand and compare the dissipative mechanisms of surface grains with that of internal grains can be of non-negligible interest.

The abovementioned critical concepts provide a new insight into the future work of this study to accomplish a better understanding of the dissipative mechanisms under fatigue loadings at different strain rate-temperature conditions and their relationship with the fatigue properties.

Conclusions and Perspectives

General Conclusions

In this research work the fatigue behavior of a ferritic-martensitic dual-phase steel was studied in HCF and VHCF regimes. The effect of frequency on fatigue and thermal response of DP600 dual-phase steel was studied by carrying out ultrasonic and conventional low-frequency tension-compression fatigue tests along with temperature measurements and microscopic observations. A clear discrepancy was observed in the S-N curves obtained from conventional 30-Hz fatigue tests and that determined from ultrasonic 20-kHz loadings. The rate- and temperature-dependent flow behavior of the ferrite phase, as a BCC structure, was found to be a decisive parameter explaining the effects of frequency on fatigue and thermal response of the material. Moreover, the significant temperature increase under ultrasonic fatigue loading at high stress amplitudes was found to play an important role in the observed phenomena. The main conclusions drawn from the results of this study can be summarized as follows:

- Under ultrasonic fatigue loading, there was a transition in material deformation mode from thermally-activated regime at stress amplitudes below the fatigue limit to athermal mode at stress amplitudes above the fatigue limit. Nonetheless, material deformation occurred in athermal regime under conventional low-frequency fatigue tests for all stress amplitude ranges;

- The higher fatigue life in the case of ultrasonic loading was attributed to the dynamic strain aging which resulted from the high temperature increases at high stress amplitudes. However, the same fatigue limits remain as an open question to be investigated in a future work, even if some insights were proposed;

- In both ultrasonic and low-frequency tests transgranular cracking along the slip bands was observed and no intergranular crack was detected. In the case of ultrasonic loading, many microvoids nucleated and coalesced along the slip bands resulting in microcrack initiations. This microvoids initiation and coalescence were not observed in the case of low-frequency tests. Diffusion of vacancies due to high temperature under ultrasonic fatigue loading is thought to be the main cause of microvoids formation;

- Surface fracture initiation from slip bands was observed in low and high cycle regimes under conventional tests, while under ultrasonic loading fracture initiation was always inclusion-induced;

- The S-N curves were replotted by normalizing the stress amplitudes by the ultimate

tensile strengths at corresponding loading temperatures in order to consider the effect of dynamic strain aging for ultrasonic loading. This replotting rationalized the S-N data, resulting in lower stress ratios for ultrasonic loading, which can explain the higher fatigue life and inclusion-induced crack initiations under 20-kHz ultrasonic tests;

- A strain rate-temperature transition map was developed based on the experimental findings for DP600 steel and the data reported in the literature for several ferrite-based steels. It was shown that no VHCF failure occurs if material deforms in thermally-activated regime and, in that condition, microcracks initiated at grain or phase boundaries for HCF failure. VCHF fatigue failure was observed only for strain rate-temperature conditions implying athermal deformation mechanisms associated with microcracks within slip bands.

Perspectives

Several complementary investigations are proposed to extend and reconfirm the results obtained in this research, as follows;

- High temperature conventional fatigue tests to verify the effect of temperature on deformation and fracture mechanisms at low frequencies and specifically to reveal the effect of dynamic strain aging on fatigue life and fatigue limit;
- Dissipated energy measurements by employing 2D diffusion equations and studying the evolution of the dissipated energy versus number of cycles.
- Transition electron microscopy (TEM) studies at different loading conditions to reveal the dislocation structures and confirm the suggested deformation regimes;
- Conducting the same experimental studies for other grades of DP steels in order to study the effect of grains and phases morphologies as well as the influence of the crystallographic texture on fatigue and deformation behaviors;
- Investigation of the effect of surface quality on fatigue response and specifically internal failure initiation;
- Microstructural computational studies through finite element (FE) simulations, which are the main focus of the future work. Numerical simulations can be employed to estimate the strain and stress fields within the polycrystalline dual phase steel to develop an understanding of the correlation between the microstructure and mechanical fields in

the material under high and low-frequency cyclic loadings. One of the objectives of the numerical simulations will be to study the effect of frequency on dissipated energy and microplasticity mechanisms. In the case of ultrasonic fatigue loading, numerical simulations enable omitting the effect of the temperature increase at high stress amplitudes and study only the effect of strain rate. Moreover, numerical estimation of dissipated energy and comparison to experimental measurements can be helpful for assessment of heat sources. In addition, numerical simulations will be employed to compare the dissipated mechanisms on the surface with those in the bulk of the material.

References

[1] C. Bathias, “There is no infinite fatigue life in metallic materials,” *Fatigue Fract. Eng. Mater. Struct.*, vol. 22, no. 7, pp. 559–565, 1999.

[2] T. Naito, H. Ueda, and M. Kikuchi, “Fatigue Behavior of Carburized Steel with Internal Oxides and Nonmartensitic Microstructure near the Surface,” *Metall. Trans. A*, vol. 15, no. 7, pp. 1431–1436, 1984.

[3] Y. Murakami, N. N. Yokoyama, and J. Nagata, “Mechanism of fatigue failure in ultralong life regime,” *Fatigue Fract. Eng. Mater. Struct.*, vol. 25, no. 8–9, pp. 735–746, 2002.

[4] K. Shiozawa, L. Lu, and S. Ishihara, “S-N curve characteristics and subsurface crack initiation behaviour in ultra-long life fatigue of a high carbon-chromium bearing steel,” *Fatigue Fract. Eng. Mater. Struct.*, vol. 24, no. 12, pp. 781–790, 2001.

[5] K. Tanaka and T. Mura, “A Dislocation Model for Fatigue Crack Initiation,” *J. Appl. Mech.*, vol. 48, no. 1, pp. 97–103, 1981.

[6] H. Mughrabi and S. D. Antolovich, “A tribute to Claude Bathias - Highlights of his pioneering work in Gigacycle Fatigue,” *Int. J. Fatigue*, vol. 93, pp. 217–223, 2016.

[7] H. Mughrabi, “On the life-controlling microstructural fatigue mechanisms in ductile metals and alloys in the gigacycle regime,” *Fatigue Fract. Eng. Mater. Struct.*, vol. 22, no. 7, pp. 633–641, 1999.

[8] Y. Murakami, T. Nomoto, and T. Ueda, “Factors influencing the mechanism of superlong fatigue failure in steels,” *Fatigue Fract. Eng. Mater. Struct.*, vol. 22, no. 7, pp. 581–590, 1999.

[9] Y. Murakami, T. Nomoto, T. Ueda, and Y. Murakami, “On the mechanism of fatigue failure in the superlong life regime ($N > 10^7$ cycles). Part I: influence of hydrogen trapped by inclusions Y.,” *Fatigue Fract. Eng. Mater. Struct.*, vol. 23, pp. 893–902, 2000.

[10] S. Nishijima and K. Kanazawa, “Stepwise S-N curve and fish-eye failure in gigacycle fatigue,” *Fatigue Fract. Eng. Mater. Struct.*, vol. 22, no. 7, pp. 601–607, 1999.

[11] S. E. Stanzl-Tschegg, Mayer H. R., A. Beste, and S. Kroll, “Fatigue and fatigue crack propagation in AlSi7Mg cast allovs under in-service loading conditions,” *Int. J. Fatigue*, vol. 17, no. 2, pp. 149–155, 1995.

[12] Q. Y. Wang, J. Y. Berard, A. Dubarre, G. Baudry, S. Rathery, and C. Bathias, “Gigacycle fatigue of ferrous alloys,” *Fatigue Fract. Eng. Mater. Struct.*, vol. 22, no. 8, pp. 667–672, 1999.

[13] C. M. Sonsino, “Course of SN-curves especially in the high-cycle fatigue regime with regard to component design and safety,” *Int. J. Fatigue*, vol. 29, no. 12, pp. 2246–2258, 2007.

[14] U. Essmann, U. Gösele, and H. Mughrabi, “A model of extrusions and intrusions in fatigued metals I. Point-defect production and the growth of extrusions,” *Philos. Mag. A*, vol. 44, no. 2, pp. 405–426, 1981.

[15] H. Mughrabi, “Fatigue mechanisms in the ultrahigh regime,” in *9th International Fatigue Congress*, 2006.

[16] H. Mughrabi, “Specific features and mechanisms of fatigue in the ultrahigh-cycle regime,” *Int. J. Fatigue*, vol. 28, no. 11, pp. 1501–1508, 2006.

[17] H. Mughrabi, “On ‘multi-stage’ fatigue life diagrams and the relevant life-controlling mechanisms in ultrahigh-cycle fatigue,” *Fatigue Fract. Eng. Mater. Struct.*, vol. 25, no. 8–9, pp. 755–764, 2002.

[18] B. Pyttel, D. Schwerdt, and C. Berger, “Very high cycle fatigue - Is there a fatigue limit?,” *Int. J. Fatigue*, vol. 33, no. 1, pp. 49–58, 2011.

[19] T. Sakai, Y. Sato, and N. Oguma, “Characteristic S-N properties of high-carbon-chromium-bearing steel under axial loading in long-life fatigue,” *Fatigue Fract. Eng. Mater. Struct.*, vol. 25, pp. 765–773, 2002.

[20] Y. Murakami, M. Takada, and T. Toriyama, “Super-Long Life Tension-Compression Fatigue Properties of Quenched and Tempered 0.46% Carbon Steel,” *Int. J. Fatigue*, vol. 20, no. 9, pp. 661–667, 1998.

[21] K. J. Miller and W. J. O’Donnell, “The fatigue limit and its elimination,” *Fatigue Fract. Eng. Mater. Struct.*, vol. 22, no. 7, pp. 545–557, 1999.

[22] T. Sakai, “Effect of stress ratio on long life fatigue behavior of high carbon chromium bearing steel under axial loading,” *Int. J. Fatigue*, vol. 28, pp. 1547–1554, 2006.

[23] J. H. Zuo, Z. G. Wang, and E. H. Han, “Effect of microstructure on ultra-high cycle fatigue behavior of Ti-6Al-4V,” *Mater. Sci. Eng. A*, vol. 473, no. 1–2, pp. 147–152, 2008.

[24] D. Wagner, C. Wang, Z. Huang, and C. Bathias, “Surface crack initiation mechanism for body centered cubic materials in the gigacycle fatigue domain,” *Int. J. Fatigue*, vol. 93, pp. 292–300, 2016.

[25] M. Sauzay and P. Gilormini, “Influence of surface effects on fatigue of microcracks nucleation,” *Theor. Appl. Fract. Mech.*, vol. 38, pp. 53–62, 2002.

[26] W. Li, T. Sakai, M. Wakita, and S. Mimura, “Effect of surface finishing and loading condition on competing failure mode of clean spring steel in very high cycle fatigue regime,” *Mater. Sci. Eng. A*, vol. 552, pp. 301–309, 2012.

[27] W. Li, H. Yuan, Z. Sun, and Z. Zhang, “Surface vs. interior failure behaviors in a structural steel under gigacycle fatigue: Failure analysis and life prediction,” *Int. J. Fatigue*, vol. 64, pp. 42–53, 2014.

[28] S. Kovacs, T. Beck, and L. Singheiser, “Influence of mean stresses on fatigue life and damage of a turbine blade steel in the VHCF-regime,” *Int. J. Fatigue*, vol. 49, pp. 90–99, 2013.

[29] V. Gaur, V. Doquet, E. Persent, C. Mareau, E. Roguet, and J. Kittel, “Surface versus internal fatigue crack initiation in steel: Influence of mean stress,” *Int. J. Fatigue*, vol. 82, pp. 437–448, 2015.

[30] T. Sakai *et al.*, “A review on fatigue fracture modes of structural metallic materials in very high cycle regime,” *Int. J. Fatigue*, pp. 1–13, 2016.

[31] K. Shiozawa, Y. Morii, S. Nishino, and L. Lu, “Subsurface crack initiation and propagation mechanism in high-strength steel in a very high cycle fatigue regime,” *Int. J. Fatigue*, vol. 28, pp. 1521–1532, 2006.

[32] M. Bao-Tong and C. Laird, “Overview of fatigue behavior in copper single crystals-I. Surface morphology and stage I crack initiation sites for tests at constant strain amplitude,” *Acta Metall.*, vol. 37, no. 2, pp. 325–336, 1989.

[33] C. Laird, “The fatigue limits of metals,” *Mater. Sci. Eng.*, vol. 22, no. C, pp. 231–236, 1976.

[34] V. Doquet, “Plasticité cyclique et amorçage de fissures en fatigue,” in *Endommagement et rupture des matériaux 1, généralités, matériaux métalliques*, M. Clavel and P. Bompard, Eds. Paris: Lavoisier, 2009, pp. 135–172.

[35] J. Polak, “On the Role of Point Defects in Fatigue Crack Initiation,” *Mater. Sci. Eng.*, vol. 92, pp. 71–80, 1987.

[36] P. J. E. Forsyth, “Fatigue damage and crack growth in aluminium alloys,” *Acta Metall.*, vol. 11, no. 7, pp. 703–715, 1963.

[37] N. Thompson and N. J. Wadsworth, “Metal fatigue,” *Adv. Phys.*, vol. 7, no. 25, pp. 72–169, 1958.

[38] N. Farabi, D. L. Chen, J. Li, Y. Zhou, and S. J. Dong, “Microstructure and mechanical properties of laser welded DP600 steel joints,” vol. 527, pp. 1215–1222, 2010.

[39] J. Polák and J. Man, “Fatigue crack initiation - The role of point defects,” *Int. J. Fatigue*, vol. 65, pp. 18–27, 2014.

[40] H. Mughrabi, “Cyclic Slip Irreversibilities and the Evolution of Fatigue Damage,” *Metall. Mater. Trans. B*, vol. 40, no. 4, pp. 431–453, 2009.

[41] Y. Furuya, “Size effects in gigacycle fatigue of high-strength steel under ultrasonic fatigue testing,” *Procedia Eng.*, vol. 2, no. 1, pp. 485–490, 2010.

[42] C. Bathias, “Coupling effect of plasticity, thermal dissipation and metallurgical stability in ultrasonic fatigue,” *Int. J. Fatigue*, vol. 60, pp. 18–22, 2014.

[43] K. Tanaka and T. Mura, “A theory of fatigue crack initiation at inclusions,” *Metall. Trans. A*, vol. 13, no. 1, pp. 117–123, 1982.

[44] H. Deng, W. Li, T. Sakai, and Z. Sun, “Very high cycle fatigue failure analysis and life prediction of Cr-Ni-W gear steel based on crack initiation and growth behaviors,” *Materials*, vol. 8, no. 12, pp. 8338–8354, 2015.

[45] A. Zhao, J. Xie, C. Sun, Z. Lei, and Y. Hong, “Effects of strength level and loading frequency on very-high-cycle fatigue behavior for a bearing steel,” *Int. J. Fatigue*, vol.

38, pp. 46–56, 2012.

[46] T. Sakai, “Review and Prospects for Current Studies on Very High Cycle Fatigue of Metallic Materials for Machine Structural Use,” vol. 3, no. 3, pp. 425–439, 2009.

[47] P. Grad, B. Reuscher, A. Brodyanski, M. Kopnarski, and E. Kerscher, “Mechanism of fatigue crack initiation and propagation in the very high cycle fatigue regime of high-strength steels,” *Scr. Mater.*, vol. 67, no. 10, pp. 838–841, 2012.

[48] T. Nakamura, H. Oguma, and Y. Shinohara, “The effect of vacuum-like environment inside sub-surface fatigue crack on the formation of ODA fracture surface in high strength steel,” *Procedia Eng.*, vol. 2, no. 1, pp. 2121–2129, 2010.

[49] A. Zhao, J. Xie, C. Sun, Z. Lei, and Y. Hong, “Prediction of threshold value for FGA formation,” *Mater. Sci. Eng. A*, vol. 528, no. 22–23, pp. 6872–6877, 2011.

[50] T. Sakai, A. Kokubu, S. Kikuchi, H. Tanaka, F. Ikai, and K. Okumoto, “A Study on Very High Cycle Fatigue Property of High Strength Steel for Particular Use as Medical Tablets Compressing Punches,” *Key Eng. Mater.*, vol. 664, pp. 221–230, 2015.

[51] A. J. McEvily, T. Nakamura, H. Oguma, K. Yamashita, H. Matsunaga, and M. Endo, “On the mechanism of very high cycle fatigue in Ti-6Al-4V,” *Scr. Mater.*, vol. 59, no. 11, pp. 1207–1209, 2008.

[52] E. Takeuchi, Y. Furuya, N. Nagashima, and S. Matsuoka, “The effect of frequency on the giga-cycle fatigue properties of a Ti-6Al-4V alloy,” *Fatigue Fract. Eng. Mater. Struct.*, vol. 31, no. 7, pp. 599–605, 2008.

[53] H. Oguma and T. Nakamura, “Fatigue crack propagation properties of Ti – 6Al – 4V in vacuum environments,” *Int. J. Fatigue*, vol. 50, pp. 89–93, 2013.

[54] Y. Yu, J. L. Gu, B. Z. Bai, Y. B. Liu, and S. X. Li, “Very high cycle fatigue mechanism of carbide-free bainite/martensite steel micro-alloyed with Nb,” *Mater. Sci. Eng. A*, vol. 527, no. 1–2, pp. 212–217, 2009.

[55] Y. Yu, J. L. Gu, L. Xu, F. L. Shou, B. Z. Bai, and Y. B. Liu, “Very high cycle fatigue behaviors of Mn-Si-Cr series Bainite/Martensite dual phase steels,” *Mater. Des.*, vol. 31, no. 6, pp. 3067–3072, 2010.

[56] Y. Yu, J. L. Gu, F. L. Shou, L. Xu, B. Z. Bai, and Y. B. Liu, “Competition mechanism between microstructure type and inclusion level in determining VHCF behavior of bainite/martensite dual phase steels,” *Int. J. Fatigue*, vol. 33, no. 3, pp. 500–506, 2011.

[57] T. J. George, J. Seidt, M. H. Herman Shen, T. Nicholas, and C. J. Cross, “Development of a novel vibration-based fatigue testing methodology,” *Int. J. Fatigue*, vol. 26, no. 5, pp. 477–486, 2004.

[58] T. Nicholas, “Step loading for very high cycle fatigue,” *Fatigue Fract. Eng. Mater. Struct.*, vol. 25, no. 8–9, pp. 861–869, 2002.

[59] N. Theodore, *High Cycle Fatigue, A Mechanics of Materials Perspective*. Elsevier Ltd, 2006.

[60] S. Stanzl-Tschegg, “Very high cycle fatigue measuring techniques,” *Int. J. Fatigue*, vol. 60, pp. 2–17, 2014.

[61] T. Sakai, H. Harada, and N. Oguma, “Crack initiation mechanism of bearing steel in very high cycle fatigue,” in *Procedeeng of European Conference of Fracture*, 2006.

[62] K. Yamaguchi *et al.*, “Gigacycle fatigue data sheets for advanced engineering materials,” *Sci. Technol. Adv. Mater.*, vol. 8, no. 7–8, pp. 545–551, 2007.

[63] Y. Furuya, T. Abe, and S. Matsuoka, “10^10-cycle fatigue properties of 1800 MPa-class JIS-SUP7 spring steel,” *Fatigue Fract. Eng. Mater. Struct.*, vol. 26, no. 7, pp. 641–645, 2003.

[64] Y. Hong, Z. Lei, C. Sun, and A. Zhao, “Propensities of crack interior initiation and early growth for very-high-cycle fatigue of high strength steels,” *Int. J. Fatigue*, vol. 58, pp. 144–151, 2014.

[65] C. Zhou, M. Wang, W. Hui, H. Dong, L. Wang, and R. Wu, “Rotating bending fatigue properties of two case hardening steels after nitriding treatment,” *Mater. Des.*, vol. 46, no. 76, pp. 539–545, 2013.

[66] Z. Lei, Y. Hong, J. Xie, C. Sun, and A. Zhao, “Effects of inclusion size and location on very-high-cycle fatigue behavior for high strength steels,” *Mater. Sci. Eng. A*, vol. 558, pp. 234–241, 2012.

[67] S. Stanzl, “A new experimental method for measuring life time and crack growth of materials under multi-stage and random loadings,” *Ultrasonics*, vol. 19, no. 6, pp. 269–272, 1981.

[68] C. Bathias and P. C. Paris, *Gigacycle Fatigue in Mechanical Practice*. New York: Marcel Dekker, 2005.

[69] W. P. Mason, *Piezoelectric Crystals and Their Application to Ultrasonics*. New York: Van Nostrad, 1950.

[70] E. A. Neppiras, “Techniques and equipment for fatigue testing at very high frequencies,” in *Proceedings of the American Society for Testing Materials 59*, Philadelphia, 1959, pp. 691–709.

[71] J. Awatani, K. Katagiri, A. Omura, and T. Shoraishi, “A Study of the Fatigue Limit of Copper,” *Metall. Trans. A*, vol. 6, no. 5, pp. 1029–1034, 1975.

[72] B. Weiss and R. Stickler, “Ultrasonic fatigue testing of thin-walled stainless steel tubes,” *Metall. Trans.*, vol. 1, no. 4, pp. 1057–1060, 1970.

[73] W. Hessler, H. Müllner, B. Weiss, and R. Stickler, “Near-threshold behaviour of polycrystalline copper,” *Met. Sci.*, vol. 15, no. 5, pp. 225–230, 1981.

[74] S. E. Stanzl-Tschegg, “Fracture mechanisms and fracture mechanics at ultrasonic frequencies,” *Fatigue Fract. Eng. Mater. Struct.*, vol. 22, no. 7, pp. 567–579, 1999.

[75] S. Stanzl and E. Tschegg, “Fatigue crack growth and threshold measurements at very high frequencies (20 kHz),” *Int. Mater. Rev.*, vol. 44, no. 1, pp. 1–34, 1999.

[76] W. Tieying and C. Bathias, “Application of fracture mechanics concepts in ultrasonic fatigue,” *Eng. Fract. Mech.*, vol. 47, no. 5, pp. 683–690, 1994.

[77] J. Ni and C. Bathias, “Development of an ultrasonic fatigue device and its application in fatigue behaviour studies,” in *10th International Conference on Experimental Mechanics*, 1994.

[78] R. Ebara, “The present situation and future problems in ultrasonic fatigue testing - Mainly reviewed on environmental effects and materials’ screening,” *Int. J. Fatigue*, vol. 28, no. 11, pp. 1465–1470, 2006.

[79] H. Mayer, “Recent developments in ultrasonic fatigue,” *Fatigue Fract. Eng. Mater. Struct.*, vol. 39, no. 1, pp. 3–29, 2016.

[80] B. Holper, H. Mayer, A. K. Vasudevan, and S. E. Stanzl-Tschegg, “Near threshold fatigue crack growth in aluminium alloys at low and ultrasonic frequency: Influences of specimen thickness, strain rate, slip behaviour and air humidity,” *Int. J. Fatigue*, vol. 25, no. 5, pp. 397–411, 2003.

[81] N. Schneider, J. Boddecker, C. Berger, and M. Oechsner, “Frequency effect and influence of testing technique on the fatigue behaviour of quenched and tempered steel and aluminium alloy,” *Int. J. Fatigue*, vol. 93, pp. 224–231, 2016.

[82] N. Tsutsumi, Y. Murakami, and V. Doquet, “Effect of test frequency on fatigue strength of low carbon steel,” *Fatigue Fract. Eng. Mater. Struct.*, vol. 32, pp. 473–483, 2009.

[83] I. Nonaka, S. Setowaki, and Y. Ichikawa, “Effect of load frequency on high cycle fatigue strength of bullet train axle steel,” *Int. J. Fatigue*, vol. 60, pp. 43–47, 2014.

[84] H. Q. Liu, Q. Y. Wang, Z. Y. Huang, and Z. J. Teng, “High-Cycle Fatigue and Thermal Dissipation Investigations for Low Carbon Steel Q345,” *Key Eng. Mater.*, vol. 664, pp. 305–313, 2015.

[85] B. Guennec, A. Ueno, T. Sakai, M. Takanashi, and Y. Itabashi, “Effect of the loading frequency on fatigue properties of JIS S15C low carbon steel and some discussions based on micro-plasticity behavior,” *Int. J. Fatigue*, vol. 66, pp. 29–38, 2014.

[86] B. Guennec, A. Ueno, T. Sakai, M. Takanashi, Y. Itabashi, and M. Ota, “Dislocation-based interpretation on the effect of the loading frequency on the fatigue properties of JIS S15C low carbon steel,” *Int. J. Fatigue*, vol. 70, pp. 328–341, 2015.

[87] Y. Furuya, S. Torizuka, E. Takeuchi, M. Bacher-Höchst, and M. Kuntz, “Ultrasonic fatigue testing on notched and smooth specimens of ultrafine-grained steel,” *Mater. Des.*, vol. 37, pp. 515–520, 2012.

[88] T. Magnin and J. H. Driver, “The influence of strain rate on the low cycle fatigue properties of single crystals and polycrystals of two ferritic alloys,” *Mater. Sci. Eng.*, vol. 39, no. 2, pp. 175–185, 1979.

[89] S. Schmid *et al.*, “Effect of frequency and biofuel E85 on very high cycle fatigue

behaviour of the high strength steel X90CrMoV18," *Int. J. Fatigue*, vol. 60, pp. 90–100, 2014.

[90] Y. Furuya, S. Matsuoka, T. Abe, and K. Yamaguchi, "Gigacycle fatigue properties for high-strength low-alloy steel at 100 Hz, 600 Hz, and 20 kHz," *Scr. Mater.*, vol. 46, no. 2, pp. 157–162, 2002.

[91] I. Marines *et al.*, "Ultrasonic fatigue tests on bearing steel AISI-SAE 52100 at frequency of 20 and 30 kHz," *Int. J. Fatigue*, vol. 25, no. 9–11, pp. 1037–1046, 2003.

[92] N. Ranc, D. Wagner, and P. C. Paris, "Study of thermal effects associated with crack propagation during very high cycle fatigue tests," *Acta Mater.*, vol. 56, no. 15, pp. 4012–4021, 2008.

[93] W. J. Peng, B. W. Qiu, R. F. Li, and H. Xue, "Ultrasonic Fatigue Tests on a High Strength Steel for Welded Structure," *Adv. Mater. Res.*, vol. 503–504, pp. 714–717, 2012.

[94] W. Peng, Y. Zhang, B. Qiu, and H. Xue, "A Brief Review of the Application and Problems in Ultrasonic Fatigue Testing," *AASRI Procedia*, vol. 2, pp. 127–133, 2012.

[95] N. Ranc, V. Favier, B. Munier, F. Vales, G. Thoquenne, and F. Lefebvre, "Thermal Response of C45 Steel in High and Very High Cycle Fatigue," *Procedia Eng.*, vol. 133, pp. 265–271, 2015.

[96] D. Wagner, N. Ranc, C. Bathias, and P. C. Paris, "Fatigue crack initiation detection by an infrared thermography method," *Fatigue Fract. Eng. Mater. Struct.*, vol. 33, no. 1, pp. 12–21, 2010.

[97] C. Stromeyer, "The determination of fatigue limits under alternating stress conditions," *Proc. Roy. Soc. London*, vol. A90, pp. 411–425, 1914.

[98] M. P. Luong, "Fatigue limit evaluation of metals using an infrared thermographic technique," *Mech. Mater.*, vol. 28, no. 1–4, pp. 155–163, 1998.

[99] R. De Finis, D. Palumbo, F. Ancona, and U. Galietti, "Fatigue limit evaluation of various martensitic stainless steels with new robust thermographic data analysis," *Int. J. Fatigue*, vol. 74, pp. 88–96, 2015.

[100] G. La Rosa and A. Risitano, "Thermographic methodology for rapid determination of

the fatigue limit of materials and mechanical components," *Int. J. Fatigue*, vol. 22, no. 1, pp. 65–73, 2000.

[101] F. Curà, G. Curti, and R. Sesana, "A new iteration method for the thermographic determination of fatigue limit in steels," *Int. J. Fatigue*, vol. 27, no. 4, pp. 453–459, 2005.

[102] G. Meneghetti, "Analysis of the fatigue strength of a stainless steel based on the energy dissipation," *Int. J. Fatigue*, vol. 29, no. 1, pp. 81–94, 2007.

[103] T. Boulanger, A. Chrysochoos, C. Mabru, and A. Galtier, "Calorimetric analysis of dissipative and thermoelastic effects associated with the fatigue behavior of steels," *Int. J. Fatigue*, vol. 26, no. 3, pp. 221–229, 2004.

[104] R. Munier, C. Doudard, S. Calloch, and B. Weber, "Determination of high cycle fatigue properties of a wide range of steel sheet grades from self-heating measurements," *Int. J. Fatigue*, vol. 63, pp. 46–61, 2014.

[105] Q. Guo, X. Guo, J. Fan, R. Syed, and C. Wu, "An energy method for rapid evaluation of high-cycle fatigue parameters based on intrinsic dissipation," *Int. J. Fatigue*, vol. 80, pp. 136–144, 2015.

[106] D. Krewerth, A. Weidner, and H. Biermann, "Application of in situ thermography for evaluating the high-cycle and very high-cycle fatigue behaviour of cast aluminium alloy AlSi7Mg (T6)," *Ultrasonics*, vol. 53, no. 8, pp. 1441–1449, 2013.

[107] H. Xue, D. Wagner, N. Ranc, and E. Bayraktar, "Thermographic analysis in ultrasonic fatigue tests," *Fatigue Fract. Eng. Mater. Struct.*, vol. 29, no. 7, pp. 573–580, 2006.

[108] X. G. Wang, V. Crupi, C. Jiang, and E. Guglielmino, "Quantitative Thermographic Methodology for fatigue life assessment in a multiscale energy dissipation framework," *Int. J. Fatigue*, vol. 81, pp. 249–256, 2015.

[109] A. Blanche, A. Chrysochoos, N. Ranc, and V. Favier, "Dissipation Assessments During Dynamic Very High Cycle Fatigue Tests," *Exp. Mech.*, vol. 55, no. 4, pp. 699–709, 2015.

[110] V. Favier *et al.*, "Very High Cycle Fatigue for single phase ductile materials: Comparison between α-iron, copper and α-brass polycrystals," *Int. J. Fatigue*, vol. 93, pp. 326–338, 2016.

[111] J. Bach, J. J. Möller, M. Göken, E. Bitzek, and H. W. Höppel, “On the transition from plastic deformation to crack initiation in the high- and very high-cycle fatigue regimes in plain carbon steels,” *Int. J. Fatigue*, vol. 93, pp. 281–291, 2016.

[112] D. Krewerth, T. Lippmann, A. Weidner, and H. Biermann, “Application of full-surface view in situ thermography measurements during ultrasonic fatigue of cast steel G42CrMo4,” *Int. J. Fatigue*, vol. 80, pp. 459–467, 2015.

[113] C. Wang, A. Blanche, D. Wagner, A. Chrysochoos, and C. Bathias, “Dissipative and microstructural effects associated with fatigue crack initiation on an Armco iron,” *Int. J. Fatigue*, vol. 58, pp. 152–157, 2014.

[114] V. Crupi, G. Epasto, E. Guglielmino, and G. Risitano, “Analysis of temperature and fracture surface of AISI4140 steel in very high cycle fatigue regime,” *Theor. Appl. Fract. Mech.*, vol. 80, pp. 22–30, 2015.

[115] Z. Y. Huang, N. Ranc, and D. Wagner, “Dislocations Gliding Study by IR Thermography in C-Mn Steels with Different Solute Atoms Content in the Gigacycle Fatigue Domain,” *Key Eng. Mater.*, vol. 664, pp. 177–187, 2015.

[116] V. Crupi, G. Epasto, E. Guglielmino, and A. Squillace, “Influence of Microstructure [Alpha + Beta and Beta] on Very High Cycle Fatigue Behavior of Ti-6Al-4V Alloy,” *Int. J. Fatigue*, vol. 95, pp. 64–75, 2016.

[117] Z. Y. Huang, Q. Y. Wang, D. Wagner, and C. Bathias, “A very high cycle fatigue thermal dissipation investigation for titanium alloy TC4,” *Mater. Sci. Eng. A*, vol. 600, pp. 153–158, 2014.

[118] Z. Y. Huang, Q. Y. Wang, D. Wagner, C. Bathias, and J. L. Chaboche, “A rapid scatter prediction method for very high cycle fatigue,” *Fatigue Fract. Eng. Mater. Struct.*, vol. 36, no. 5, pp. 462–468, 2013.

[119] C. Mareau, V. Favier, B. Weber, A. Galtier, and M. Berveiller, “Micromechanical modeling of the interactions between the microstructure and the dissipative deformation mechanisms in steels under cyclic loading,” *Int. J. Plast.*, vol. 32–33, pp. 106–120, 2012.

[120] A. Giertler and U. Krupp, “Investigation of the damage mechanisms during very high cycle fatigue (VHCF) of a tempered carbon steel,” *Procedia Struct. Integr.*, vol. 2, pp.

1207–1212, 2016.

[121] O. Bouaziz, H. Zurob, and M. Huang, “Driving force and logic of development of advanced high strength steels for automotive applications,” *Steel Res. Int.*, vol. 84, no. 10, pp. 937–947, 2013.

[122] G. Jha, S. Das, A. Lodh, and A. Haldar, “Development of hot rolled steel sheet with 600MPa UTS for automotive wheel application,” *Mater. Sci. Eng. A*, vol. 552, pp. 457–463, 2012.

[123] S. Majumdar, S. Roy, and K. K. Ray, “Fatigue performance of dual-phase steels for automotive wheel application,” *Fatigue Fract. Eng. Mater. Struct.*, vol. 40, no. 3, pp. 315–332, 2017.

[124] N. Saeidi, F. Ashrafizadeh, B. Niroumand, and F. Barlat, “Evaluation of fracture micromechanisms in a fine-grained dual phase steel during uniaxial tensile deformation,” *Steel Res. Int.*, vol. 85, no. 9, pp. 1386–1392, 2014.

[125] “Dual phase steels.” [Online]. Available: http://www.dierk-raabe.com/dual-phase-steels/.

[126] C. C. Tasan *et al.*, “An Overview of Dual-Phase Steels: Advances in Microstructure-Oriented Processing and Micromechanically Guided Design,” *Annu. Rev. Mater. Res.*, vol. 45, no. 1, pp. 391–431, 2014.

[127] S. Li, Y. Kang, and S. Kuang, “Effects of microstructure on fatigue crack growth behavior in cold-rolled dual phase steels,” *Mater. Sci. Eng. A*, vol. 612, pp. 153–161, 2014.

[128] M. J. Hadianfard, “Low cycle fatigue behavior and failure mechanism of a dual-phase steel,” *Mater. Sci. Eng. A*, vol. 499, pp. 493–499, 2009.

[129] Y. Motoyashiki and A. Bru, “Microstructural influence on small fatigue cracks in a ferritic – martensitic steel,” *Eng. Fract. Mech.*, vol. 75, pp. 768–778, 2008.

[130] S. K. Akay, M. Yazici, A. Bayram, and A. Avinc, “Fatigue life behaviour of the dual-phase low carbon steel sheets,” *J. Mater. Process. Technol.*, vol. 209, no. 7, pp. 3358–3365, 2009.

[131] M. Okayasu, “Fatigue properties of ultra-fine grained dual phase ferrite / martensite low carbon steel,” *Int. J. Fatigue*, vol. 30, pp. 1358–1365, 2008.

[132] T. Hilditch, H. Beladi, P. Hodgson, and N. Stanford, “Role of microstructure in the low cycle fatigue of multi-phase steels,” *Mater. Sci. Eng. A*, vol. 534, pp. 288–296, 2012.

[133] C. Doudard, S. Calloch, P. Cugy, A. Galtier, and F. Hild, “A probabilistic two-scale model for high-cycle fatigue life predictions,” *Fatigue Fract. Eng. Mater. Struct.*, vol. 28, no. 3, pp. 279–288, 2005.

[134] C. Doudard and S. Calloch, “Influence of hardening type on self-heating of metallic materials under cyclic loadings at low amplitude,” *Eur. J. Mech. A/Solids*, vol. 28, no. 2, pp. 233–240, 2009.

[135] A. Chrysochoos, B. Berthel, F. Latourte, S. Pagano, B. Wattrisse, and B. Weber, “Local energy approach to steel fatigue,” *Strain*, vol. 44, no. 4, pp. 327–334, 2008.

[136] N. Connesson, F. Maquin, and F. Pierron, “Dissipated energy measurements as a marker of microstructural evolution: 316L and DP600,” *Acta Mater.*, vol. 59, no. 10, pp. 4100–4115, 2011.

[137] C. Mareau, V. Favier, B. Weber, and A. Galtier, “Influence of the free surface and the mean stress on the heat dissipation in steels under cyclic loading,” *Int. J. Fatigue*, vol. 31, no. 8–9, pp. 1407–1412, 2009.

[138] R. Munier, C. Doudard, S. Calloch, and B. Weber, “Towards a faster determination of high cycle fatigue properties taking into account the influence of a plastic pre-strain from selfheating measurements,” *Procedia Eng.*, vol. 2, no. 1, pp. 1741–1750, 2010.

[139] A. Blanche, “Effets dissipatifs en fatigue à grand et très grand nombre de cycles (PhD Thesis),” Université Montpellier 2, 2012.

[140] S. X. Li, “Effects of inclusions on very high cycle fatigue properties of high strength steels,” *Int. Mater. Rev.*, vol. 57, no. 2, pp. 92–114, 2012.

[141] U. Krupp *et al.*, “Significance and mechanism of the crack initiation process during very high cycle fatigue of duplex stainless steel,” *Procedia Eng.*, vol. 74, pp. 143–146, 2014.

[142] U. Krupp *et al.*, “The behavior of short fatigue cracks during Very High Cycle (VHCF)

Fatigue of duplex stainless steel," *Eng. Fract. Mech.*, vol. 145, pp. 197–209, 2015.

[143] B. Dönges, A. Giertler, U. Krupp, C. P. Fritzen, and H. J. Christ, "Significance of crystallographic misorientation at phase boundaries for fatigue crack initiation in a duplex stainless steel during high and very high cycle fatigue loading," *Mater. Sci. Eng. A*, vol. 589, pp. 146–152, 2014.

[144] E. Bayraktar, I. M. Garcias, and C. Bathias, "Failure mechanisms of automotive metallic alloys in very high cycle fatigue range," *Int. J. Fatigue*, vol. 28, no. 11, pp. 1590–1602, 2006.

[145] G. Chai, "The formation of subsurface non-defect fatigue crack origins," *Int. J. Fatigue*, vol. 28, no. 11, pp. 1533–1539, 2006.

[146] P. J. McGrath, "An investigation of residual stresses induced by forming process on the fatigue resistance of automotive wheels (PhD Thesis)," University of Plymouth, 2001.

[147] "ArcelorMittal." [Online]. Available: http://automotive.arcelormittal.com/.

[148] C. Bathias, "Piezoelectric fatigue testing machines and devices," *Int. J. Fatigue*, vol. 28, no. 11, pp. 1438–1445, 2006.

[149] N. Marti, "Effet de la fréquence et de la température sur les mécanismes de microplasticité en fatigue (PhD Thesis)," ENSAM, 2014.

[150] N.-L. PHUNG, "Fatigue sous très faibles amplitudes de contraintes : Analyse des mécanismes précurseurs de l'amorçage de fissures dans le cuivre polycritallin (PhD Thesis)," ENSAM, 2012.

[151] "ASTM E8, Standard Test Methods for Tension Testing of Metallic Materials," in *Annual book of ASTM Standards, American Society for Testing and Materials, Vol. 03.01*, 2012.

[152] "Evapo-Rust Super Safe Rust Remover." [Online]. Available: http://www.evapo-rust.com/.

[153] N. Torabian, V. Favier, S. Ziaei-Rad, J. Dirrenberger, F. Adamski, and N. Ranc, "Thermal response of DP600 dual-phase steel under ultrasonic fatigue loading," *Mater. Sci. Eng. A*, vol. 677, pp. 97–105, 2016.

[154] C. Doudard, S. Calloch, F. Hild, and S. Roux, “Identification of heat source fields from infrared thermography: Determination of ‘self-heating’ in a dual-phase steel by using a dog bone sample,” *Mech. Mater.*, vol. 42, no. 1, pp. 55–62, 2010.

[155] N. Torabian, V. Favier, J. Dirrenberger, F. Adamski, S. Ziaei-Rad, and N. Ranc, “Correlation of the high and very high cycle fatigue response of ferrite based steels with strain rate-temperature conditions,” *Acta Mater.*, vol. 134, pp. 40–52, 2017.

[156] I. H. Onn, N. Ahmad, and M. N. Tamin, “Fatigue Characteristics of Dual Phase Steel Sheets,” in *9th International Conference on Fracture& Strength of Solids*, 2013, pp. 1–9.

[157] C. Bathias and A. Pineau, *Fatigue of Materials and Structures*. WILEY, 2010.

[158] W. Li, T. Sakai, Q. Li, L. T. Lu, and P. Wang, “Reliability evaluation on very high cycle fatigue property of GCr15 bearing steel,” *Int. J. Fatigue*, vol. 32, no. 7, pp. 1096–1107, 2010.

[159] X. Liu, C. Sun, and Y. Hong, “Faceted crack initiation characteristics for high-cycle and very-high-cycle fatigue of a titanium alloy under different stress ratios,” *Int. J. Fatigue*, vol. 92, pp. 434–441, 2016.

[160] Y. Hong, X. Liu, Z. Lei, and C. Sun, “The formation mechanism of characteristic region at crack initiation for very-high-cycle fatigue of high-strength steels,” *Int. J. Fatigue*, vol. 89, pp. 108–118, 2015.

[161] C. R. Sohar, A. Betzwar-Kotas, C. Gierl, B. Weiss, and H. Danninger, “Gigacycle fatigue behavior of a high chromium alloyed cold work tool steel,” *Int. J. Fatigue*, vol. 30, no. 7, pp. 1137–1149, 2008.

[162] A. Seeger, “The temperature dependence of the criticla shear stress and of work-hardening of metal crystals,” *Philos. Mag. Ser. 7*, vol. 45, no. 336, pp. 771–773, 1954.

[163] H. Mughrabi, K. Herz, and X. Stark, “Cyclic deformation and fatigue behaviour of alpha-iron mono-and polycrystals,” *Int. J. Fract.*, vol. 17, no. 2, pp. 193–220, 1981.

[164] J. D. Campbell and W. G. Ferguson, “The temperature and strain rate dependence of the shear strength of mild steel,” *Philos. Mag.*, vol. 21, no. 169, pp. 63–82, 1970.

[165] A. R. Rosenfield and G. T. Hahn, “Numerical descriptions of the ambient low-temperature and high-strain rate flow and fracture behavior of plain carbon steel,” *Trans. Am. Soc. Mater.*, vol. 59, pp. 962–977, 1966.

[166] U. Essmann, U. Gösele, and H. Mughrabi, “A model of extrusions and intrusions in fatigued metals I . Point-defect production and the growth of extrusions,” *Philos. Mag. A*, vol. 44, no. September 2014, pp. 405–426, 1981.

[167] J. Polák and M. Sauzay, “Growth of extrusions in localized cyclic plastic straining,” *Mater. Sci. Eng. A*, vol. 500, pp. 122–129, 2009.

[168] J. H. Kim, M. G. Lee, D. Kim, D. K. Matlock, and R. H. Wagoner, “Hole-expansion formability of dual-phase steels using representative volume element approach with boundary-smoothing technique,” *Mater. Sci. Eng. A*, vol. 527, no. 27–28, pp. 7353–7363, 2010.

[169] A. Alaie, J. Kadkhodapour, S. Ziaei Rad, M. Asadi Asadabad, and S. Schmauder, “Formation and coalescence of strain localized regions in ferrite phase of DP600 steels under uniaxial tensile deformation,” *Mater. Sci. Eng. A*, vol. 623, pp. 133–144, 2015.

[170] Q. Lai *et al.*, “Damage and fracture of dual-phase steels : Influence of martensite volume fraction,” *Mater. Sci. Eng. A*, vol. 646, pp. 322–331, 2015.

[171] A. Pierman, O. Bouaziz, T. Pardoen, P. J. Jacques, and L. Brassart, “The influence of microstructure and composition on the plastic behaviour of dual-phase steels,” *Acta Mater.*, vol. 73, pp. 298–311, 2014.

[172] H. Shen, S. E. Podlaseck, and I. R. Kramer, “Effect of vacuum on the fatigue life of aluminum,” *Acta Metall.*, vol. 14, pp. 341–346, 1966.

[173] W. A. Wood and K. R. Sargant, “Systematic microstructural changes peculiar to fatigue deformation,” *Acta Metall.*, vol. 11, pp. 643–652, 1963.

[174] S. Guo *et al.*, “Thermographic analysis of the fatigue heating process for AZ31B magnesium alloy,” *Mater. Des.*, vol. 65, pp. 1172–1180, 2015.

[175] A. Ekrami, “High temperature mechanical properties of dual phase steels,” *Mater. Lett.*, vol. 59, no. 16, pp. 2070–2074, 2005.

[176] C. Sommer, H. Mughrabi, and D. Lochner, “Influence of temperature and carbon content on the cyclic deformation and fatigue behaviour of α-iron. Part II: Crack initiation and fatigue life,” *Acta Materialia*, vol. 46, no. 5. pp. 1537–1546, 1998.

[177] K. Pohl, P. Mayr, and E. Macherauch, “Cyclic deformation behavior of a low carbon steel in the temperature range between room temperature and 850 K,” *Int. J. Fract.*, vol. 17, no. 2, pp. 221–233, 1981.

[178] G. Schoeck, “The Portevin-Le Chatelier effect. A kinetic theory,” *Acta Metall.*, vol. 32, no. 8, pp. 1229–1234, 1984.

[179] D. V. Wilson and J. K. Tromans, “Effects of strain ageing on fatigue in low-carbon steel,” *Acta Metall.*, vol. 18, pp. 1197–1208, 1970.

[180] K. V Jata and E. A. Starke, “Fatigue Crack Growth and Fracture Toughness Behavior of an AI-Li-Cu Alloy,” *Metall. Trans. A*, vol. 17, no. 6, pp. 1011–1026, 1986.

[181] B. Guennec, A. Ueno, T. Sakai, M. Takanashi, and Y. Itabashi, “Effect of the loading frequency on fatigue properties of JIS S15C low carbon steel and some discussions based on micro-plasticity behavior,” *Int. J. Fatigue*, vol. 66, pp. 29–38, 2014.

[182] M. Vincent, Y. Nadot, and A. Dragon, “Interaction between a surface defect and grain size under high cycle fatigue loading : Experimental approach for Armco iron,” *Int. J. Fatigue*, vol. 87, pp. 81–90, 2016.

[183] C. Sommer, H. Mughrabi, and D. Lochner, “Influence of temperature and carbon content on the cyclic deformation and fatigue behaviour of α-iron. Part I. Cyclic deformation and stress–behaviour,” *Acta Materialia*, vol. 46, no. 5. pp. 1527–1536, 1998.

[184] S. Stanzl-tschegg, “Life time and cyclic slip of copper in the VHCF regime,” *Int. Journalof Fatigue*, vol. 29, pp. 2050–2059, 2007.

[185] N. L. Phung, V. Favier, N. Ranc, F. Valès, and H. Mughrabi, “Very high cycle fatigue of copper: Evolution, morphology and locations of surface slip markings,” *Int. J. Fatigue*, vol. 63, pp. 68–77, 2014.

[186] G. M. Sinclair and C. E. Feltner, “Fatigue Strength of Crystalline Solids,” in *Properties of crystalline Solids*, 1961, pp. 129–142.

[187] C. Mareau, D. Cuillerier, and F. Morel, “Experimental and numerical study of the evolution of stored and dissipated energies in a medium carbon steel under cyclic loading,” *Mech. Mater.*, vol. 60, pp. 93–106, 2013.

High and very high cycle fatigue behavior of DP600 dual-phase steel: correlation between temperature, strain rate, and deformation mechanisms

ABSTRACT :

This work is an attempt towards a better understanding of the high cycle and very high cycle fatigue behaviors of a ferritic-martensitic dual-phase steel, with a regard to temperature and strain rate effects, resulting from accelerated fatigue loading frequencies. The influence of frequency on fatigue response of DP600 steel was investigated by conducting ultrasonic and conventional low frequency fatigue tests. Fractography studies and microscopic observations on the surface of specimens were carried out to study the deformation and fracture mechanisms under low and ultrasonic frequencies. Moreover, in situ infrared thermography was carried out to investigate the thermal response and dissipative mechanisms of the material under fatigue tests. The S-N curves were determined from ultrasonic 20-kHz fatigue loadings and conventional tests at 30 Hz. Fatigue life for a given stress amplitude was found to be higher in the case of ultrasonic fatigue whereas the fatigue limit was the same for both cases. Moreover, crack initiation was always inclusion-induced under ultrasonic loading while under conventional tests it occurred at slip bands or defects on the surface. The inevitable temperature increase under ultrasonic fatigue at high stress amplitudes along with the rate dependent deformation behavior of ferrite, as a body centered cubic (BCC) structure, were found as the key parameters explaining the observed fatigue behavior and thermal response under low and ultrasonic frequencies. The discrepancies observed between conventional and ultrasonic fatigue tests were assessed through the mechanisms of screw dislocation mobility in the ferrite phase as a BCC structure. The higher fatigue life and inclusion-induced crack initiations in the case of ultrasonic loading were attributed to the dynamic strain aging, which resulted from the high temperature increases at high stress amplitudes. The existence of a transition in deformation regime from thermally-activated to athermal regime under ultrasonic fatigue loading by increasing the stress amplitude was confirmed. Below the fatigue limit, deformation occurred in thermally-activated regime while it was in athermal regime above the fatigue limit. Under conventional loading deformation occurred in athermal regime for all stress amplitudes. From the analysis of the experimental data gathered in this work, guidelines were given regarding the comparison and interpretation of S-N curves obtained from conventional and ultrasonic fatigue testing. A transition map was produced using the experimental results for DP600 steel as well as data available in the literature for other ferrite-based steels, showing the correlation between thermally-activated screw dislocation movement and the absence of failure in very high cycle fatigue.

Keywords : Very high cycle fatigue, Ultrasonic fatigue, Dual-phase steel, Frequency effect, Infrared thermography, BCC structure, Dislocations, Strain ageing.